NASA CONTRACTOR REPORT

NASA CR-1557

XB-70 STRUCTURAL MODE CONTROL SYSTEM DESIGN AND PERFORMANCE ANALYSES

by John H. Wykes, Louis U. Nardi, and Alva S. Mori

Prepared by
NORTH AMERICAN ROCKWELL CORPORATION
Los Angeles, Calif.
for Flight Research Center

NATIONAL AERONAUTICS AND SPACE ADMINISTRATION • WASHINGTON, D. C. • JULY 1970

1. Report No. NASA CR-1557	2. Government Accession No.	3. Recipient's Catalog No.
4. Title and Subtitle XB-70 STRUCTURAL MODE CONTROL SYSTEM DESIGN AND PERFORMANCE ANALYSES		5. Report Date July 1970 6. Performing Organization Code
7. Author(s) John H. Wykes, Louis U. Nardi, and Alva S. Mori		8. Performing Organization Report No.
9. Performing Organization Name and Address North American Rockwell Corporation Los Angeles Division Los Angeles, California		10. Work Unit No. 11. Contract or Grant No. NAS 4-1175 13. Type of Report and Period Covered
12. Sponsoring Agency Name and Address National Aeronautics and Space Administration Washington, D.C. 20546		14. Sponsoring Agency Code 720-02-00-02-24

15. Supplementary Notes

16. Abstract

Under a joint NASA/USAF program, a system to suppress the structural motion of flexible airframes was designed for installation and flight test on the XB-70 airplane. The system was constrained to controlling only the symmetric structural modes using the existing elevons as force generators. The minimum-change design operates through the existing pitch augmentation servo. Analytical evaluations show that the system is stable and effective in controlling motion of the first three structural modes without degrading basic handling qualities.

157 p. Refs p 156-7
1. Airplanes - XB-70

17. Key Words Suggested by Author(s)	18. Distribution Statement
XB-70 airplane - Aircraft structural response - Structural mode suppression	Unclassified - Unlimited

19. Security Classif. (of this report)	20. Security Classif. (of this page)	21. No. of Pages	22. Price*
Unclassified	Unclassified	157	$3.00

* For sale by the Clearinghouse for Federal Scientific and Technical Information Springfield, Virginia 22151

CONTENTS

LIST OF FIGURES

LIST OF TABLES

XB-70 STRUCTURAL MODE CONTROL SYSTEM DESIGN AND PERFORMANCE ANALYSES

By John H. Wykes, Louis U. Nardi, and Alva S. Mori

North American Rockwell Corporation/Los Angeles Division
Los Angeles, California

SUMMARY

Under a joint NASA/USAF program, a system to suppress the structural motion of flexible airframes was designed for installation and flight test on the XB-70 airplane. The system was constrained to controlling only the symmetric structural modes using the existing elevons as force generators. The minimum-change design operates through the existing pitch augmentation servo. Analytical evaluations show that the system is stable and effective in controlling motion of the first three structural modes without degrading basic handling qualities.

INTRODUCTION

While any aircraft flying through turbulence has the problems of increased structural loads and fatigue, degradation of handling qualities, and a rough ride to some degree, they are especially severe for a flexible aircraft because of the induced structural motion. A flexible aircraft tends to be one having a low-load-factor design requirement and an efficient (high load-carrying ability with a minimum of material) structural design. Typical of this class of aircraft are the B-52, XB-70, C-5A, Supersonic Transport (SST), and Advanced Manned Strategic Aircraft (AMSA).

While much can be done with the configuration design to minimize the effects of atmospheric turbulence on flexible aircraft, the remaining effects are still significant. Normal stability augmentation systems have been developed over the years to make up for configuration aerodynamic deficiencies in damping and frequency of the whole-vehicle motion. It was a natural next step, considering this high level of control system technology, to attempt to augment the existing low aerodynamic damping of structural motion using active control techniques. Many of the early applications of active control of structural mode principles were employed by ballistic missile booster control system designers. They had need to stabilize the structural mode dynamics which were being influenced by normal control system action. This missile work stimulated aircraft control system designers to explore these structural mode

control ideas. Some of the results from these early investigations into the conceptual feasibility of the use of active controls to stabilize structural dynamics on flexible aircraft are described in references 1 and 2. The analytical study efforts reported in references 3 through 9 investigated practical system design and evaluation techniques within the framework of more realistic and consistent flexible airplane and flight condition constraints. During approximately the same time period, the Air Force embarked upon a program to extend the structural life of the B-52. As part of this program, an automatic flight control system was designed which incorporated structural mode control features to reduce structural loads and fatigue. Reference 10 describes the design and flight test efforts of this program. Following this program, the Air Force initiated the Loads Alleviation and Mode Stabilization (LAMS) Program utilizing a B-52. The stated objectives of the LAMS Program were to demonstrate the capabilities of advanced flight control techniques to alleviate gust loads and control structural oscillations on large flexible aircraft using only conventional aerodynamic control surfaces and appropriate feedbacks. This design-flight test study has now been completed; reference 11 contains a more detailed description of this program.

Both of the previously discussed B-52 programs have provided valuable flight test information on the practical design and flight test of structural mode control systems; however, these tests were conducted at subsonic speeds on a typical subsonic flexible airplane configuration. The availability of the XB-70 offered an opportunity to evaluate design techniques and demonstrate structural mode control principles at subsonic, transonic, and supersonic speeds for a combination of vehicle geometry and flight conditions. The results of this program will provide valuable experience in designing and operating mode control systems in a typical supersonic airframe. This report discusses the results of the analytical and analog-simulator design and performance evaluation phase of a joint NASA/USAF program to flight-test a structural mode control system in the XB-70 airplane. The specific program objectives were to:

(1) Apply and verify the Identical Location of Accelerometer and Force (ILAF) techniques for damping airplane structural motion using active control principles developed under recent USAF contracts and reported in reference 5.

(2) Design the longitudinal-symmetric structural mode control system to activate the XB-70 elevons through the existing flight augmentation control system (FACS).

(3) Demonstrate the ability of the system to operate over a wide range of mach-altitude, vehicle geometry, and vehicle weight conditions.

The specific structural mode control system performance objectives were to:

(1) Reduce the structural response (and thus improve ride qualities and reduce structural loads) through increased structural mode damping.

(2) Have a minimum effect on whole-vehicle handling qualities.

Because of the use of an existing airplane, many design variables normally available to the control system designer were constrained. However, the preliminary studies of reference 5, which used the XB-70 as the study model, indicate that despite the design constraints a measurably effective system can be designed to demonstrate the ILAF structural mode control system principles in flight.

Symbols used in this report are defined in appendix A. Measurements used in the program are presented in U.S. Customary Units; the equivalent dimensions in the International System of Units may be found from the conversion table (appendix A).

BASIC VEHICLE CHARACTERISTICS

The XB-70, designed and built by the North American Rockwell Corporation, is a large, delta-wing, multiengine, jet airplane designed for supersonic cruise at a mach number of 3 and altitudes above 70,000 feet. Two airplanes were built, designated the XB-70-1 and XB-70-2. The Identical Location of Accelerometer and Force (ILAF) control system was designed for the XB-70-1. The three-view drawing (figure 1) shows the general airplane configuration and overall dimensions. The basic design incorporates a thin, low-aspect-ratio wing with a 65.57-degree sweptback leading edge, folding tips, twin vertical stabilizers, and a movable canard with trailing-edge flaps. The XB-70-1 was manufactured with the wings mounted at a geometric dihedral angle of zero. Geometric characteristics of the airplane are given in appendix B. The existing control system aspects pertinent to the integration of the new structural mode control system are covered in this section in some depth.

Flight Augmentation Control System (FACS)

The basic XB-70 FACS is a conventional command augmentation system designed to improve aircraft handling qualities through simultaneous operations with the hydromechanical column-to-surface control system. A block diagram of the specific XB-70 pitch augmentation system implementation is shown in figure 2. Pilot input transducer signals and aircraft response sensor (gyro and accelerometer) signals are blended in the FACS electronics to produce mechanical servo displacements. These motions add to, or subtract from, pilot mechanical inputs at the master cylinder to provide the designed control surface motion without force feedback to the controls. This combined signal commands the motion of the inboard elevon panel; the motion of this panel, in turn, commands the motion of all the remaining outboard panels. The primary reason for this elevon actuator arrangement was to reduce the level of valve friction as reflected at the master cylinder and servo to provide satisfactory resolution and control of the surface with the given level of system spring constant or stiffness. This arrangement results in an actuation lag from the inboard elevon panel to the outer elevon panels. With the wingtips in the 0-degree position, five outboard panels are slaved to the inboard panel. In the 25- to 65-degree wingtip position, the two outer panels are disengaged and centered, while the three remaining outboard panels are slaved to the inboard panel. In the FACS, the signals from the pilot input, gyro, and accelerometer are blended with appropriate gains and filtered to reduce the transmission of high-frequency motions. The gain levels are varied according to an altitude function from the central air data system (CADS) to compensate for changes in the effectiveness of the control surface, and the signals are transmitted to the control surface through the FACS servo.

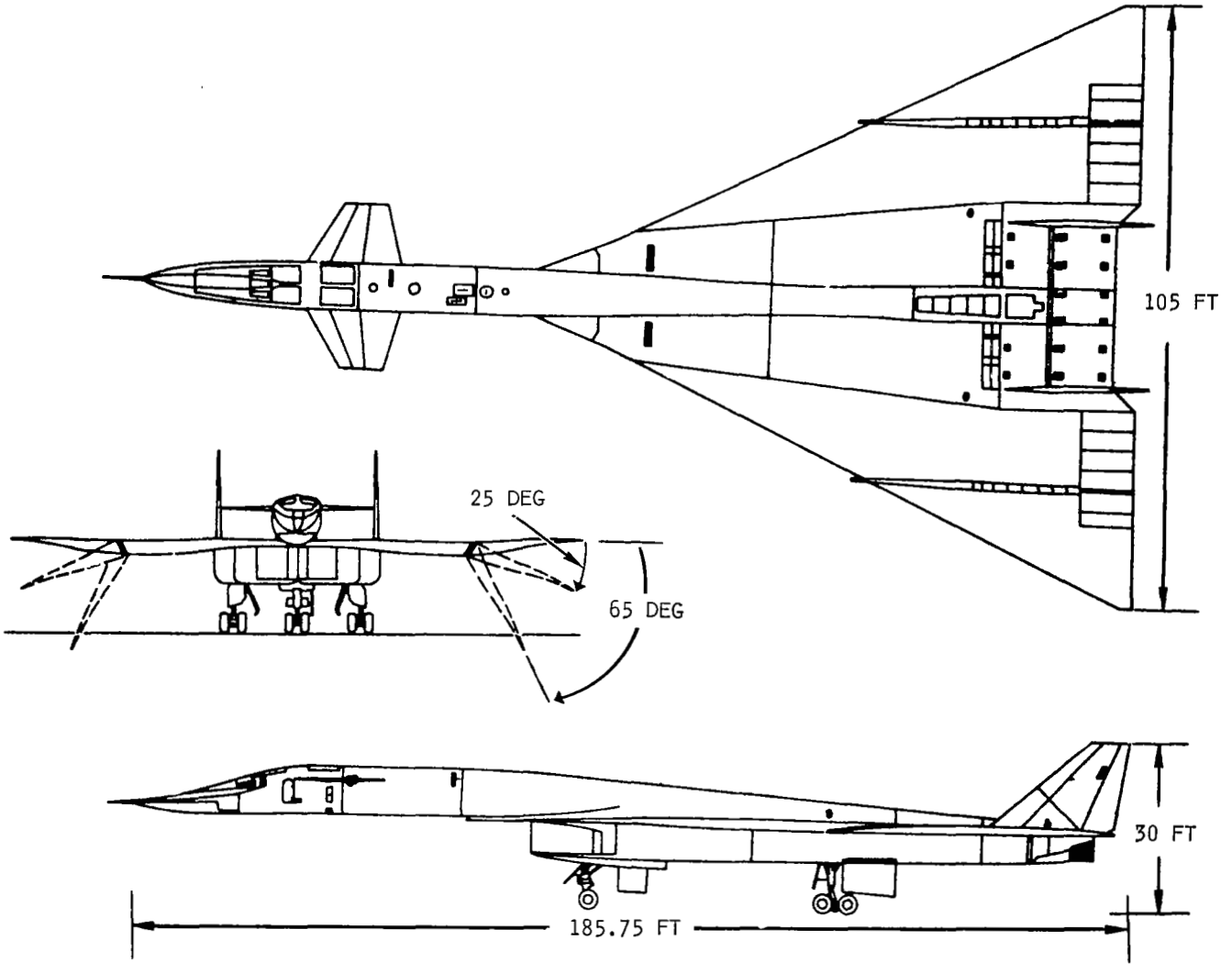

Figure 1.- XB-70-1 configuration.

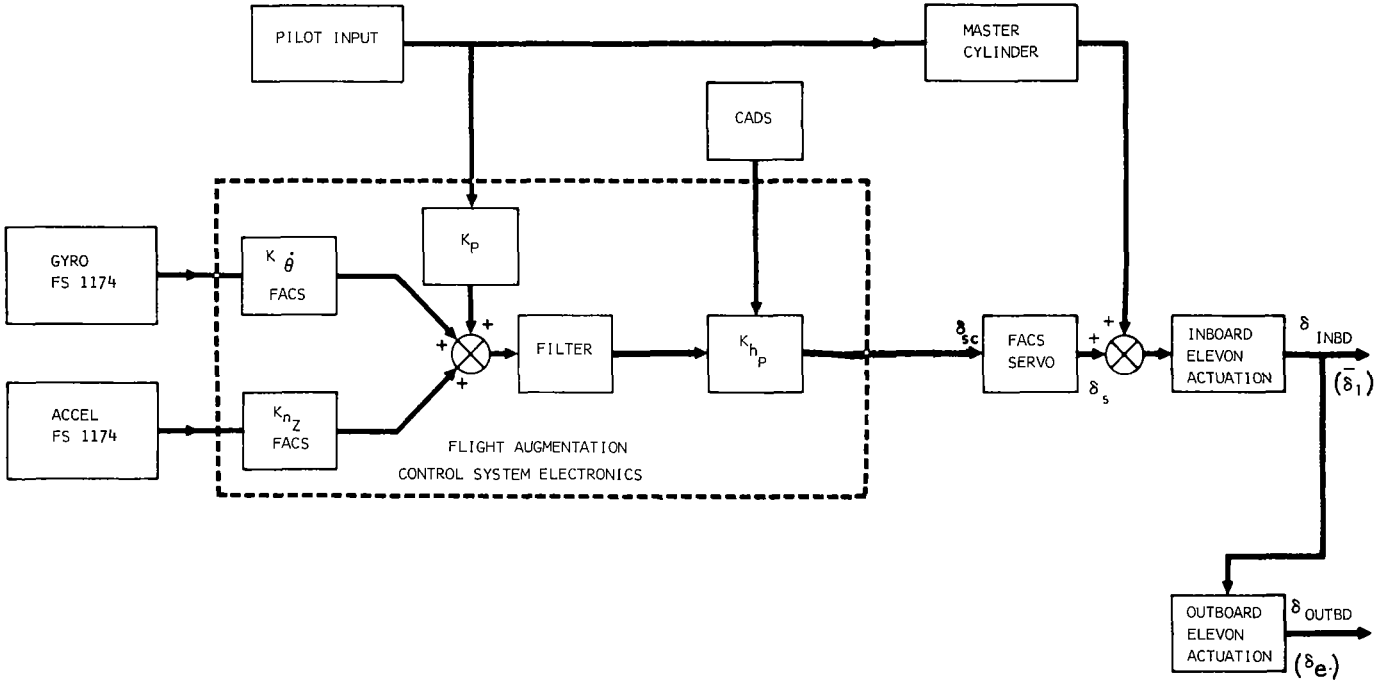

Figure 2.- XB-70 pitch flight augmentation control system.

The pitch FACS is a dual-channel mechanization with a single mechanical servo movement. The two operating channels are force summed in the servo to prevent movement of the servo unless there is agreement between the operating channels. The operation of this fail-safety concept is based upon the very high gain characteristic of the servo valve. Unbalanced differences between the channels cause full opposing pressures in the servo, resulting in a locked condition. If these differences exist beyond a specified period of time (2 seconds), the system will disengage and the servo is slowly centered. This arrangement has been called a fail-soft system in that the component failure does not result in a significant surface motion such as would be the case in a g-limiter. To provide the ability for normal operation, a balance or alinement function compensates for differences in component tolerances to prevent nuisance disengagements.

In this report, the term SAS (stability augmentation system) is used interchangeably for FACS.

Elevon surface amplitudes available.- The control surface amplitudes which can be commanded by the ILAF system in the present design are shown in figure 3. At low frequencies, the amplitude is limited by the existing servo authority (±7.5°). At higher frequencies, the amplitude is limited by the available surface rate capability. The inboard elevon panel actuators have a resolution of approximately ±0.05 degree. At this level, the outboard actuators will not be activated.

Elevon surface rates available.- The variation of available control surface rate as a function of surface load is shown in figure 4. In the XB-70, the design 28-degrees-per-second maximum no-load rate was for a worst-case situation of all actuators online and hydraulic fluid temperature of 80° F. For the typical flight condition at mach 0.90 and 25,000 feet, the wingtip is deflected, locking out the two outboard elevons. As shown on figure 4, this makes a higher surface rate available to the remaining active surfaces. A typical in-flight hydraulic temperature of 175° F shows that the lowered viscosity makes an additional increment in surface rate possible. In addition to these effects, an aiding hinge moment and apparent accumulator effect at higher frequencies can permit increased rate performance.

Pitch control system frequency response characteristics.- The form of presentation of the frequency response characteristics was determined both by the analysis approach utilized and the need to have data in a form which could match flight test measurements. The main parameters utilized in presenting these data are shown in figure 2; δ_s is the servo output motion, δ_1 is the inboard elevon motion, and δ_e the outboard elevon motion. For analysis purposes, it is convenient to use the inboard actuator motion as the reference motion. Thus, in the describing-function stability analyses to be discussed,

NOTE: NO ELEVON LOAD, δ_T = 0 DEG CONDITION

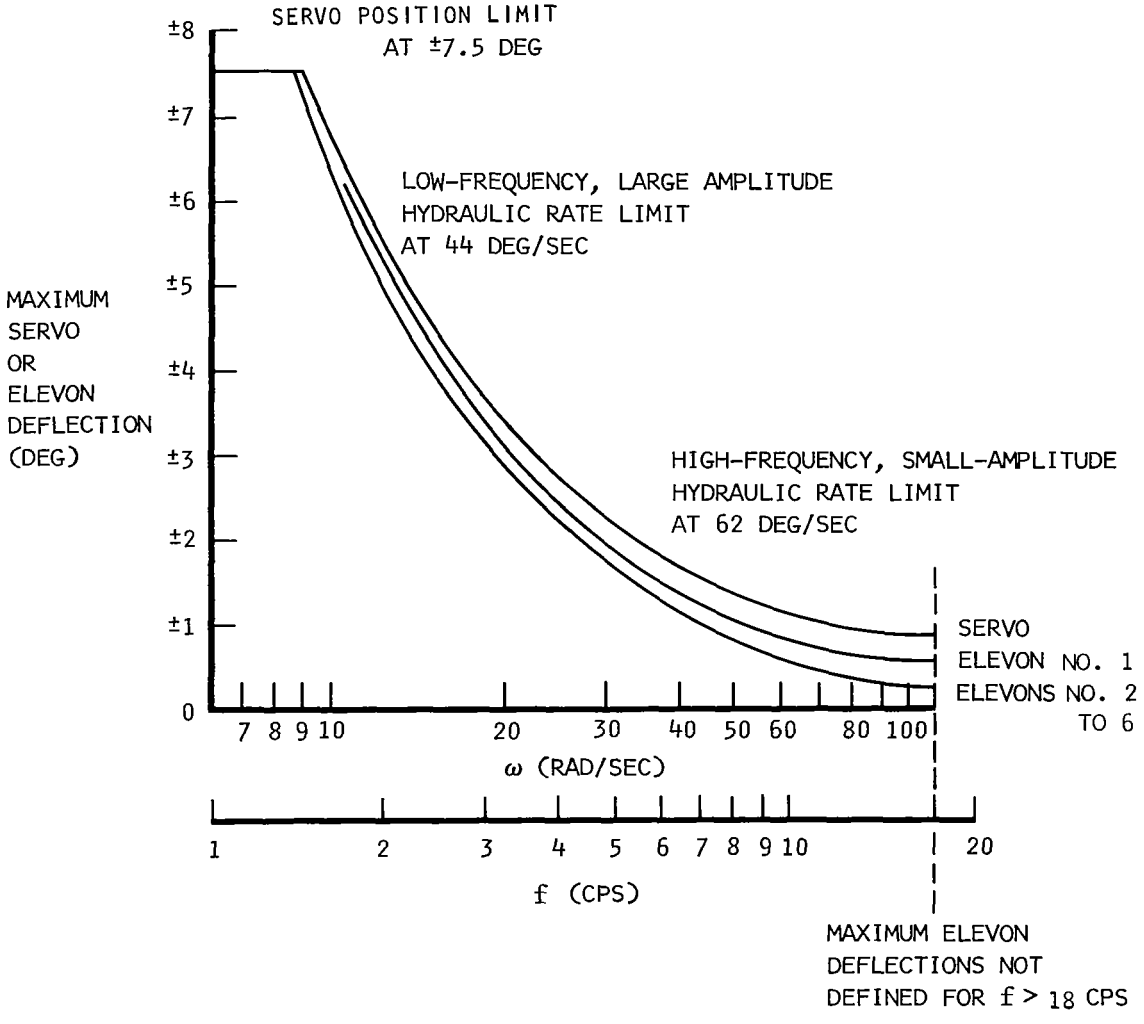

Figure 3.- Maximum SAS servo and elevon deflection limits due to hydraulic rate limits - composite simulator-airplane data.

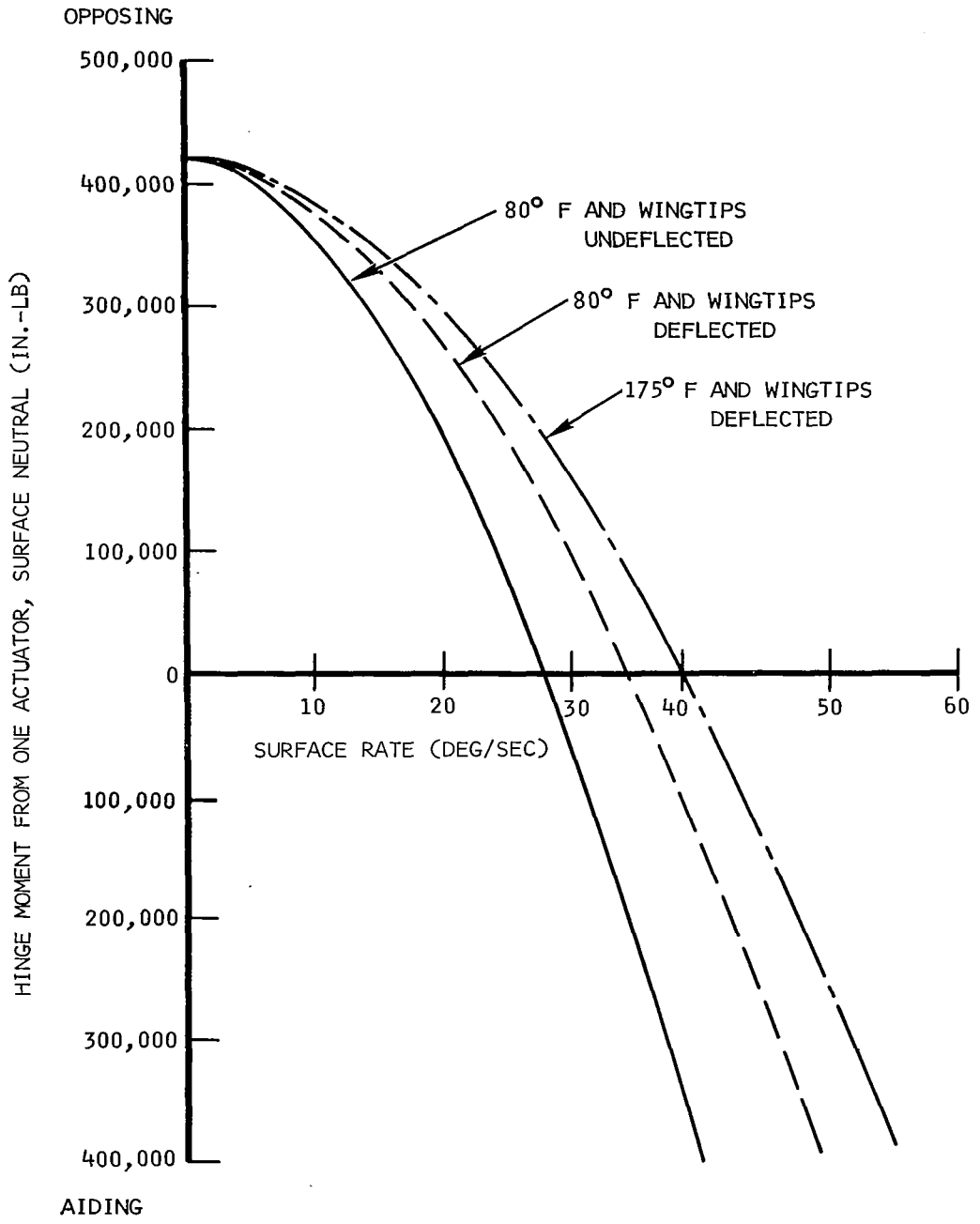

Figure 4.- Estimated effects of temperature and wingtip position on elevon deflection rates - analytical data.

the airplane frequency response is referenced to the inboard elevon motion. The outboard elevon motions are a function of this inboard elevon motion, but do not show explicitly in the analysis. In order to indicate that proper amplitude and phase relationships between the inboard and outboard elevon panels are accounted for and implied in the data, the reference inboard motion is designated $\bar{\delta}_1$. The feedback loop frequency response, then, is presented as the ratio $\bar{\delta}_1$ (output) over sensor signal input.

Since the servo and actuator data are nonlinear functions of frequency and amplitude, it is convenient to show these data as families of curves with either a constant amplitude input or output as the varying parameter. Describing-function stability analyses were most easily conducted within this format of data.

Figure 5a shows the frequency responses of the SAS servo for constant amplitudes of servo command inputs, while figure 5b shows the same frequency responses for constant amplitudes of inboard elevon motion of the varying amplitudes. These data were obtained from the XB-70 simulator. (Refer to appendix C.) The SAS servo does not exhibit any significant threshold or hysteresis effects, but rate saturation does limit the servo output, resulting in lower amplitude ratios and greater phase lags with increasing frequency as shown.

Servo motion activates the inboard actuator. The frequency response data for this are shown in figure 6a for constant inboard elevon motions of varying magnitudes and in figure 6b for constant servo output motions of varying magnitudes. The families of constant servo output at low amplitudes indicate low amplitude ratios and large phase lags for the frequency responses because of threshold and hysteresis. As the servo output amplitudes are increased, threshold and hysteresis effects decrease, but actuator rate saturations limit the maximum elevon deflections approximately inversely with frequency. These actuator rate saturations are functions of the number of elevons being driven, operating hydraulic fluid temperatures, and surface load, as well as functions of the amplitudes and frequencies of oscillations. The responses presented are no-load conditions and are composites of simulator and airplane measured data. The data of figure 7 are convenient crossplots of the data of figure 6a.

To complete the presentation of the frequency response data of the control elements from the servo through the outboard actuator, figure 8 shows the outboard elevon motion resulting from inboard elevon motion at several values of constant inboard elevon amplitudes of varying magnitudes. These data show a marked dependence on inboard elevon input amplitudes; inputs above ± 0.1 degree must be applied before the outboard elevons show any appreciable response throughout the frequency range of interest ($f \approx 10$ cps). Airplane test results were the basis of the data shown.

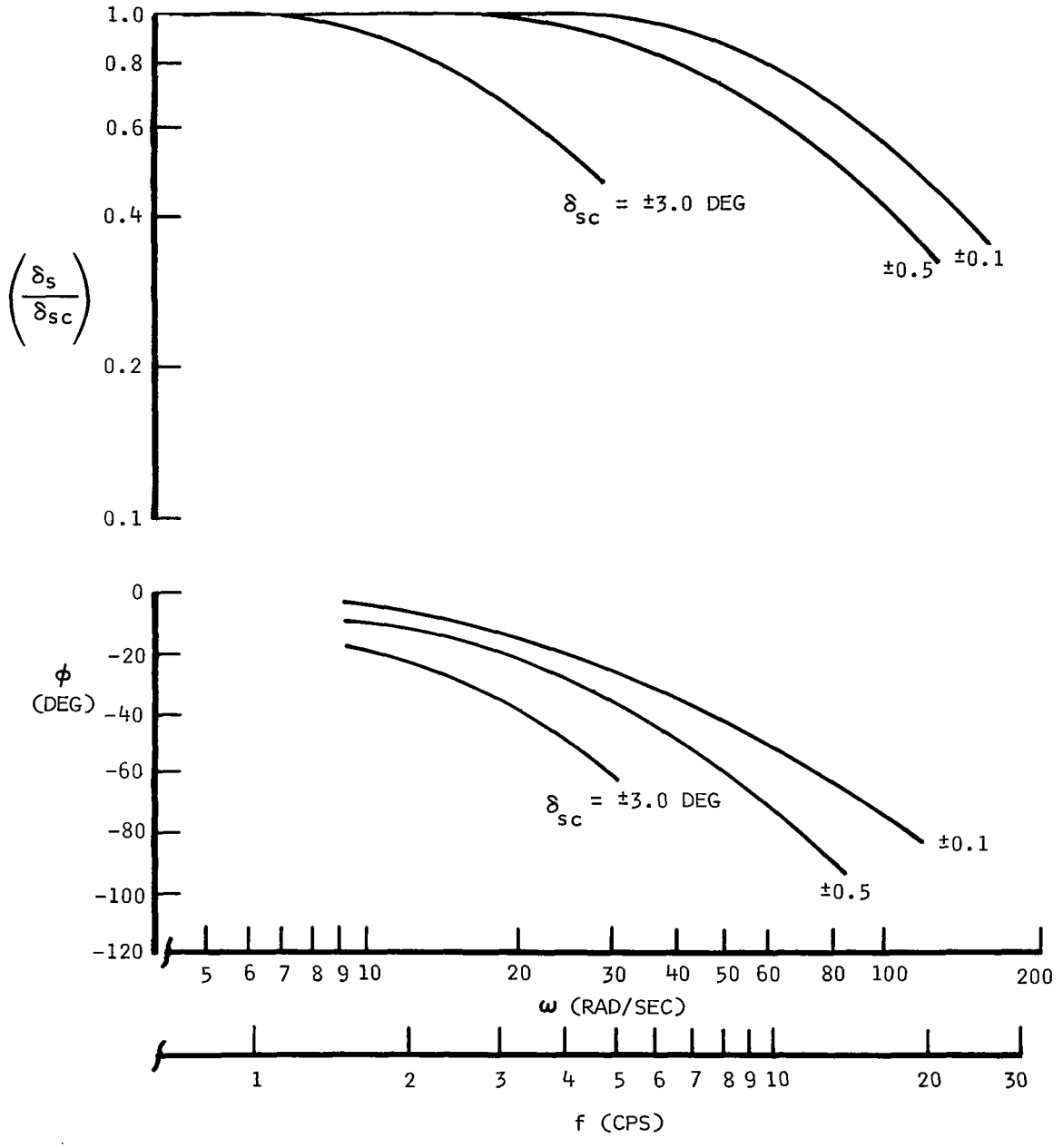

(a) REFERENCED TO CONSTANT SERVO COMMANDS

Figure 5.- Frequency response of SAS servo - simulator data.

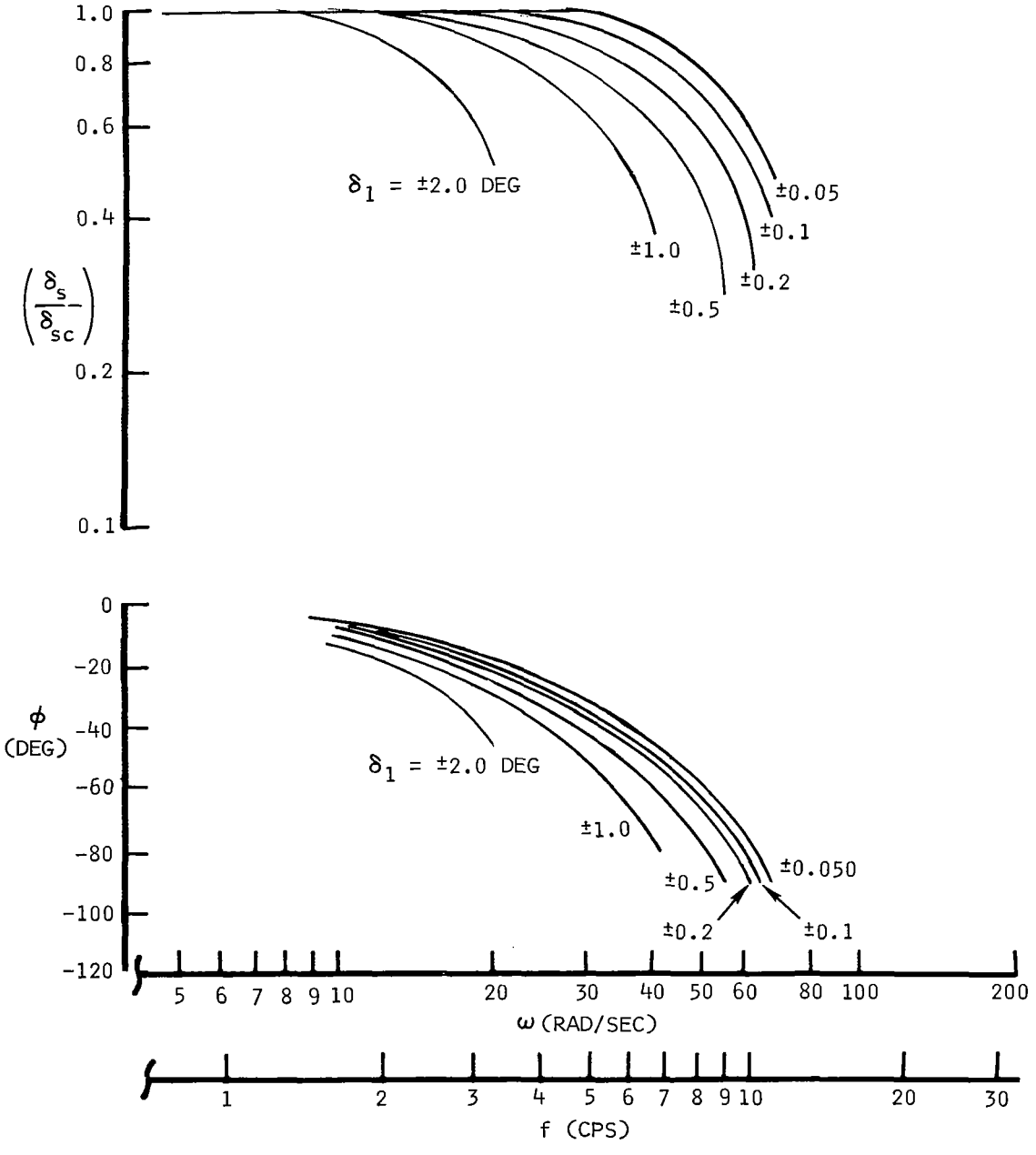

(b) REFERENCED TO CONSTANT INBOARD ELEVON DEFLECTIONS

Figure 5.- Concluded.

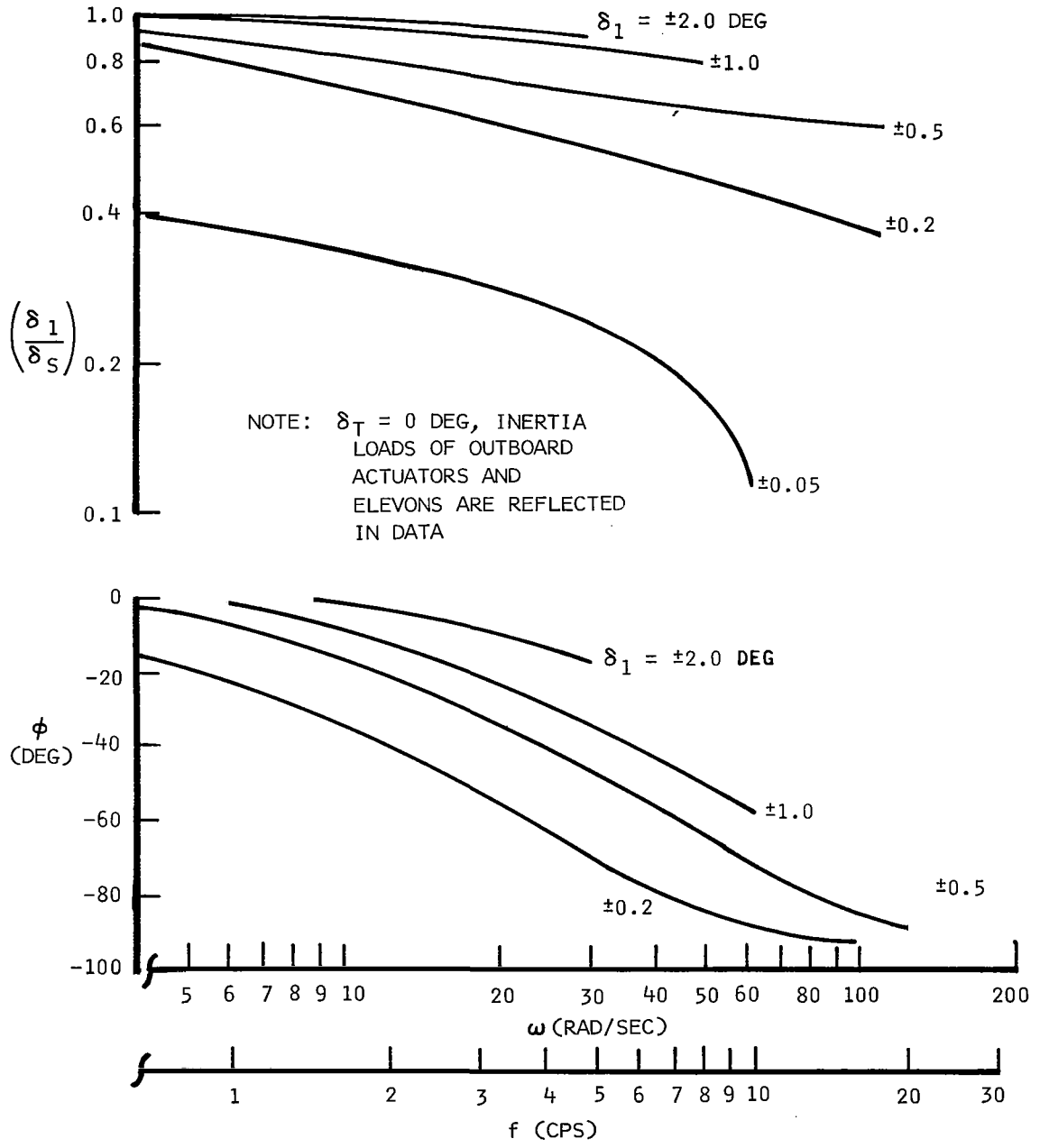

(a) REFERENCED TO CONSTANT INBOARD ELEVON DEFLECTIONS

Figure 6.- Frequency response from SAS servo output through inboard actuator output - composite simulator and airplane data.

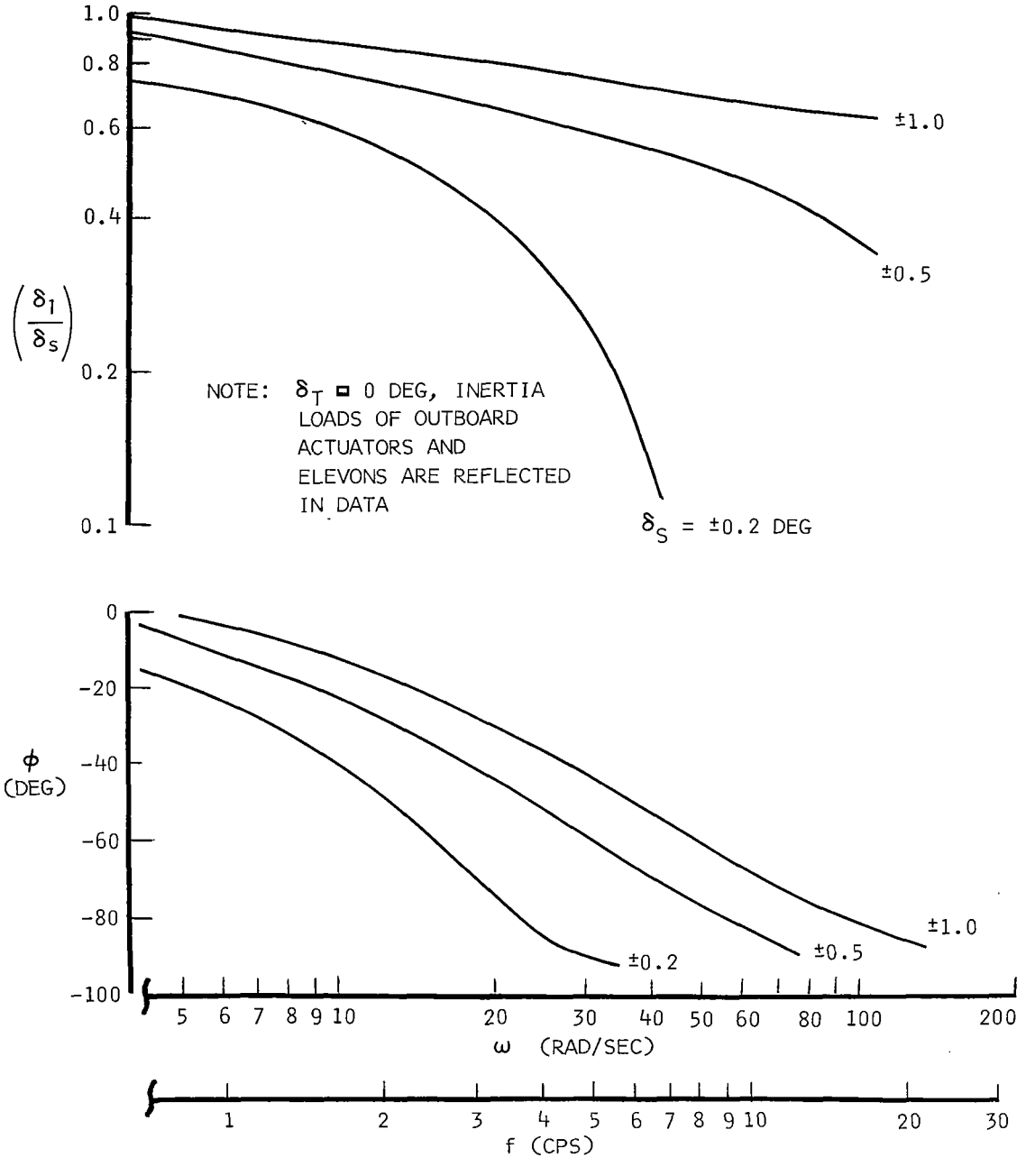

(b) REFERENCED TO CONSTANT SERVO OUTPUT DEFLECTIONS

Figure 6.- Concluded.

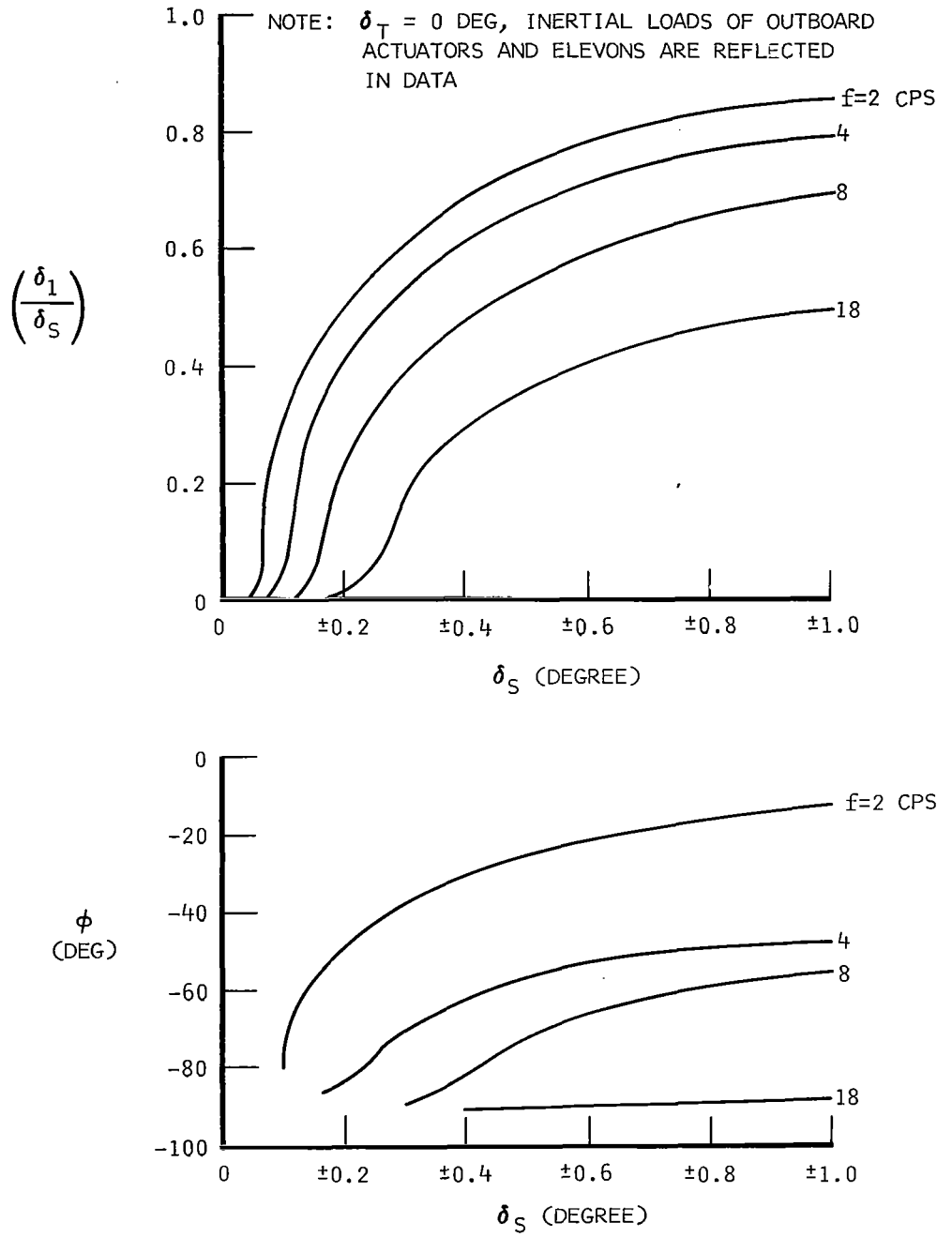

Figure 7.- Servo to inboard elevon small amplitude response - composite simulator and airplane data.

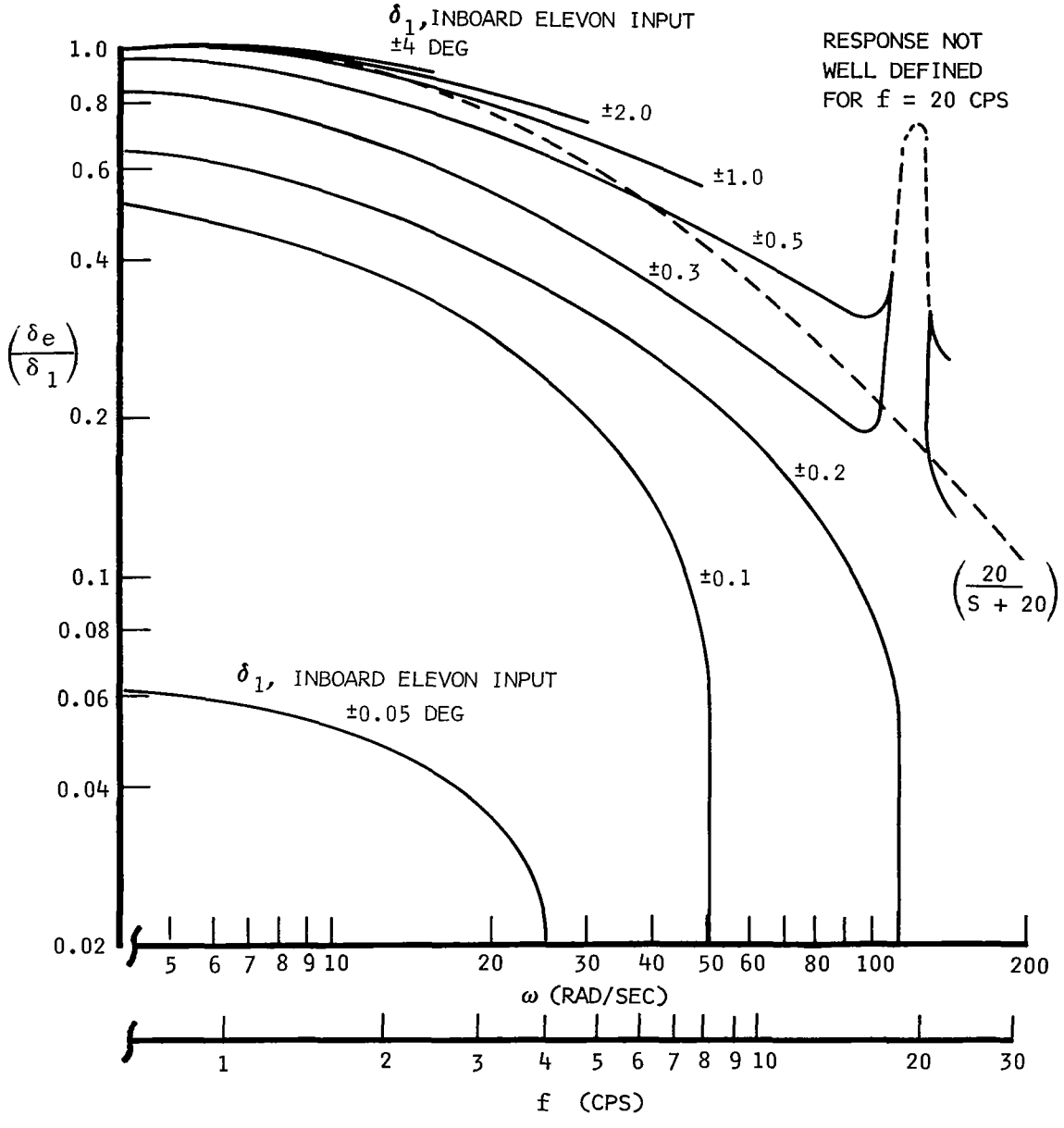

(a) AMPLITUDE

Figure 8.- Frequency response from inboard elevon to outboard elevon - airplane data.

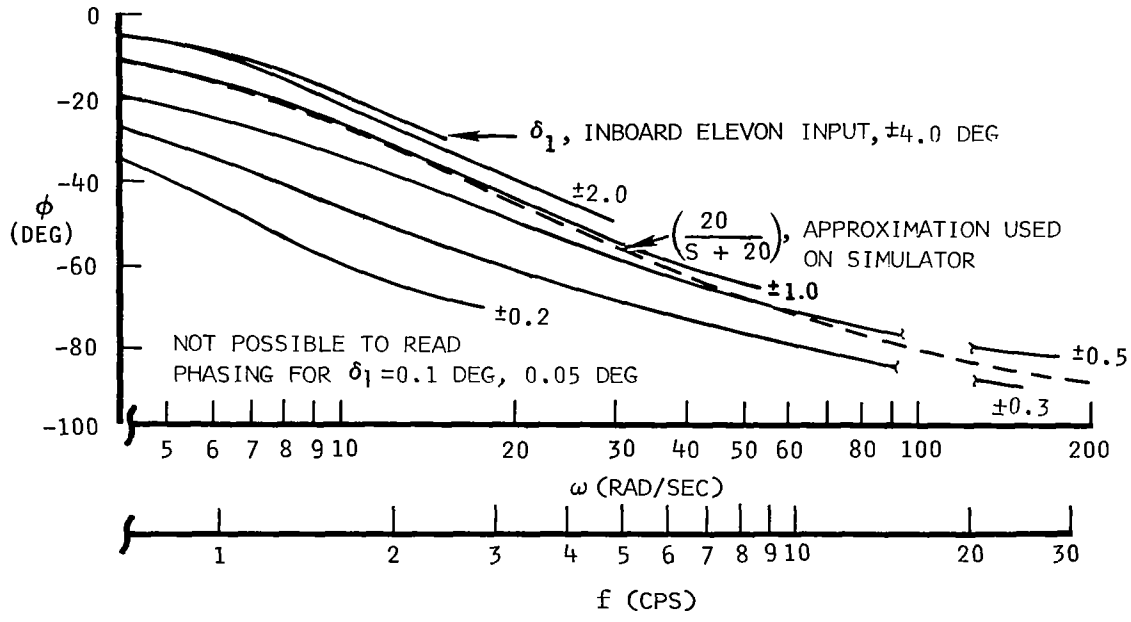

(b) PHASE ANGLE

Figure 8.- Concluded.

On the simulator, the outboard elevon actuators were not "hardware simulated" but were "analog simulated" with the transfer function of $20/(S + 20)$. This approximation is shown on the figure for comparative purposes.

Elevon natural frequency.- Ground vibration testing of the airplane and control system frequency response data (excitation put in at the pitch FACS servo) show that the resonant frequency is approximately 20 cps. This mode of motion includes the servodynamics, the mass and stiffness of the cables from the servo to the actuator, the actuator mass and stiffness including the hydraulic oil bulk modulus, the elevon attachment point backup structural compliance, and the inertia and stiffness characteristics of the elevon panels themselves.

Both in-flight temperature changes of the hydraulic fluid and aerodynamic loading of the surface affect this ground test resonant frequency. An analysis was performed to ascertain the magnitude of these influences. The effect of temperature on the bulk modulus was determined using the same techniques and data used in the elevon single-degree-of-freedom flutter analyses. The total system stiffness was divided into two components: one due to the structural aspects and the second due to the bulk modulus. The bulk modulus change due to temperature was determined from the hydraulic fluid manufacturer's curves and was a much greater influence on system stiffness than the temperature effect on the structure. Knowing the analytical percentage change on the total stiffness due to temperature, it was possible then to ratio the ground test results to predict in-flight values. The effect of in-flight aerodynamic stiffening was obtained by combining the known mass and aerodynamic characteristics into a frequency correction to the vibration test results.

Table I summarizes the results of this analysis. The ground vibration test results show that each of the six elevon panels has its own natural frequency, some slightly below and some slightly higher than the approximate 20 cps average. Existing flight test records were inspected to obtain the indicated temperature rise for the typical flight conditions shown. These temperatures are for an area near the elevon actuators. The effect of these typical temperatures on the 20 cps ground test average is shown to be small and in a direction to decrease the frequency. The effect of the aerodynamics on the panels is in a direction to increase the ground test average frequency. When a total of these two opposing effects is calculated, it is shown that there is a slight increase over the ground-test value, the maximum increment being approximately 1.08 cps.

TABLE I

TEMPERATURE AND AERODYNAMIC EFFECTS ON ELEVON SINGLE-DEGREE-OF-FREEDOM FREQUENCY

GROUND VIBRATION TEST RESULTS, XB-70 NO. 1

Elevon Panel No.	Frequency (cps)	
1	20.7	19.9 cps average
2	19.3	
3	19.3	
4	19.8	
5	19.8	
6	21.2	

EXPECTED IN-FLIGHT FREQUENCIES

Flight Condition	Temp (°F)	f (Temp) cps	f (Aero) cps	f (Avg)	Δf From Ground Test
M = 0.9, 25,000 ft	132	19.70	21.8	20.75	+0.75
M = 1.4, 40,000 ft	106	19.85	22.3	21.08	+1.08
M = 2.4, 60,000 ft	195	19.55	21.5	20.53	+0.53
M = 2.7, 64,000 ft	243	19.35	20.9	20.13	+0.13

Shaker Vane

A small shaker (exciter) vane was located on the XB-70 as indicated in figure 9 at fuselage station 324.5. This vane has a total of 4 square feet of exposed surface area, low sweep angle, and moderate aspect and taper ratios. This vane had been installed to aid in flight-test investigation of the airplane's dynamic structural characteristics. This shaker can excite the lower symmetrical structural modes up through approximately 8 cps. The surface can be trimmed to ±6 degrees. From this trim position, ±12.5 degrees of vane deflection is available to excite the structure. Both variable frequency and deflection controls are provided.

It is expected that the shaker vane will allow the structural mode control system performance to be evaluated under well-controlled flight-test conditions. For instance, by sweeping through a range of frequencies with the ILAF system on and off, response comparisons may be obtained to evaluate the ILAF system performance.

Because the shaker vane surface is so small, the frequency dependent aerodynamic effects are negligible over the frequency range of interest. Thus, the quasi-steady normal force coefficient data, as shown in figure 10, have been used in calculating all generalized force data for use in analyses.

Analytical Model

The analytical model of the XB-70 utilizes the modal approach for describing both the static and dynamic flexible airplane characteristics. All of the basic data for the mach-altitude and weight configuration cases reported herein (with the exception of the light weight and mach 1.4 case) are detailed in reference 5 and will not be repeated here. The wingtip at 25-degrees configuration data used herein have been assumed equal to the zero tip deflection data of reference 5. Details of assumptions and logic used in assembling these data are also covered in some depth in the cited reference.

The flexible air vehicle equations of motion used in this study are presented for reference in appendix D.

AREA = 4 SQ FT; EXPOSED TOTAL OF BOTH SIDES
AR = 3.93; BASED ON TOTAL EXPOSED SPAN AND AREA
$\Lambda_{C/4}$ = 2 DEG
λ = 0.5

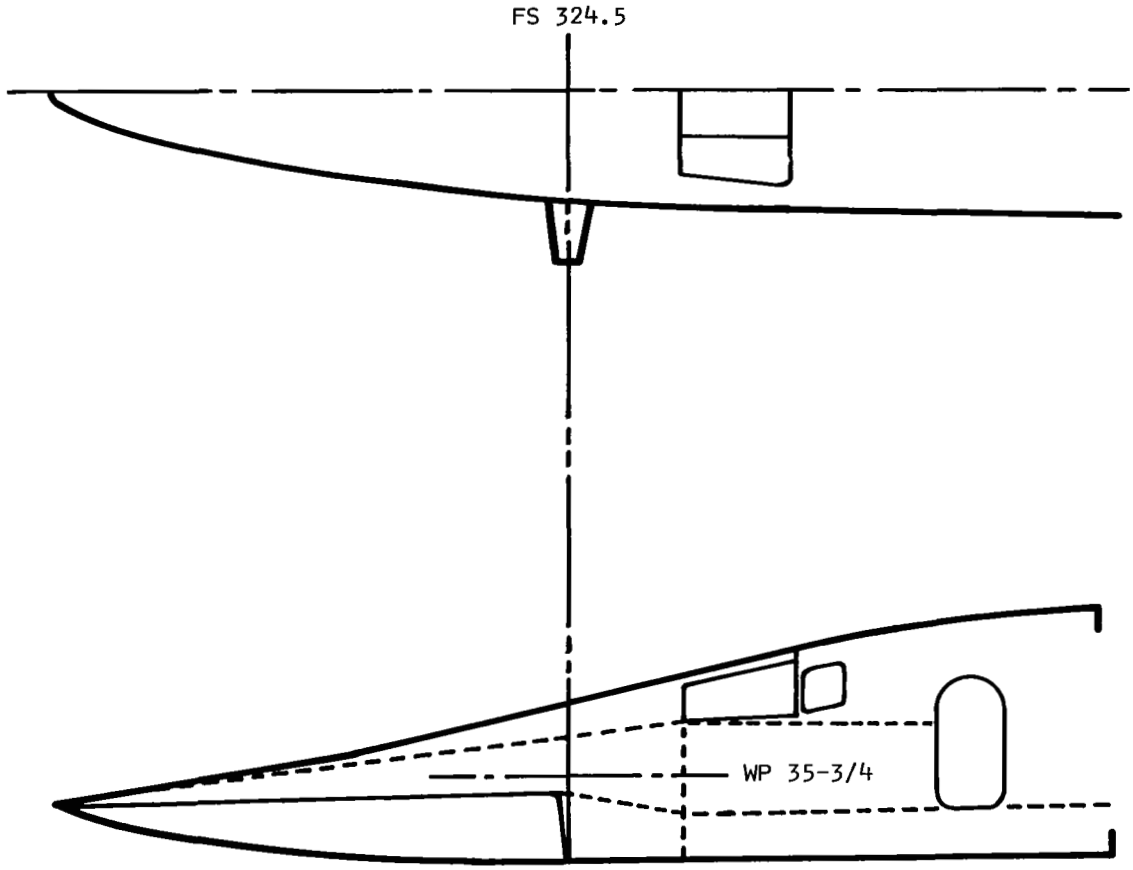

Figure 9.- XB-70 shaker vane location.

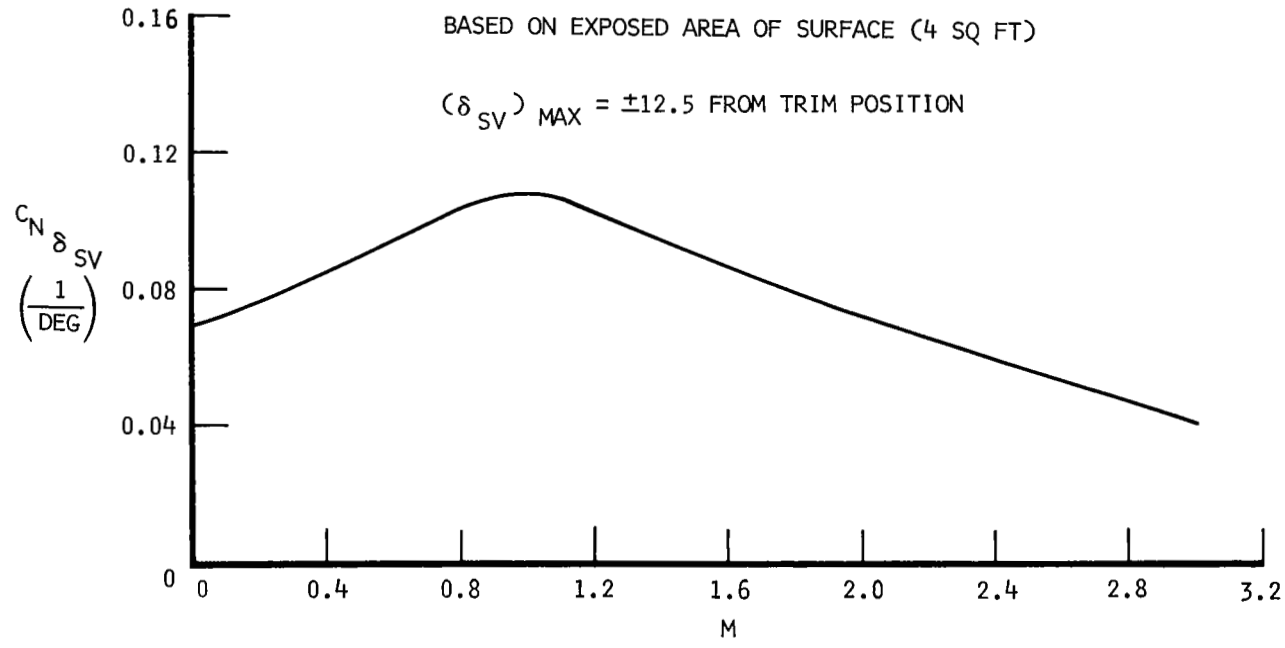

Figure 10. - XB-70 shaker vane normal force effectiveness coefficient versus mach number.

STRUCTURAL MODE CONTROL SYSTEM DESIGN

Before proceeding into the detailed aspects of the design of the structural mode control system for the XB-70, a brief review of some of the fundamental ideas involved will be presented. An understanding of these ideas will help the reader appreciate the capabilities and limitations of the particular design approach taken.

Fundamental Ideas

An active control system in an airplane used to augment structural dynamic stability and alleviate the effects of gust does basically one of two things: (1) it keeps the external excitation energy from getting into the vehicle, or (2) it gets rid of the energy once it enters the vehicle. To say it another way: the control system (1) desensitizes the vehicle to the excitation, or (2) provides damping to the vehicle motion resulting from the excitation. The main source of external excitation is generally turbulent air.

One way to implement the first approach is to identify the gust environment fast enough ahead of time to activate controls which effectively cancel any input force. Thus, some kind of gust probe ahead of the airplane is needed. This system requires considerable detailed knowledge of the vehicle characteristics over a wide range of vehicle weight and flight conditions so that proper anticipatory timing circuitry may be provided together with effective control forces. For some simple relatively rigid subsonic airplanes, this type of system has been successfully implemented in the past. However, for a flexible airplane whose mission requires subsonic to supersonic flight and large weight changes during flight, this approach becomes too complicated to be practical. The approach utilized by North American Rockwell and others currently applying these systems to modern flexible aircraft is to provide sensors on board the airplane which sense the vehicle reaction motion to external excitation and activate controls to attenuate the ensuing motion. This approach will work well either in a continuous excitation environment or in response to a sharp one-time excitation input.

ILAF Principle

To solve the structural dynamic stability augmentation system design problem, it is extremely important to consider the motion sensing and control force generating aspects concurrently. As will become apparent, these two elements are essential to system effectiveness and stability. The logic behind this statement can best be illustrated by considering a sensor-force

scheme developed at North American Rockwell (under USAF sponsorship) called the Identical Location of Accelerometer and Force (ILAF) system. The basic function of this system is to get rid of gust (or other) excitation energy by applying damping forces to the airplane structure. The required damping velocity signal is obtained by processing an accelerometer signal.

The ILAF techniques were the results of efforts to design a simple, stable system, and one that would operate effectively over a wide range of mach-altitude conditions and vehicle weight and geometry configuration changes. It is not intended here to review all of the ramifications of the ILAF approaches; these are adequately covered in references 3 through 6. However, the following simplified discussion is presented in order to readily assist the reader in interpreting the performance results to be reviewed.

A simplified illustration of the key ideas involved in the ILAF system technique is displayed in figure 11. The measure of controllability of a particular structural mode is called the generalized control force. This force is the product of the normalized natural vibration mode shape (ϕ_i^F) at the force application point and the force magnitude (F); that is, ($F\phi_i^F$). The structural acceleration at a given point on the vehicle is the product of the normalized mode shape (ϕ_i^A) at a given point on the vehicle and the generalized coordinate acceleration ($\ddot{\eta}_i$); that is, ($\phi_i^A \ddot{\eta}_i$). For the control system to be stable at effective gain levels of a fixed polarity, the polarity of ϕ_i^F and ϕ_i^A must always be the same. One way of insuring this requirement is to place the sensing element (accelerometer) at the force application point; thus, $\phi_i^F = \phi_i^A$. With this arrangement, both the magnitude and polarity of ϕ_i^F and ϕ_i^A may change as fuel or vehicle geometry changes during flight and yet the net effect on the polarity of the feedback loop is not changed. This sensing scheme solves the basic problem of designing for changing vehicle and flight condition combinations. Many systems can be conceived which work well at one design point; but it is a much more difficult task to produce a design which will accommodate the normal wide range of vehicle and flight conditions experienced in flight.

The second key idea in the ILAF system is the use of approximate integration of the accelerometer signal to obtain the required velocity signal to activate the damping force. This approximate integration makes use of the existing lags in the aerodynamics, actuator, and other system components; thus, in theory, little additional network shaping is required.

Figure 12 is a typical root loci of an ILAF system installed in a typical large, low-load-factor design, flexible vehicle. The figure includes the longitudinal short-period (rigid-body) mode and four symmetrical structural modes.

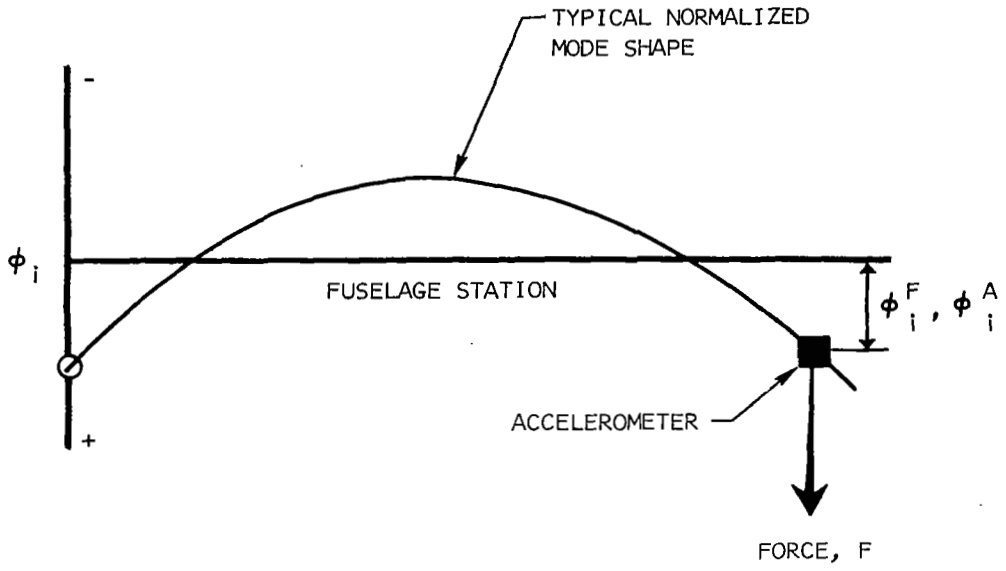

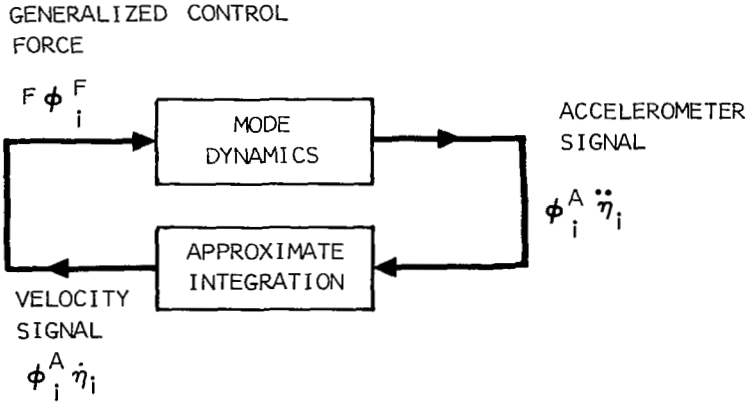

KEY SYSTEM FEATURES:

1. IDENTICAL LOCATION OF ACCELEROMETER AND FORCE

2. APPROXIMATE INTEGRATION OF ACCELERATION TO OBTAIN VELOCITY SIGNAL

Figure 11.- Simplified explanation of ILAF features.

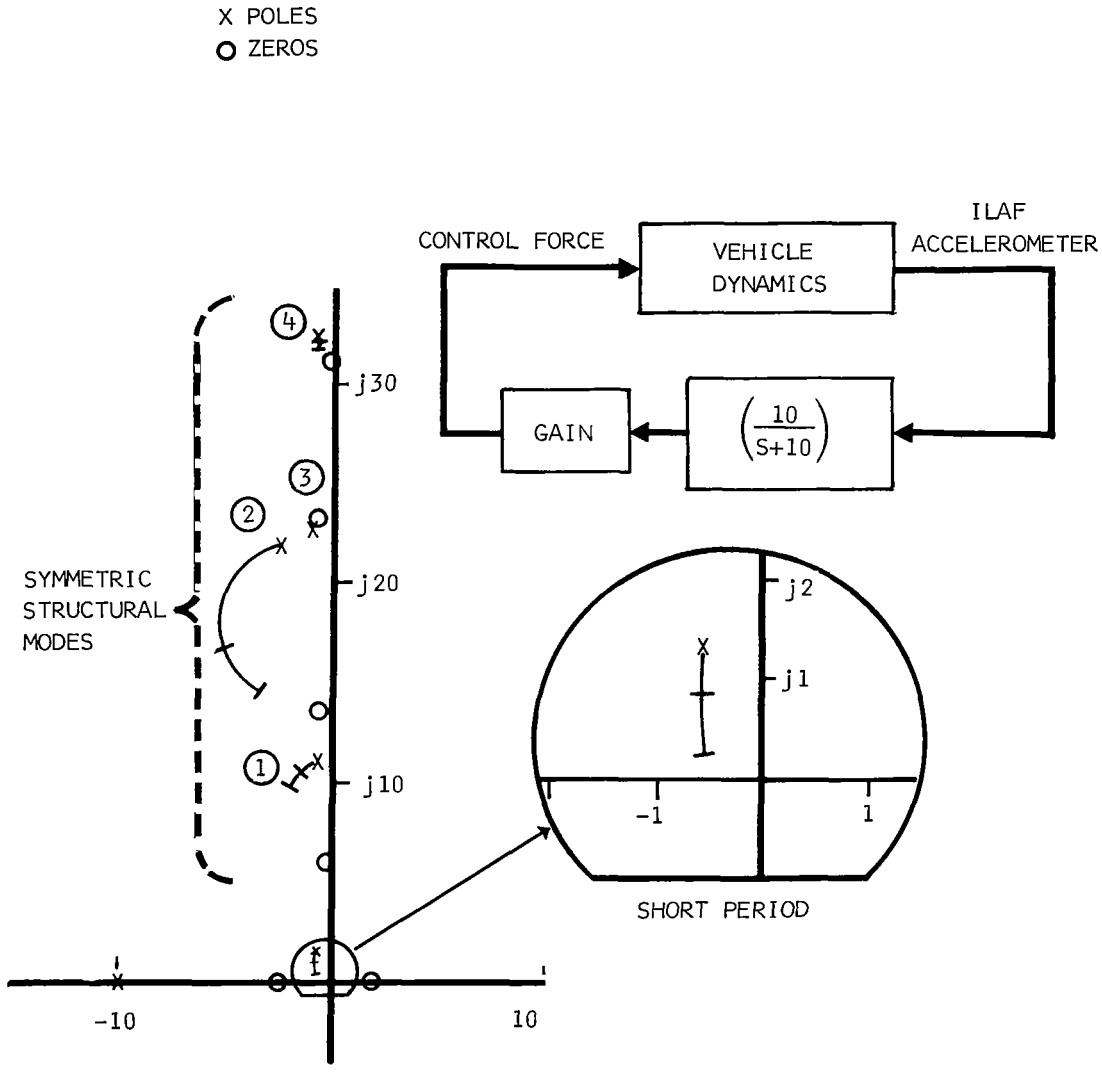

Figure 12.- Typical ILAF system root loci indicating pole-zero arrangement and effect on short period.

The main response characteristics of a typical ILAF system are illustrated by this figure; that is, the technique interlaces the structural mode poles and zeros so that, as system gain is increased, the loci for the structural modes loop out into the left hand (stable) plane indicating increased damping. While the ILAF system may not always be effective for all modes (because of node line locations relative to sensor and force locations) as is the situation for the third mode illustrated, the system at least maintains stability in these modes.

The basic ILAF system can affect the short-period motion as shown in the blown-up section of figure 12. One design approach that could be employed to maintain satisfactory short-period characteristics would be to integrate the ILAF system into the standard stability augmentation system. This, however, has not been the design approach adopted for implementation on past ILAF system studies (references 3 to 6) nor is it the approach used in the present design study. In general, it has been desirable to separate the ILAF structural mode damping function from the basic SAS handling qualities function as a basic system fail-safety enhancement. If the ILAF system were to fail, there would be no need to shut off the SAS, and vice versa. In the specific XB-70 ILAF system design under discussion, one of the ground rules was a minimum modification requirement which precluded the integration of the SAS and ILAF system to solve the interface problem posed in figure 12; thus, the idea of the separation of short-period and structural motion approach conveniently met this requirement.

Figure 13a illustrates the specific XB-70 system installation. The technique, however, is a general one which has been effective on a number of flexible aircraft studied at North American Rockwell. The implementation requires the use of an accelerometer located approximately near the center of gravity, or about midship, in addition to the primary ILAF accelerometer located at the control surface. As indicated, these sensors pick up three components of acceleration: (1) that seen at the CG when the vehicle as a whole accelerates ($n_{z_{CG}}$), (2) that due to rotary acceleration about the CG which appears as linear acceleration at a distance ℓ off of the CG ($\frac{\ell}{g}\dot{q}$) and, (3) that due to structural acceleration at a particular point on the vehicle ($\sum_{i=1}^{n} -\frac{\phi_i}{g}\ddot{\eta}_i$). Experience from working on several flexible vehicles shows that the resulting signal consists essentially of a reinforced structural signal and some small pitch acceleration; the whole-vehicle translation acceleration of the CG is nearly completely canceled.

Other sensing schemes, such as those presented in figures 13b and 13c, can effectively eliminate rigid-body motion and isolate the structural motion

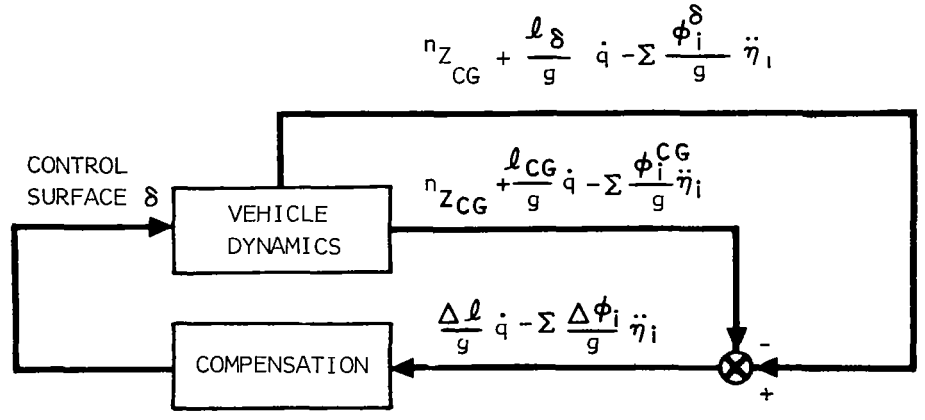

(a) TWO LINEAR ACCELEROMETERS

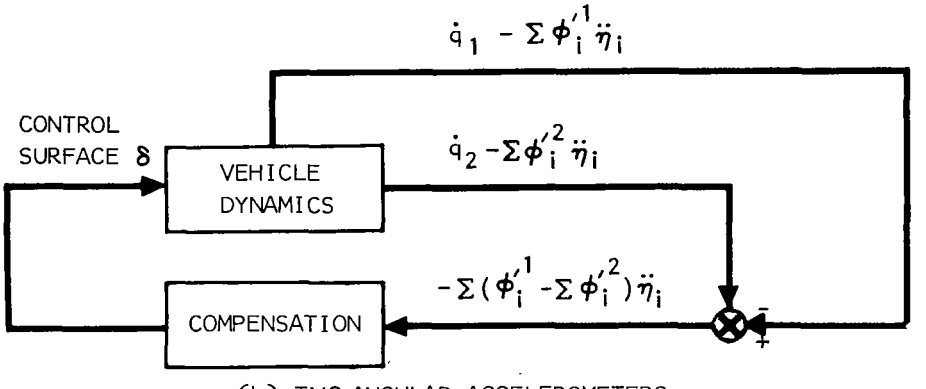

(b) TWO ANGULAR ACCELEROMETERS

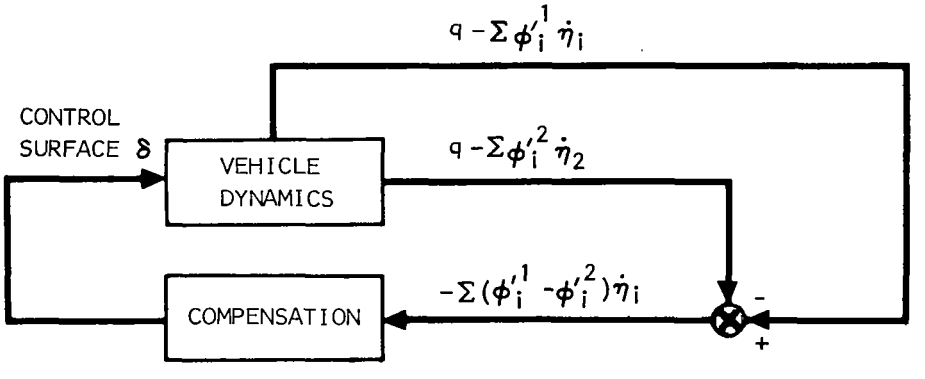

(c) TWO RATE GYROS

Figure 13.- Schemes for separation of sensed structural motion from rigid-body motion, longitudinal-symmetric modes.

signal. The sensing scheme illustrated in the figure 13b block diagram shows that, for two rotary accelerometers located at two different locations on the vehicle, each sensor signal contains a whole-vehicle pitch acceleration component ($\dot{q}$) and a structural flexing acceleration proportional to mode shape slope ($\sum_{i=1}^{n} \phi_i' \ddot{\eta}_i$). When one sensor signal is subtracted from the second sensor signal (with the same gain), the difference is a signal containing pure structural bending acceleration information and no whole-vehicle acceleration. The sensing approach presented in the figure 13c block diagram shows two rate gyros located at two different stations. The signal from each gyro contains a whole-vehicle rate component (q) and a structural bending rate ($\sum_{i=1}^{n} \phi_i' \dot{\eta}_i$) component. Subtracting one signal from the other (at the same gain) cancels the whole-vehicle component leaving only the structural bending signal. The title generally associated with these types of multiple sensor schemes is "sensor blending." It is important to note that, while the rotary accelerometer and rate gyro sensing schemes shown in figures 13b and 13c can eliminate all rigid-body mode signals from the blended sensor signals, and thus interfere less with handling qualities than ILAF, more detailed structural mode shape information is required and more extensive analytical stability checking is needed during design in order to insure system stability for all vehicle weight, geometry, and mach-altitude conditions. (Rate gyro sensing was used in the system reported in reference 11.) ILAF, on the other hand, tends to be a more dependably stable system at all vehicle-flight conditions through its basic concept.

The effectiveness of the secondary, or midship accelerometer, in separating structural and whole vehicle motion is demonstrated in the comparison of the root loci of figures 12 and 14. The effectiveness of the ILAF technique in damping the structural motion is changed little, while the influence on the short-period motion is markedly reduced.

Typical Design Problem

With a basic sensor-force scheme explained, it is informative to consider next some of the detailed aspects of a typical system design.

Figure 15 is intended to summarize the key problems inherent in any typical structural dynamic stability augmentation system design. The case specifically illustrated is an ILAF system using linear accelerometers as sensors and delta wing trailing edge controls as force generators. At the top of the figure is a sketch of the frequency response of the net sensor

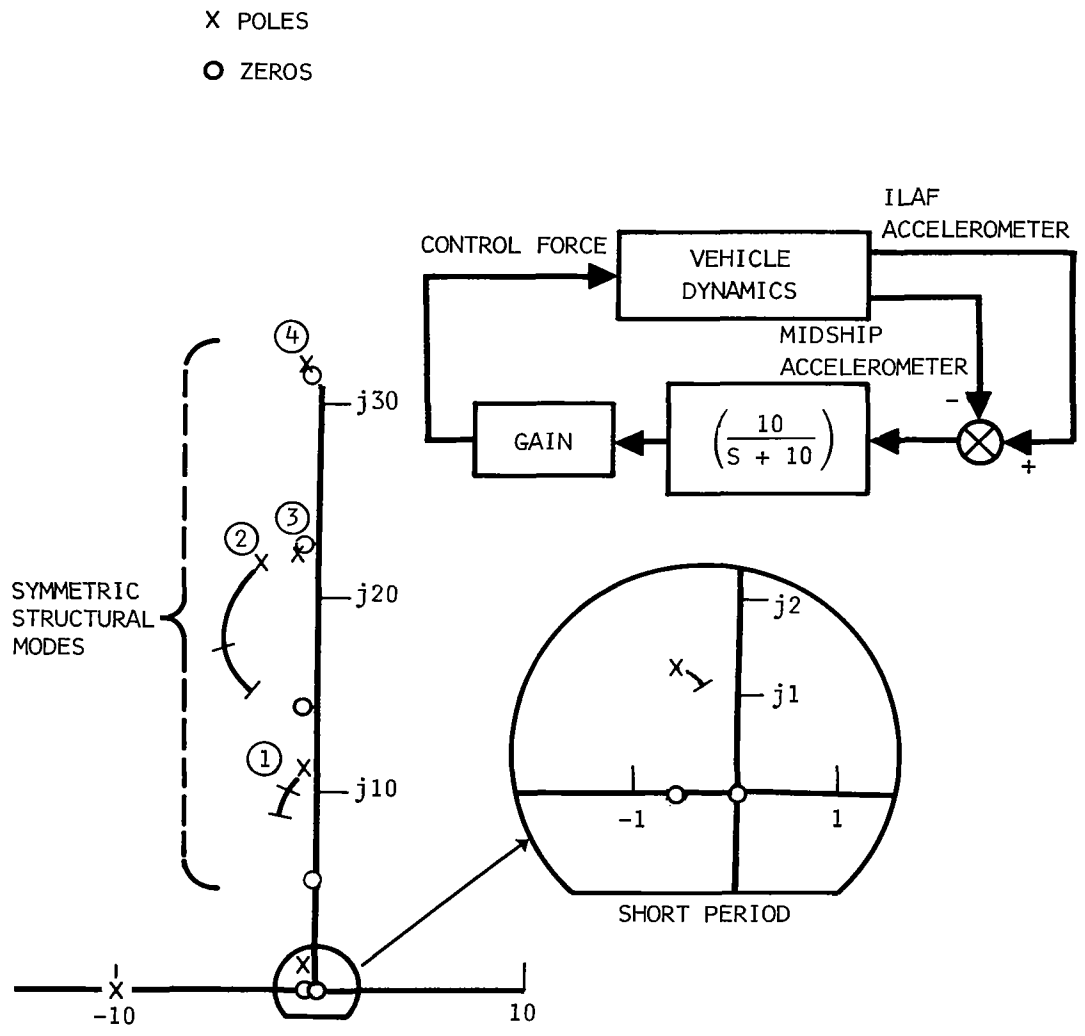

Figure 14.- Typical ILAF system root loci indicating pole-zero arrangement and separation of short-period and structural motion.

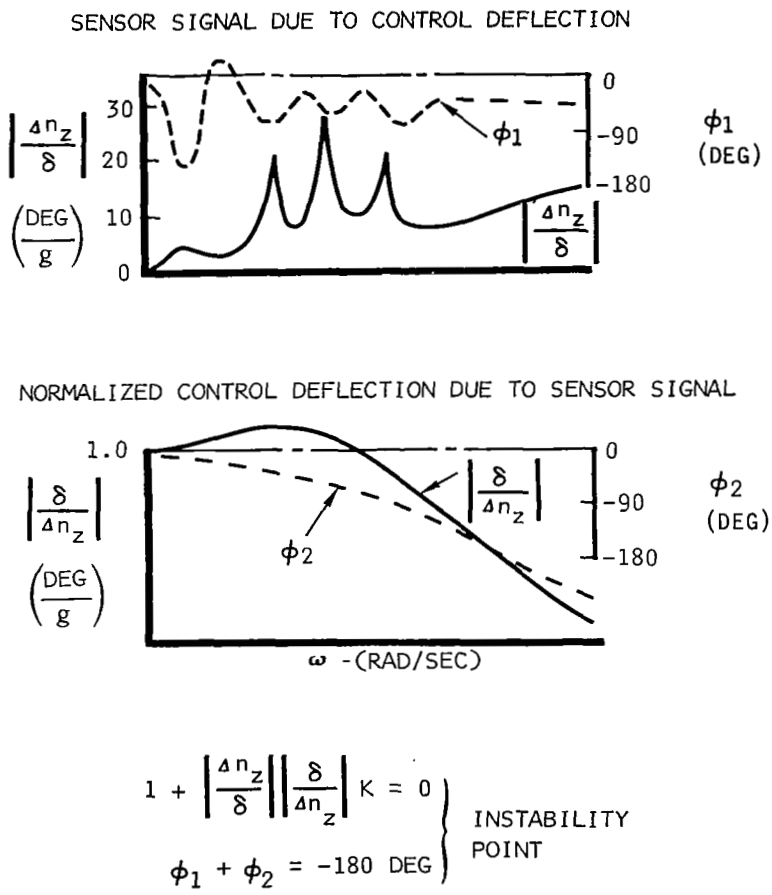

Figure 15.- The key features of a typical design problem. n_z refers to ILAF sensor location.

vector amplitude and the associated phase angle. The amplitude curve shows some small response at the short-period frequency range and large response in the range of frequencies of the structural modes to be controlled. The amplitude continues to rise at high frequencies due to control surface inertia characteristics. The phase angle is shown to approach -180 degrees at the short-period frequency, but returns to oscillate between 0 and -90 degrees. At the bottom of the figure is the frequency response of the normalized (at $\omega = 0$) control deflection due to a unit sensor signal input. This frequency response includes sensor dynamics, system compensation, and servo and actuator dynamics. The system compensation was designed to maintain a high amplitude through the frequency range of the modes to be controlled and then drop off at higher frequencies.

At the bottom of the figure are the relationships which define an instability in terms of the amplitudes $\left(\left|\frac{\Delta n_z}{\delta}\right|^{*} \text{ and } \left|\frac{\delta}{\Delta n_z}\right|\right)$ and the corresponding phase angles (ϕ_1 and ϕ_2). (K is a gain factor associated with the normalized $\left|\frac{\delta}{\Delta n_z}\right|$.) Thus, at any frequency where the combined phase angles just equal -180 degrees, and the factor $\left(\left|\frac{\Delta n_z}{\delta}\right| \left|\frac{\delta}{\Delta n_z}\right| K\right)$ is greater than -1 at that frequency, the system is unstable at that gain. The crux of the design problem, then, is to maintain high control authority through the frequency range of the structural modes to be controlled, but to attenuate it markedly at the higher frequencies. At the same time, the phase angle lag magnitude must be minimized throughout the frequency range so that a combined phase angle of -180 degrees occurs at as high a frequency as possible.

Relative to the aforementioned system compensation and stability, one detail that has needed attention in several system designs, including that for the XB-70, has been the control surface natural resonance. (See discussion on page 18.) The resulting lightly damped resonant response can produce surface deflection magnitudes great enough to induce an instability in a closed loop system. The solution to this problem is filtering of the feedback signal. On the XB-70, as will be shown, this takes the form of a notch filter. This control surface resonance problem is not unique to the XB-70 and will need to be considered in any structural mode control system design.

* Δn_z refers to incremental acceleration from ILAF sensors.

General Limitations and Constraints for the XB-70

The ILAF technique of structural mode control was implemented on the XB-70 under a number of limitations and constraints. Since the flight test on the XB-70 was to be a demonstration of a control principle and not of an operational system, the system was designed to operate on the symmetric modes only. Furthermore, the design was to operate through the existing pitch axis FACS to actuate the elevons to obtain the necessary structural damping forces. Thus it can be seen that the system to be designed was an add-on system. Another basic design ground rule was that the ILAF system should not degrade short-period dynamics and handling qualities.

XB-70 Longitudinal-Symmetric ILAF System Design Synthesis

The basic ideas associated with the ILAF technique for implementing structural mode control have been reviewed in the preceding part of this section. The specific application to the XB-70 longitudinal-symmetric modes will be discussed next.

The basic elements of the XB-70 ILAF system designed are illustrated in figure 16. The structural mode control forces are produced by the elevons. The main ILAF sensing elements are linear accelerometers located near the elevon hinge line. Since one of the principal design constraints was that the system was not to interfere with the basic handling qualities of the aircraft, and for fail-safety reasons, the rigid-body mode separation scheme in figure 13a was utilized. As shown, the specific implementation of this scheme takes the form of a linear accelerometer located near the nominal center of gravity of the airplane. The signal from this accelerometer is subtracted from one half of the combined signals of the accelerometers located at the elevon hinge line on either wing panel. (In subsequent discussions, the wing-located accelerometers are referred to as the primary ILAF accelerometers, while the midship accelerometer is called the secondary accelerometer.) Summing the wing accelerometer signals in the manner described eliminates roll acceleration and antisymmetric structural acceleration signals.

The original longitudinal SAS sensing elements are also shown on figure 16 to complete the identification of all sensing elements involved in the combined SAS-ILAF system.

Sensor location details.- An important design aspect of synthesizing a structural mode control system is locating the sensors so as to minimize the effects of flight condition variations, and to maximize the number of modes directly controllable. Although the ILAF concept greatly simplifies the

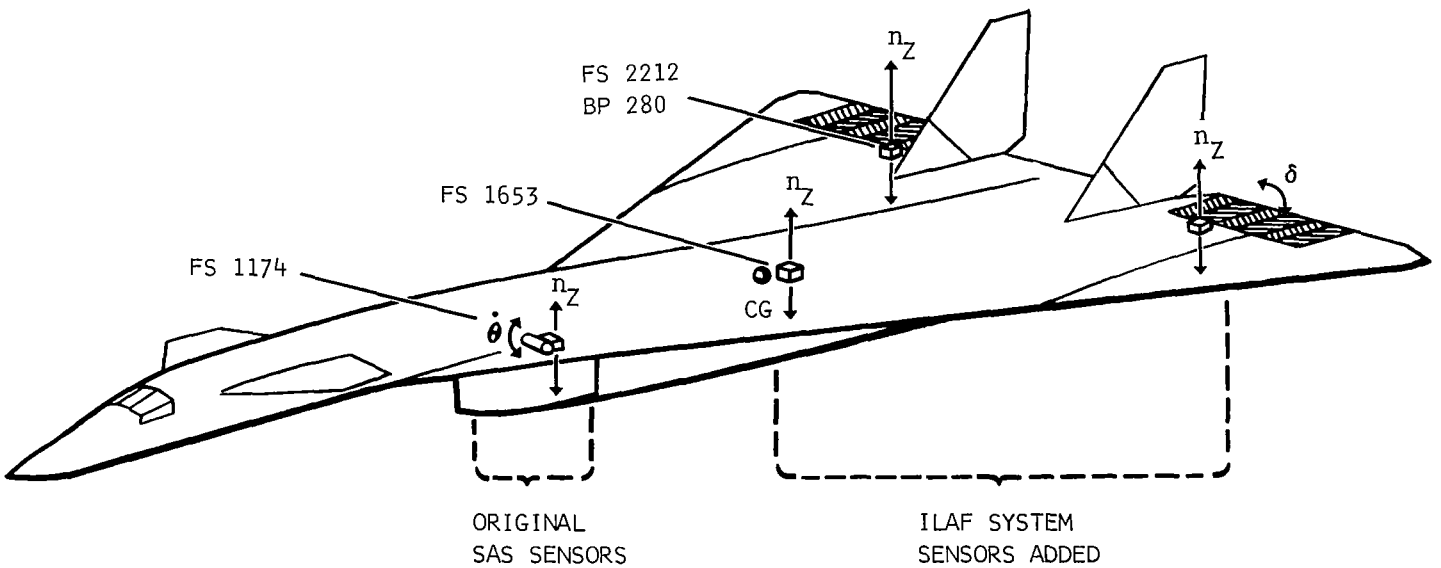

Figure 16.- XB-70 ILAF system sensor and control surface locations for longitudinal-symmetric modes.

type of sensor and the location selection problems by specifying that accelerometers be located near the control surfaces, the XB-70 elevons span a length of about 17 feet and, thus, some guidelines are still necessary to pinpoint a more precise location of the one accelerometer (per wing panel). Pertinent to the combined sensor-control force problem is the fact that the control force is not at a point location; thus the ILAF principle is diluted to some degree when applied to a large wing surface such as the XB-70 possesses. To provide an appreciation of this point, consider the aerodynamic loadings induced by a trailing edge surface as shown in figure 17. At subsonic speeds, aerodynamic loads are induced forward on the airfoil as well as in the vicinity of the deflected surface. On the other hand, at supersonic speeds, the load induced by the surface deflection is localized to the area of the control surface. Remembering that the generalized control force for a given mode is $\int_{\text{surface}} F(x, y)\ \phi_i\ (x, y)\ dS_w$, which represents the summation over the wing area of the local load times the local mode shape deflection, it can be seen that the one sensor signal and aerodynamic generalized force will be more nearly matched from a mode shape point of view for the supersonic case. (It should be noted that, while some of the subsonic load is induced forward and causes some obscuring of force input and sensor signal matching, most of the load is still concentrated near the control surface.) It can be seen that the best matching of the control force and the sensor location required some investigation to optimize it for the various vehicle weight, geometry, and flight combinations to be experienced. The details of this type of study are covered in this subsection.

Figure 18 indicates the nine locations near the elevons investigated for the combinations of weights and wingtip positions where structural data were available. These nine locations near the elevons including an area of approximately 50 square feet (15 x 3.33) were investigated to optimize the accelerometer location and uncover any potential location sensitivity problem that might exist. To assist in the preliminary location of the accelerometers, an "ILAF effectiveness indicator" or "ILAF figure of merit" was used to consider the mode shape deflections at the elevon and pilot locations (emphasizing ride quality) as well as at the accelerometer locations. Later, more detailed root locus and frequency response analyses were conducted to refine the sensor placement. One restriction on the ILAF gain or performance is the allowable amount that ILAF will affect the rigid-body mode handling qualities; therefore, the distance from the airplane CG to the accelerometer location was used to reflect this restriction in the "ILAF effectiveness indicator" defined in figure 19. This figure indicates the estimated ILAF performance for (1) the primary accelerometer located between fuselage station (FS) 2172 and 2212, and butt plane (BP) between 180 and 361, and (2) the secondary accelerometer located between FS 1653 and 1944 within the fuselage. Regardless of the accelerometer locations, the data indicate that the ILAF system will be very effective for the first structural mode. As the primary accelerometer is moved spanwise toward the wingtip, the second structural mode can be controlled

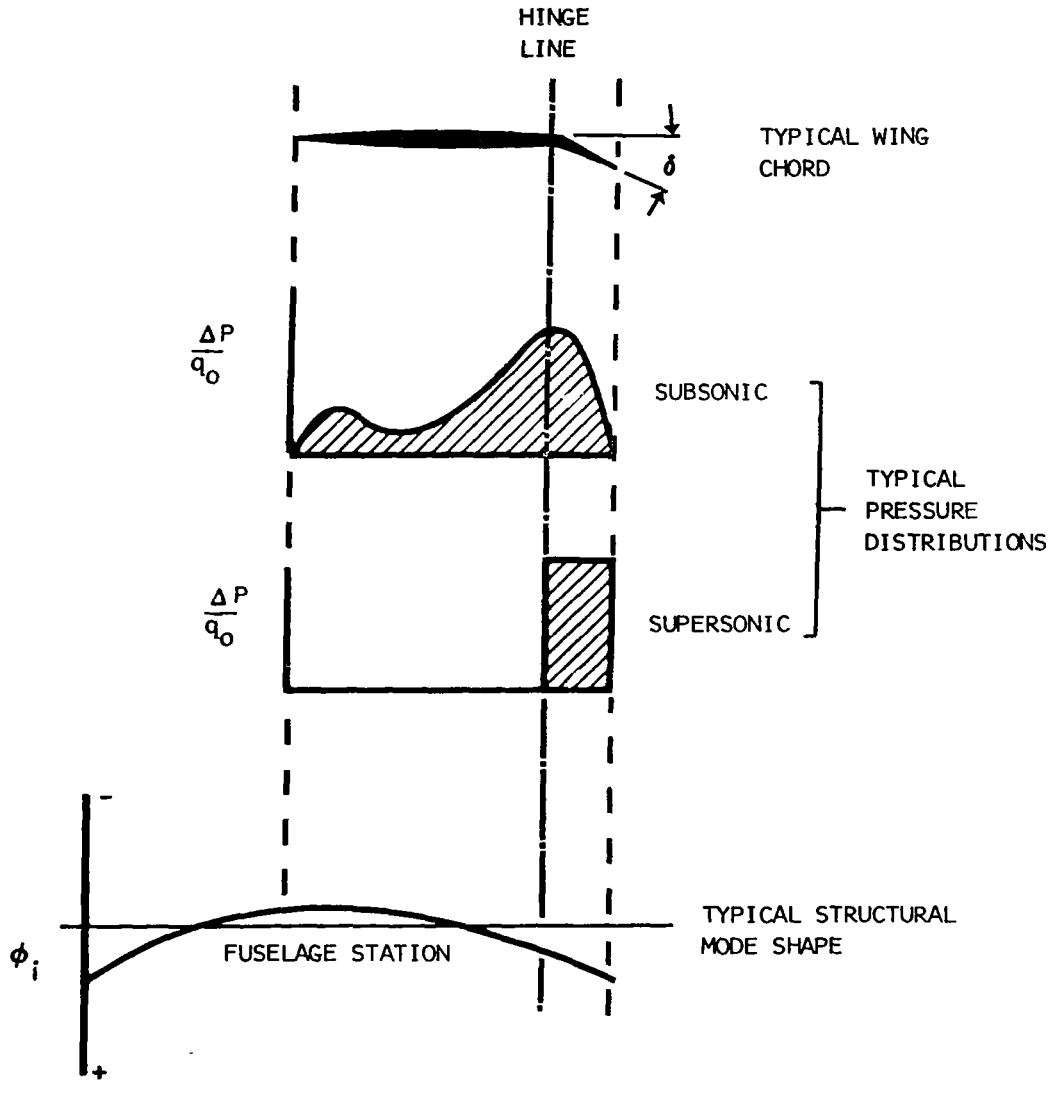

Figure 17.- Realistic trailing edge control induced airloads and generalized forces.

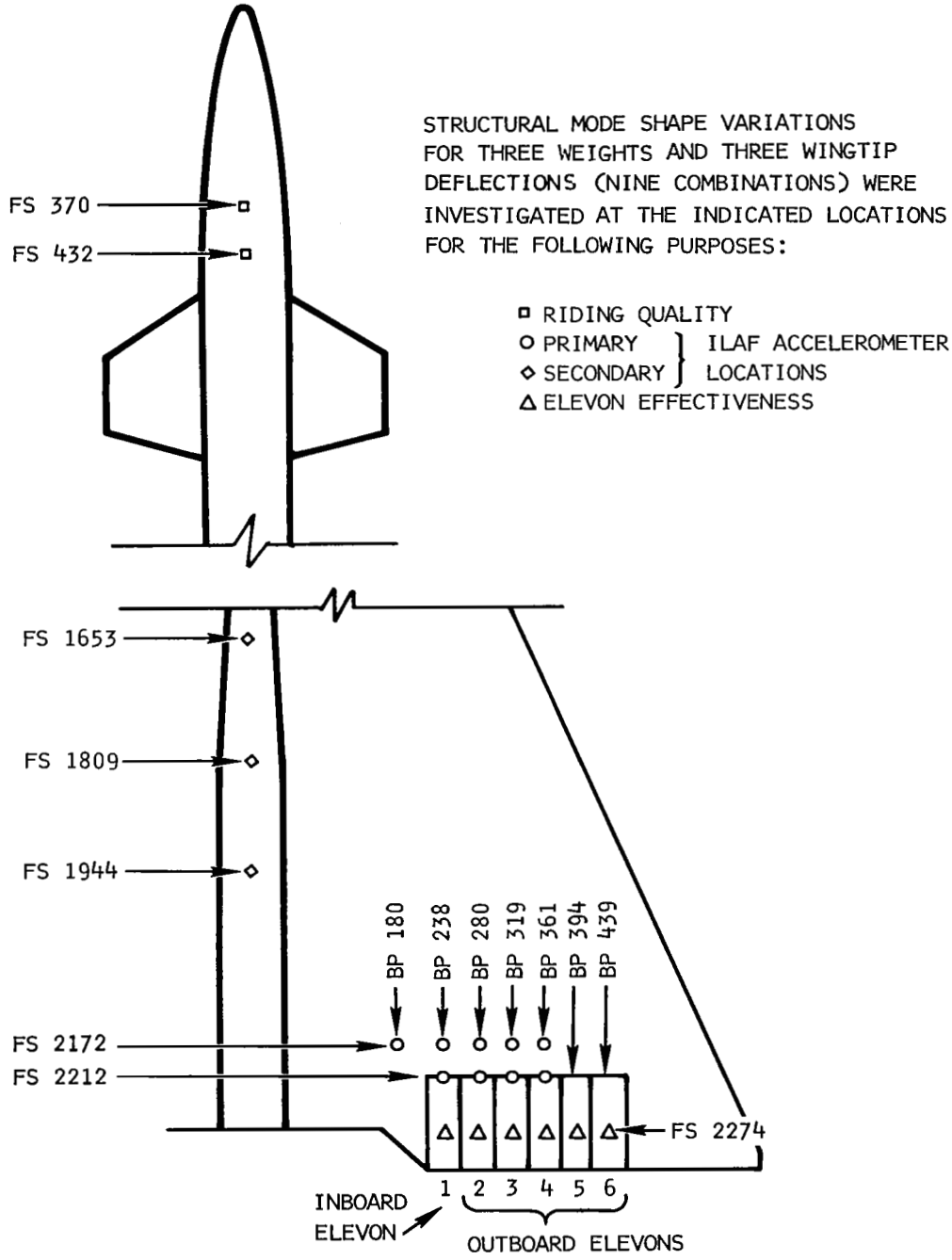

Figure 18. - Sensor locations used during the ILAF system design studies.

$$\left.\begin{matrix}\text{ILAF}\\ \text{EFFECTIVENESS}\\ \text{INDICATOR}\end{matrix}\right\} = \frac{\left(\phi_i^{A_1} - \phi_i^{A_2}\right)\Phi_i^{\delta}}{\left(\ell_{A_1} - \ell_{A_2}\right)\left(\phi_i^{P}\right)^2}$$

$\phi_i^{A_1}$, $\phi_i^{A_2}$, ϕ_i^{P} = STRUCTURAL MODE i DEFLECTION AT THE PRIMARY ILAF ACCELEROMETER (A_1), SECONDARY ILAF ACCELEROMETER (A_2), AND PILOT LOCATIONS

Φ_i^{δ} = STRUCTURAL MODE i DEFLECTION AVERAGED OVER THE FOUR INBOARD ELEVON LOCATIONS (WING TIPS DOWN)

ℓ_{A_1}, ℓ_{A_2} = DISTANCE FROM CG TO PRIMARY (A_1) OR SECONDARY (A_2) ILAF ACCELEROMETER

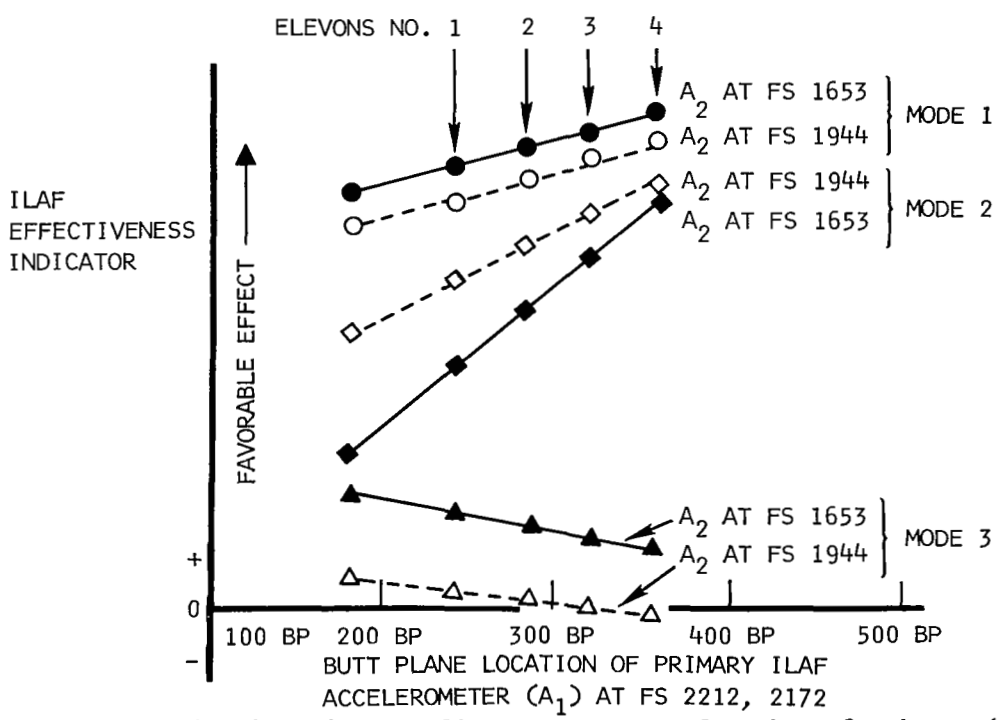

Figure 19.- Estimation of ILAF effectiveness as a function of primary (A_1) and secondary (A_2) accelerometer locations. Heavy weight, δ_T = 25 degrees, M = 0.90, h_p = 25,000 feet.

almost as effectively as the first mode; however, this is accomplished at the expense of less control of the third mode. As a compromise between controlling modes 2 and 3, and considering the availability of packaging space and component environmental control, the primary accelerometer was finally located at elevon No. 2 (FS 2212, BP 280), and the secondary accelerometer located in the air induction control system (AICS) package (FS 1653, BP 0).

As discussed earlier, ILAF in most cases provides a compatible sensor and generalized force polarity match regardless of variations with flight conditions because the accelerometer signals and the control surface effectiveness (aerodynamic generalized force derivatives) are both functions of the structural mode deflection. However, in special cases when structural mode shape node lines run through the control surfaces, a change in the polarity of either mode shape deflection or control surface generalized force derivative without a change in the polarity of the other can occur depending upon the aerodynamic effects; such a special case exists on the XB-70. The third structural mode has a node line between elevons No. 5 and 6. Figure 20 shows the results of a check of mode deflection and elevon derivative polarity compatibility for modes 1, 2, and 3 at elevons No. 1, 2, 3, 4, 5, and 6 at the mach 0.9 at 25,000 feet, heavy weight, δ_T = 25 degrees, flight condition. The data show all is well with modes 1 and 2; however, there are mode 3 deflection-elevon-derivative polarity mismatches at elevons No. 4 and 5. In addition, the magnitudes of the derivatives for elevons No. 4, 5, and 6 are much greater than for elevons No. 1, 2, and 3 in relation to the corresponding mode deflections. This means that control power over the third mode will be greater when the wingtip position is at 25 or 65 degrees rather than at the 0-degree position as shown by the average of the four and six elevon derivatives. At the 25- or 65-degree wingtip positions, the two outboard panels are disconnected and locked.

These study results reinforced the decision to locate the wing accelerometer sensor at FS 2212 and BP 280.

Root loci studies.- Figure 21 shows a simplified block diagram of the ILAF system used in root loci studies conducted to estimate the necessary gain and shaping requirements as well as validate the selected sensor locations. Initially, these simplifications of the physical system were made to expedite generation of root loci data when qualitative effects were still under study. Later, more exact approximations of the physical system were included to obtain quantitative estimations of gains, shaping, performance, and stability margins. As shown in the block diagram, initial simplifications included (1) approximating the nonlinear inboard actuator, outboard actuator, and SAS servo with transfer functions; (2) combining of inboard elevon No. 1 effects with effects of outboard elevons No. 2 through 6; (3) no shaping in the feedback loop; and (4) omission of the sensor dynamics.

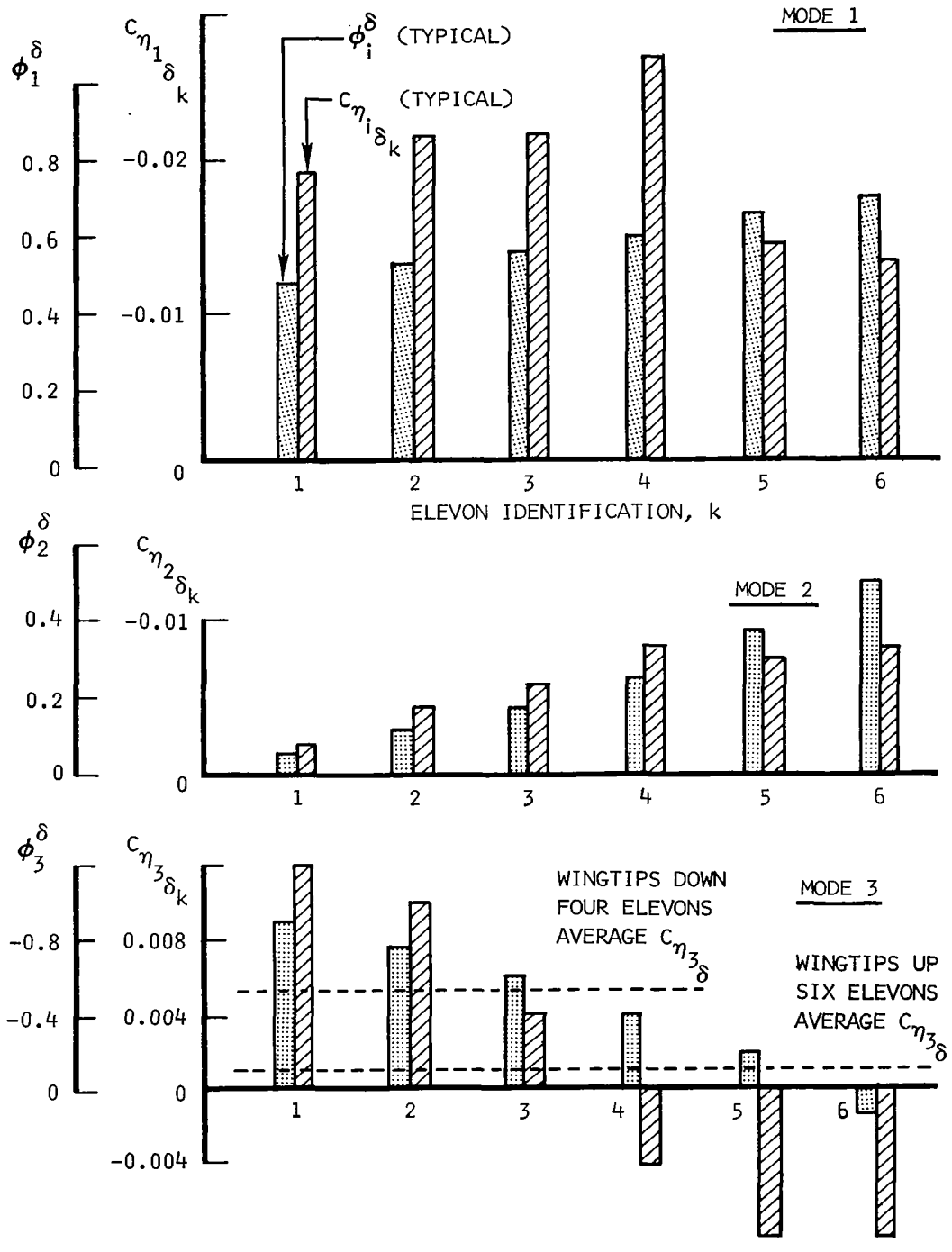

Figure 20.- Relationship of mode shape deflection at elevon to elevon effectiveness. Heavy weight, δ_T = 25 degrees, M = 0.90 h_p = 25,000 feet.

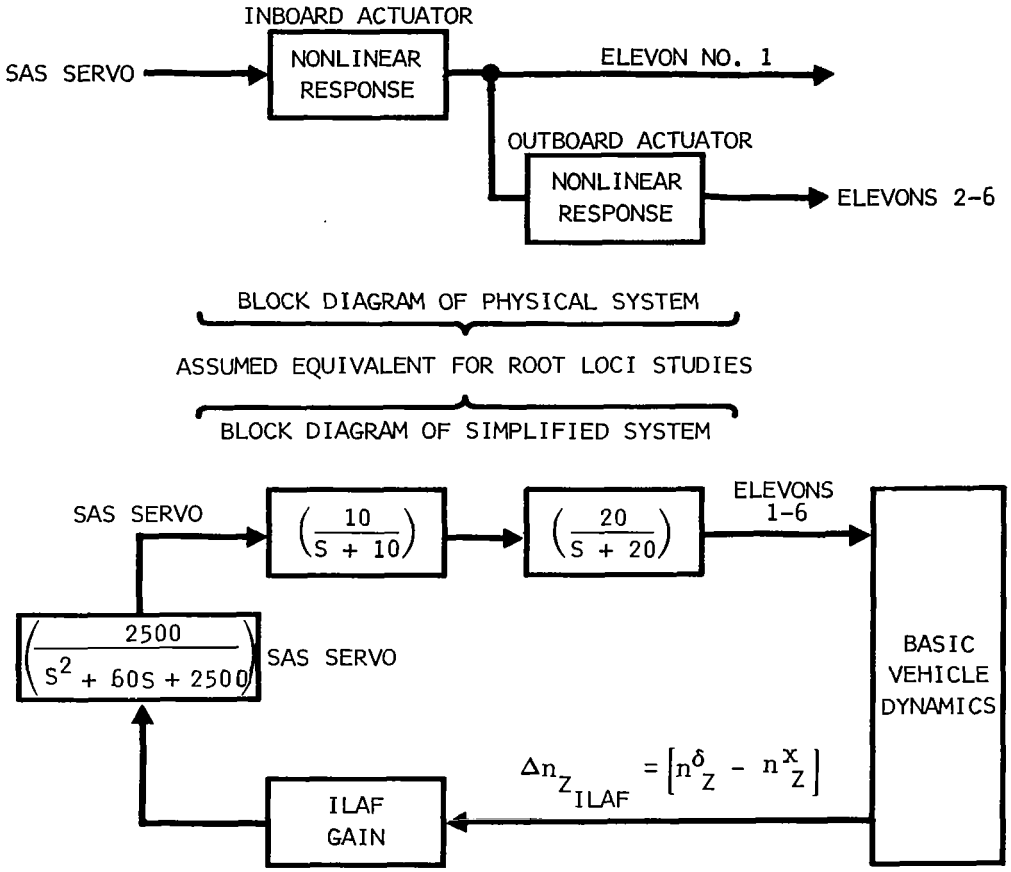

$$\Delta n_{Z_{ILAF}} = \left[\begin{array}{l}(\text{ACCELEROMETER AT ELEVON NO. 1 OR ELEVON NO. 4}) - \\ (\text{ACCELEROMETER AT FS 1653 OR FS 1800})\end{array}\right]$$

Figure 21.- Simplified block diagram of ILAF for root loci studies.

Figures 22a through 22e present root loci for five typical flight conditions for the primary accelerometer at elevon No. 1 and the secondary accelerometer at FS 1653. Results indicate significant control of mode 1 for all conditions, fair or signicant control of mode 2 depending upon flight conditions, and marginal control of modes 3 and 4 for all conditions. These results indicate a definite need for a lead-lag network in the feedback to improve performance or control of the third mode. All the root loci are presented for the same maximum gain of 0.3 radian per g to show the effects of varying flight conditions. For instance, it is noted that a given gain will affect the rigid-body mode of a light weight condition more than a heavy weight condition. Also, the relatively greater effect of ILAF for the sea level and 25,000-foot altitude conditions over that of the 70,000-foot condition suggests using the FACS altitude gain schedule in the ILAF loop.

The five root loci presented are for the cases with accelerometer locations most representative of the final selection, and for the cases with the wingtips deflected to the appropriate position for the flight condition. That is, the five root loci presented are for the primary accelerometer located at elevon No. 1 and the secondary accelerometer at FS 1653; wingtips are up for the mach 0.4 at sea level case, δ_T = 25 degrees for the mach 0.9 at 25,000 feet case, and δ_T = 65 degrees for the mach 3.0 at 70,000 feet case. Exploratory root loci were also obtained for various combinations of primary accelerometer located at elevon No. 4, secondary accelerometer at FS 1800, for wingtips both up and down. There were no significant differences in the initial structural mode damping increments between data with the secondary accelerometer at FS 1653 or 1800. Variations of the data for the two primary accelerometer locations and wingtip positions are summarized in table II and figure 23. Moving the wingtips down and/or locating the primary accelerometer at elevon No. 1 (instead of elevon No. 4) increases the ILAF effect on the third structural mode. This increased effect may be favorable or unfavorable depending upon the phase of the ILAF feedback. For a given ILAF gain, moving the wingtips down also has the following effects: (1) some loss in control of the second mode, and (2) less interference with rigid-body mode handling qualities - a favorable effect because four elevons will move the rigid-body roots only about 4/6 the amount as six elevons. The first structural mode can be adequately controlled, regardless of wingtip positions, accelerometer locations, or flight conditions investigated. The elevon inertia, SAS servo, and actuator dynamics were not of primary concern in the structural mode frequency range in this initial simplified description of the ILAF system indicated in the block diagram; however, subsequent simulator tests and more detailed analytical studies were conducted to determine the gain and shaping network requirements at all frequencies for proper system operation.

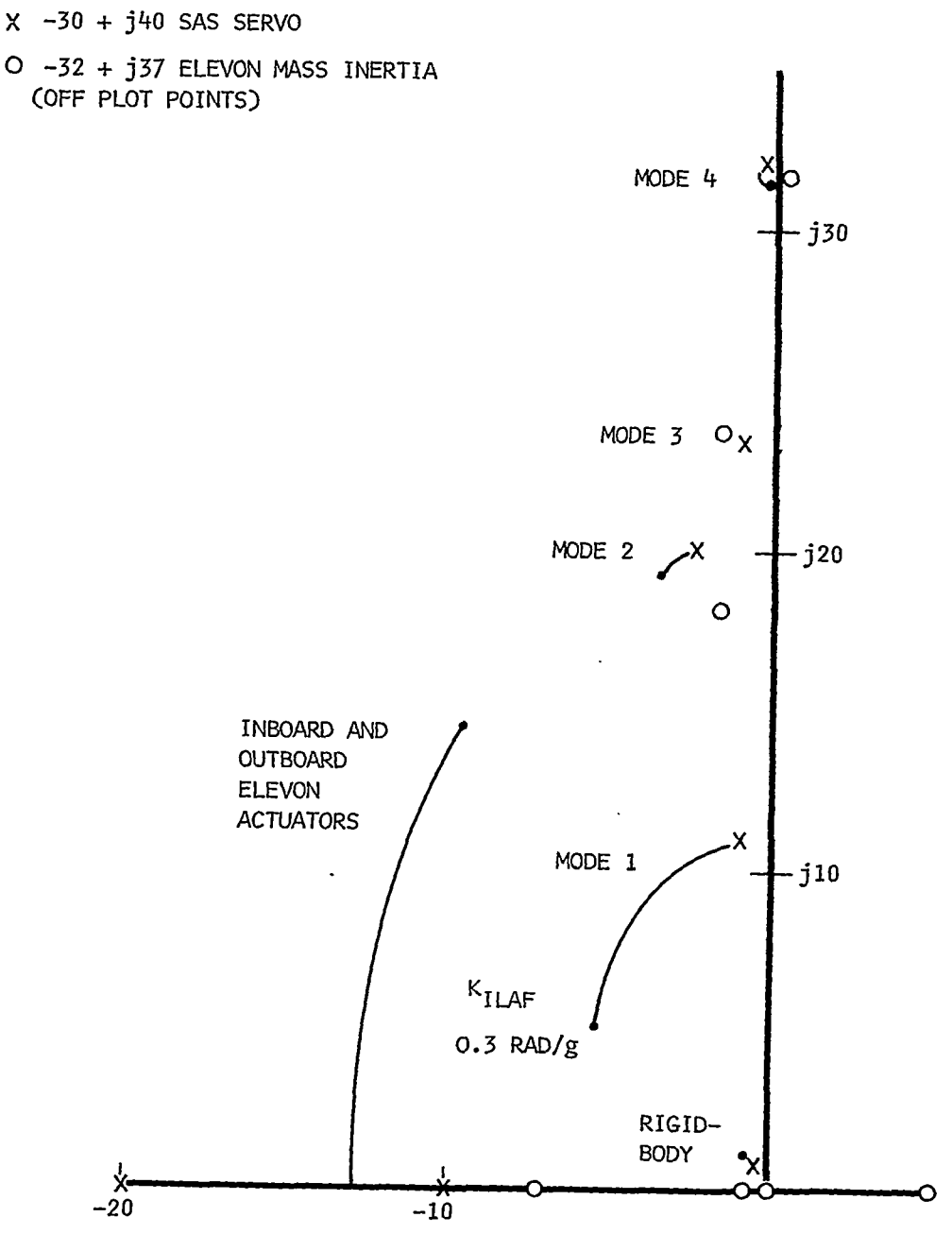

(a) HEAVY WEIGHT, δ_T = 0 DEGREES, M = 0.4, SEA LEVEL

Figure 22.- Root loci of ILAF to determine gain and shaping requirements.

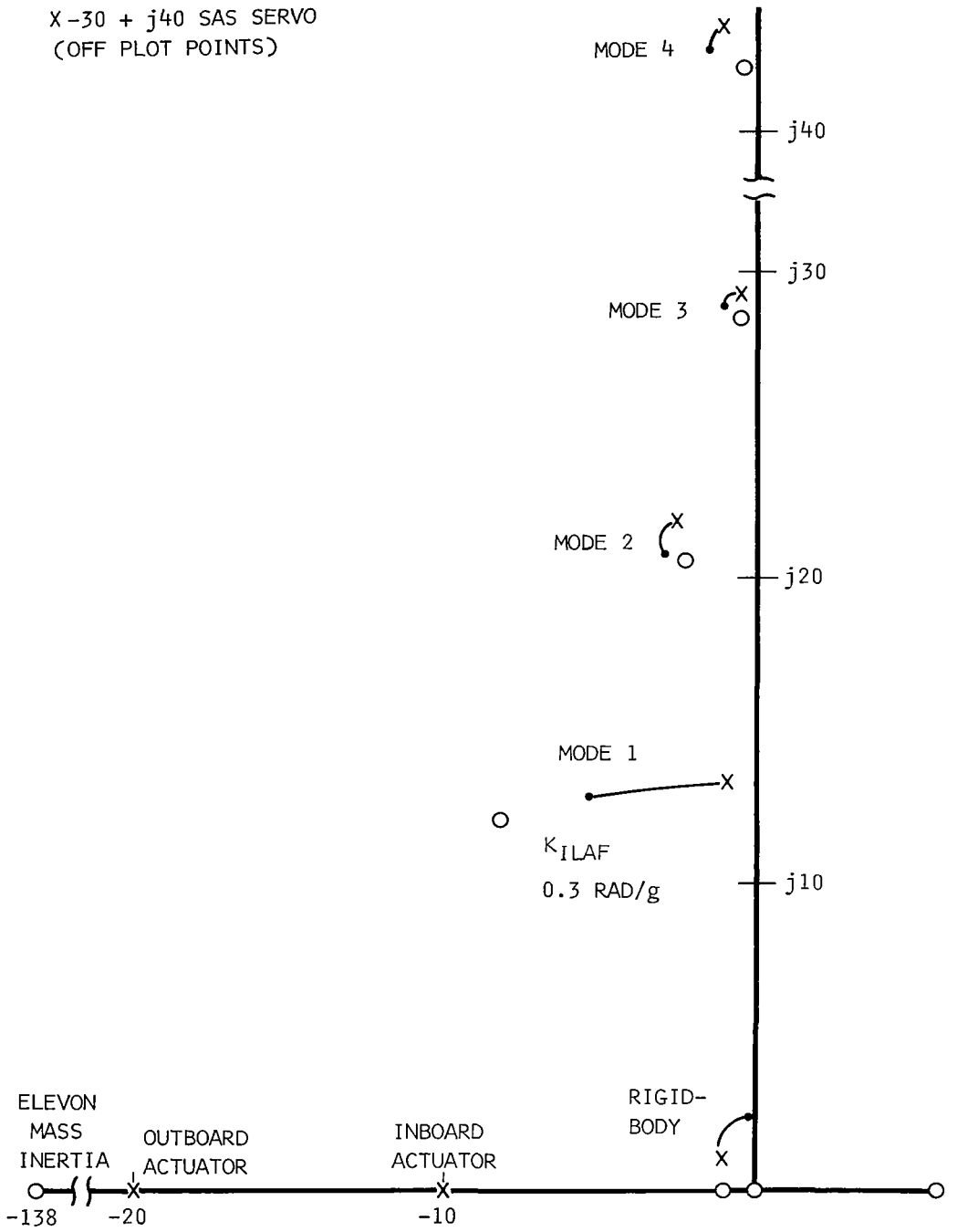

(b) LIGHT WEIGHT, δ_T = 0 DEGREES, M = 0.4, SEA LEVEL

Figure 22.- Continued.

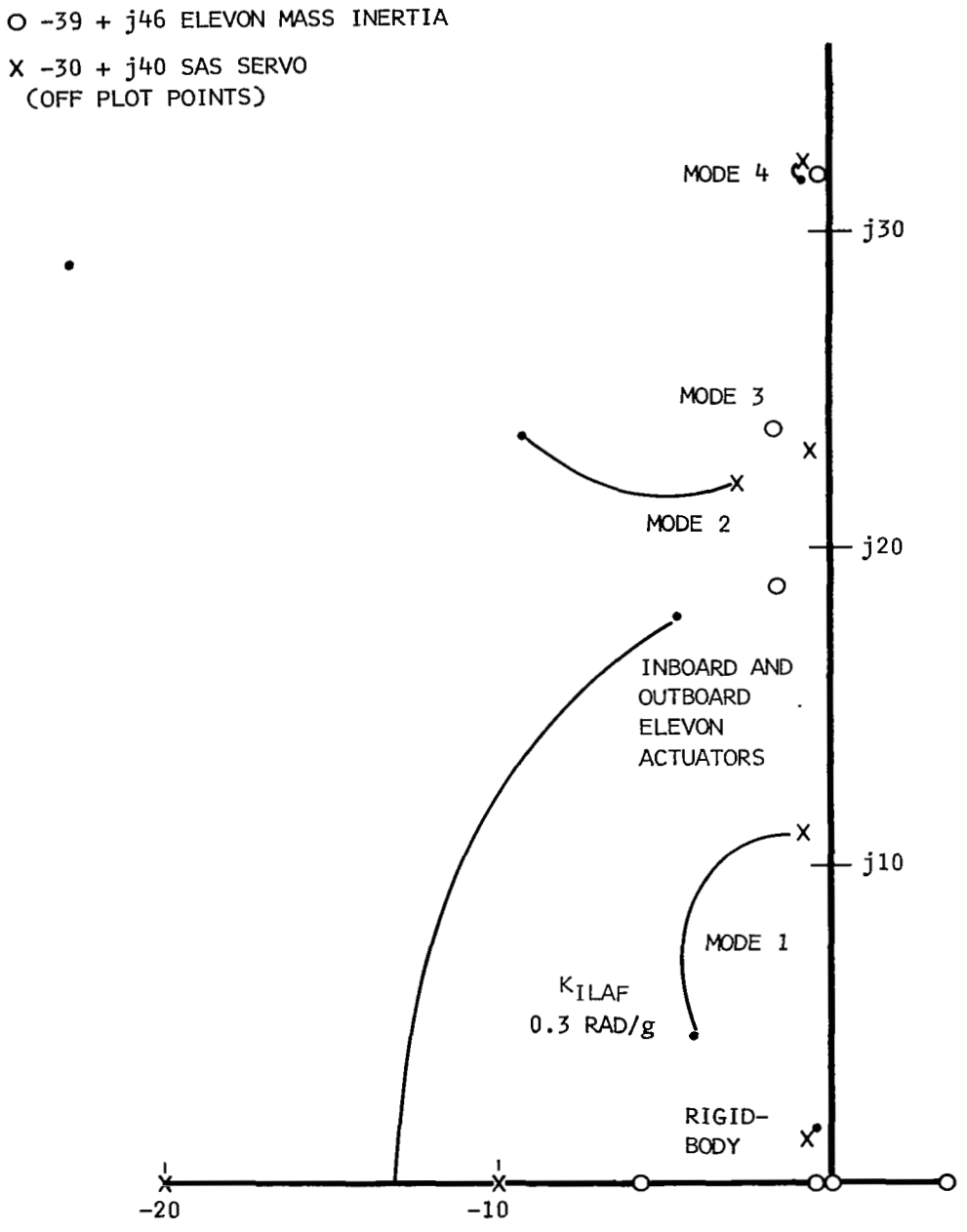

(c) HEAVY WEIGHT, δ_T = 25 DEGREES, M = 0.9, 25,000 FEET

Figure 22.- Continued.

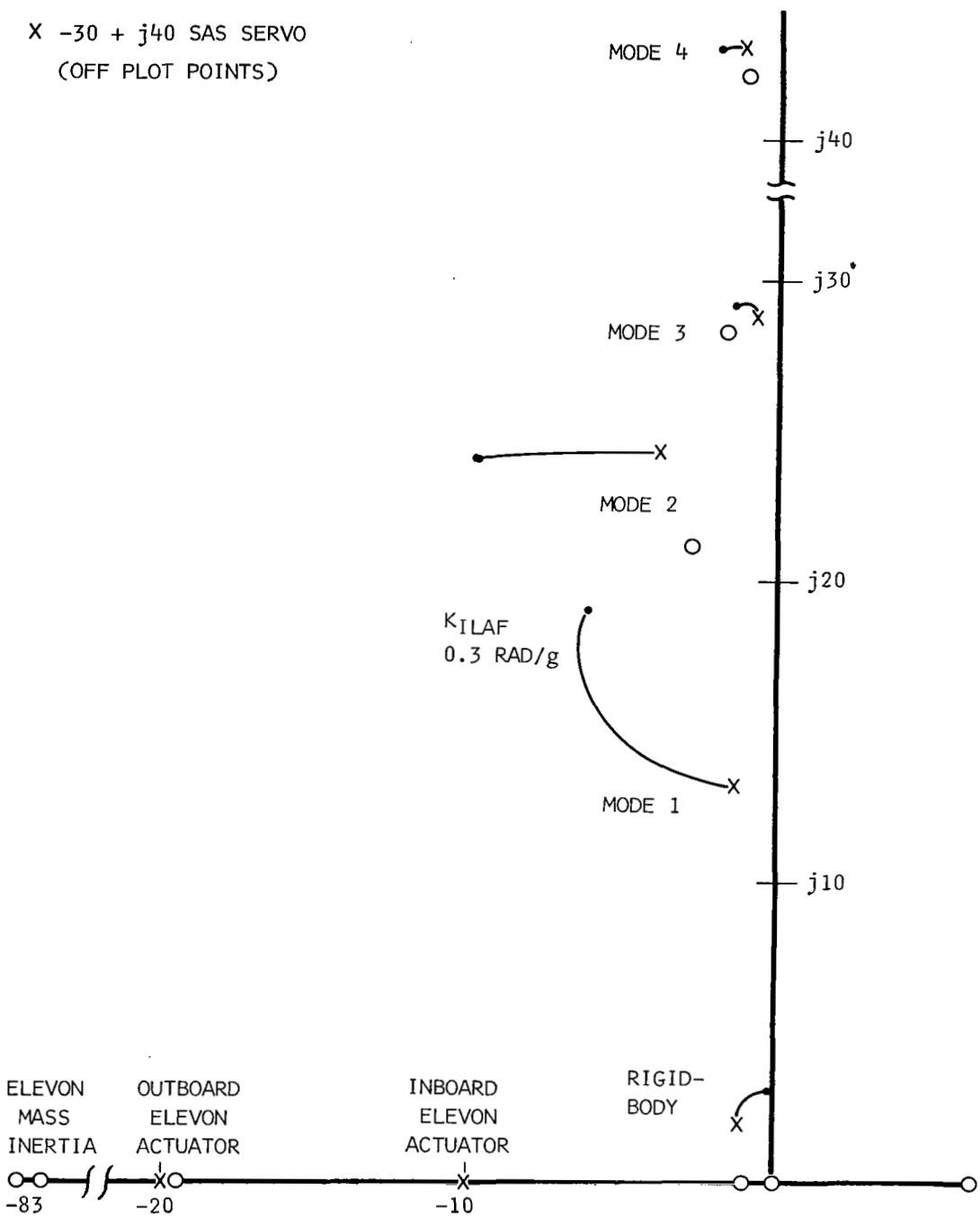

(d) LIGHT WEIGHT, δ_T = 25 DEGREES, M = 0.9, 25,000 FEET

Figure 22.- Continued.

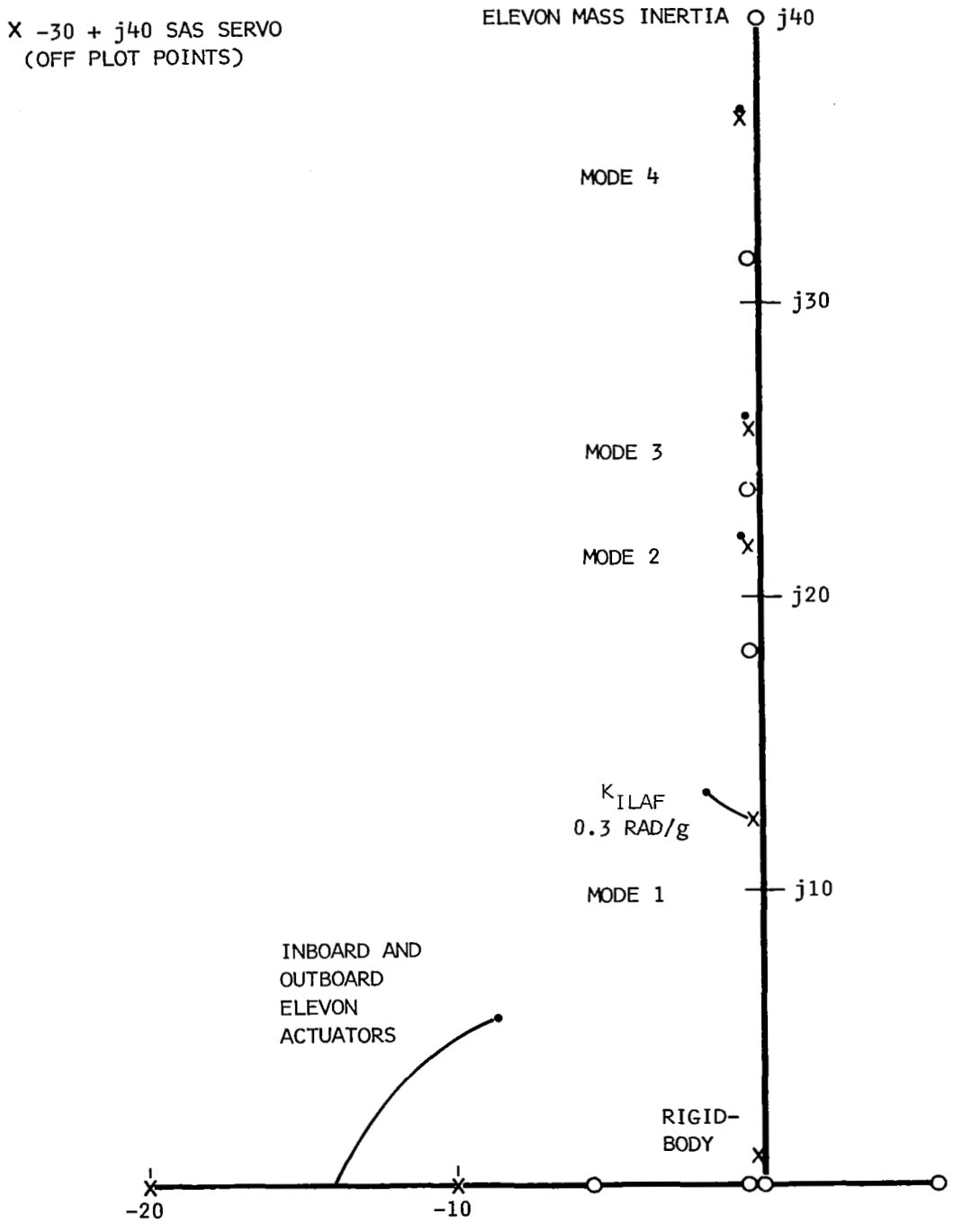

(e) MEDIUM WEIGHT, δ_T = 65 DEGREES, M = 3.0, 70,000 FEET

Figure 22. - Concluded.

TABLE II

SUMMARY CHART OF ROOT LOCI DATA

Legend:

✓✓ Damping significantly improved
✓ No significant effect
XXX Potential adverse effect without any shaping, favorable effect with lead-lag
* Root loci plot presented in report

	Accelerometer at Elevon No. 1		Accelerometer at Elevon No. 4	
	Tips Up	Tips Down	Tips Up	Tips Down
M = 0.4, SL Heavy wt	* Mode 4 ✓ 3 XXX 2 ✓ 1 ✓✓	Mode 4 ✓ 3 ✓ 2 ✓ 1 ✓✓	Mode 4 ✓ 3 ✓ 2 ✓ 1 ✓✓	
M = 0.4, SL Light wt	* Mode 4 ✓ 3 ✓ 2 ✓ 1 ✓✓	Mode 4 ✓ 3 ✓ 2 ✓ 1 ✓✓	Mode 4 ✓ 3 ✓ 2 ✓ 1 ✓✓	
M = 0.9, SL Heavy wt			Mode 4 ✓ 3 ✓ 2 ✓✓ 1 ✓✓	Mode 4 ✓ 3 ✓ 2 ✓✓ 1 ✓✓
M = 0.9, SL Light wt	Mode 4 ✓ 3 XXX 2 ✓✓ 1 ✓✓			
M = 0.9, 25,000 ft Heavy wt	Mode 4 ✓ 3 XXX 2 ✓✓ 1 ✓✓	* Mode 4 ✓ 3 XXX 2 ✓✓ 1 ✓✓	Mode 4 3 XXX 2 ✓ 1 ✓✓	Mode 4 ✓ 3 ✓ 2 ✓✓ 1 ✓✓
M = 0.9 25,000 ft Light wt	Mode 4 ✓ 3 XXX 2 ✓✓ 1 ✓✓	* Mode 4 ✓ 3 XXX 2 ✓✓ 1 ✓✓		Mode 4 ✓ 3 ✓ 2 ✓✓ 1 ✓✓
M = 3, 70,000 ft Medium wt		* Mode 4 ✓ 3 XXX 2 XXX 1 ✓✓		

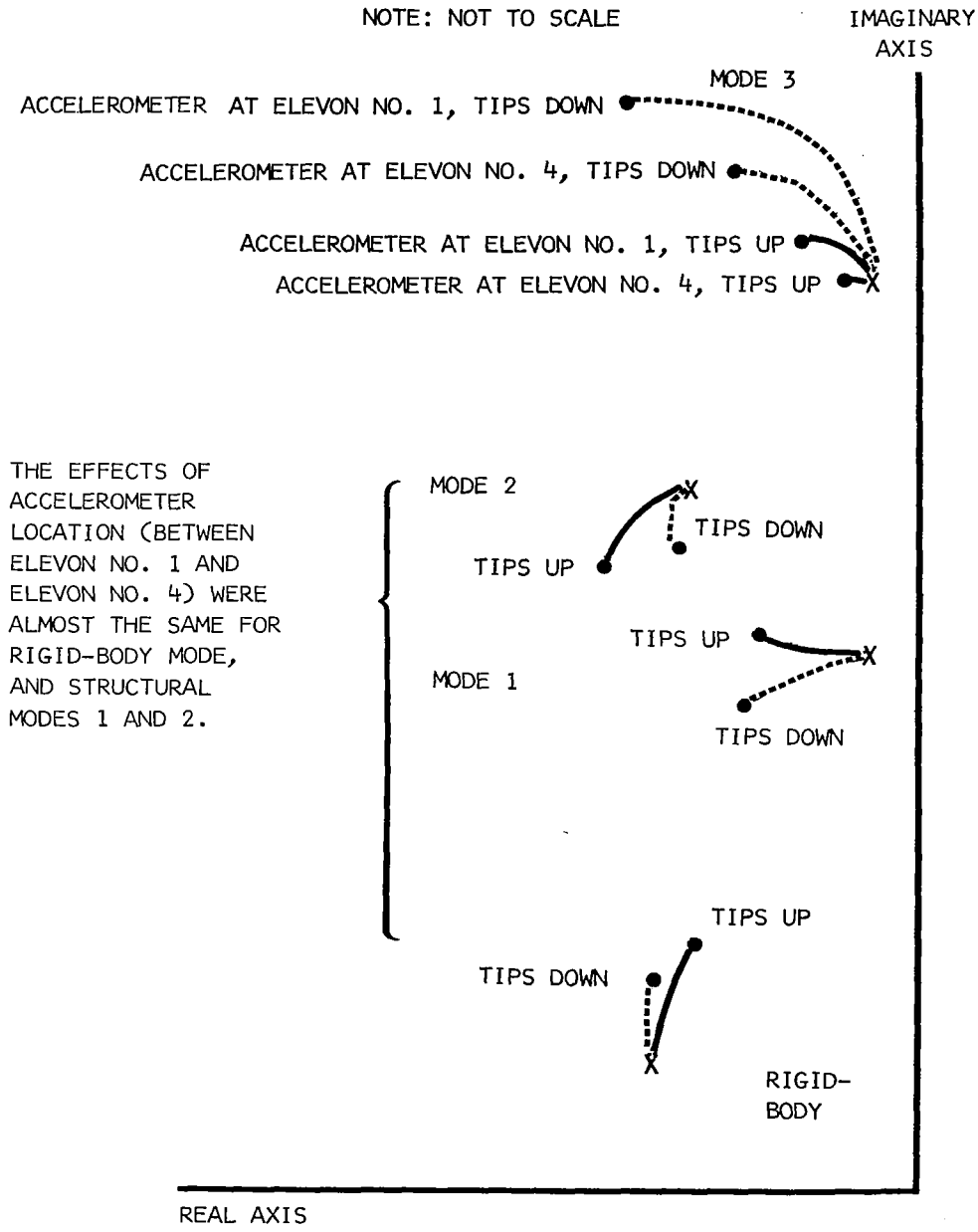

Figure 23.- Root loci sketches illustrating the effects of tip position and accelerometer location.

System Mechanization

The specific mechanization of the ILAF system and how it integrates with the existing FACS is shown in the block diagram of figure 24. As illustrated, the ILAF system operates through the existing pitch FACS servo. The ILAF engage switch contacts are located at the point where the ILAF signals are introduced into the FACS computer. This mechanization and specific implementation of the ILAF system is considered to be the most direct method of accomplishing the objectives (limited flight-test demonstration of the concept) in a minimum program. The methods used and the design alternatives selected have been based upon ability to accomplish the objectives without extensive redesign or qualification of aircraft modifications for flightworthiness. This is the primary reason for utilization of the existing actuation arrangement. The electronic equipment which is added has been designed using components and techniques which were previously used and qualified in the original FACS design and installation. A limiter has been added in the existing FACS electronics to prevent the servo from being driven against its physical limits. The combined FACS and ILAF signals may occasionally command motions greater than the ±7.5 degrees of servo authority.

The ILAF system accelerometer signals are blended as indicated earlier and are shaped by both a notch filter and a compensation network. The signals are gain adjusted from a manual control in the cockpit and are integrated into the FACS electronics at a point where advantage can be taken of the existing altitude gain scheduling. The notch filter reduces the transmission of signals sensed by the accelerometers which are caused by elevon motions at the control surface natural frequency. This natural frequency is a result of the actuator dynamics, structural installation compliance, and elevon surface inertia. The available data indicate that this frequency value is approximately 20 cps. The notch filter design was predicated on the fact that the in-flight environment would not change the 20 cps resonant point significantly. This assumption was based on the analysis results discussed earlier in connection with descriptions of the basic airplane characteristics. The compensation network provides a small amount of phase lead in the signal transmission for improvement of the third mode damping as determined from the analytical modes available for analysis. It is required to maintain good signal transmission in the range of the important structural modes (up to 10 cps) and to roll-off (attenuate) at higher frequencies. The notch filter assists in the roll-off at higher frequencies. The lead characteristics of the compensation needed for improved performance do not allow use of additional filters to obtain a sharper roll-off at high frequencies above the third mode frequency. As much attenuation as possible at higher frequencies is desirable in the ILAF design because the accelerometers sense the response to increasing proportions of surface inertia reaction forces over the aerodynamic forces at very high frequency. The feedback of the response due to the control surface inertia forces is destabilizing.

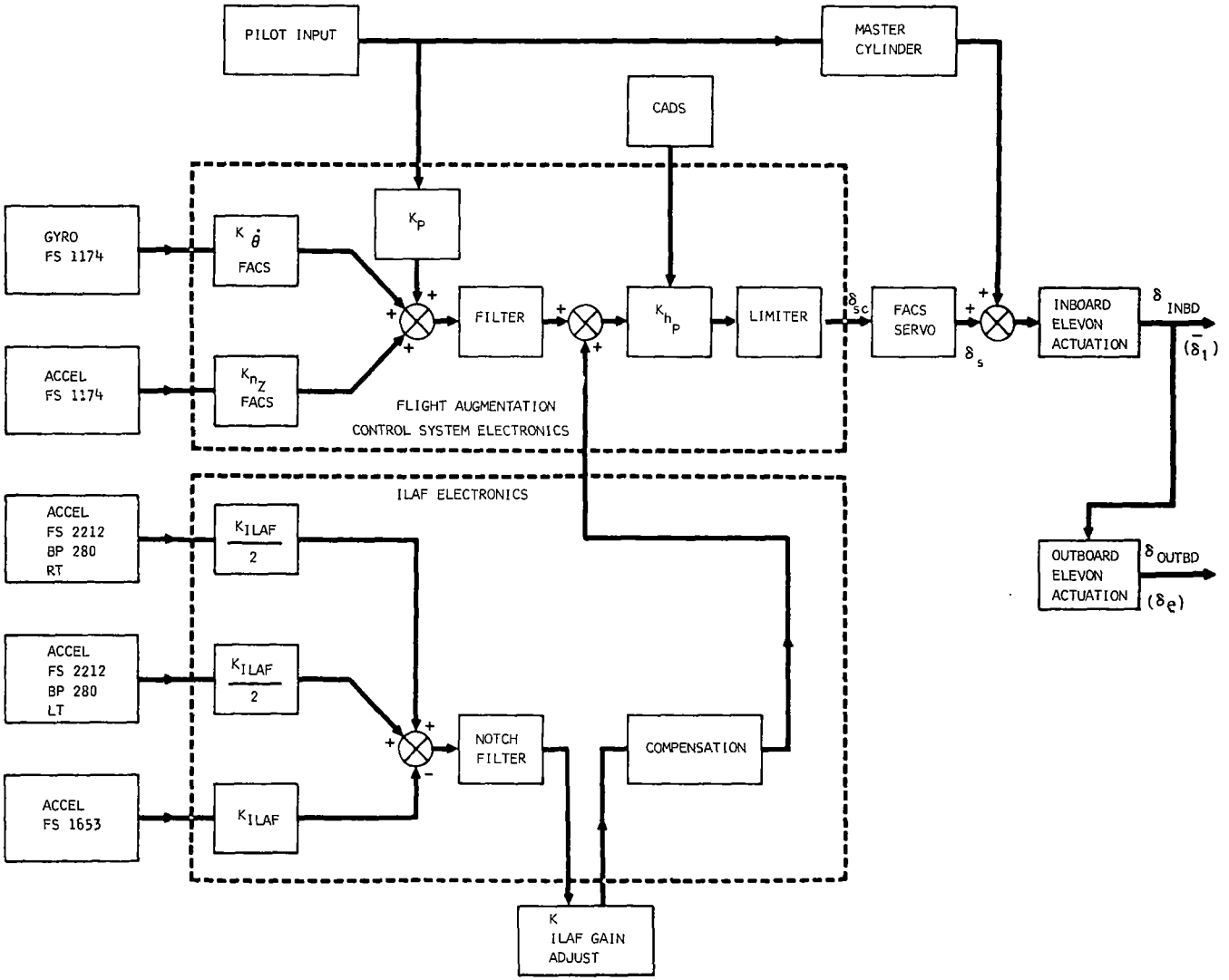

Figure 24.- XB-70 integrated longitudinal-symmetric FACS and ILAF system.

Figures 25a and 25b show the breadboard test frequency responses of the notch filter in combination with the lead-lag compensation. Also shown are the accelerometer dynamics (linear for outputs of $\pm\Delta$1g) obtained from the manufacturer's data.

Figures 26 and 27 show the composite frequency responses from the blended ILAF accelerometer input through inboard elevon output for constant amplitudes of inboard elevon output. These data include the characteristics of accelerometers, shaping, servo, and inboard elevon actuator shown in figures 25, 5, and 6. These composite frequency response curves together with an analytical model of the whole vehicle and structural dynamics were used to check ILAF system gain and phase margins. In cases where limit cycle instabilities were possible, maximum amplitudes of the inboard elevon panel could be estimated using these composite frequency response data.

The altitude gain function of the central air data system increases the maximum ILAF gain by a factor of 4 at high altitude above the sea level value. The calibration of the ILAF gain adjust is shown in figure 28.

System Qualification

The ILAF system has been qualified by similarity with the existing pitch FACS and other equipment in the XB-70. Test specifications have been provided to bench-test both the FACS and ILAF individually and electronically integrated. These specifications include tests of the installation.

Additional engineering operational tests are to be conducted to verify the functional performance, phasing, and integration prior to flight. These tests will provide specific data for use in subsequent flight-test support analyses.

The flight program support will consist of preflight tests to detect unknown ILAF failures prior to flight and periodic ILAF gain calibration. The present FACS preflight and periodic tests will also be conducted.

Fail-Safety

A fail-safe ILAF system has been designed using the failure protection concept proven in the existing pitch FACS. Fail-safety is defined here as the protection from adverse effects of control system component failure rather than protection from instability caused by unknown factors. This system has been extensively tested during XB-70 simulation efforts and failure mode analysis in the XB-70 program, and confidence has been established during previous flight test. Therefore, to implement the ILAF system and to interface

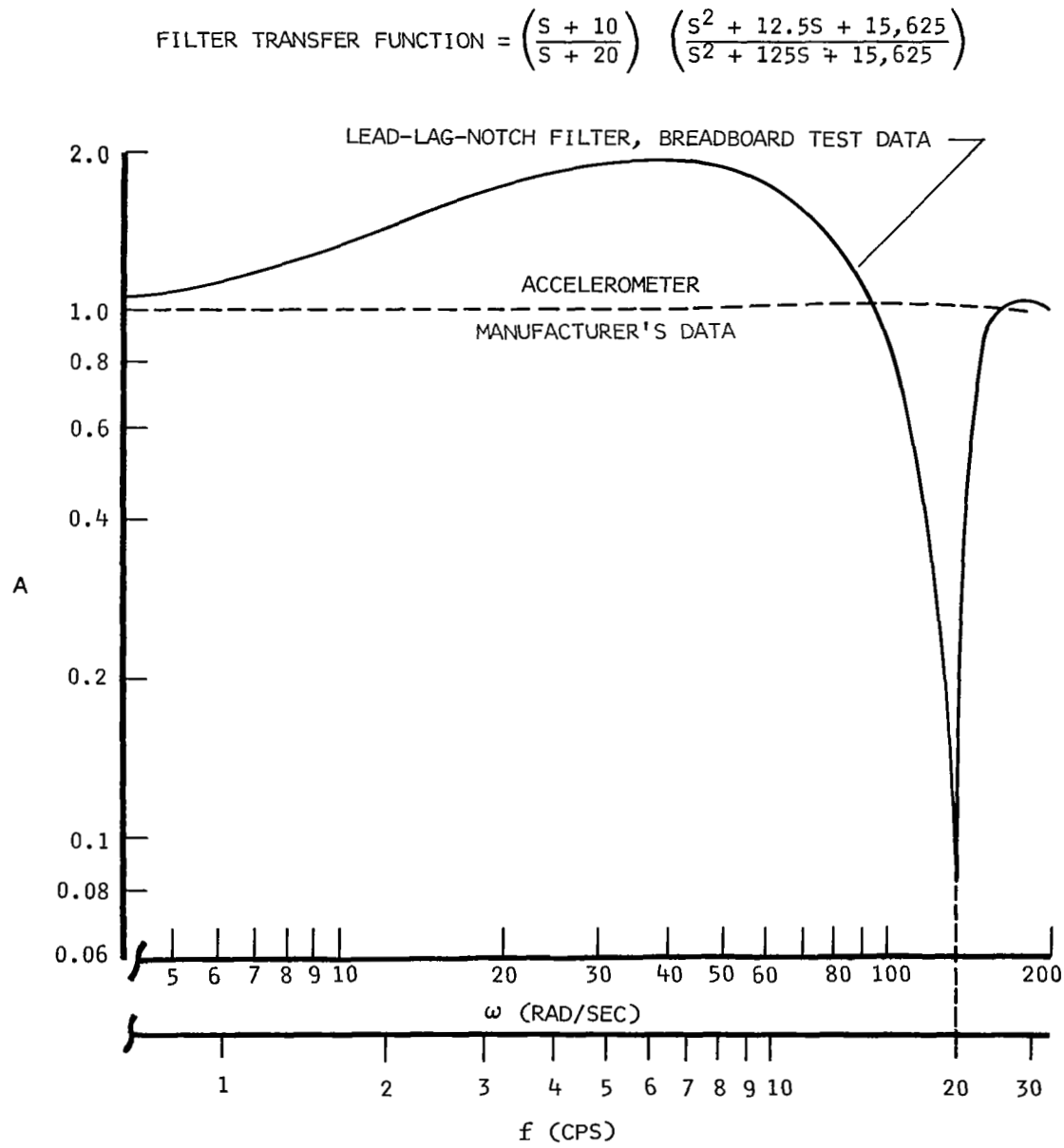

(a) AMPLITUDE

Figure 25.- Frequency response of ILAF shaping and accelerometer dynamics.

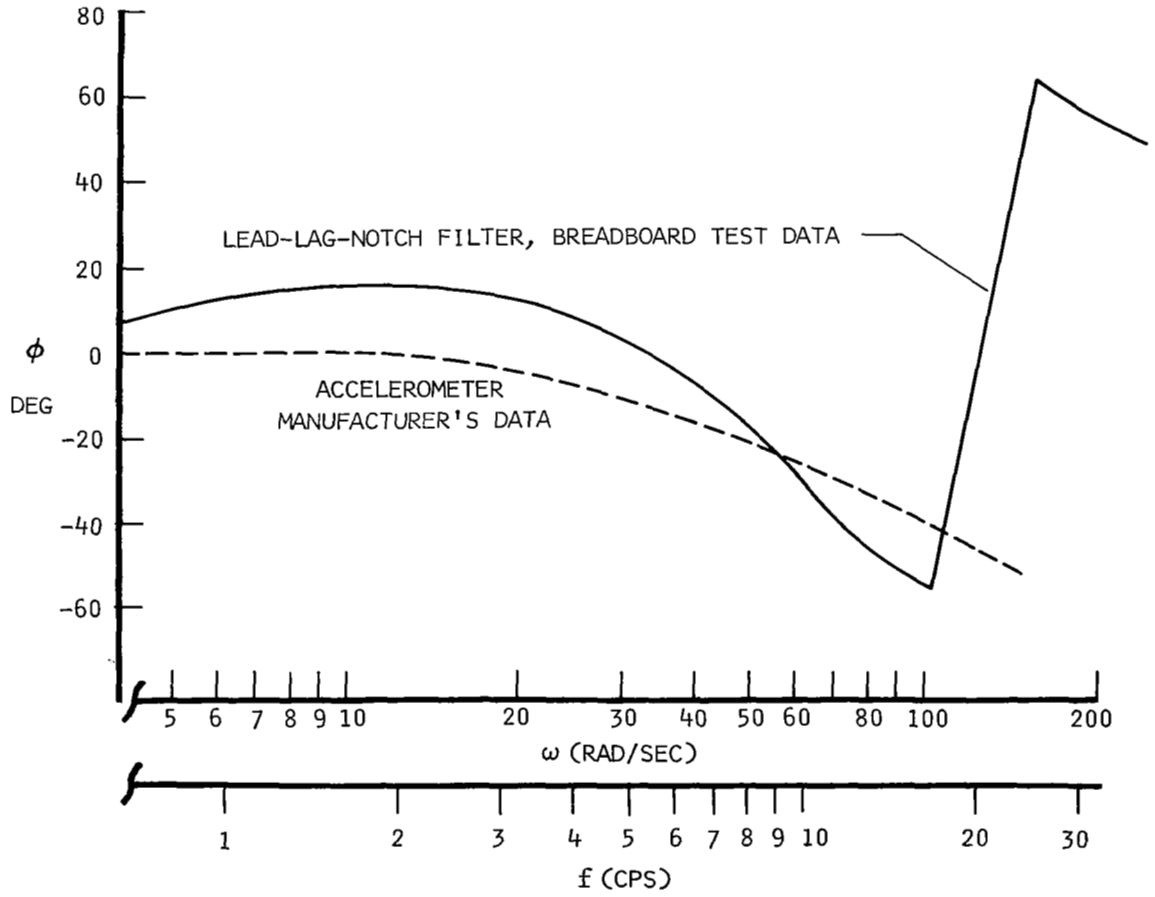

(b) PHASE ANGLE

Figure 25.- Concluded.

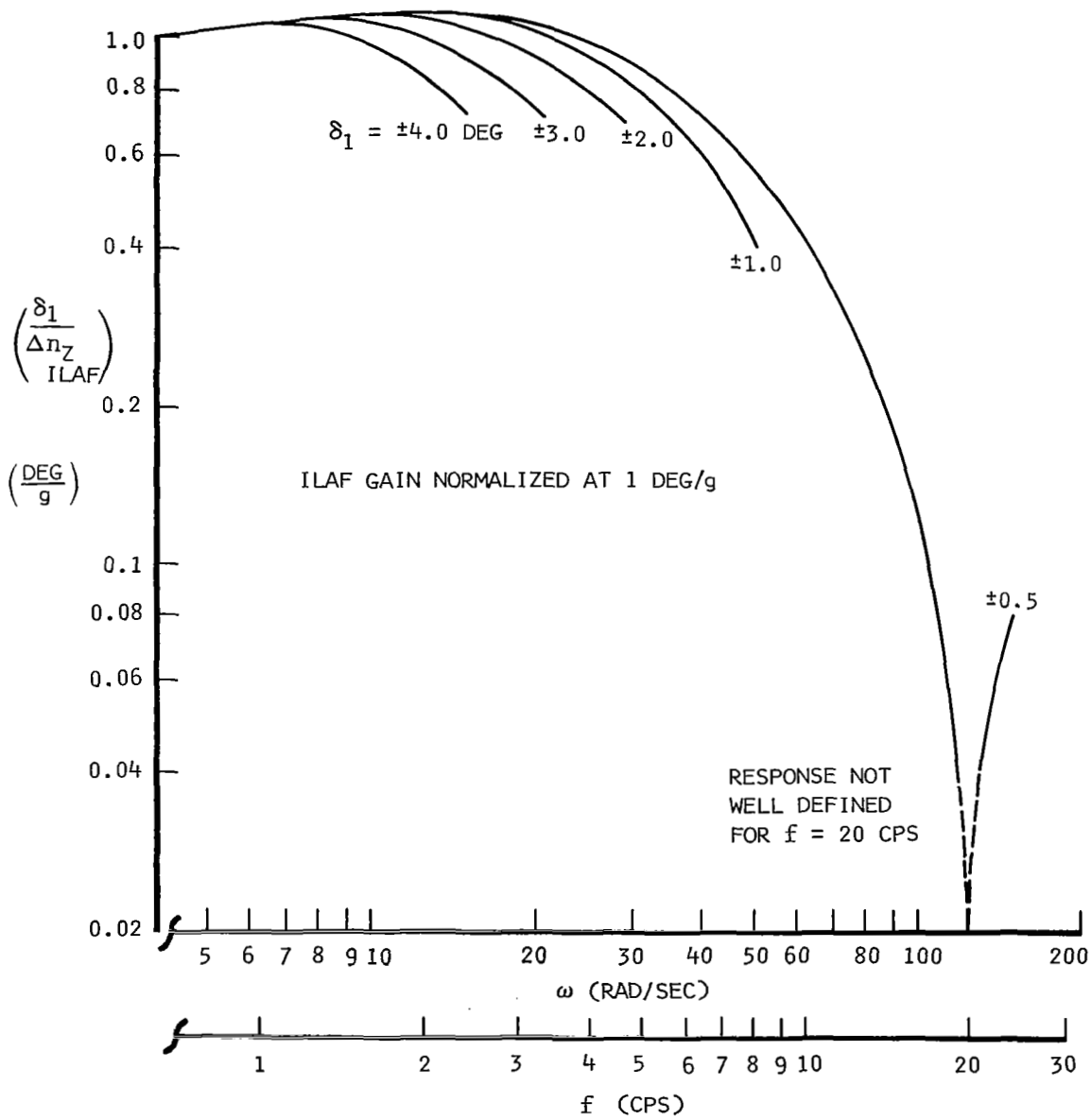

(a) AMPLITUDE

Figure 26.- Frequency response from blended ILAF accelerometer input through inboard elevon output for large amplitudes - composite breadboard, simulator, and airplane data.

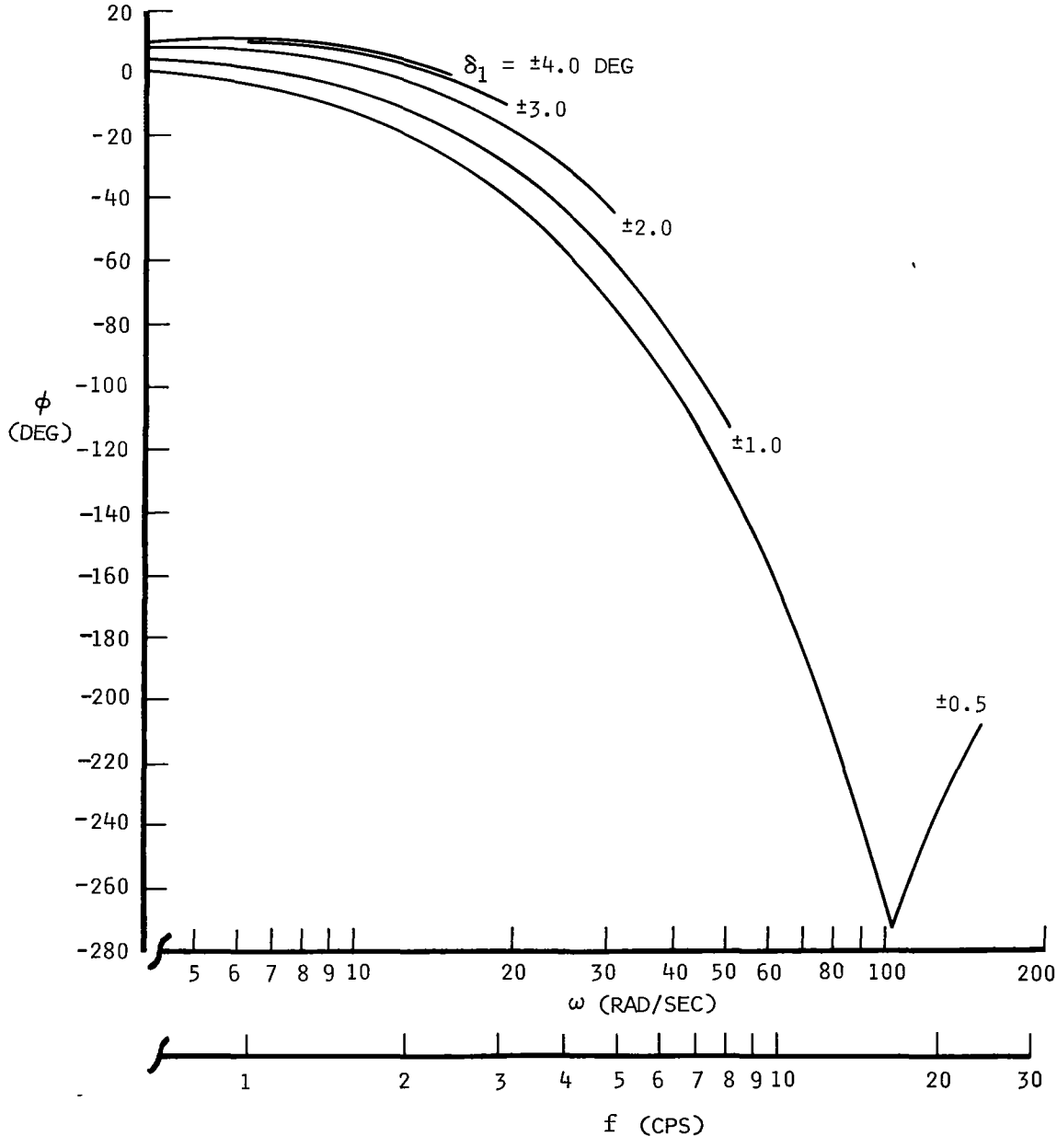

(b) PHASE ANGLE

Figure 26.- Concluded.

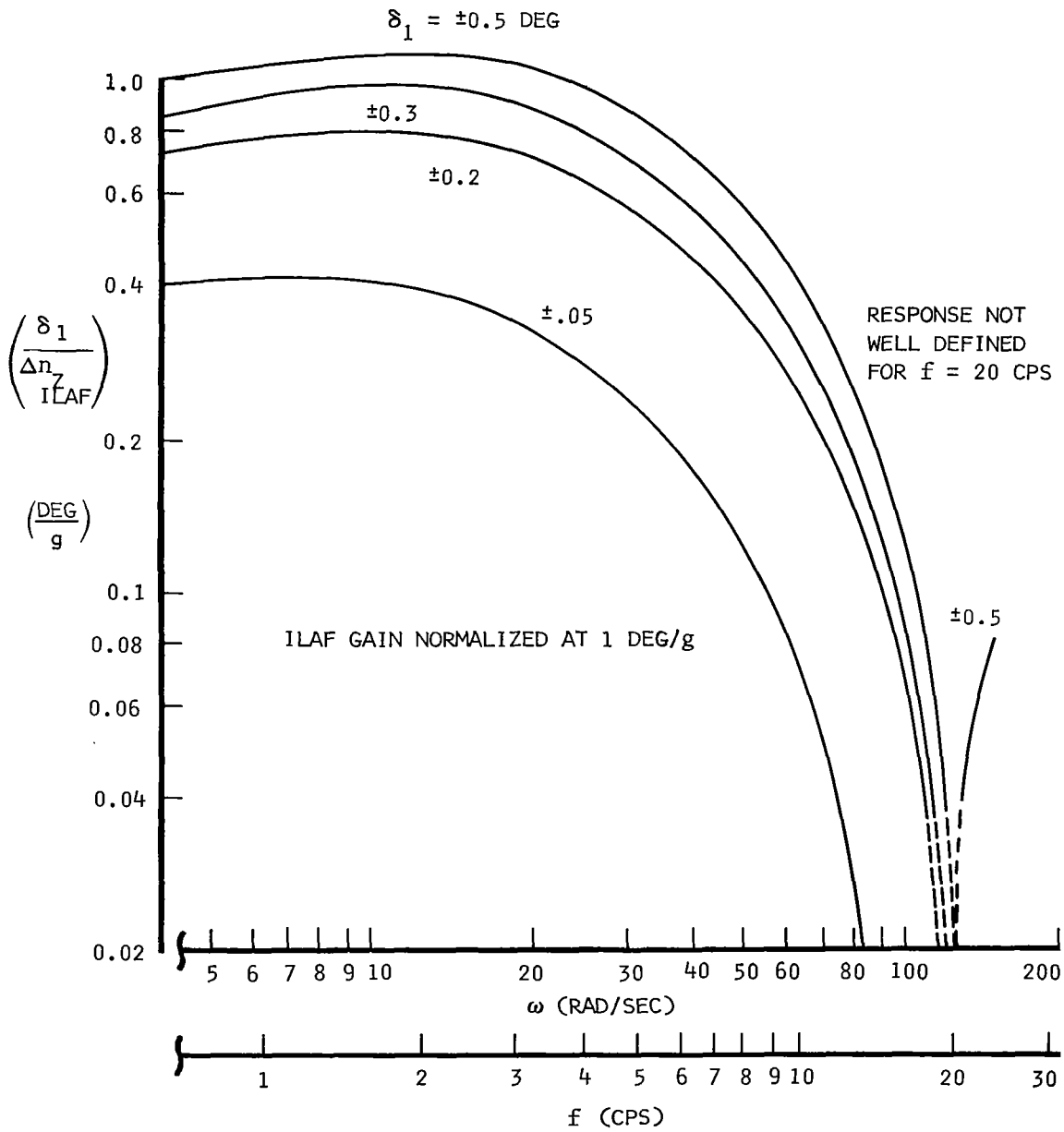

(a) AMPLITUDE

Figure 27.- Frequency response from blended ILAF accelerometer input through inboard elevon output for small amplitudes - composite breadboard, simulator, and airplane data.

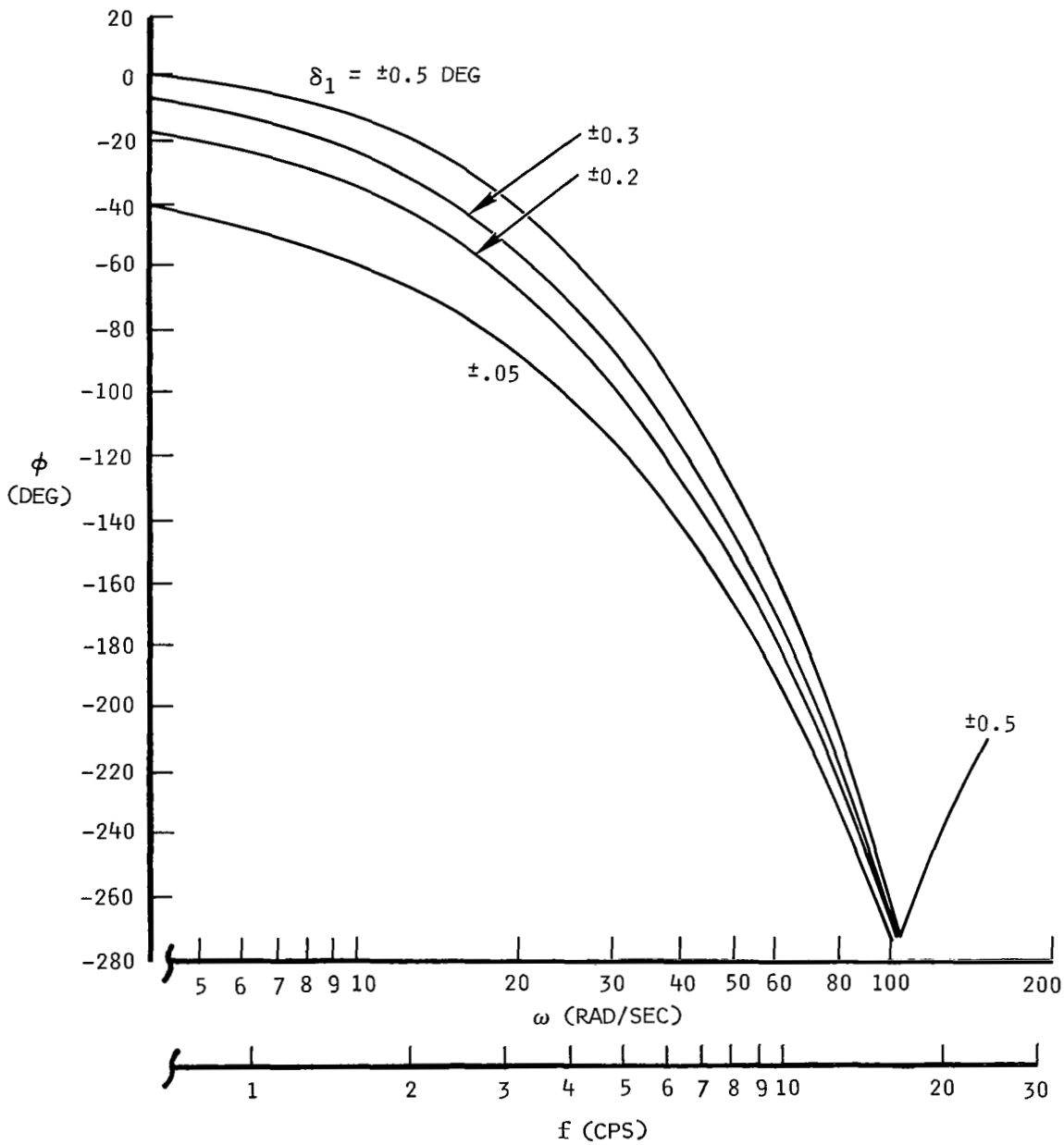

(b) PHASE ANGLE

Figure 27.- Concluded.

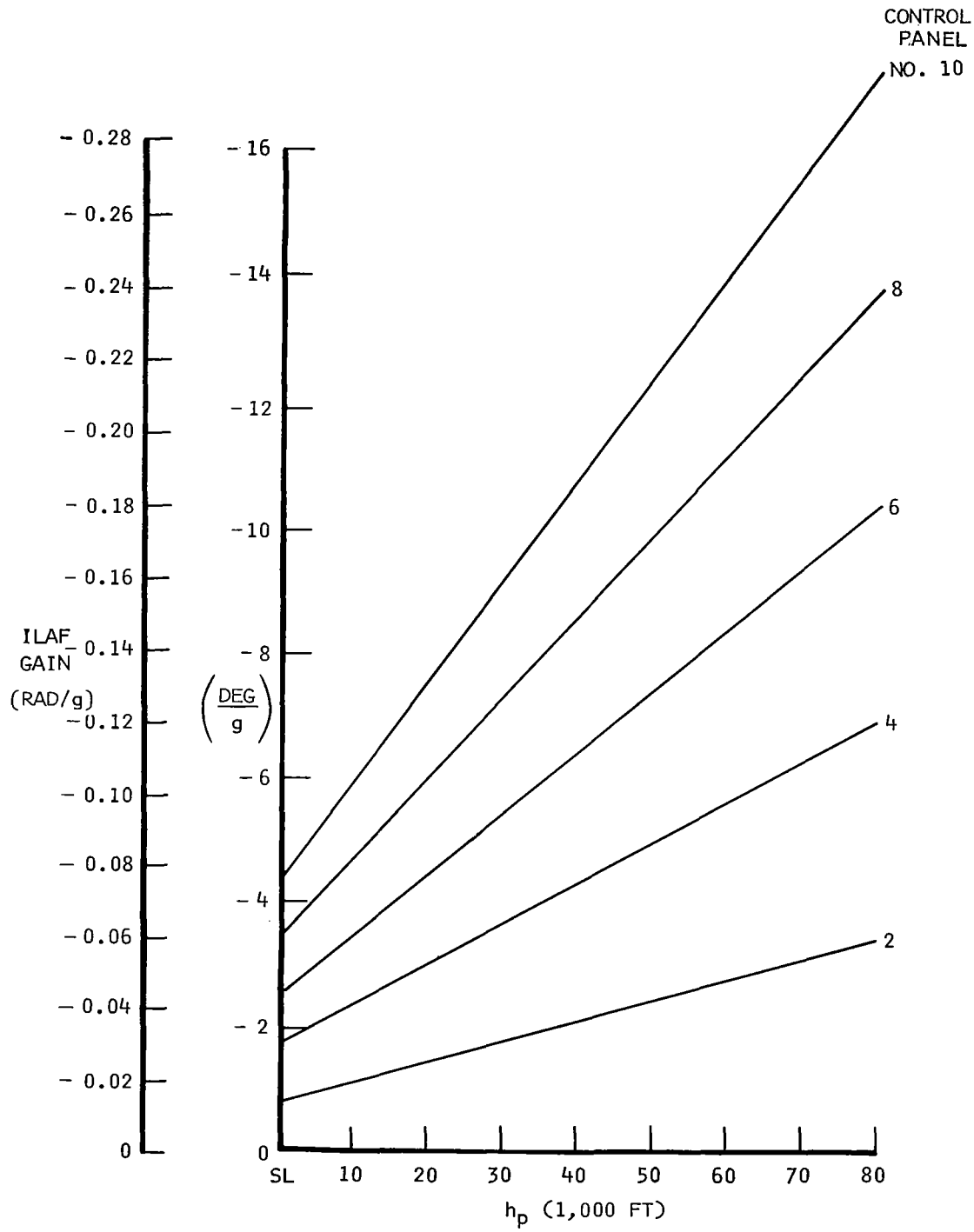

Figure 28.- ILAF gain as a function of control panel selector setting and altitude.

it satisfactorily with the existing pitch FACS, each ILAF component previously discussed is a matched pair, but electrically independent. The two channels are provided power from the respective FACS channel power supplies. The pitch FACS must be engaged for ILAF operation, but the FACS can operate without ILAF. This is not utilizing the full fail-safety potentials inherent in the concept of separation of whole-vehicle motion and structural motion as discussed earlier; that is, the ILAF system on the XB-70 cannot be operated independently of the FACS. This was a cost and timing limitation and not a technical one. In operation, an ILAF component failure will result in a pitch FACS disengagement without a transient. However, the FACS can be reengaged. With this implementation, the possiblity of a nuisance disengagement of the pitch FACS has been increased when the ILAF system is engaged. However, operation of the integrated FACS and ILAF equipment on the XB-70 flight simulator indicates that excessive undesired disengagements should not occur.

ILAF SYSTEM PERFORMANCE AND STABILITY ANALYSES

Two techniques have been utilized to obtain the ILAF response and stability characteristics. Linear digital analyses have been conducted using mathematical models of the aircraft and control system, and flight simulator testing has been conducted using actual hardware and an analog model of the airframe dynamics. Appendix D contains a description of the equations of motion used for both the digital analyses and the analog-simulator studies. Appendix C summarizes the pertinent analog-simulator features utilized in this program.

The format of the discussion will be to present, first, the linear digital analyses results and to follow with the analog-simulator nonlinear results.

A primary feature of importance in the linear digital analysis results is the power spectral density format of the gust response characteristics. The most accurate representations of the available aerodynamic data variations with frequency are included in these analyses. A primary feature of importance in the flight control simulator analysis results is the utilization of the best available representation of the control system nonlinearities and the ability to readily obtain transient response data and performance data near system threshold and saturation conditions. Both analysis approaches provide an indication of gust sensitivity and frequency response to exciter vane inputs for relative comparison. Using these two approaches, most aspects of the performance and stability could be predicted.

The reader is urged to use caution in interpreting the results presented in this report because of the chronology of data available as the program progressed and some limitations of the analytical models used in the analyses. The following points should be kept in mind:

(1) Limited XB-70 control system data were available at frequencies of concern at and above the range of structural modes of interest at the initiation of the program. The available data were linearized to obtain representative response characteristics. It was assumed that use of these data would be conservative with respect to stability margins because the amplitudes and phase shift at higher frequencies were slightly greater than those anticipated due to nonlinear effects. These linear response characteristics were used in all digital analyses of the ILAF response to gust and shaker vane inputs. Thus, these results would not indicate the effects of threshold or saturation and would indicate lower stability margins than those believed available. The results would provide an indication of performance which could be achieved at an allowable gain.

(2) The results of simulator tests and air vehicle tests eventually provided a very complete description of the ILAF and XB-70 control system response characteristics including all predominant nonlinear effects. These data have been used in stability analyses to obtain a better estimate of stability margins. However, the data available are for no-airload test conditions.

(3) The flight simulator control system characteristics above 7 cps do not match those of the airplane. Therefore, the simulator results are valid for performance characteristics below 7 cps and may not be representative above 7 cps.

(4) The air vehicle dynamic model has not been validated with flight-test results.

(5) In the linear digital analyses, both the gust excitation and control surface aerodynamic variations with frequency are included.

(6) The flight simulator data were obtained using quasi-steady gust data to simplify the gust excitation mechanization, but the control surface unsteady aerodynamic effects were represented. This provided a better simulation for stability indications. However, the control surface resonant frequency was lower on the simulator than on the airplane. The ILAF notch filter on the simulator was adjusted downward to allow an indication of an airplane solution with a typical resonance even though the resonance occurs at a different value of frequency. The ability to make a simple adjustment in the notch frequency in order to obtain the results in this section has provided confidence in being able to properly adjust the notch on the aircraft. The simulation program time available did not allow more detailed investigation of the sensitivity in this area. The ILAF control system describing function data have been generated from integrated component frequency response data obtained during flight simulation testing and during air vehicle testing. The characteristics at low frequency are similar for both the air vehicle and simulator. The airplane data have been used to represent the characteristics at high frequency (those above 10 cps).

Flight Conditions

Both the digital computer and analog-simulator analyses were conducted at flight conditions typical of those flown in the past by the XB-70 and likely to be flown in the future. These conditions are shown in figure 29 where the crosshatched area indicates nominal past flight-test areas. The conditions illustrated are:

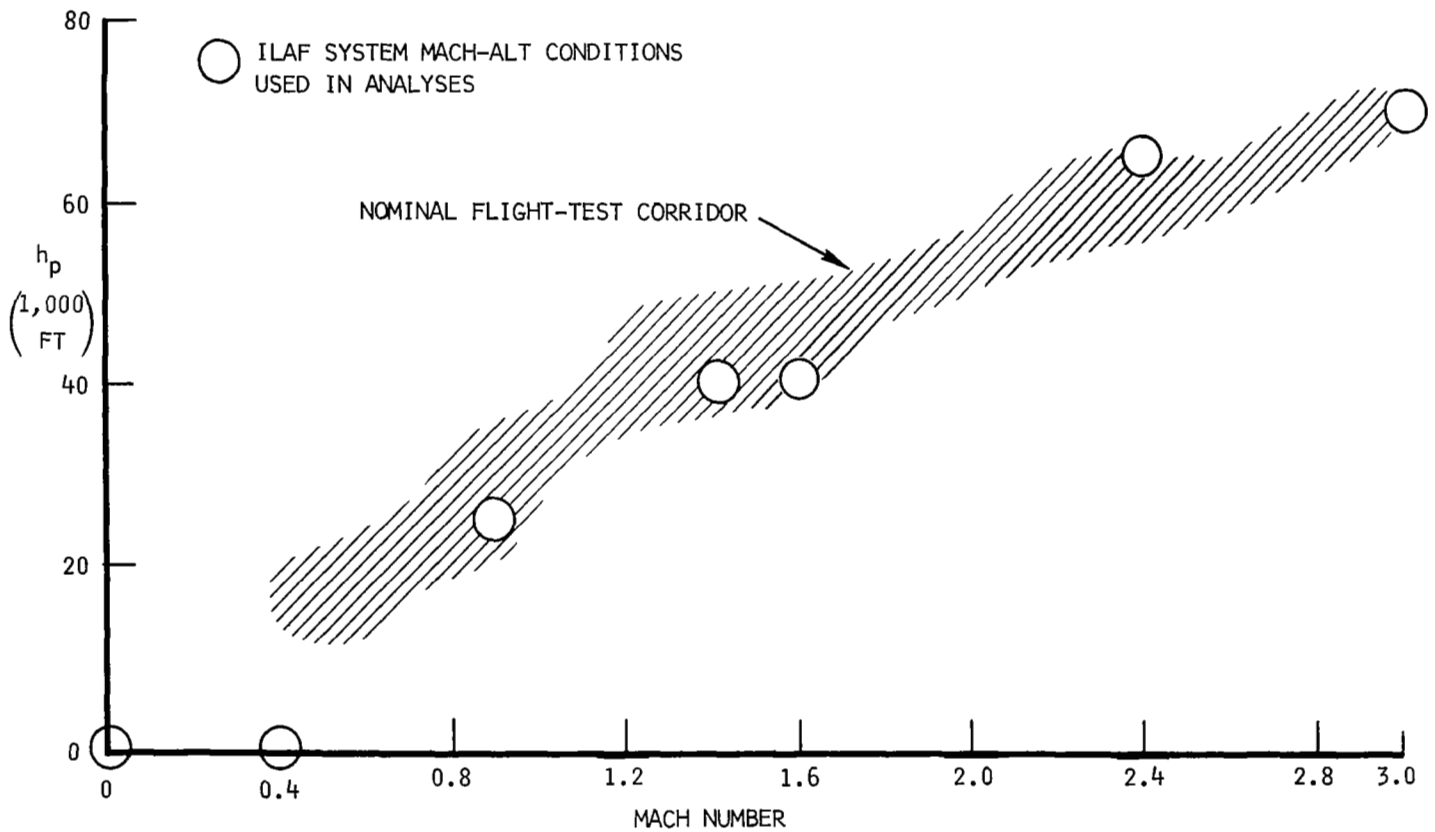

Figure 29.- ILAF system analysis flight conditions.

Mach	Altitude	Weight	Tip (Degrees)
0	SL	Heavy and light	0
0.4	SL	Heavy and light	0
0.9	25,000 feet	Heavy and light	25
1.4	40,000 feet	Light	65
1.6	40,000 feet	Light	65
2.4	64,000 feet	Medium	65
3.0	70,000 feet	Medium	65

Only the mach 0.4 and 0.9 heavy weight cases and the mach 3.0 medium weight case were studied using the analog-simulator. A check of ground operation (M = 0) was also made on the analog simulator.

It is not likely that the mach 3.0 at 70,000 feet case will be flown; however, the data were already on hand and it does provide a high mach number data point for interpolation purposes.

In order to evaluate the ILAF system in as severe an environment as possible, weight cases representing no fuel (light) and full fuel (heavy) were utilized at subsonic and low supersonic mach numbers. The mach 2.4 and 3.0 medium weight is representative of the practical weight configuration the airplane is likely to fly at these speeds. It is not possible to fly the airplane heavily loaded at these speeds because of the fuel expenditure required to reach these flight conditions, nor it is practical to expect the airplane to fly at these speeds with nearly no fuel.

The M = 1.6 and M = 2.4 cases were studied in digital analyses late in the design cycle. They were selected as being conditions which would most likely be flown. The analyses results were similar to those obtained for the M = 1.4 and M = 2.5 cases and thus are not presented herein.

The basic structural, mass, and aerodynamic data used in this design study were essentially the data that were used and published in reference 5. It was known that certain differences existed in these data when compared to those for the actual airplane to be flown. This was particularly true in the areas of

structure and mass. Based on actual ground vibration tests of the airplane, it is known that the physical airplane is stiffer than represented by the cited data. However, it was felt that the program would be unduly delayed if a new model reflecting all that was known about the actual flight vehicle was assembled. In light of these facts, the basic data and the results obtained for calculations using these data are more appropriately referred to as "design" rather than "predicted" data.

Response and Stability, Digital Analyses

Gust environment response.- A fundamental indication of the effect of a gust environment is the statistical parameter root mean square (rms) of some meaningful airplane response parameter; in this study, the normal load factor at the pilot station has been emphasized. The manner in which this parameter was determined is indicated in figure 30.

Table III presents a summary of the typical performance results to be expected from the ILAF system operation. The data shown are rms normal load factors experienced at the XB-70 pilot station for an rms gust intensity of 1 root per second. The data summary reveals that the basic stability augmentation system (SAS) provides some measure of load factor reduction. The last column of the table is a figure of merit for the ILAF system operation. Shown is a ratio of the rms normal load factor with the SAS plus ILAF system operating over the rms normal load factor with the SAS only operating. The data show that a measurable improvement in ride quality will be achieved at all flight conditions analyzed.

Table IV is a companion to table III and presents the rms elevon rates associated with the data shown in the latter table. The data show the separate rms elevon rates attributable to the SAS operation and that due to the ILAF when both are operated together. The next to last column of the table indicates that ILAF system operation demands from 4 to 16 times the rms rate that the SAS does.

The last column in the table is an indication of the absolute level of elevon rates to be expected from the ILAF system operation. Statistics can show that the peak response parameter value to be experienced in a Gaussian random process is 3σ, where σ is the rms value of the parameter. The elevon peak values obtained in this manner are shown in the last column. The surface-rate-available data, as presented in an earlier discussion, demonstrated that the XB-70 has sufficient elevon rate capacity to permit the ILAF system to cope with moderate gust intensities.

Figures 31a through 31e are the power spectral density plots of normal load factor at the pilot associated with the data shown in tables III and IV.

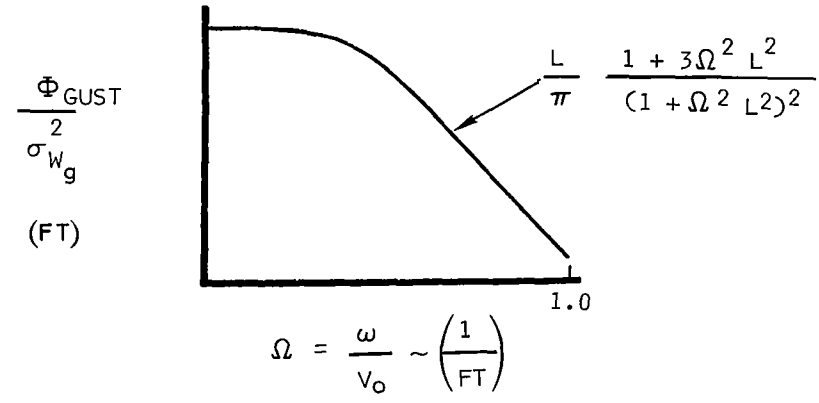

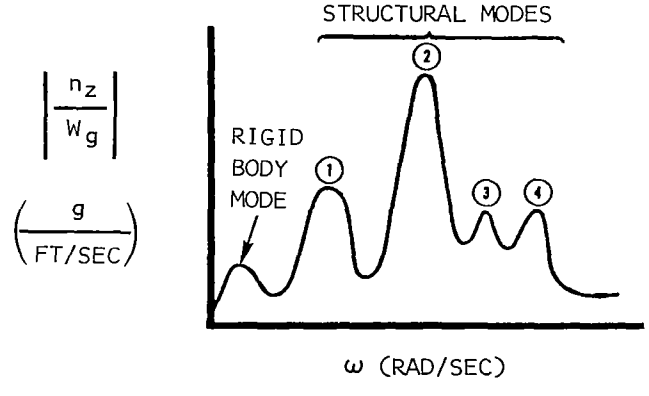

$$\sigma_{n_Z} = \sqrt{\int_0^{\omega} C.O. \left|\frac{n_Z}{W_g}\right|^2 \frac{\Phi(\omega)}{\sigma^2_{W_g}} d\omega}$$

Figure 30.- Illustration of typical root mean square gust response calculation.

TABLE III

RMS NORMAL LOAD FACTOR AT PILOT STATION FOR UNIT RMS VERTICAL GUST VELOCITY.

ANALYTICAL DATA

$\left(\frac{g}{ft/sec}\right)_{rms}, \sigma_{W_g}$ = 1 (ft/sec)rms					
Flight Condition		$\sigma_{n_{z_p}}$ Basic Vehicle	$\sigma_{n_{z_p}}$ SAS Only	$\sigma_{n_{z_p}}$ SAS + ILAF	Performance $\frac{\sigma_{n_{z_p}}\ (SAS + ILAF)}{\sigma_{n_{z_p}}\ (SAS)}$
M = 0.4 SL	Light wt	0.0483	0.0476	0.0376	0.79
δ_T = 0 deg	Heavy wt	0.0679	0.0668	0.0622	0.93
M = 0.90 25,000 ft	Light wt	0.0447	0.0406	0.0335	0.82
δ_T = 25 deg	Heavy wt	0.0571	0.0540	0.0344	0.60
M = 3.0 70,000 ft	Medium wt	0.0117	0.0110	0.00663	0.60
δ_T = 65 deg					

TABLE IV

RMS ELEVON RATES FOR UNIT VERTICAL GUST VELOCITY.

ANALYTICAL DATA

$\left(\frac{\text{deg/sec}}{\text{ft/sec}}\right)$ rms, σ_{W_g} = 1 (ft/sec) rms					
Flight Condition		$\sigma_{\dot{\delta}_e}$ SAS	$\sigma_{\dot{\delta}_{\bar{e}}}$ ILAF	Factor $\sigma_{\dot{\delta}_{\bar{e}}ILAF} / \sigma_{\dot{\delta}_{\bar{e}}SAS}$	ILAF Peak Rates (Deg/Sec)
M = 0.40 SL	Light wt	0.290	1.73	5.96	5.19
δ_T = 0 deg	Heavy wt	0.443	1.71	3.86	5.13
M = 0.90 25,000 ft	Light wt	1.010	4.54	4.50	14.12
δ_T = 25 deg	Heavy wt	0.368	2.29	6.21	6.87
M = 3.0 70,000 ft	Medium wt	0.105	1.85	15.80	5.55
δ_T = 65 deg					

These data serve to illustrate several points. First, they show that the ILAF system can operate without interfering with the SAS short-period performance. Secondly, these plots show the effectiveness of the ILAF system in providing damping to the individual structural modes; in general, the system is very effective in damping the first mode and has a varying performance on the other modes. The analytical model for these calculations included the short-period mode and four symmetric structural modes.

It should be pointed out that the ILAF system gains represented in the data are nominal settings and have not been optimized; the intent was to show that the ILAF system can have a measurable effect on the XB-70. The actual gains used in the power spectral density calculations are indicated on figures 31a through 31e.

Figure 32 is a typical example of the SAS and ILAF performance in reducing normal load factor at a number of different locations throughout the XB-70.

Figure 33 is a typical frequency response plot of the elevon activity associated with the SAS and ILAF systems in a gust field of unit rms velocity. The lower plot shows the elevon activity when only the SAS is operating. The upper plot shows the elevon component due to SAS and the component due to ILAF when both systems are operating together. (This separation of components can only be done analytically and cannot be obtained from test data.) In comparing this upper and lower plot, it is to be noted that the SAS operation is little affected by the ILAF system and that most of the ILAF system activity is found in the structural mode frequency range.

Shaker vane excitation response.- The shaker vane location and details have already been discussed. The airplane frequency response in the form of pilot normal load factor for a unit (1 degree half amplitude) shaker vane input with the SAS and with the SAS plus ILAF system operating are shown in figures 34a through 34e. Again, it should be noted that a nominal rather than optimized system gain has been utilized. These data show that the ILAF system does not change the short-period frequency range response, but does markedly affect the first symmetric structural mode. Depending on the flight and vehicle conditions, the ILAF system has moderate to little effect on the second and third structural modes. The fourth mode is little changed.

The frequency response of elevon action due to systems operation per unit (1 degree half amplitude) shaker vane input is shown in figures 35a through 35e. These are companion plots to those of figures 34a through 34e. These plots again demonstrate the fact that the ILAF interferes little with the SAS operation. In addition, however, these data give an indication of both the linear system elevon deflection to be expected at a given frequency of oscillation and the elevon rates to be expected ($\dot{\delta}_e = \omega\delta_e$).

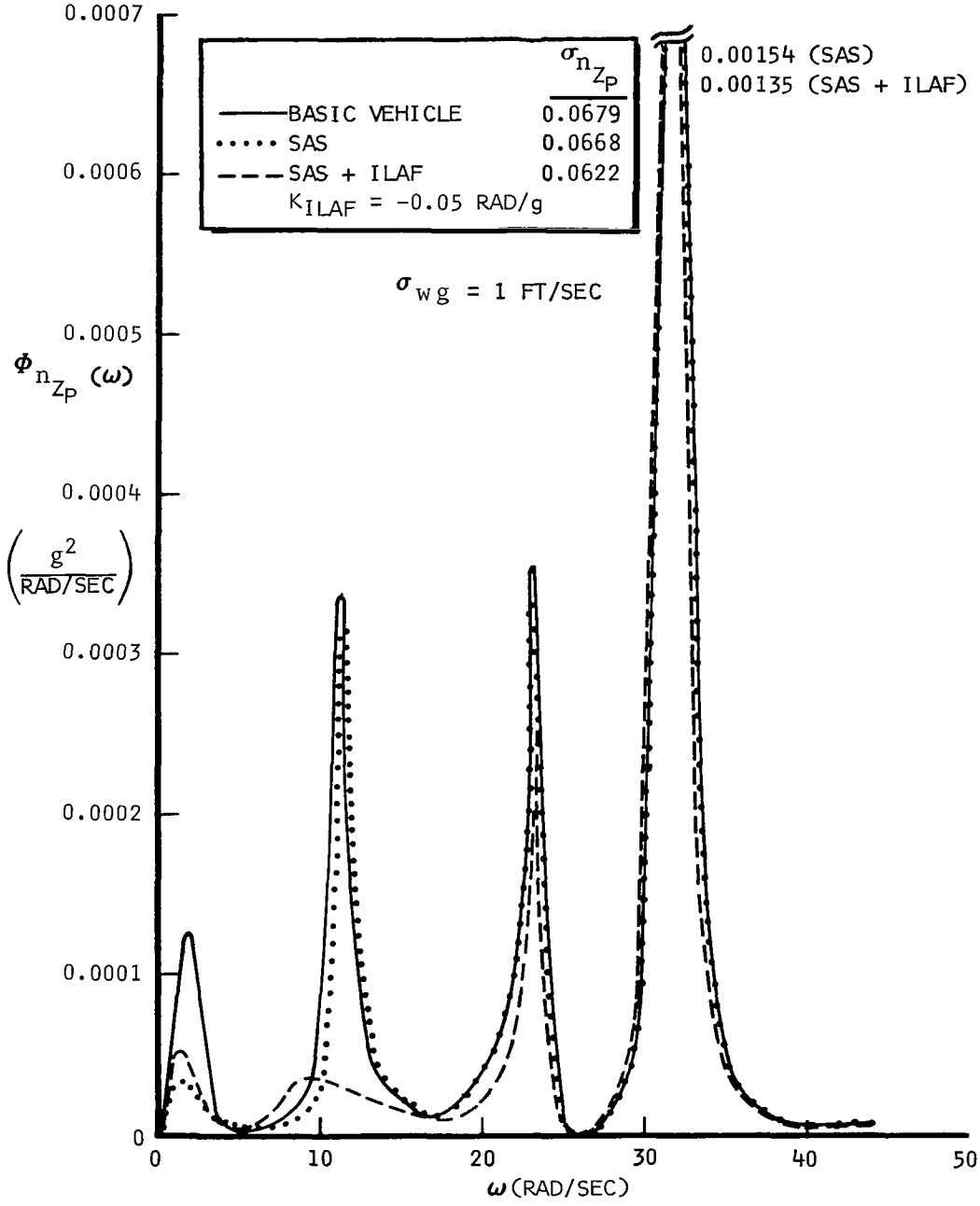

(a) HEAVY WEIGHT, δ_T = 0 DEGREES, M = 0.40, SEA LEVEL

Figure 31.- Effects of control system on normal load factor power spectral density at pilot station of XB-70 due to turbulence - analytical data.

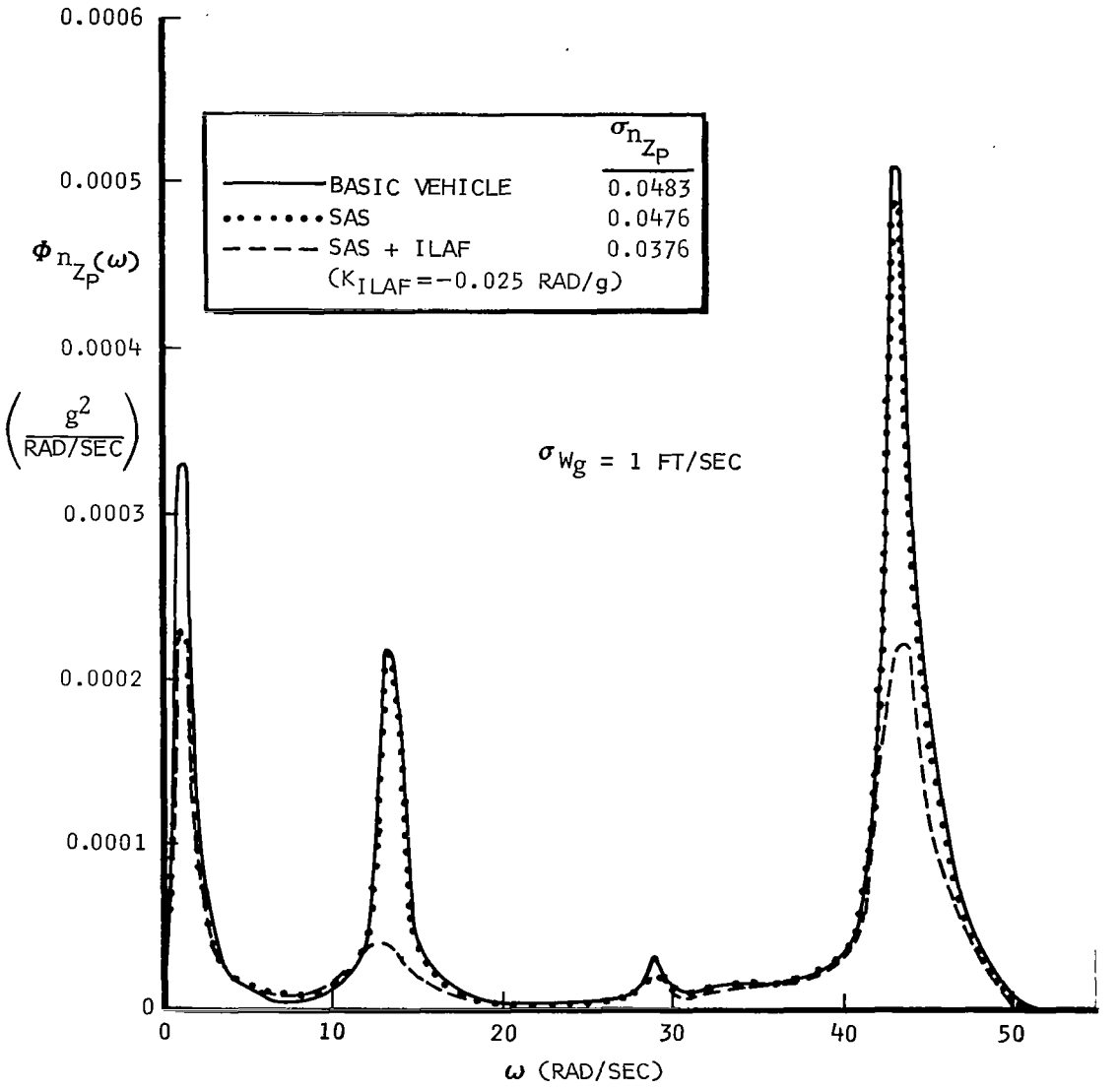

(b) LIGHT WEIGHT, δ_T = 0 DEGREES, M = 0.40, SEA LEVEL

Figure 31.- Continued.

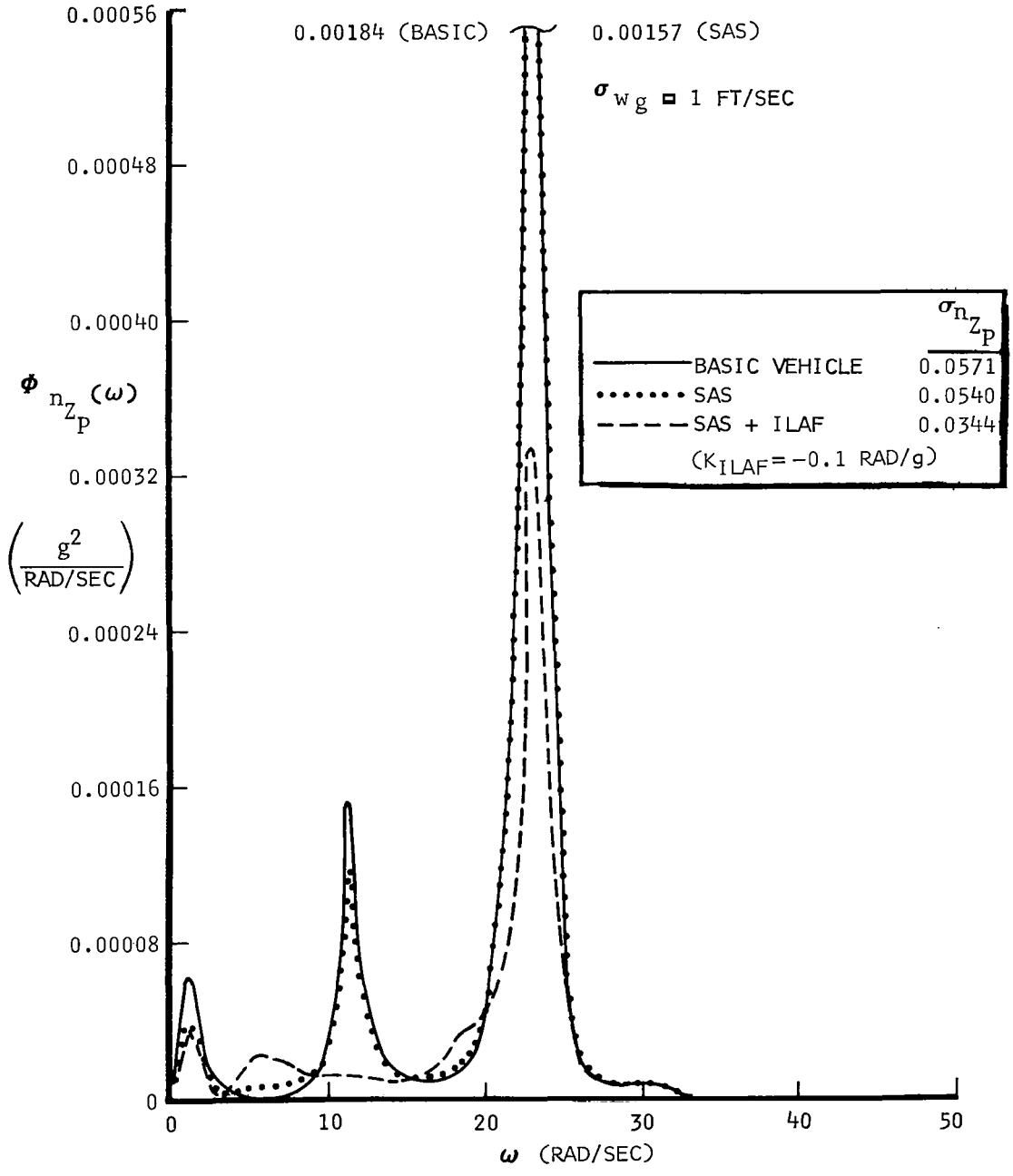

(c) HEAVY WEIGHT, δ_T = 25 DEGREES, M = 0.90, 25,000 FEET

Figure 31.- Continued.

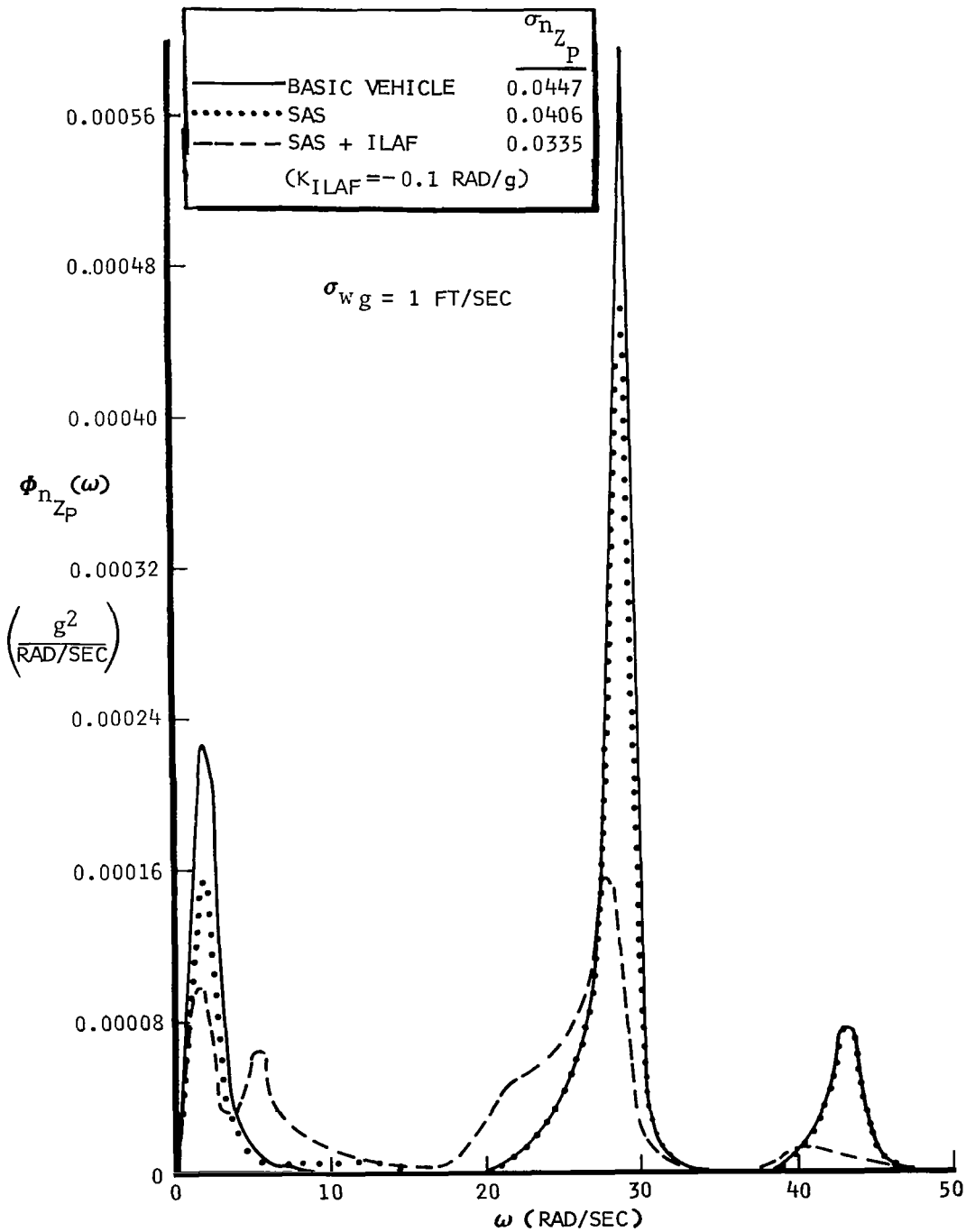

(d) LIGHT WEIGHT, δ_T = 25 DEGREES, M = 0.90, 25,000 FEET

Figure 31.- Continued.

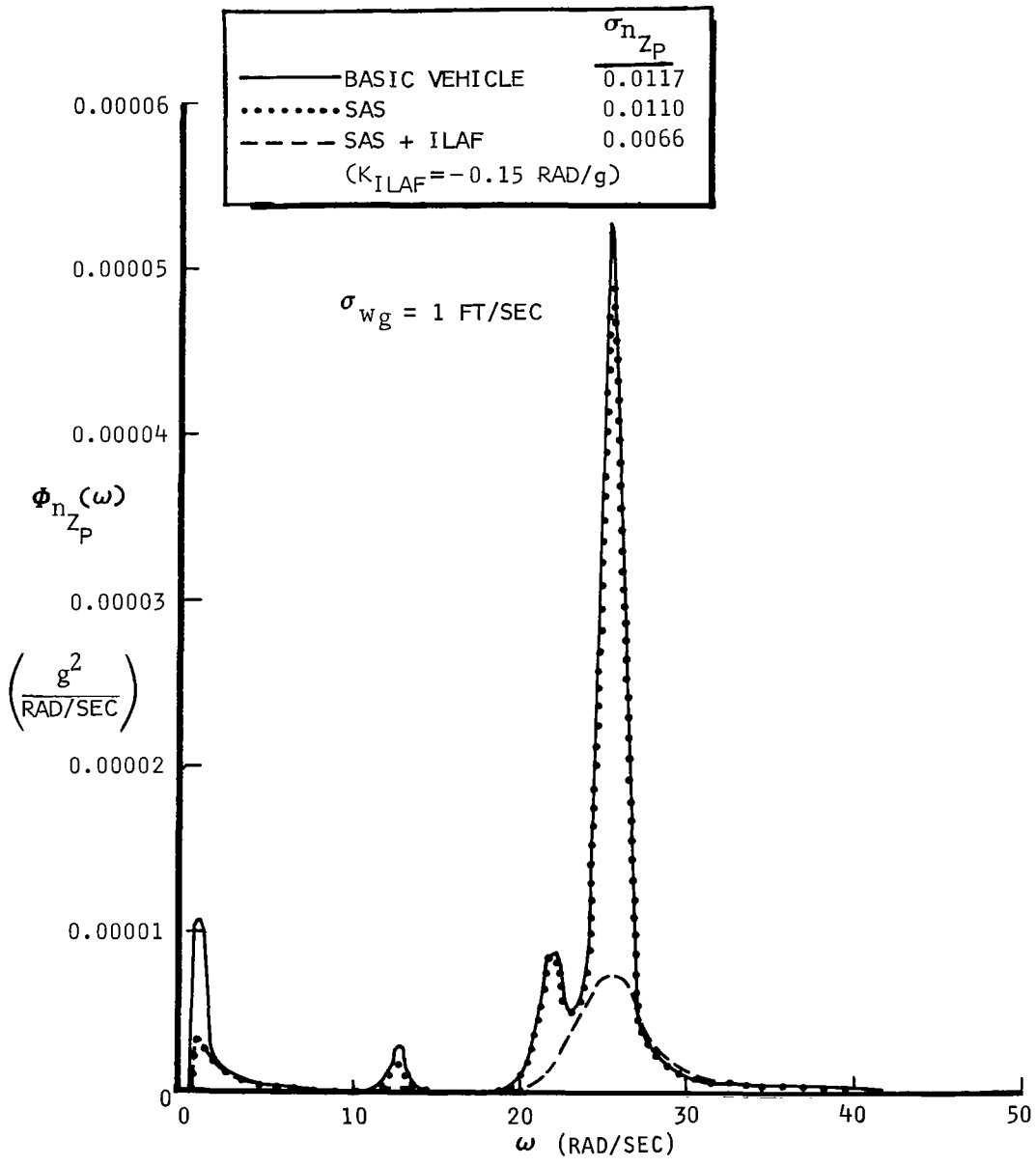

(e) MEDIUM WEIGHT, δ_T = 65 DEGREES, M = 3.0, 70,000 FEET

Figure 31.- Concluded.

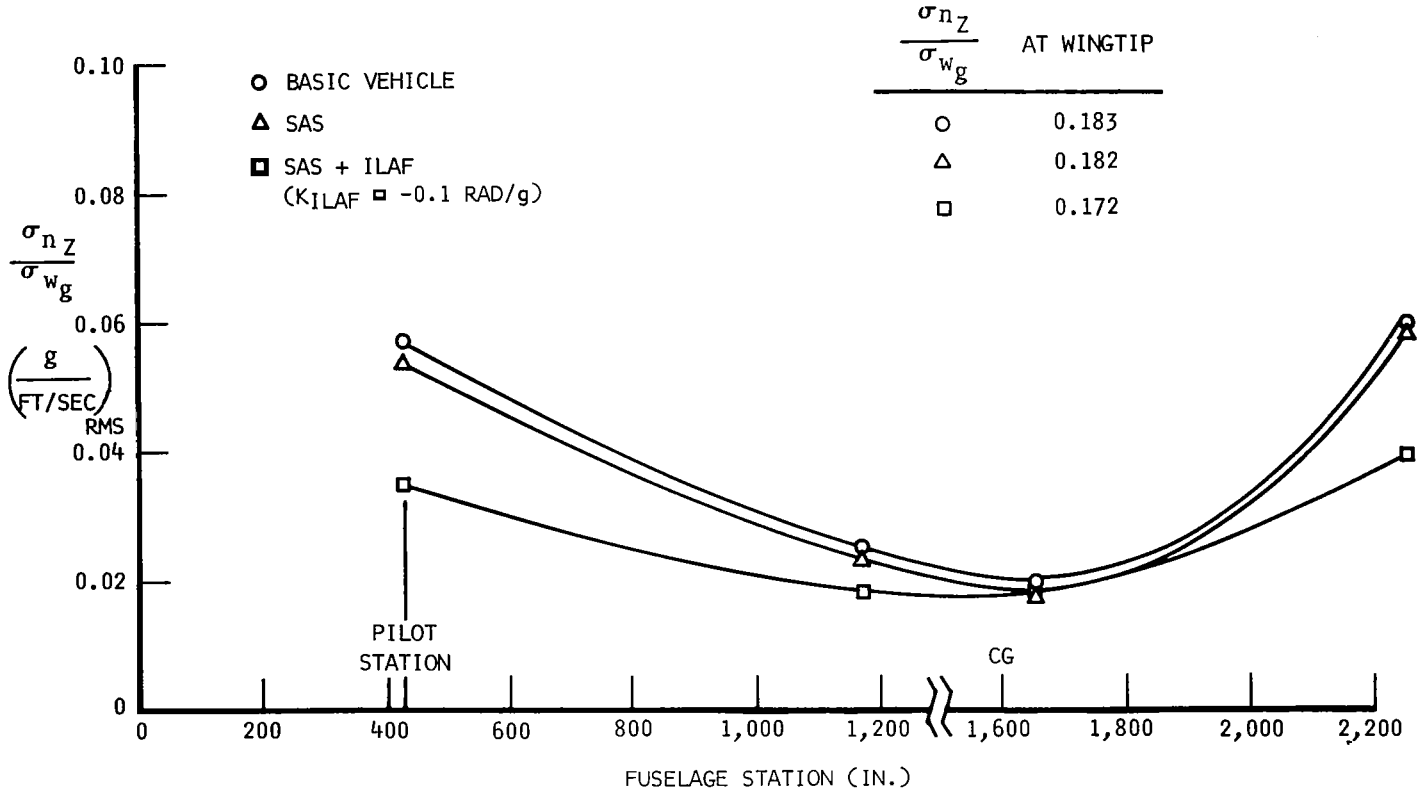

Figure 32.- Typical control system performance in turbulence, rms normal load factor at a number of locations on the XB-70 - analytical data.

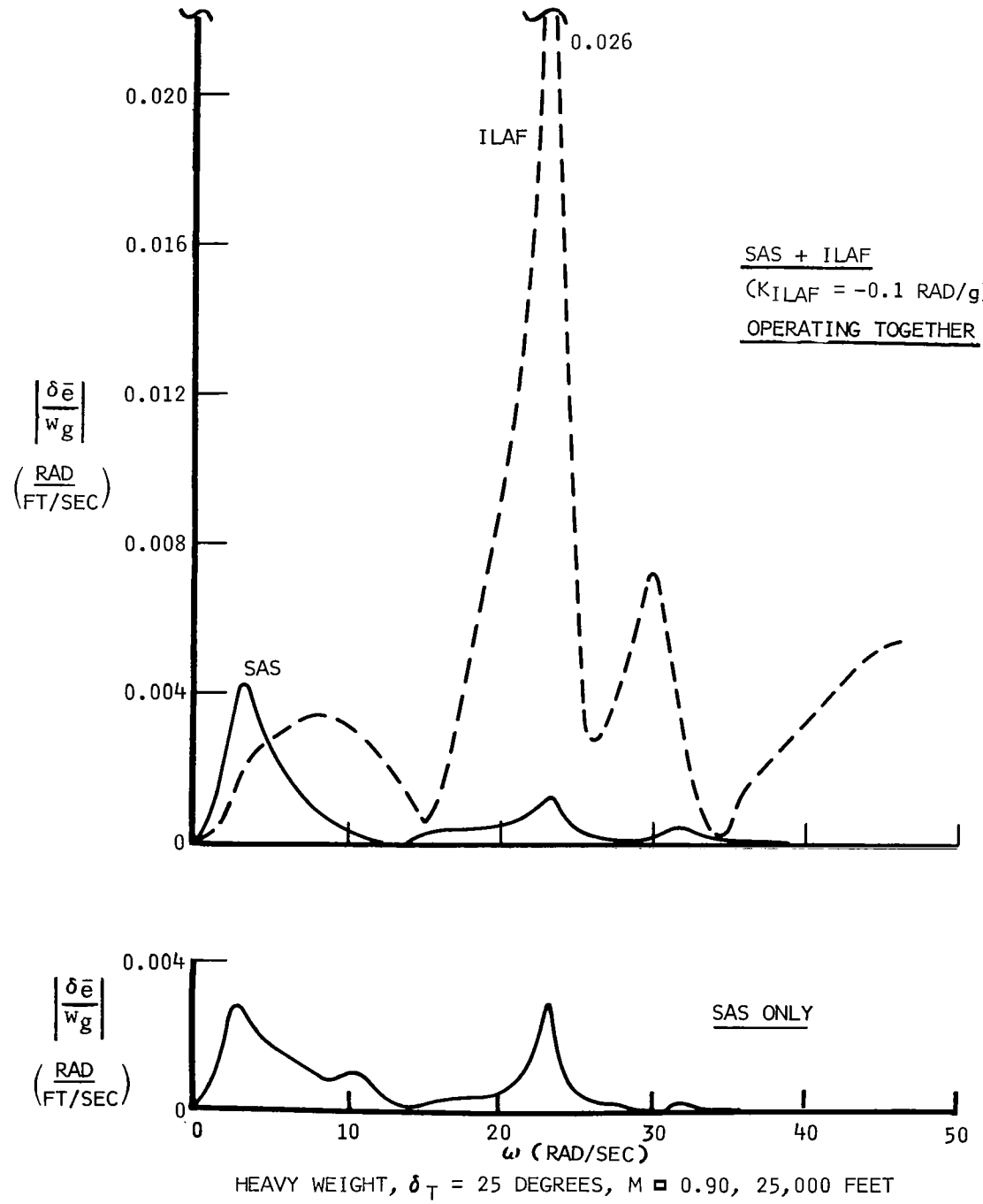

Figure 33.- Typical elevon deflections due to SAS and ILAF operation, frequency response amplitude for a unit of gust velocity - analytical data.

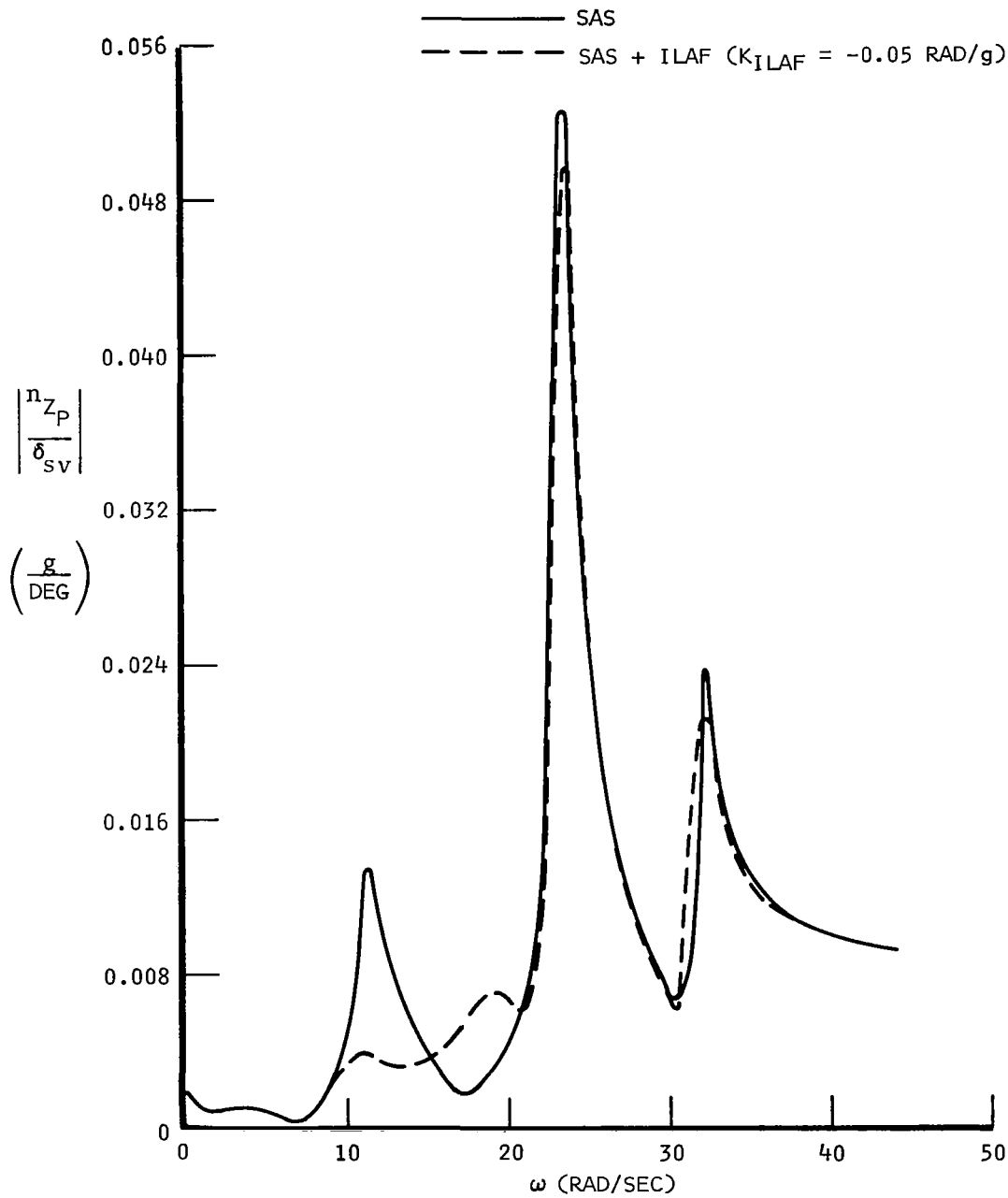

(a) HEAVY WEIGHT, δ_T = 0 DEGREES, M = 0.40, SEA LEVEL

Figure 34.- XB-70 pilot station normal load factor frequency response amplitude due to 1 degree of shaker vane excitation - analytical data.

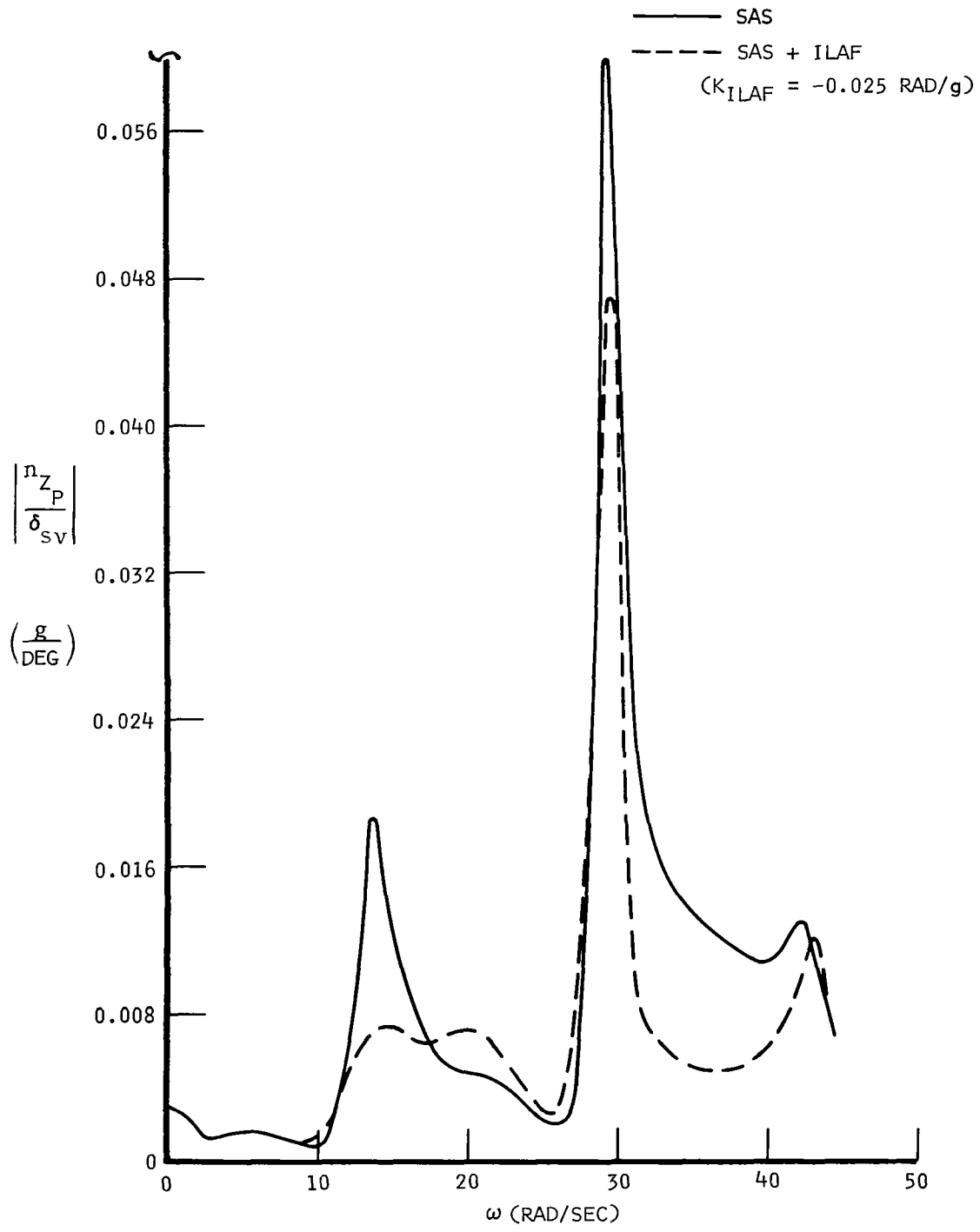

(b) LIGHT WEIGHT, δ_T = 0 DEGREES, M = 0.40, SEA LEVEL

Figure 34.- Continued.

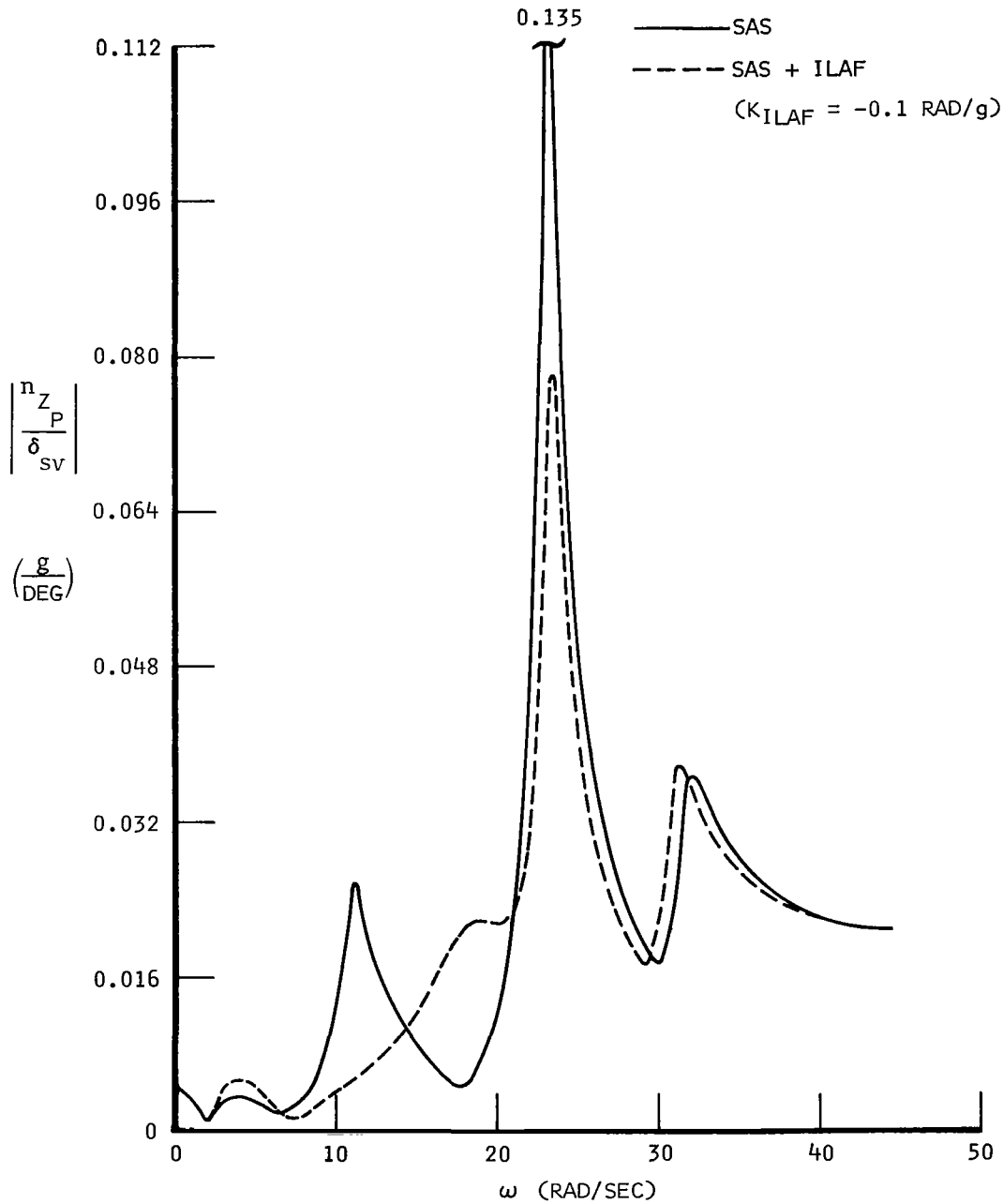

(c) HEAVY WEIGHT, δ_T = 25 DEGREES, M = 0.90, 25,000 FEET

Figure 34.- Continued.

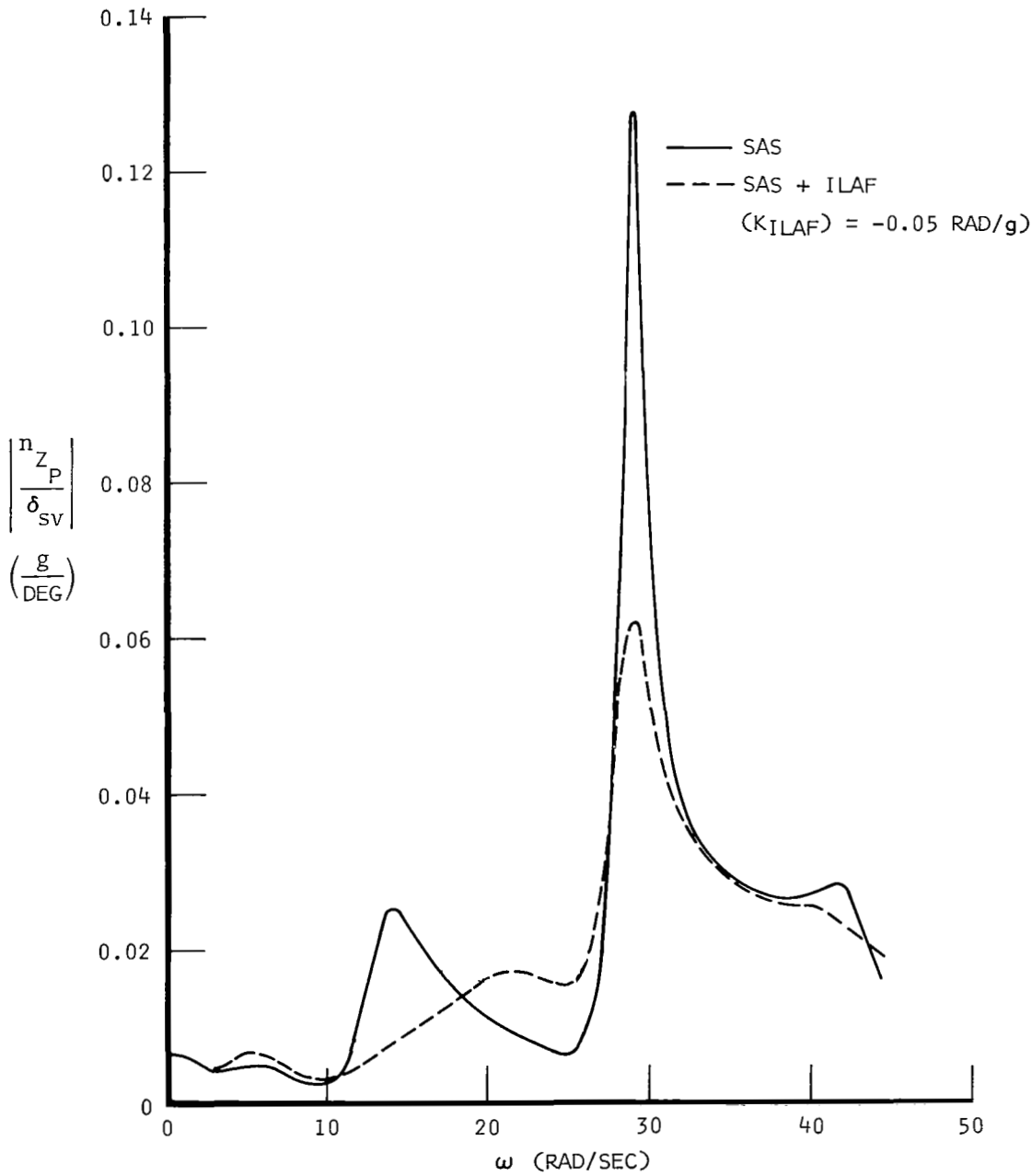

(d) LIGHT WEIGHT, δ_T = 25 DEGREES, M = 0.90, 25,000 FEET

Figure 34.- Continued.

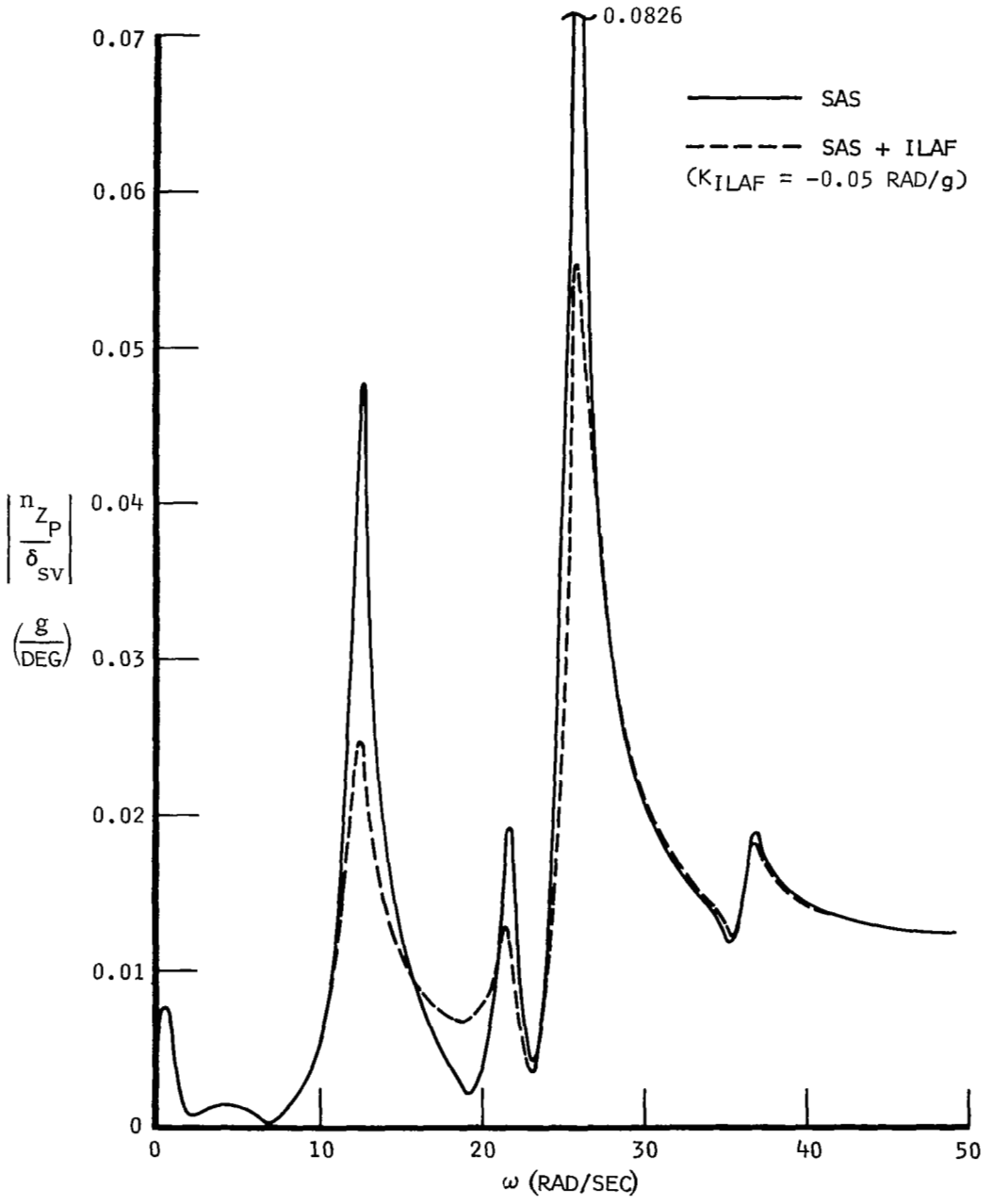

(e) MEDIUM WEIGHT, δ_T = 65 DEGREES, M = 3.0, 70,000 FEET

Figure 34.- Concluded.

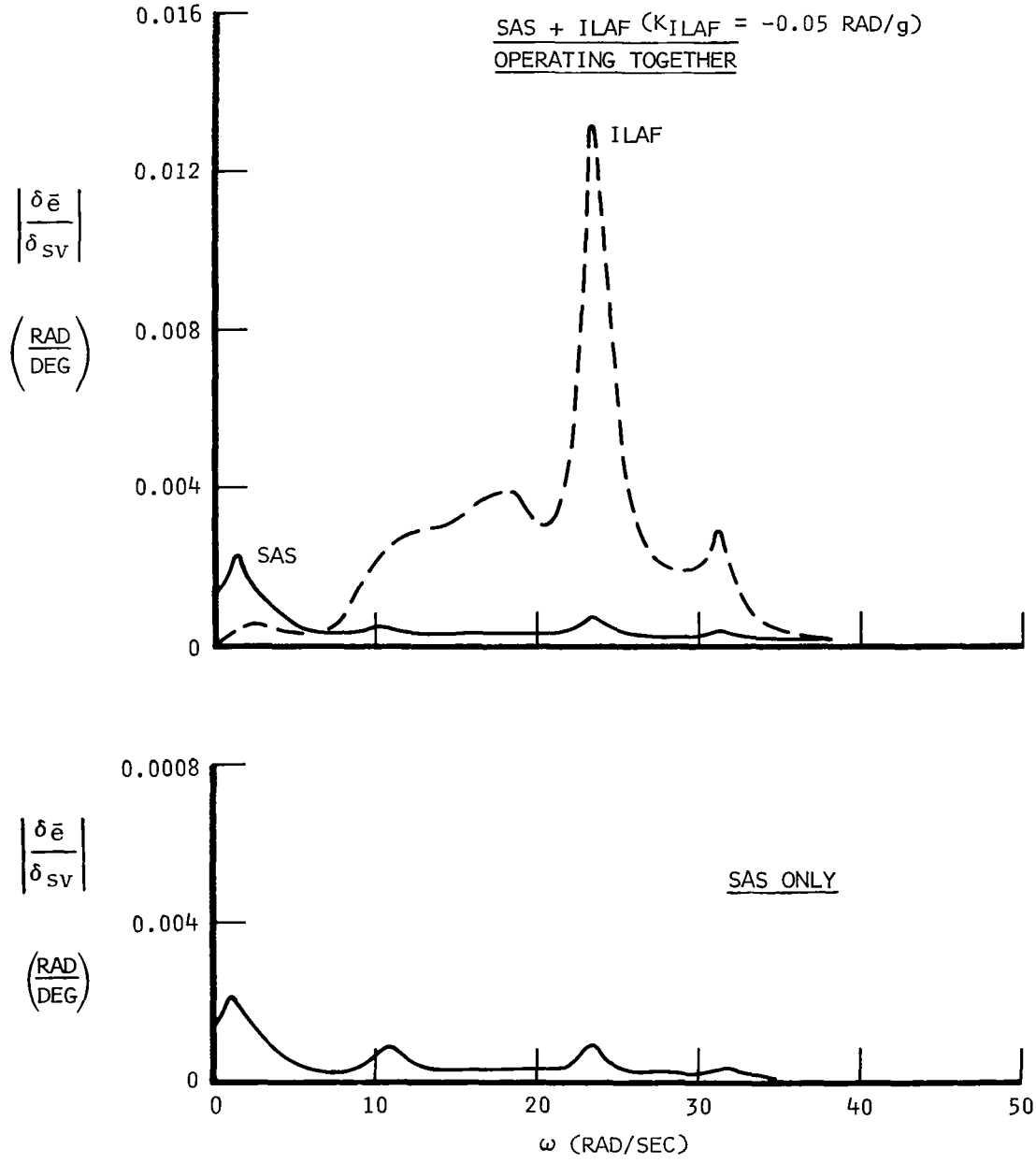

(a) HEAVY WEIGHT, δ_T = 0 DEGREES, M = 0.40, SEA LEVEL

Figure 35.- Elevon deflections due to SAS and ILAF operation, frequency response amplitude due to 1 degree of shaker vane excitation - analytical data.

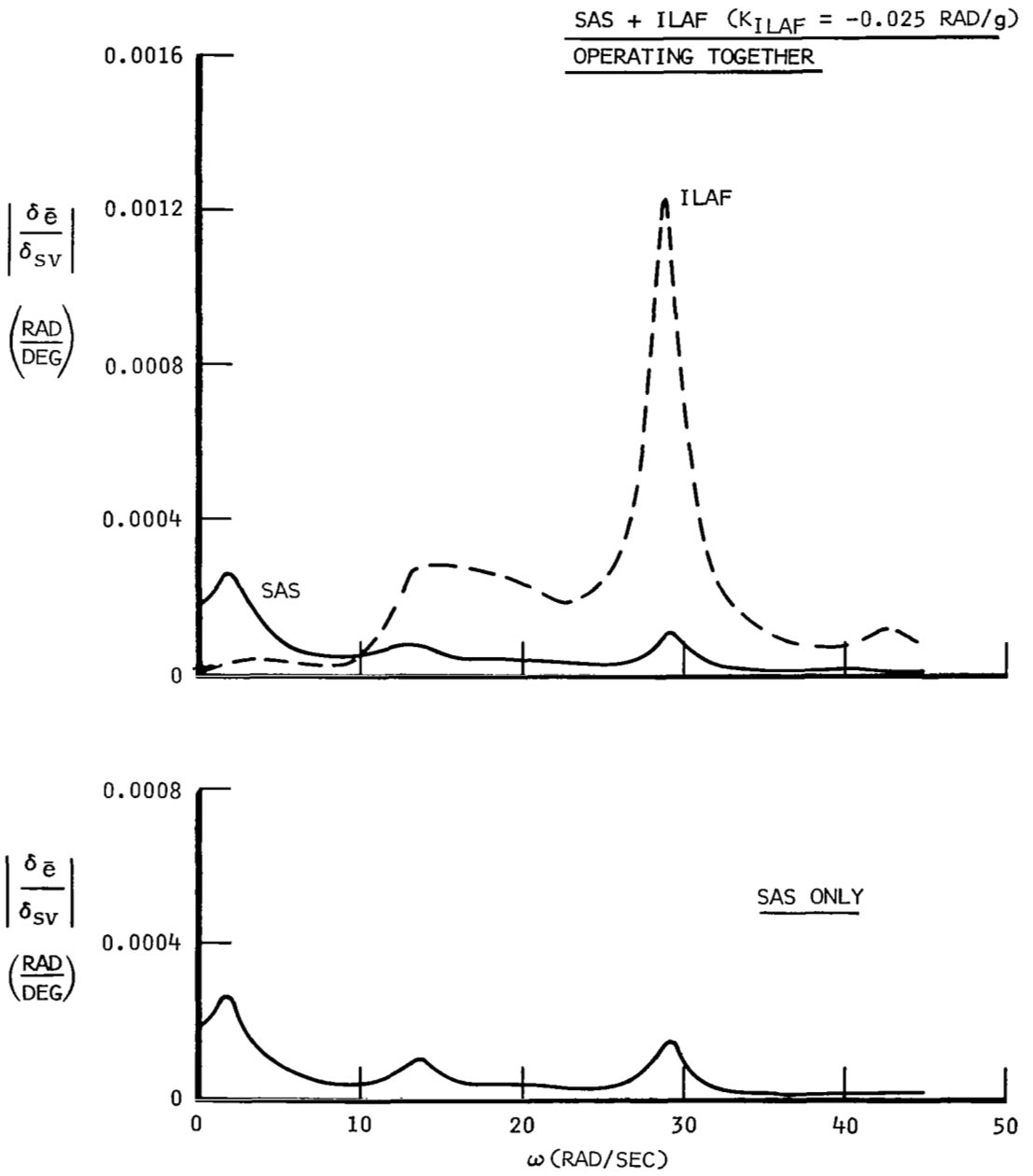

(b) LIGHT WEIGHT, δ_T = 0 DEGREES, M = 0.40, SEA LEVEL

Figure 35.- Continued.

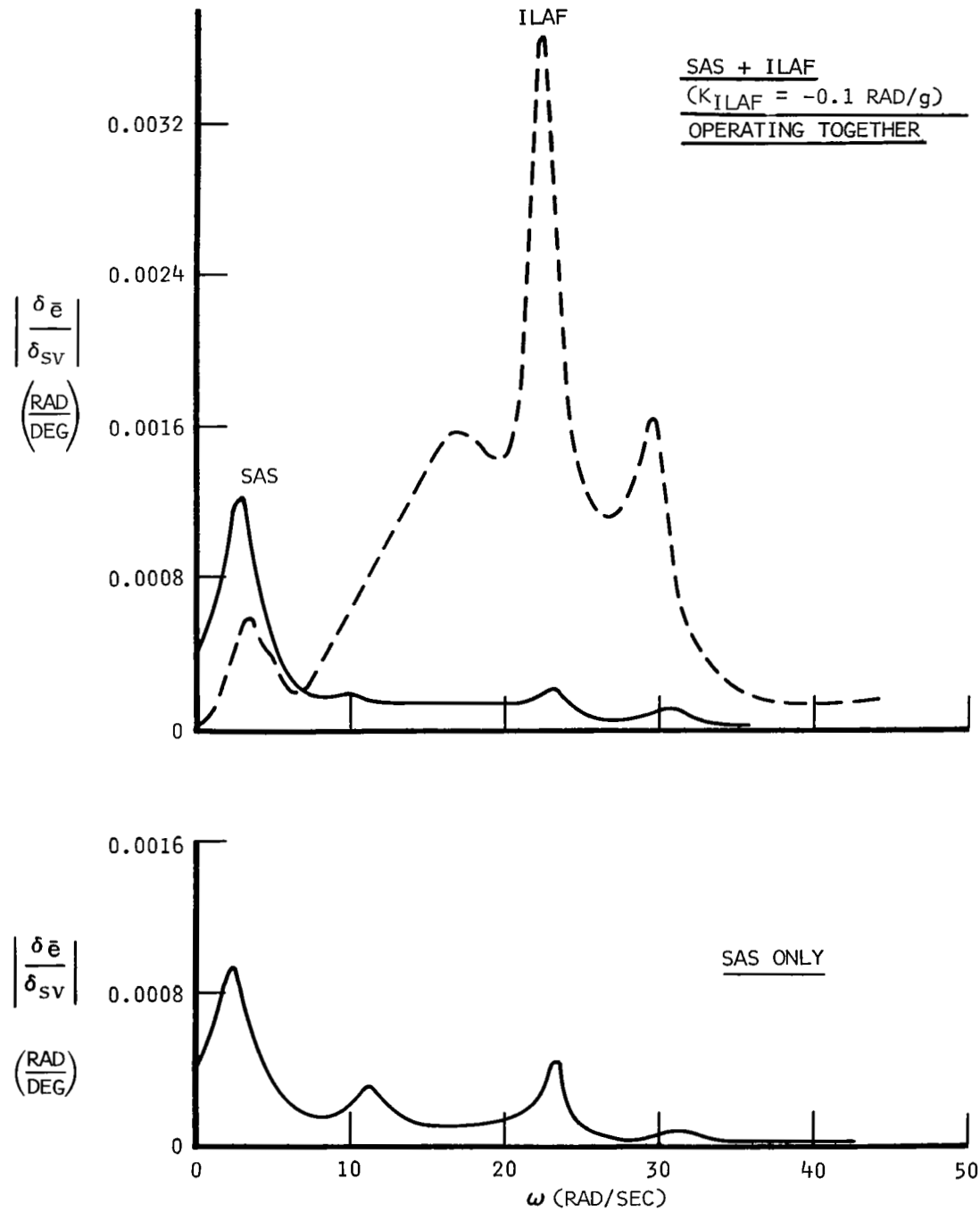

(c) HEAVY WEIGHT, δ_T = 25 DEGREES, M = 0.90, 25,000 FEET
Figure 35.- Continued.

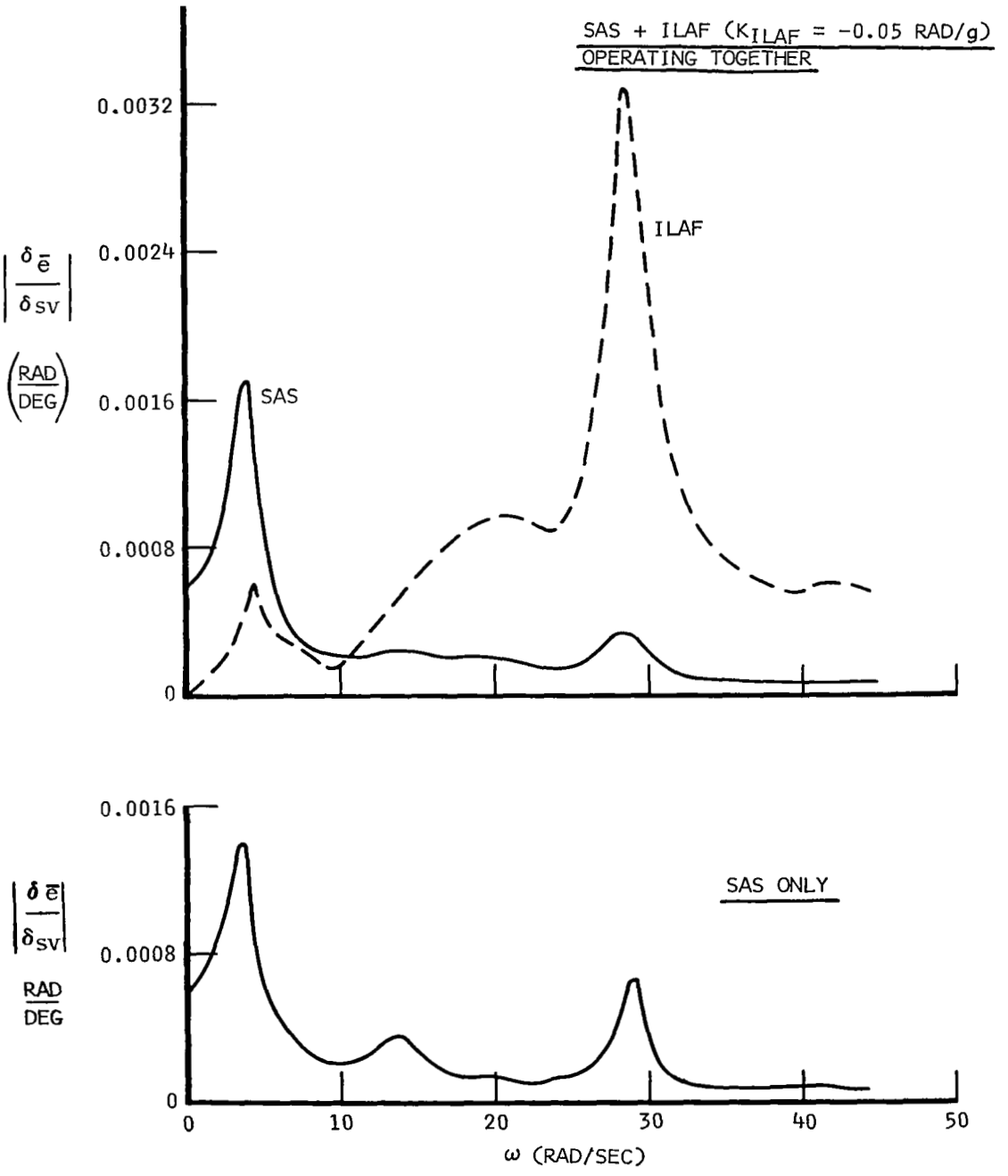

(d) LIGHT WEIGHT, δ_T = 25 DEGREES, M = 0.90, 25,000 FEET

Figure 35.- Continued.

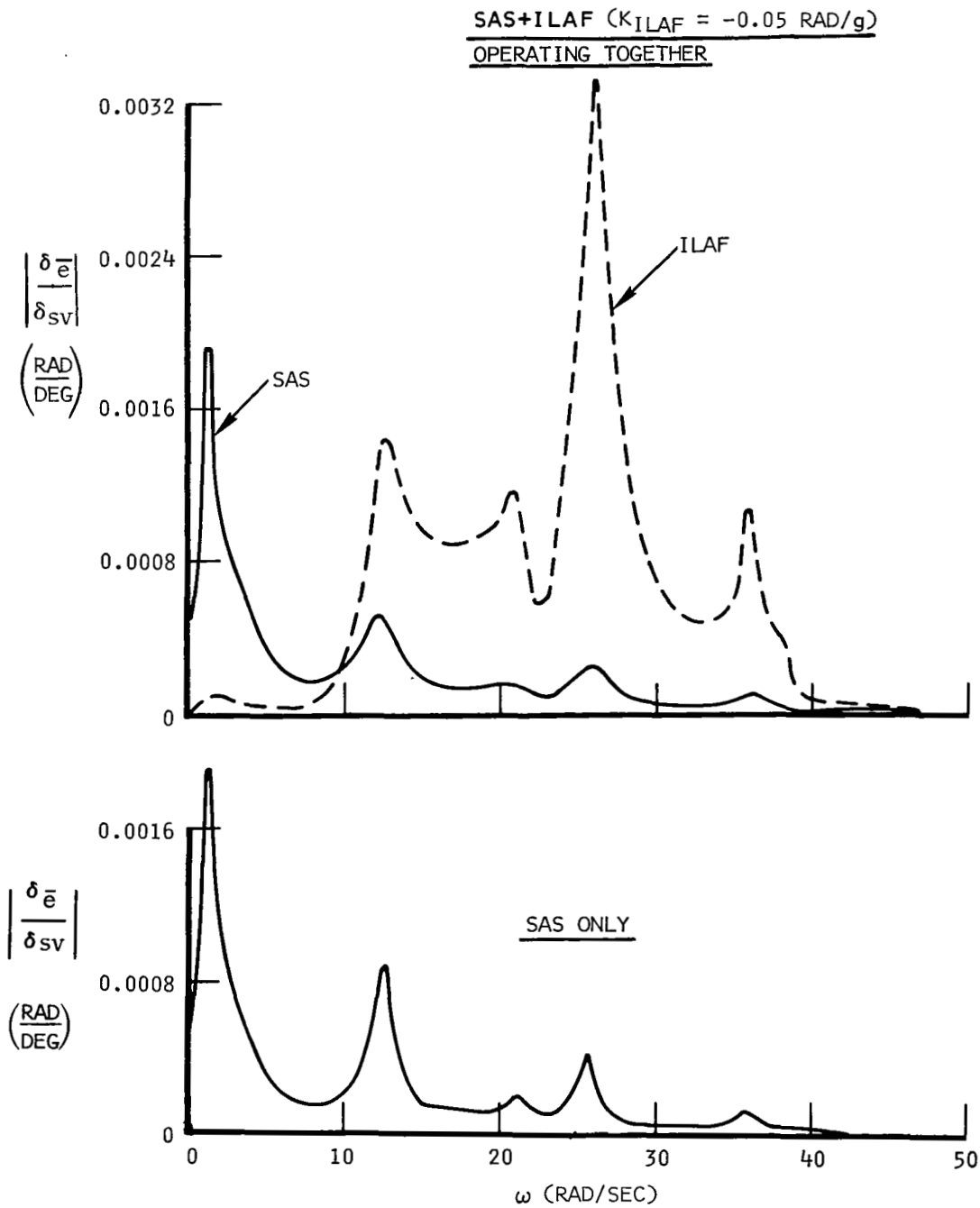

(e) MEDIUM WEIGHT, δ_T = 65 DEGREES, M = 3.0, 70,000 FEET

Figure 35. - Concluded.

Linear digital stability analysis.- The linear digital stability analysis was done by inspecting the phase angle of the characteristic determinant describing the vehicle-control system combination as a function of frequency. A continually decreasing phase angle as frequency is increased is indicative of a stable system; conversely, any increasing of the phase angle with frequency is indicative of an unstable system. This manner of examining stability is convenient for single loop and necessary for multiloop systems with frequency-dependent vehicle response variables. This stability evaluation technique is based upon the ideas Landahl presented in reference 12.

Stability augmentation systems mounted in a flexible airframe can often be caused to go unstable on the ground at zero airspeed. A check was made of this possibility with the ILAF system in the XB-70. Figure 36a indicates that, with ILAF system gain at maximum setting, the vehicle-system combination is unstable. However, the operating procedures and switches for the ILAF system were established to prevent operation on the ground and so preclude a ground instability problem.

Because of the on-ground marginal stability, it was decided to check whether an in-flight, low-speed instability could occur. Figures 36b and 36c show that the system will be stable at takeoff and at landing for nominal in-flight ILAF system gains (the speeds indicated are well below takeoff and landing speeds).

In-flight ILAF system stability for the basic flight and vehicle conditions previously discussed are shown in figures 36d through 36h. The air vehicle with SAS operating is presented as the base against which the ILAF system is compared. The format of the stability analyses has additional information besides indicating general stability. When the frequency range sweeps through either the rigid-body or a structural mode, the phase angle shifts through 180 degrees. The rate of change of this angle with increasing frequency is a measure of the damping in that mode; the shallower the slope, the greater the damping. With this information in mind, the stability plots can reveal where the ILAF system is adding damping or is ineffective. As the plots show, the linear system-vehicle combination is stable for all nominal ILAF gains at the conditions checked.

Describing function analysis. - Frequency response data have been obtained from both the flight simulator and aircraft ground tests to describe the amplitude and phase shift characteristics of the ILAF signal transmission from the acceleration sensing through elevon motion at a no-airload-on-the-elevon condition. These frequency response data include the effects of position limiting, surface rate limiting, FACS servo rate limiting, and other threshold and hysteresis types of nonlinearities. The family of possible response transmission characteristics has been defined as a function of the signal amplitude. These response characteristics have been previously shown in figure 24a through 26b.

NOTE: CONTINUOUSLY DECREASING PHASE ANGLE WITH
INCREASING FREQUENCY INDICATES STABLE SYSTEM

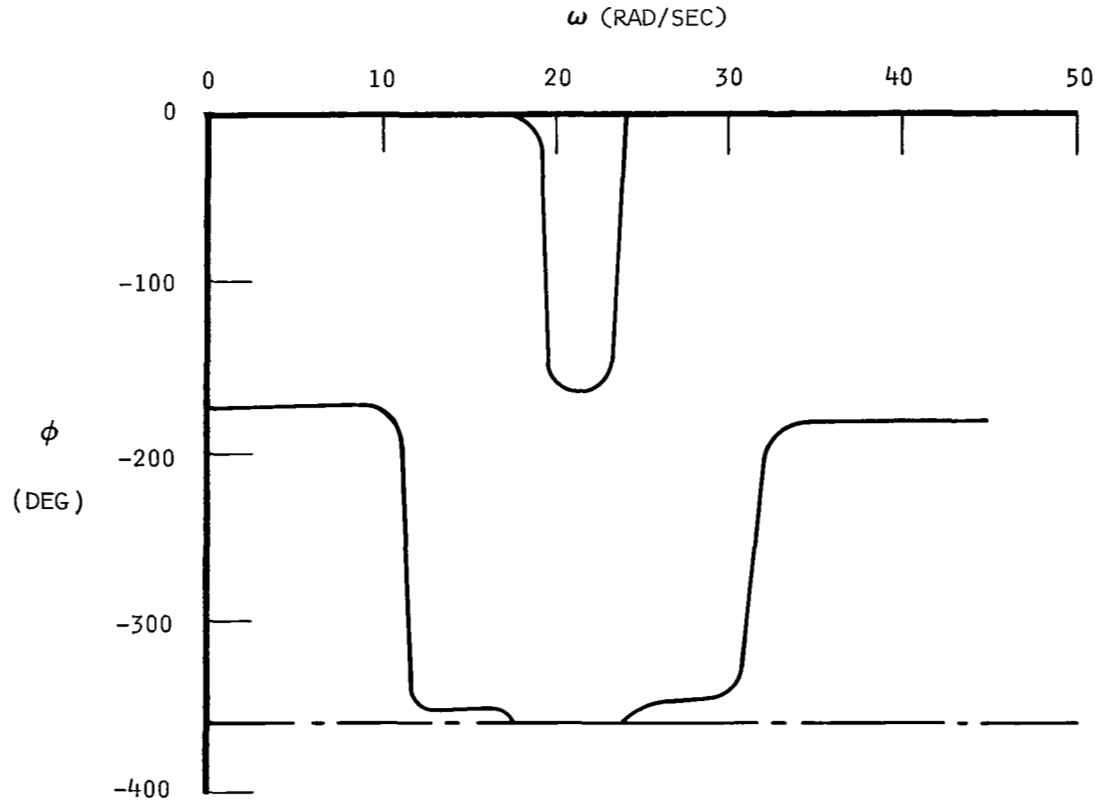

SAS + ILAF (K_{ILAF} = -0.075 RAD/g)

(a) HEAVY WEIGHT, δ_T = 0 DEGREES, M = 0, SEA LEVEL

Figure 36.- XB-70 control system stability analysis, characteristic determinant phase angle - analytical data.

NOTE: CONTINUOUSLY DECREASING PHASE ANGLE WITH INCREASING FREQUENCY INDICATES STABLE SYSTEM

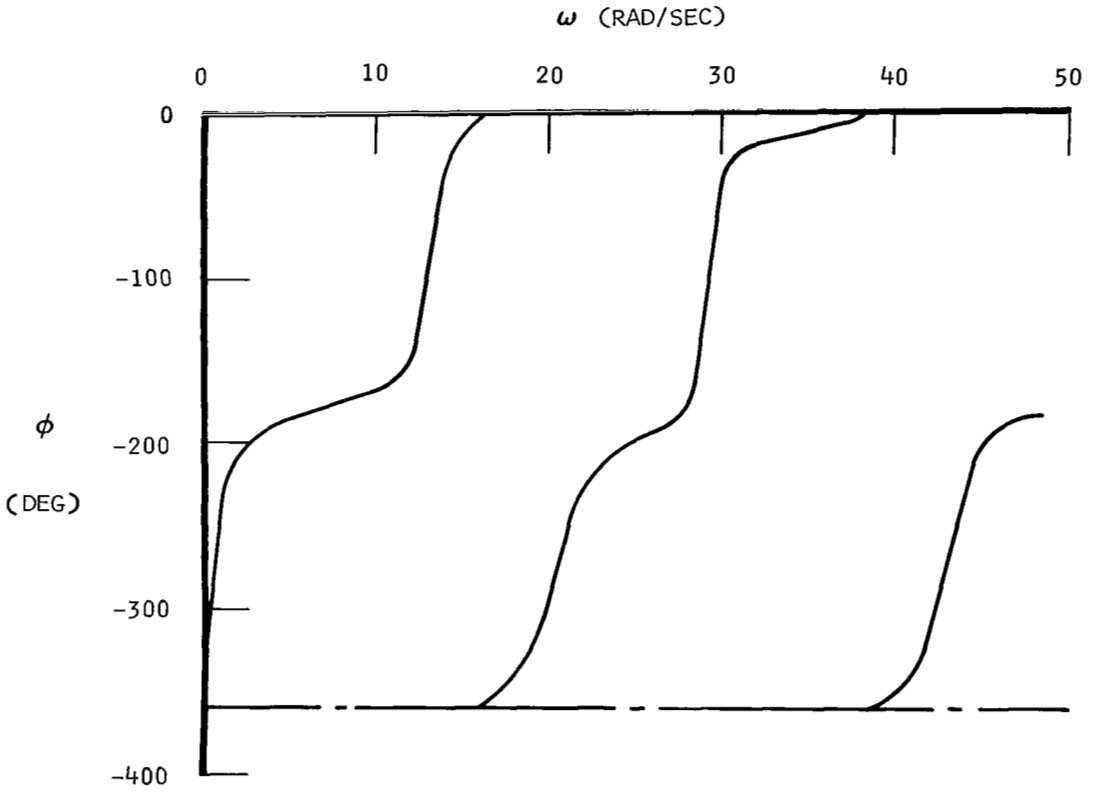

SAS + ILAF (K_{ILAF} = -0.025 RAD/g)

(b) LIGHT WEIGHT, δ_T = 0 DEGREES, M = 0.18, SEA LEVEL

Figure 36.- Continued.

NOTE: CONTINUOUSLY DECREASING PHASE ANGLE WITH
INCREASING FREQUENCY INDICATES STABLE SYSTEM

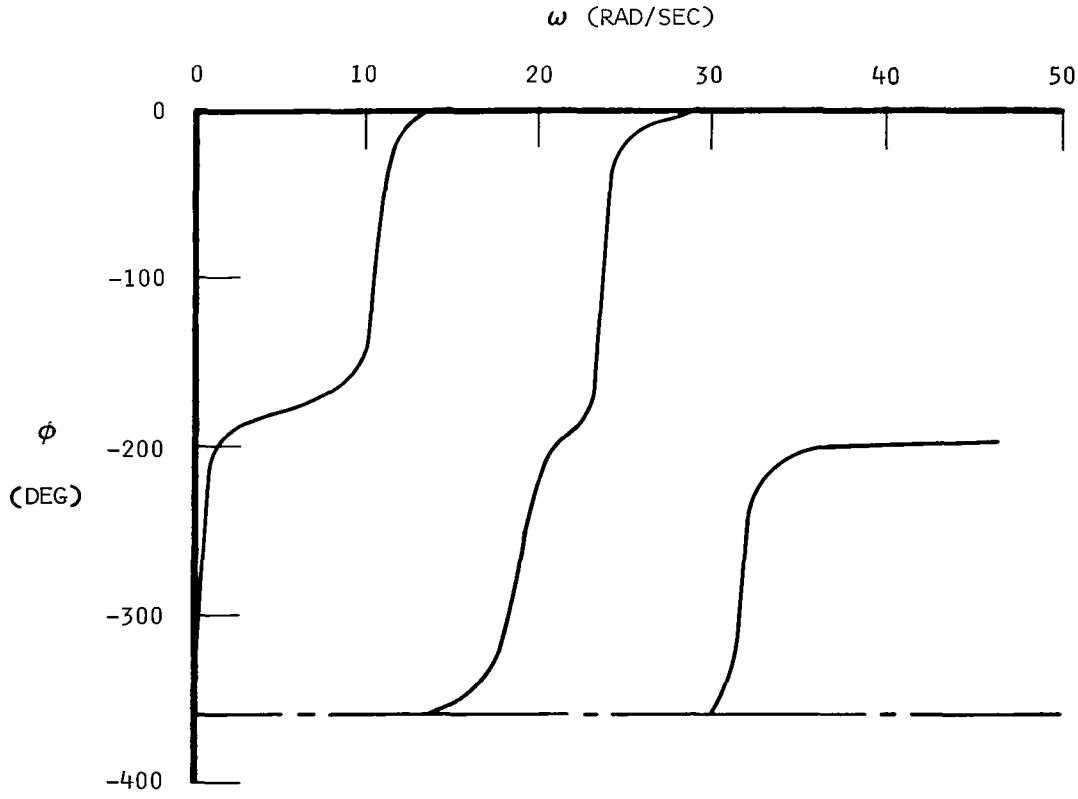

SAS + ILAF (K_{ILAF} = -0.05 RAD/g)

(c) HEAVY WEIGHT, δ_T = 0 DEGREES, M = 0.18, SEA LEVEL

Figure 36.- Continued.

NOTE: CONTINUOUSLY DECREASING PHASE ANGLE WITH
INCREASING FREQUENCY INDICATES STABLE SYSTEM

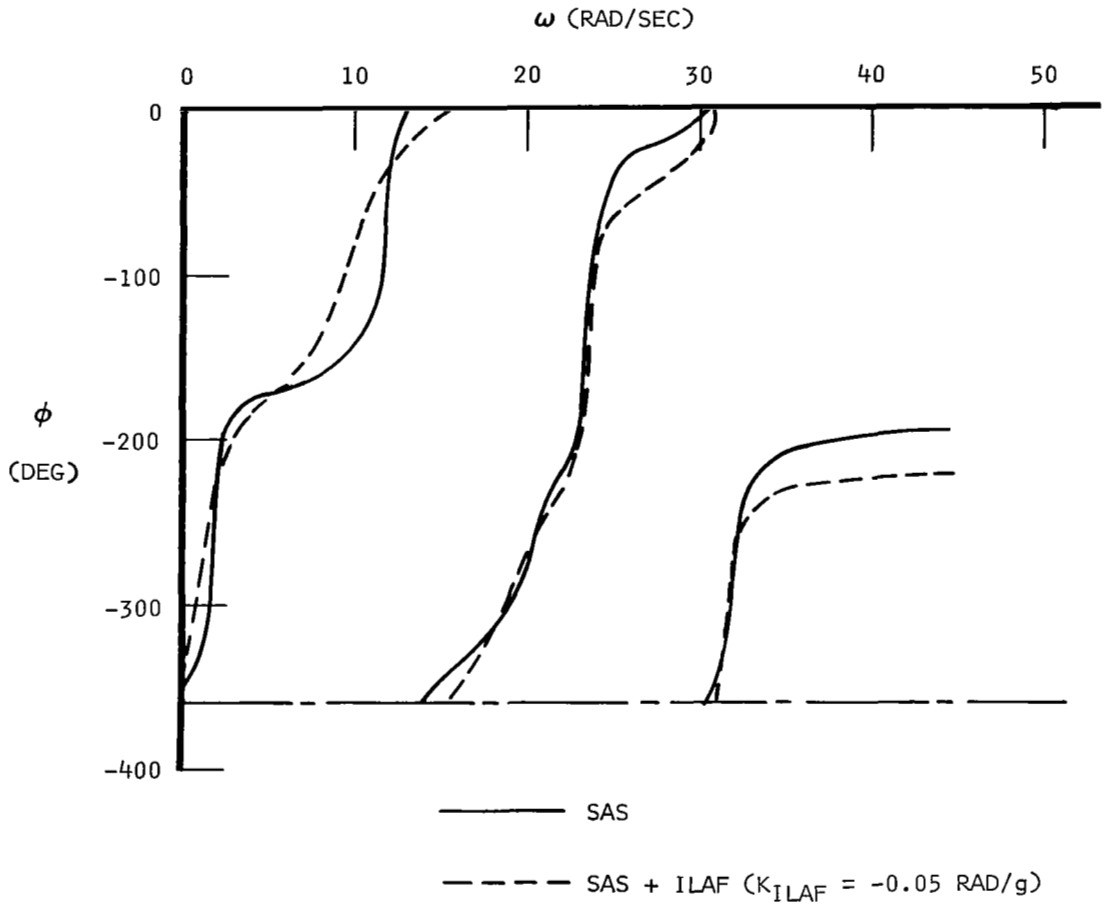

(d) HEAVY WEIGHT, δ_T = 0 DEGREES, M ▫ 0.40, SEA LEVEL

Figure 36.- Continued.

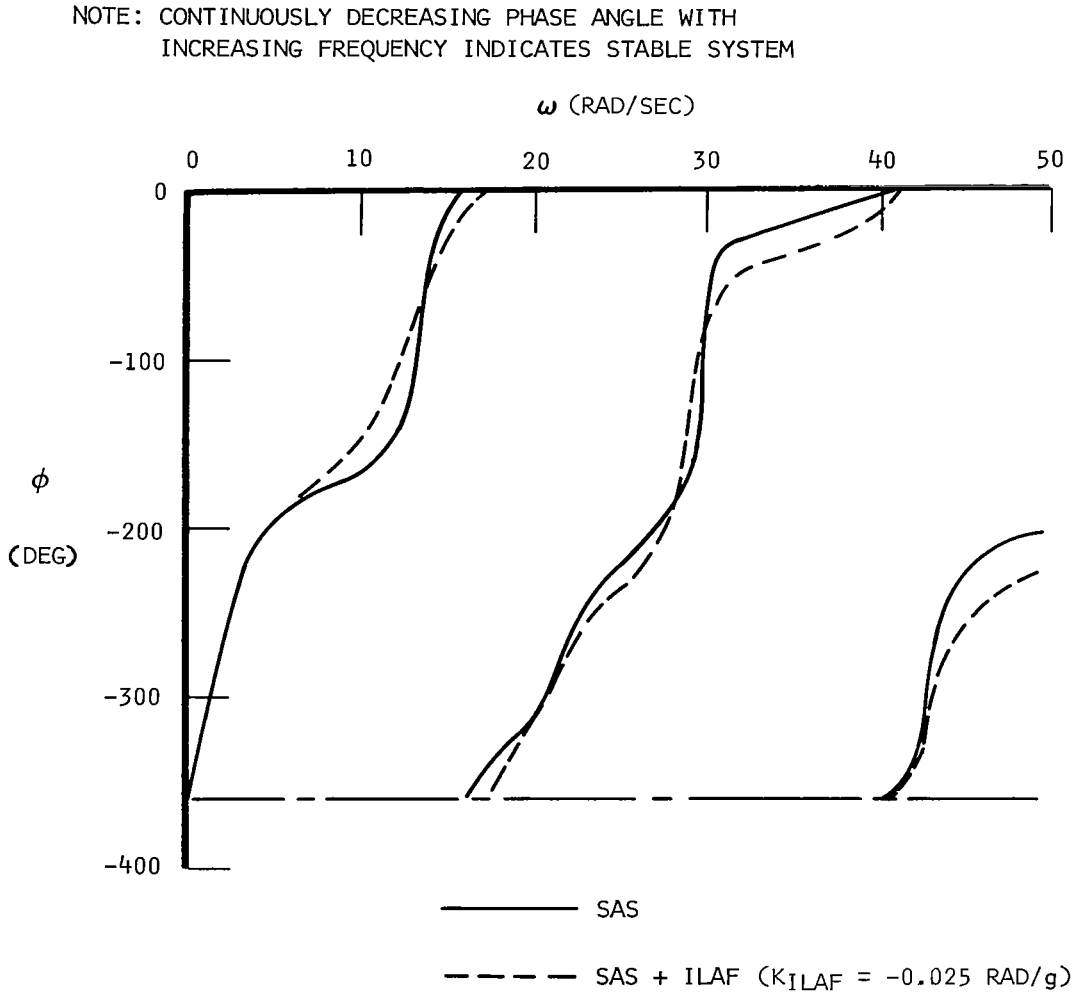

(e) LIGHT WEIGHT, δ_T = 0 DEGREES, M ◻ 0.40, SEA LEVEL

Figure 36.- Continued.

NOTE: CONTINUOUSLY DECREASING PHASE ANGLE WITH INCREASING FREQUENCY INDICATES STABLE SYSTEM

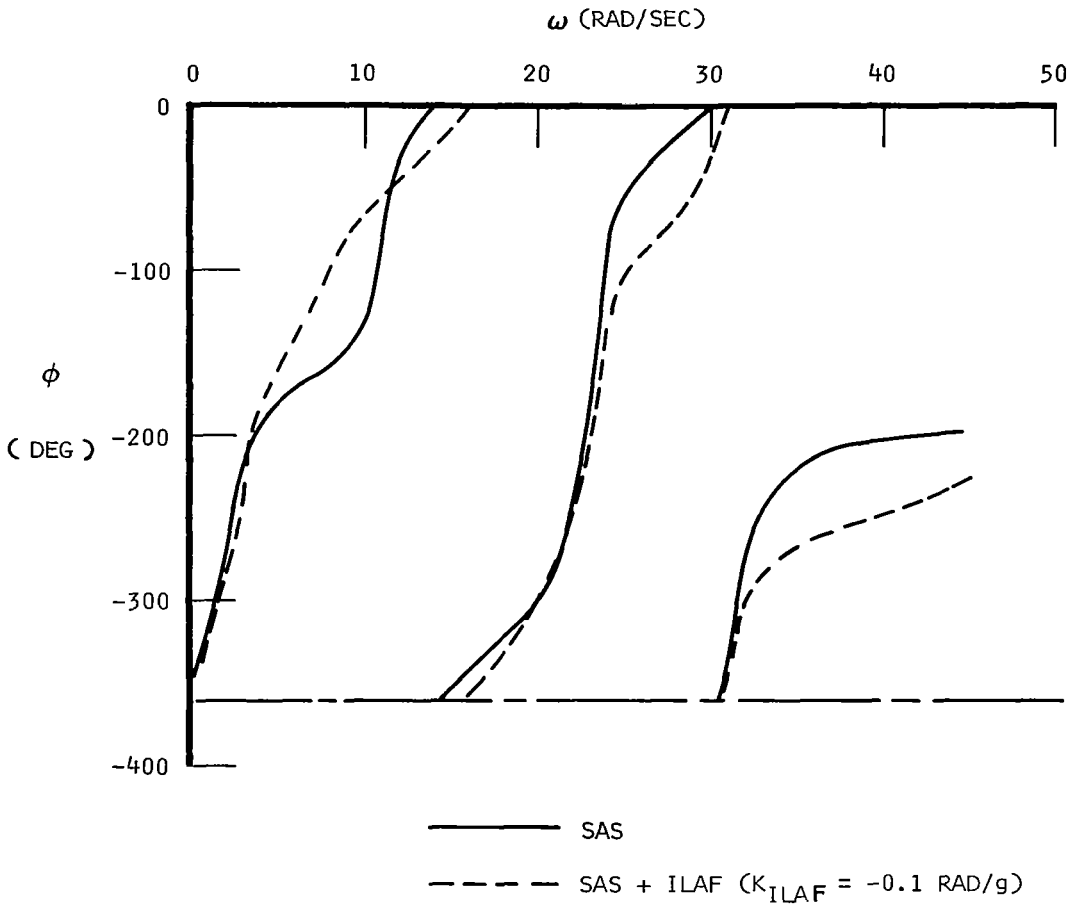

(f) HEAVY WEIGHT, δ_T = 25 DEGREES, M = 0.90, 25,000 FEET

Figure 36.- Continued.

NOTE: CONTINUOUSLY DECREASING PHASE ANGLE WITH
INCREASING FREQUENCY INDICATES STABLE SYSTEM

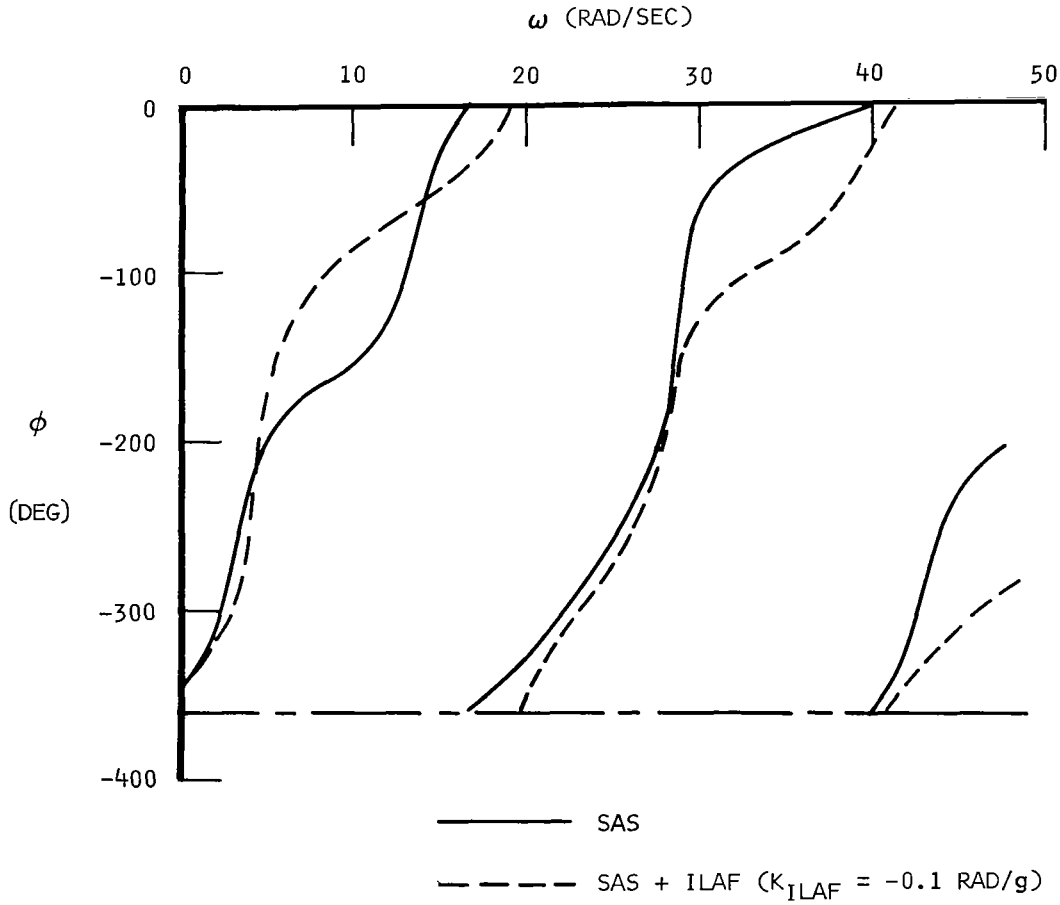

(g) LIGHT WEIGHT, δ_T = 25 DEGREES, M = 0.90, 25,000 FEET

Figure 36. - Continued.

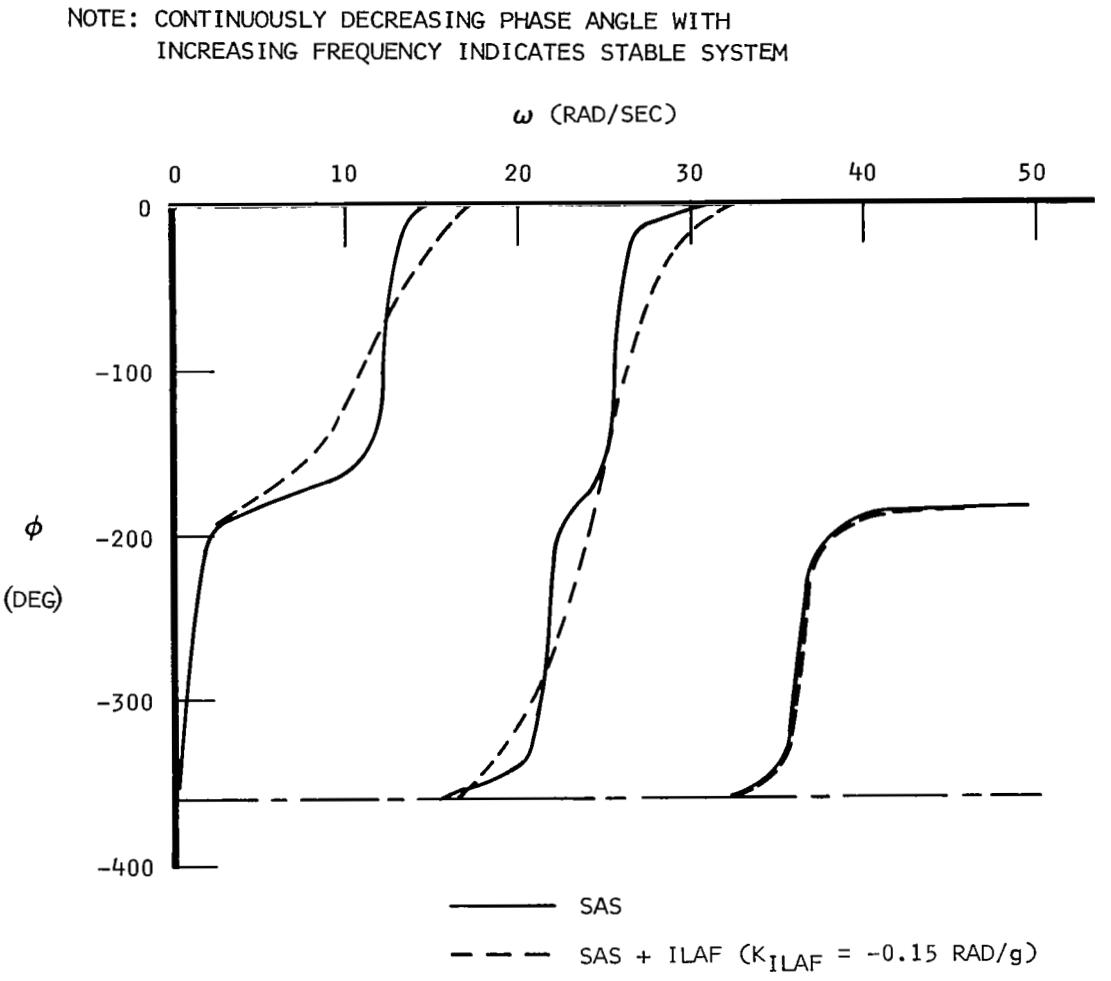

(h) MEDIUM WEIGHT, δ_T = 65 DEGREES, M = 3.0, 70,000 FEET

Figure 36.- Concluded.

These data indicate that the largest amplitude and phase-shift combination occurs at a response level of approximately ±0.5 degree of surface. For smaller amplitudes, the phase shift is greater but the amplitude ratio is smaller. These data were used to predict stability margins from a describing function analysis.

The analysis was accomplished in the following manner:

(1) The control characteristics (describing functions) indicated possible amplitudes and phase-shift combinations from the ILAF sensing to the displacement of all elevon panels referenced to the deflection of the inboard elevon. This was defined as $(\bar{\delta}_1/\Delta_{n_z})K_{ILAF}$.

(2) The frequency response characteristics of the aircraft dynamics indicated the response sensed at the ILAF accelerometers due to inboard elevon motion. The actuation lag between the inboard and outboard panels was included in the model as shown in the following:

$$\frac{\Delta n_z{}_{ILAF}}{\bar{\delta}_1} = \frac{\Delta n_z{}_{ILAF}}{\delta_1} + \left(\frac{\Delta n_z{}_{ILAF}}{\delta_e}\right)\left(\frac{\delta_e}{\bar{\delta}_1}\right)$$

Experimental data were used to represent the transfer function at a selected amplitude.

(3) This type of stability analysis indicated points of possible oscillatory instability. In this case, the K_{ILAF} value which resulted in an oscillation condition was solved for from the characteristic equation of the system:

$$0 = 1 - K_{ILAF}\left(\frac{\bar{\delta}_1}{\Delta n_z{}_{ILAF}}\right)\left(\frac{\Delta n_z{}_{ILAF}}{\bar{\delta}_1}\right)$$

(4) The frequencies where the phase angles of $\frac{1}{K_{ILAF}}\left(\frac{\bar{\delta}_1}{\Delta n_z{}_{ILAF}}\right)^{-1}$ = the phase angles of $\left(\frac{\Delta n_z{}_{ILAF}}{\bar{\delta}_1}\right)$ indicate potential points of instability for high gain.

(5) The amplitude characteristics were examined at these critical frequencies to solve for the value of gain which will maintain stability. A total loop gain less than unity will maintain stability.

(6) The analysis is shown graphically on figures 37a through 37c for three cases. The mach 3.0 case was selected because the inertial reaction forces are relatively large. The mach 0.90 case was also analyzed to indicate the effect of the addition of another structural mode. The mach 0.4 illustrates

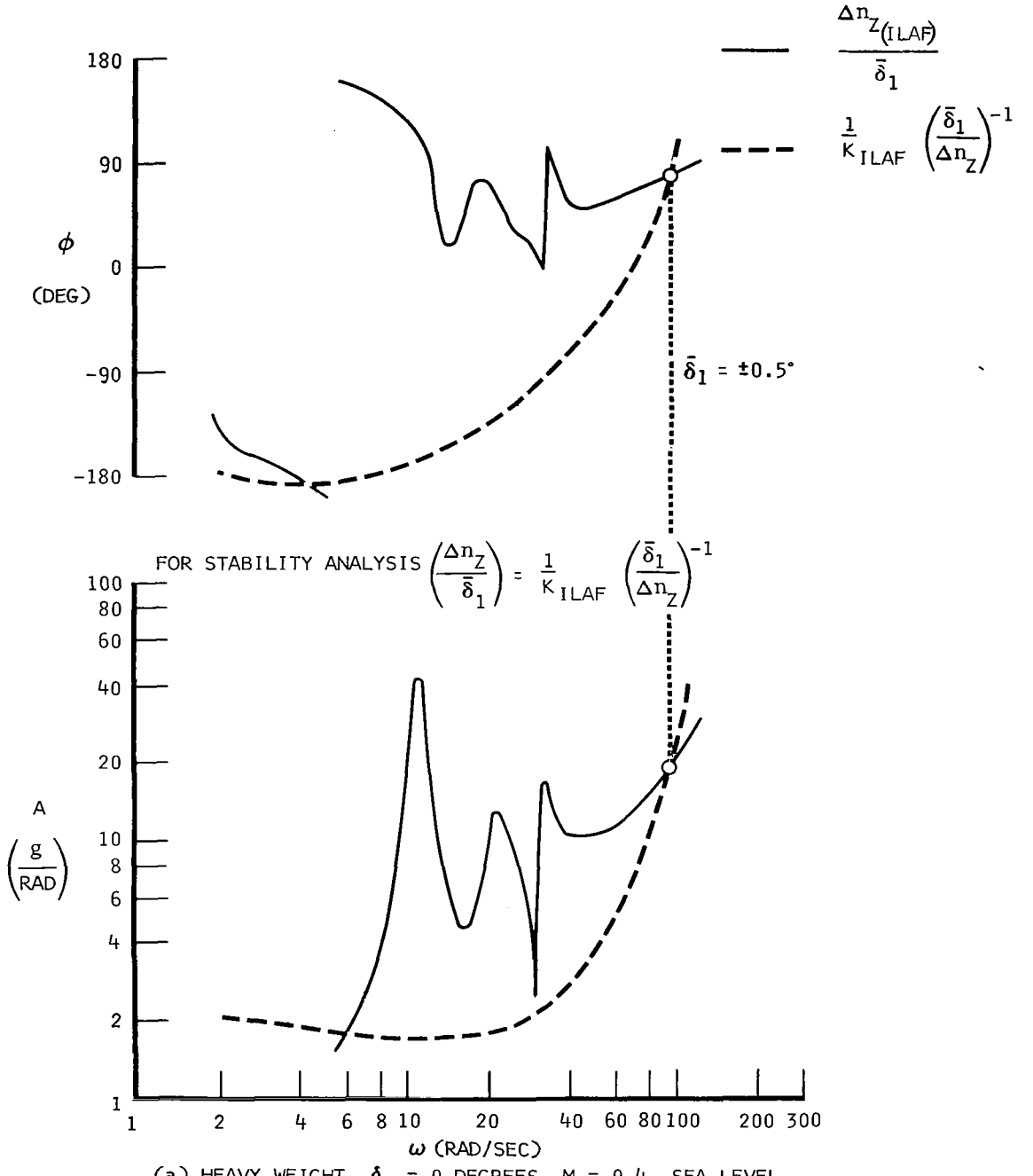

(a) HEAVY WEIGHT, δ_T = 0 DEGREES, M = 0.4, SEA LEVEL

Figure 37.- Graphical stability analysis (describing function) using ILAF and XB-70 control system frequency response data - composite analytical and test data.

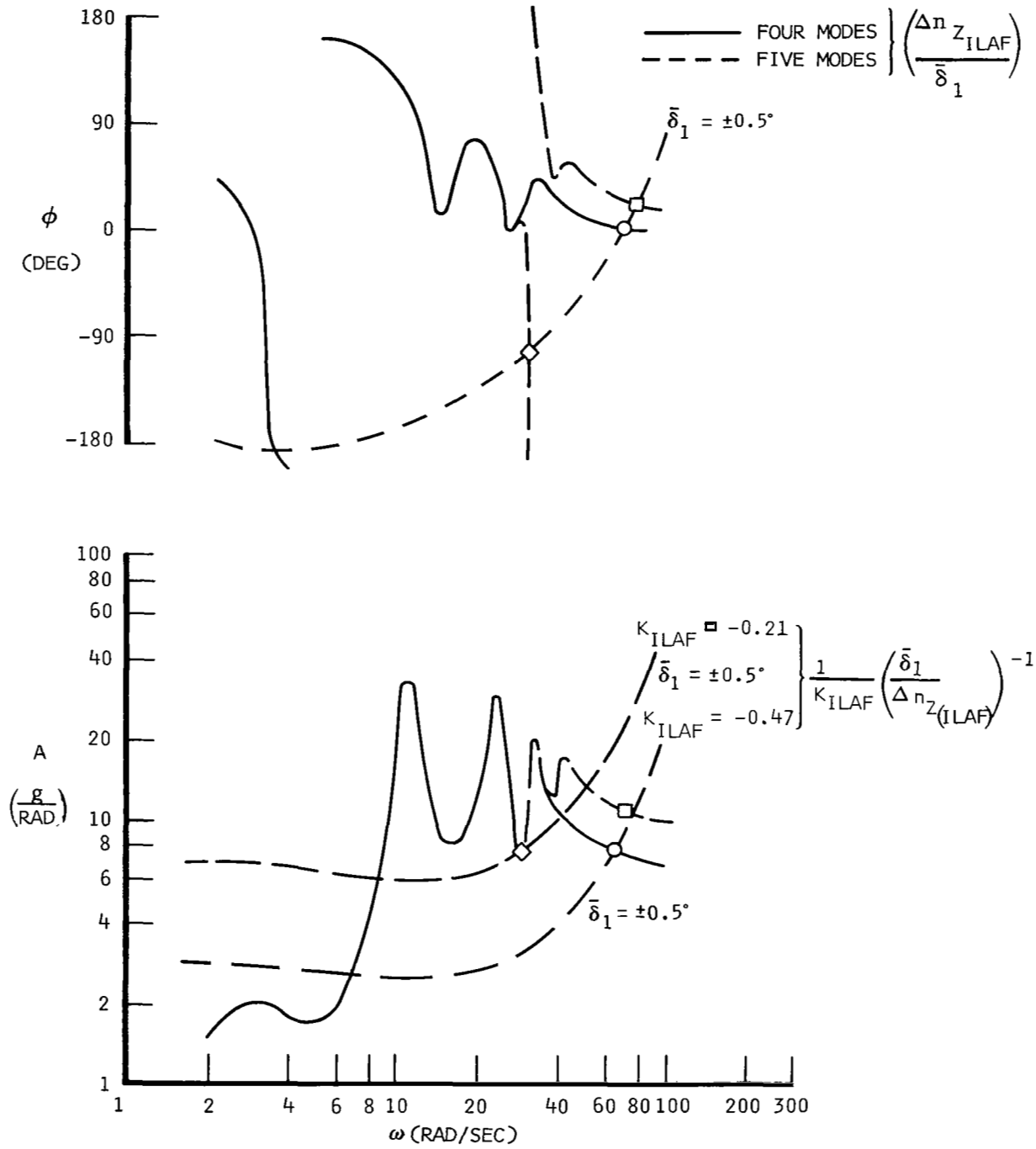

(b) HEAVY WEIGHT, δ_T = 25 DEGREES, M = 0.9, 25,000 FEET

Figure 37.- Continued.

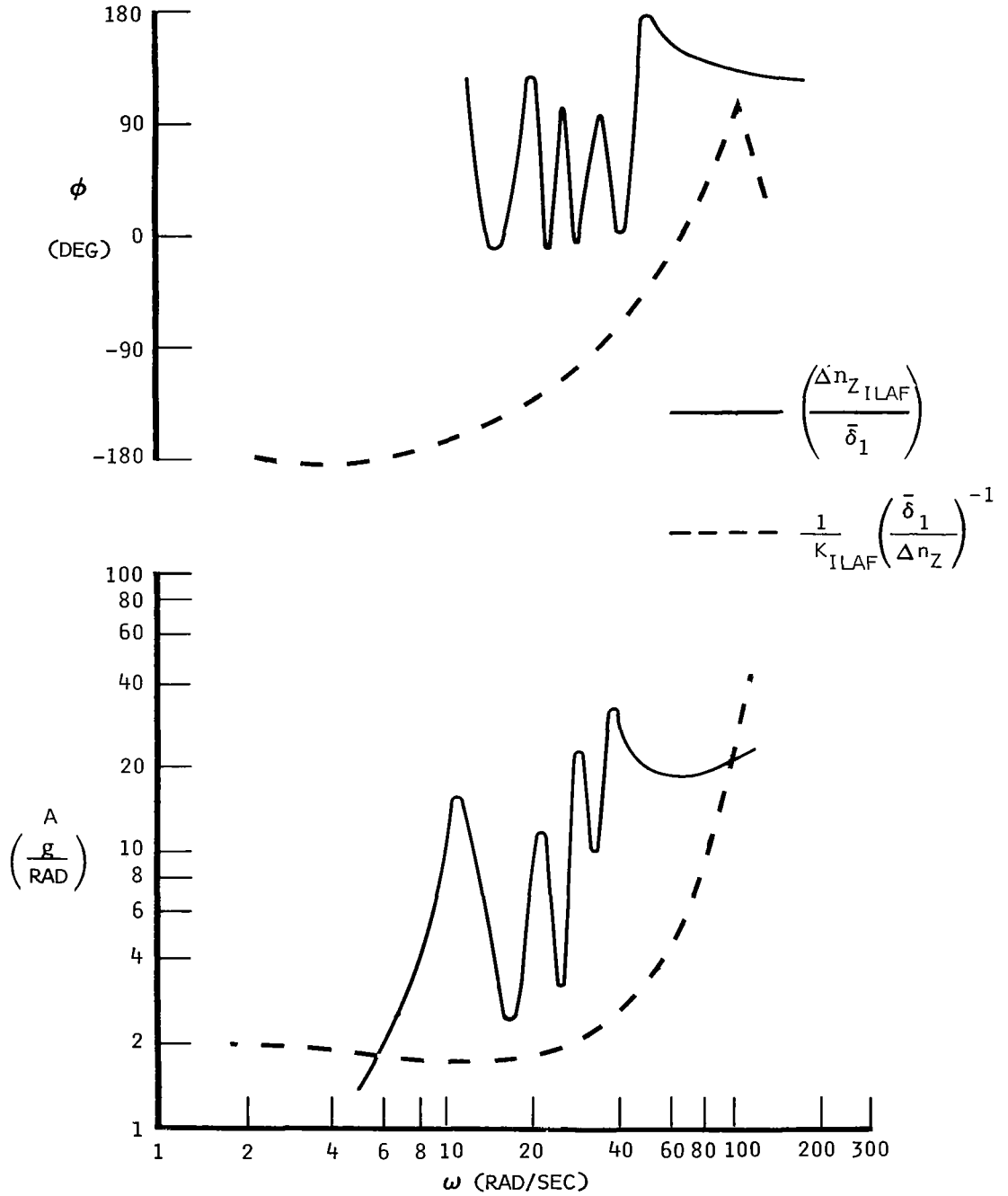

(c) MEDIUM WEIGHT, δ_T = 65 DEGREES, M = 3.0, 70,000 FEET

Figure 37.- Concluded.

a low-speed case. On the phase plots, the intersections indicate frequencies of potential instabilities. The amplitude portion of these figures then allows the determination of the maximum allowable gain. The two amplitude curves are caused to intersect at the critical frequencies determined from the phase plots by varying the magnitude of the one including K_{ILAF}; K_{ILAF} required to cause these intersections is the critical gain.

The results indicated the following maximum allowable system gains and the frequency of the potential instability:

Mach	h_p	Weight	Wingtip Pos (deg)	No. of Modes	ω_{INS} (rad/sec)	max K_{ILAF} (rad/g)
0.4	Sea level	Heavy	0°	Four	95	-0.50
0.9	25,000 ft	Heavy	25°	Four	72	-0.47
0.9	25,000 ft	Heavy	25°	Five	75 31	-0.39 -0.21
3.0	70,000 ft	Medium	65°	Four	None	∞

The basic design model of the airplane has included only four structural modes. To obtain some idea of the effect on stability of additional modes in the model, a check was made at one flight condition. This is shown in figure 37b. The addition of the fifth mode lowers the stability margin, although a large margin still exists. The stability margin is lowered because a large phase-shift change occurs near the fourth structural mode when the fifth mode is introduced. The plant is no longer a minimum-phase plant as was the case with only four modes in the analysis. A minimum-phase plant has all left-hand plane zeros. The ILAF concept would provide a minimum-phase plant for a point force application and sensing, but the realistic subsonic loading due to elevon deflections, combined with the more complex higher mode shapes, tends to conform less to the basic ILAF idea. An alternate sensor location (small variation near elevon) may improve this condition to some degree. These data on the higher mode effects were not available at the time of sensor location selection. These results indicate that, although confidence in the system stability has been obtained, a cautious flight-test program is still required.

Response and Stability, Simulation Analyses

Response performance and stability results have been obtained during flight simulation studies using actual system hardware wherever possible. (Refer to appendix C.) Response characteristics and stability have been

determined for inputs from vertical gusts, the shaker vane, pilot commands, and combinations of these inputs for various ILAF system gain levels. These data are necessary to assist in determining the values of ILAF gain setting to be recommended for use in flight test.

Because of the hydromechanical amplitude nonlinear characteristics, ILAF performance is a function of input magnitudes in addition to gain settings and flight conditions. Figure 38 shows the pilot acceleration ratio for response with SAS plus ILAF over response with SAS only as a function of gust magnitude and shaker vane magnitude with the ILAF gain setting at 6 (figure 28). At this gain, ILAF essentially has no performance for the mach 0.4 at sea level condition for gust inputs because of the servo-through-elevon threshold effects. For shaker vane inputs, a significant reduction in mode 1 response is possible at all flight conditions. Possible improvements in modes 2 or 3 depend upon flight condition. If shaker vane inputs are too large, hydraulic rates are saturated, and ILAF can adversely affect mode 3. This is not considered a serious problem because shaker inputs should be limited to ±4 degrees at mode 3 frequencies to prevent overstressing the airplane. Mode 4 response was insignificant except at the mach 0.4 at sea level condition.

Figure 39 shows that increasing the ILAF gain setting from 6 to 10 increases signal levels over the hydromechanical thresholds, thus increasing the effect of ILAF, especially for mode 4 at mach 0.4 at sea level. The maximum ILAF gains for stability shown in figures 40 and 41 are the gains where limit cycles were encountered near the simulator natural frequency. These gain values may not represent true gains limitations on the airplane because of two major factors: (1) The simulator and airplane may have different resonance characteristics, and (2) the analog computer air vehicle model included only four structural modes. Subsequent digital computer data show that including fifth mode effects decreases the allowable gains.

Based upon simulator data presented in figures 38 through 41, a trade-off between ILAF performance and stability margins was made to select optimum gains. For these optimum gains, figures 42a through 42c show partial frequency responses of pilot accelerations resulting from shaker vane inputs of various amplitudes. Shaker vane inputs of ±12.5 degrees for modes 1 and 2, and ±4 degrees for modes 3 and 4 were considered best for evaluation because of shaker vane effectiveness hydromechanical threshold, and rate saturation. It could be difficult to evaluate modes 2, 3, and 4 in flight. Modes 3 and 4 will be difficult to evaluate because of modulated transients. These modulated transients appear to be beats resulting from low damping ratios of modes 3 and 4 coupled with the close proximity of frequencies between modes 3 and 4. These modulated transients could be excited by changes in shaker vane amplitudes or frequencies when these frequencies were near mode 3 or mode 4 frequencies.

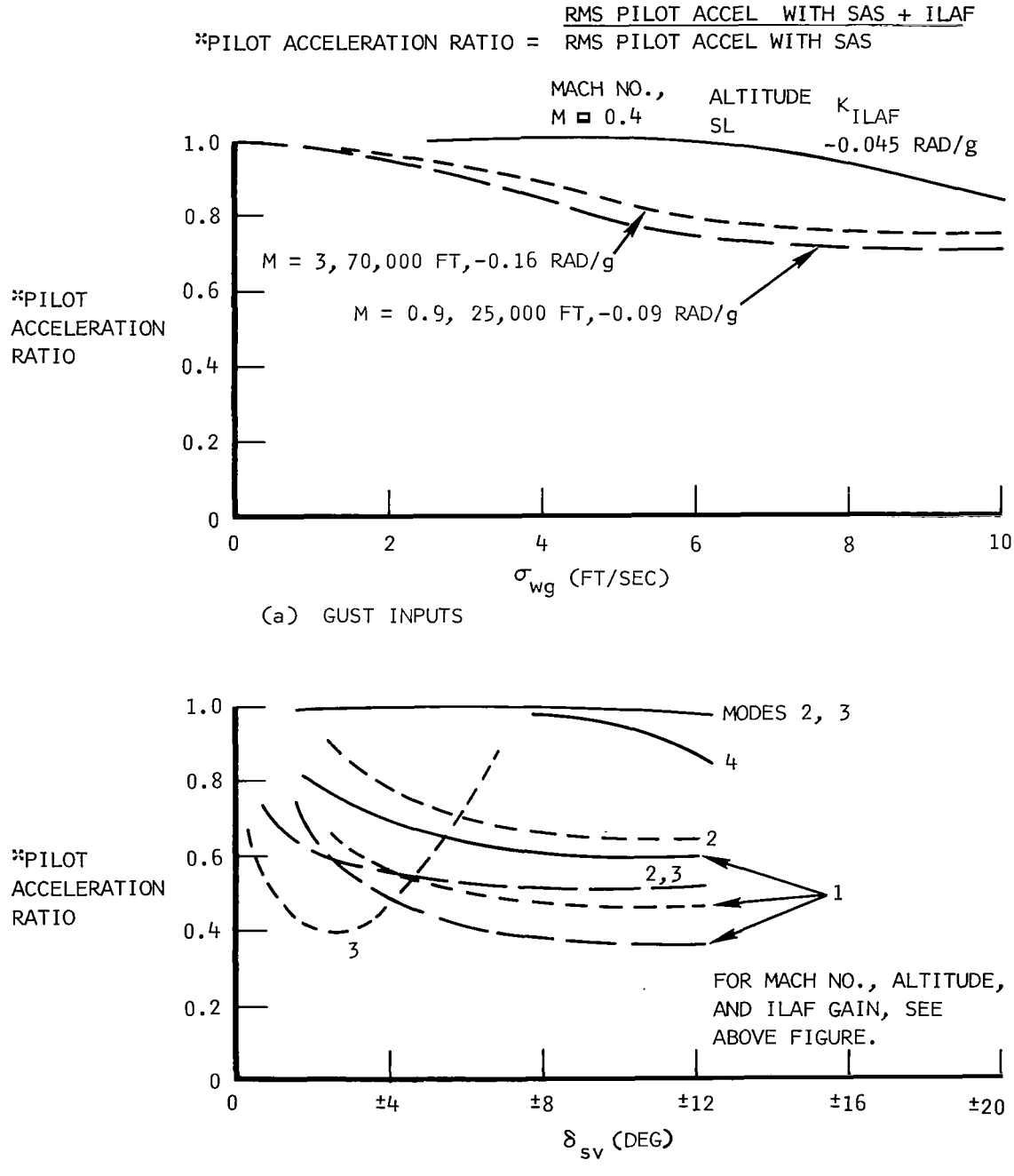

Figure 38.- Performance of ILAF system for gust and shaker vane excitation with ILAF gain select at No. 6 - simulator data.

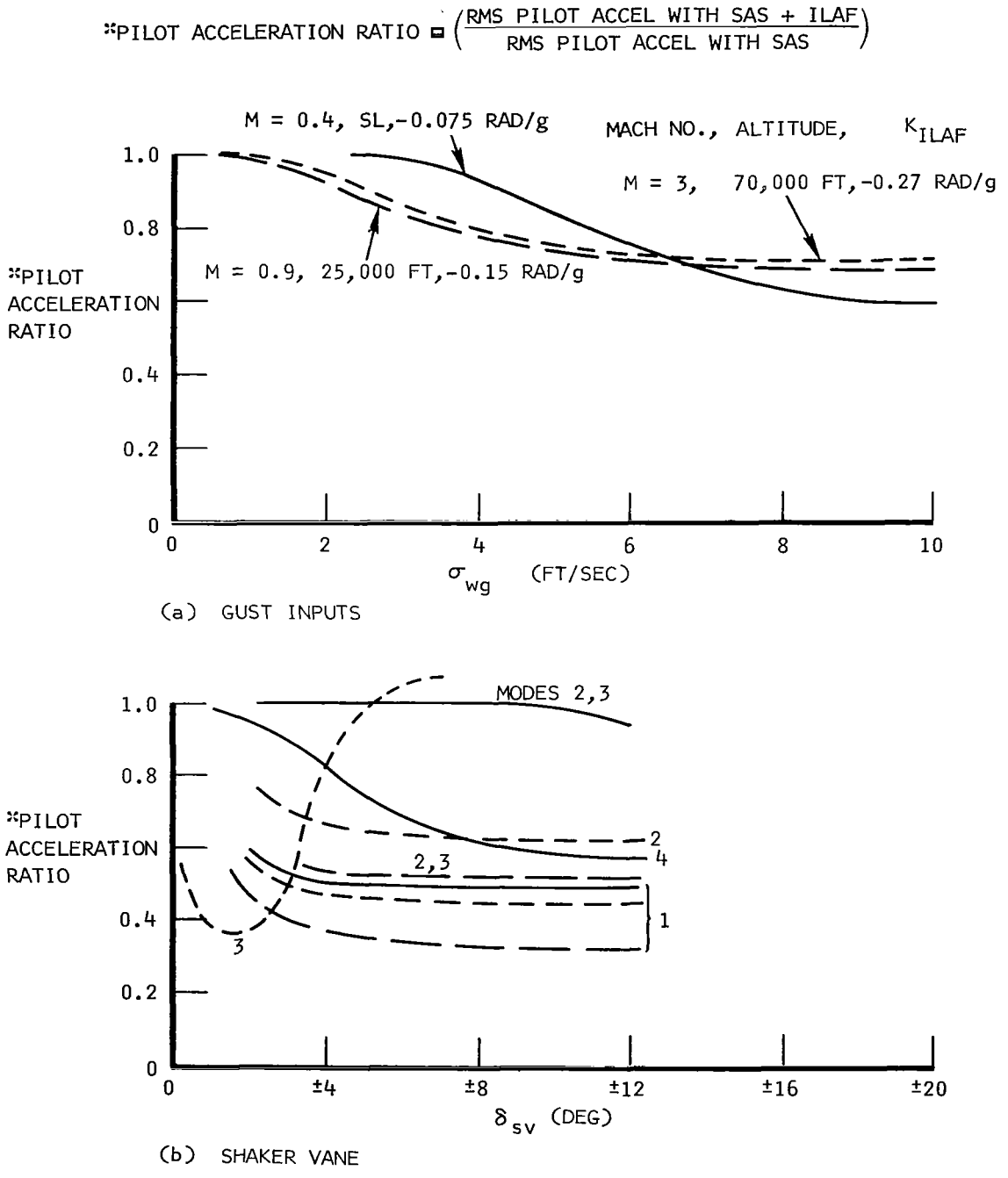

Figure 39.- Performance of ILAF system for gust and shaker vane excitation with ILAF gain select at No. 10 - simulator data.

$$*\text{PILOT ACCELERATION RATIO} = \left(\frac{\text{RMS PILOT ACCEL WITH SAS + ILAF}}{\text{RMS PILOT ACCEL WITH SAS}}\right)$$

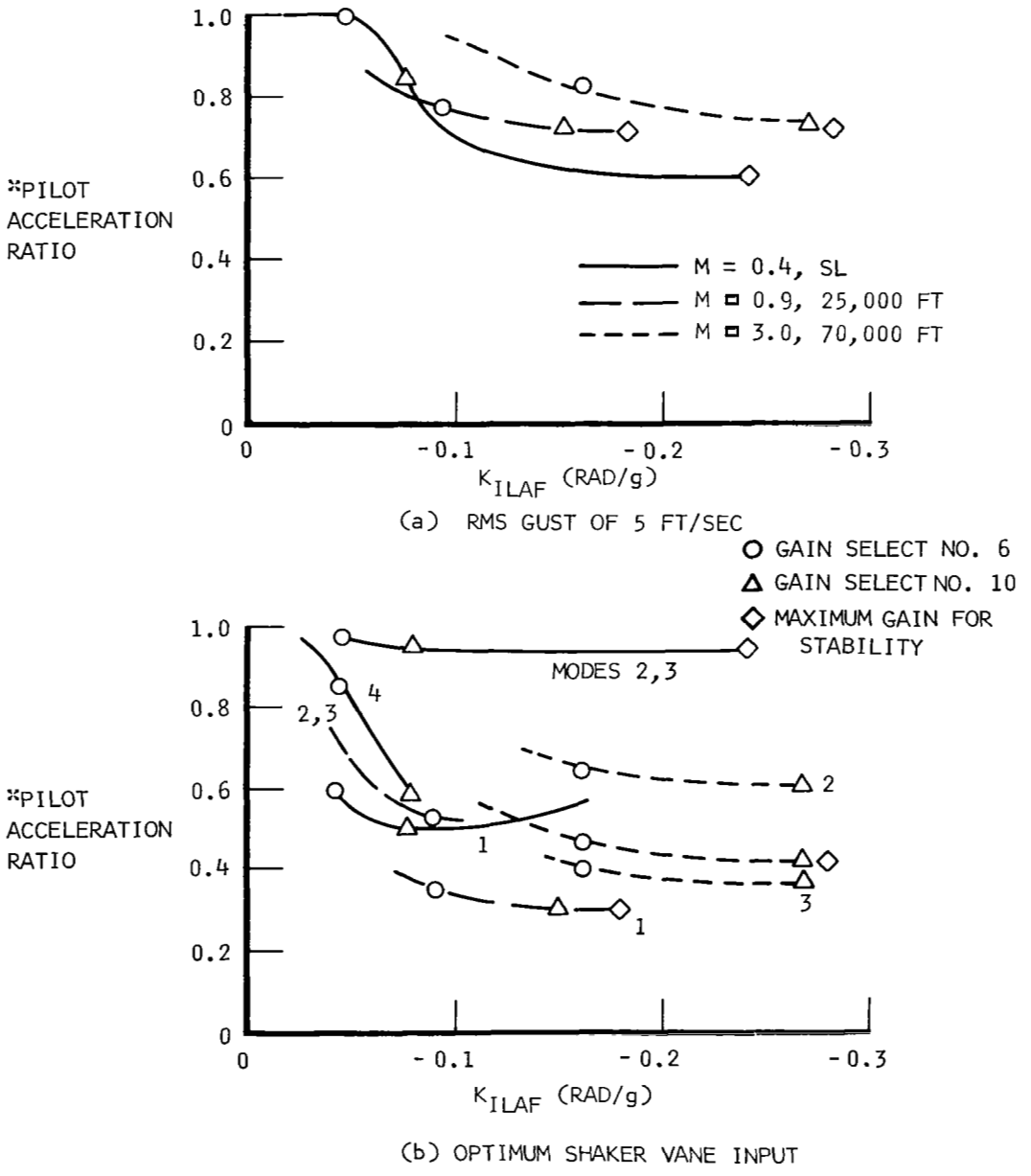

Figure 40.- Gust response and shaker vane response performance versus ILAF system gain - simulator data.

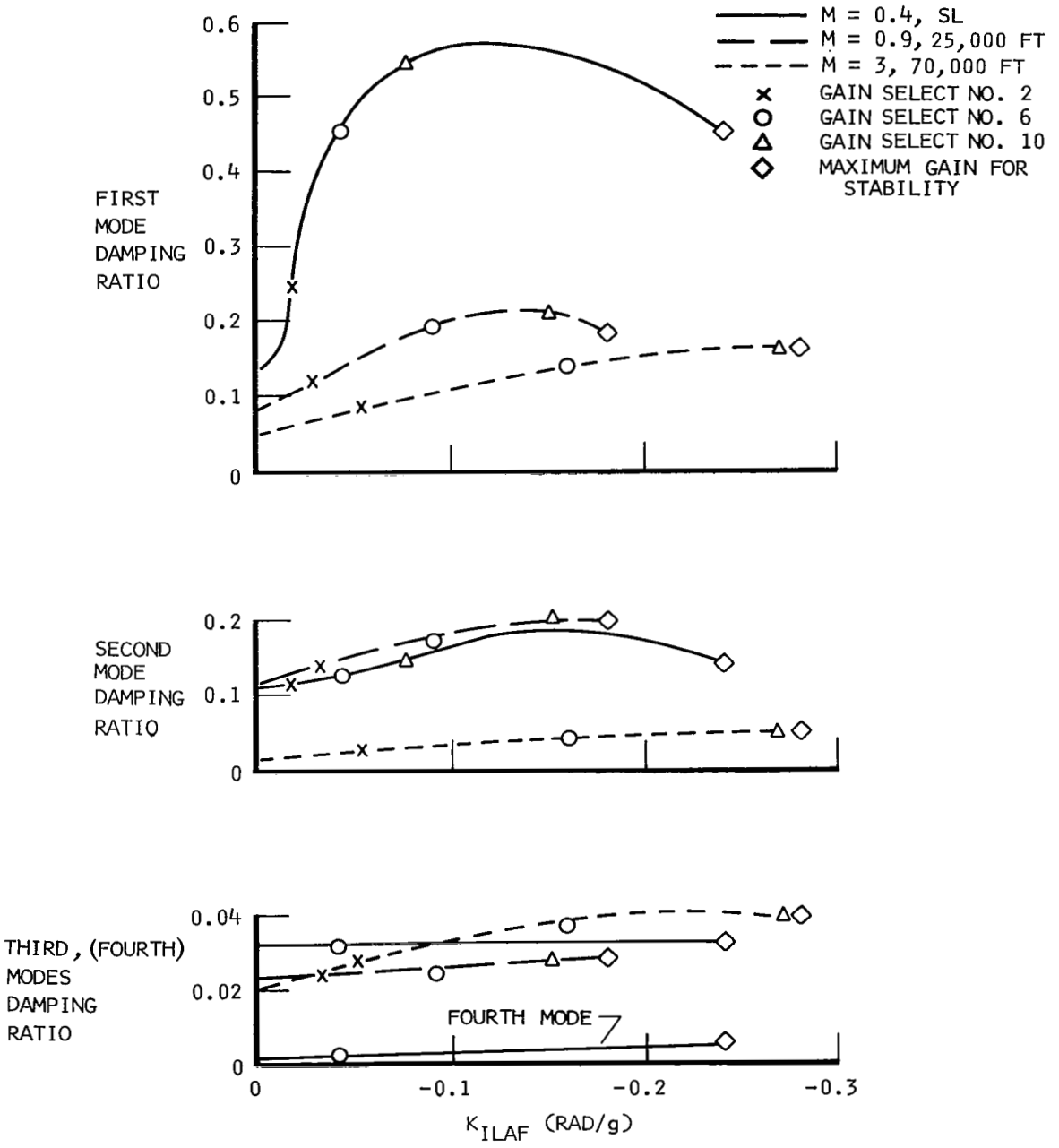

Figure 41.- Structural mode damping versus ILAF system gain - simulator data.

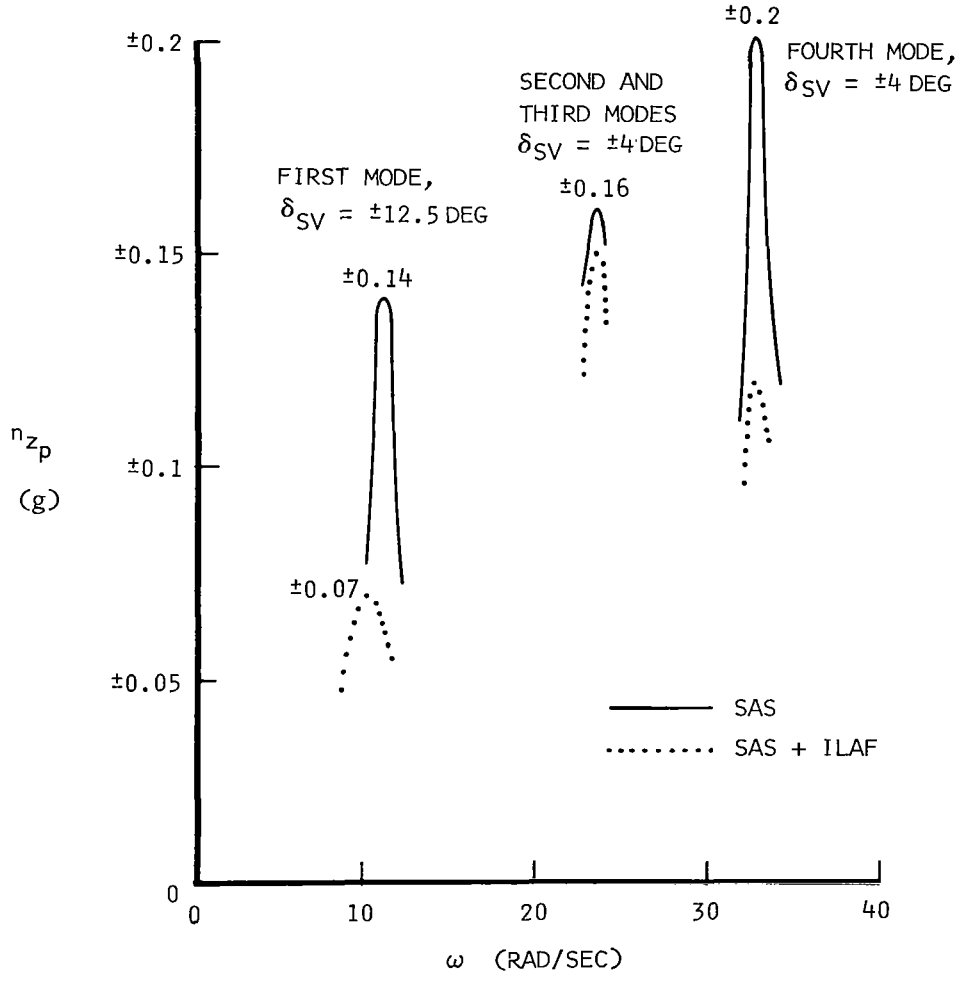

(a) HEAVY WEIGHT, δ_T = 0 DEGREE, M = 0.4, SEA LEVEL, K_{ILAF} = - 0.075 RAD/g

Figure 42.- Partial frequency response of pilot acceleration resulting from shaker vane inputs at selected ILAF gains - simulator data.

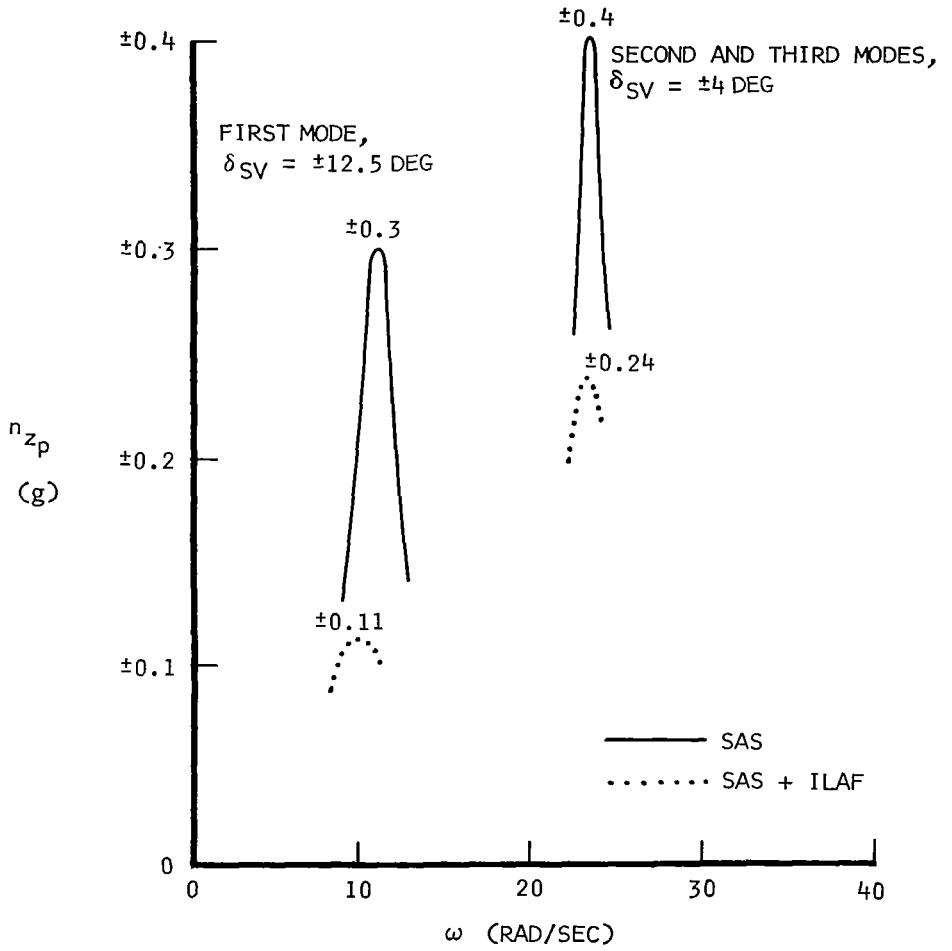

(b) HEAVY WEIGHT, δ_T = 25 DEGREES, M = 0.9, 25,000 FEET, K_{ILAF} =-0.09 RAD/g

Figure 42.- Continued.

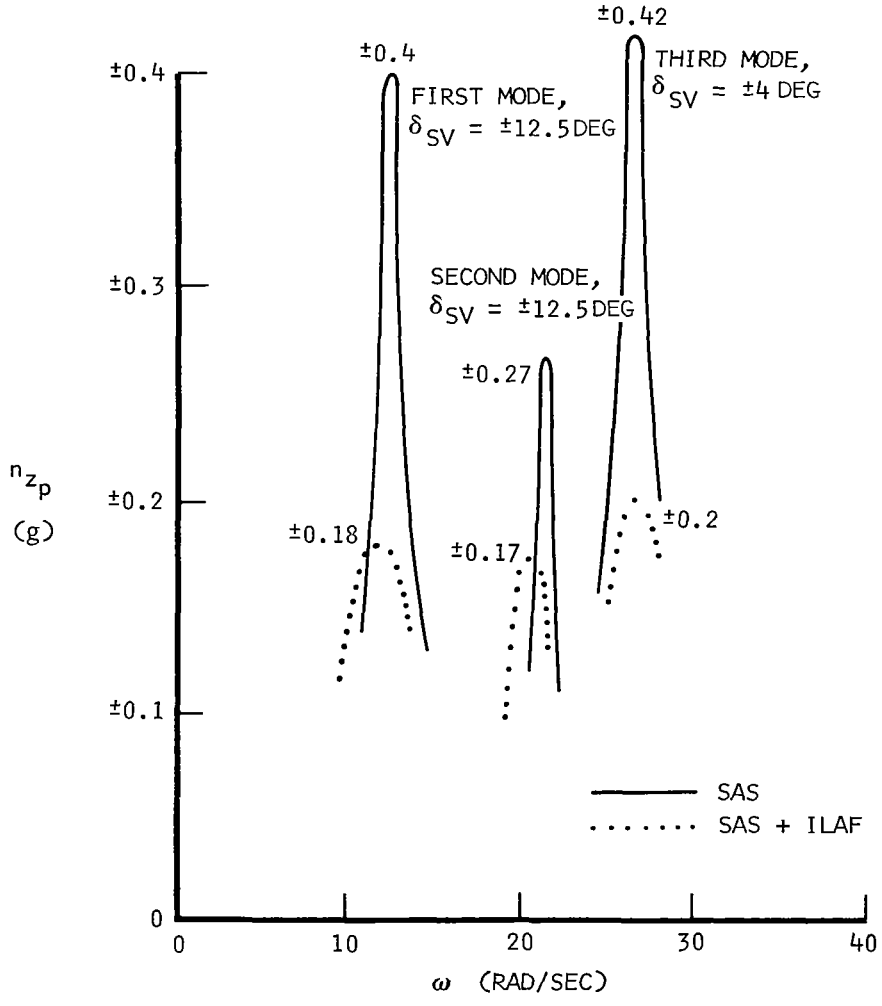

(c) MEDIUM WEIGHT, δ_T = 65 DEGREES, M = 3.0, 70,000 FEET, K_{ILAF} =-0.16 RAD/g

Figure 42.- Continued.

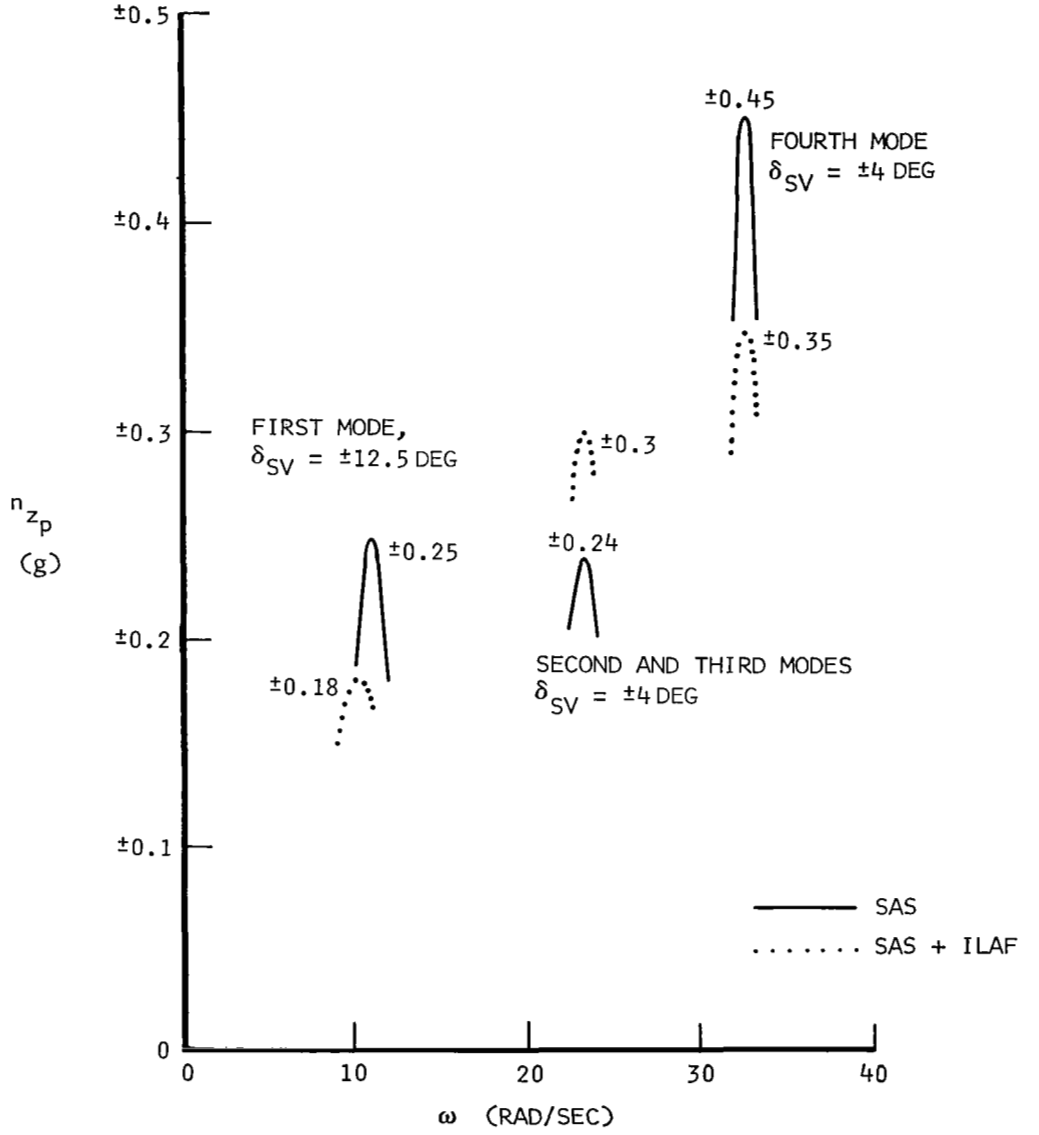

(d) HEAVY WEIGHT, δ_T 0 DEGREES, M = 0.4, SEA LEVEL, K_{ILAF} = -0.075 RAD/g
σ_{w_g} = 5 FT/SEC SUPERIMPOSED GUSTS

Figure 42.- Continued.

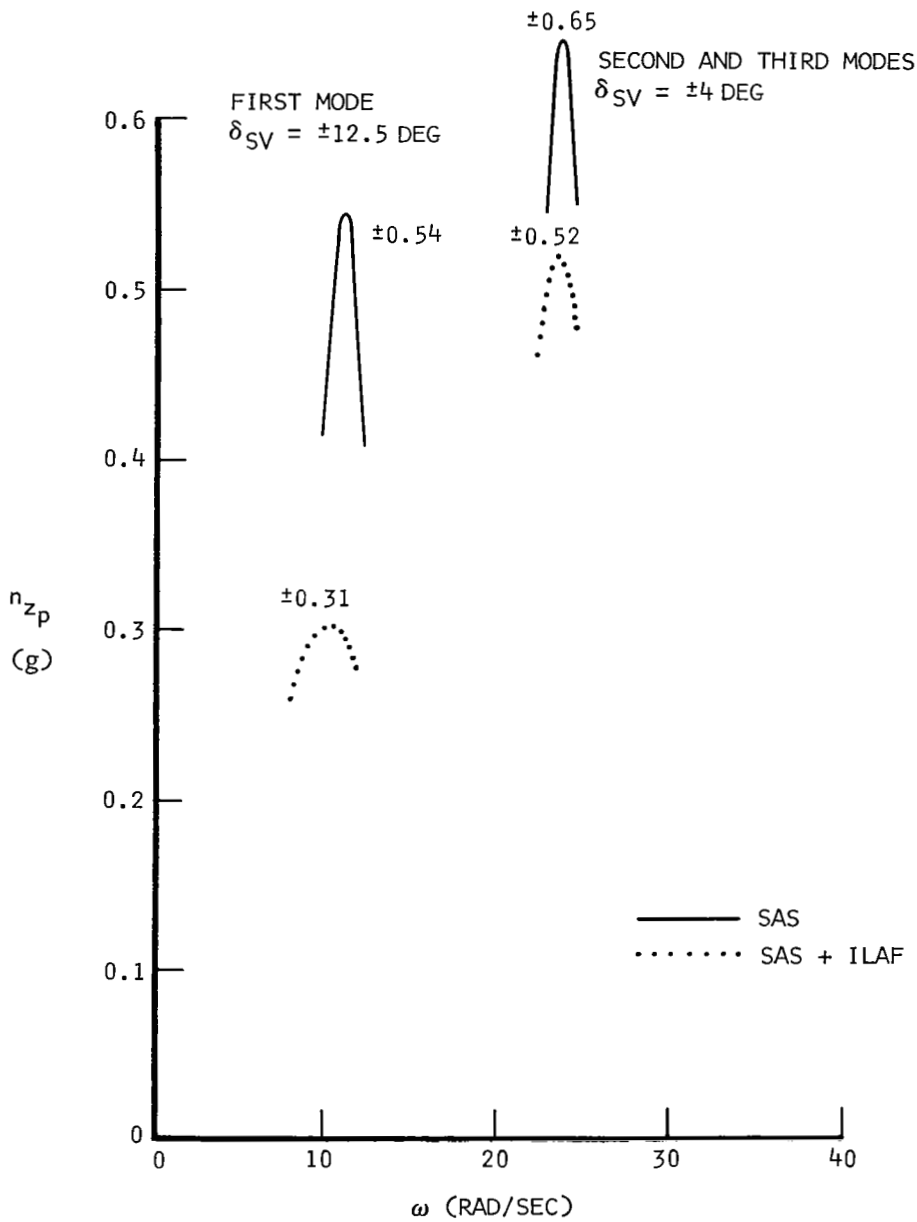

(e) HEAVY WEIGHT, δ_T = 25 DEGREES, M = 0.9, 25,000 FEET, K_{ILAF} = -0.09 RAD/g
σ_{w_g} = 5 FT/SEC SUPERIMPOSED GUSTS

Figure 42.- Concluded.

To evaluate ILAF effects on various parameters, table V compares the response of seven parameters with SAS operating alone against SAS plus ILAF. The tabulated data are for shaker vane inputs of ±12.5 degrees at modes 1 and 2, and ±4 degrees at modes 3 and 4. Optimum ILAF gains varying with the three flight conditions are as indicated. In general, SAS plus ILAF shows lower accelerations at the pilot, SAS accelerometer, and ILAF accelerometer locations along with the increased servo and elevon activities. The maximum servo and elevon rates are very near the rate limitation of the actuators. The elevon activity is less than the servo activity because of control system attenuation. In some cases, as indicated in the table, there was servo activity without any elevon activity because of the threshold of surface response.

To obtain combined input data, the ILAF system was evaluated for simultaneous inputs of gust and shaker vane. Figures 42d and 42e show partial frequency responses of pilot accelerations resulting from shaker vane inputs of similar amplitudes as previously presented in figures 42a and 42b; however, rms gust environment of 5 feet per second was superimposed. The responses of other parameters are presented in table VI. When using shaker vane inputs for ILAF evaluation, it appears that, as gust magnitudes increase, the apparent effectiveness of ILAF decreases. This is because the gust mainly excites mode 3 and/or mode 4, and ILAF does not control these modes as well as indicated by linear analysis because of the servo-through-inboard-elevon hydromechanical system threshold discussed previously.

Assuming that it is necessary for the peak accelerations with SAS alone to be greater than 1.6 times the peak accelerations with SAS plus ILAF to allow pilot evaluation of ILAF, figure 43 shows that shaker vane inputs must be increased as gust rms increases above 4 feet per second. Regardless of the gust magnitudes, shaker vane magnitudes of more than ±3 degrees are necessary to cause accelerations sufficient to break out the ILAF threshold levels. Upper limits of shaker vane inputs were determined by the ±12.5 degrees for evaluation of mode 1, and ±0.7 g pilot acceleration arbitrary limit for evaluation of modes 2 and 3. These data indicate the desirability of not flying through turbulence when evaluating ILAF system performance using the shaker vane.

The hydromechanical system nonlinearities have significantly affected the ILAF performance characteristics. Rate saturation, threshold, and hysteresis have affected both stability margins and performance. Threshold levels increased with frequency, thus simulator ILAF performance on modes 3 and 4 was not as impressive as that indicated by linear digital analysis. Since gust inputs mainly excite mode 3 and/or mode 4, the ILAF was not effective for gust inputs unless the gust rms level exceeded about 8 feet per second at some gain conditions. With all other conditions being equal, the airplane ILAF evaluation will be even less effective for gust inputs than the simulator ILAF tests, because the simulator outboard elevon actuator was analog-simulated, neglecting

TABLE V

EVALUATION OF ILAF FOR SHAKER VANE INPUTS

SIMULATOR DATA

Numbers in table represent maximum half amplitudes (plus, minus) for shaker vane inputs

		Shaker Vane Inputs of ±12.5 Degrees						Shaker Vane Inputs of ±4.0 Degrees			
		First Structural Mode			Second Structural Mode			Third Structural Mode			Fourth Mode
Flight condition K_{ILAF} (Rad/g)		0.4, SL -0.075	0.9, 25,000 -0.09	3.0, 70,000 -0.16	0.4, SL -0.075	0.9, 25,000 -0.09	3.0, 70,000 -0.16	0.4, SL -.075	0.9, 25,000 -.09	3.0, 70,000 -.16	0.4, SL -0.075
n_z (g) Pilot	SAS SAS + ILAF	0.14 0.07	0.30 0.11	0.40 0.18	See mode 3	See mode 3	0.27 0.17	0.16 0.15	0.40 0.24	0.42 0.20	0.20 0.12
n_z (g) SAS	SAS SAS + ILAF	0.21 0.11	0.07 0.04	0.15 0.08			0.12 0.08	0.04 0.06	0.09 0.04	0.11 0.05	0.15 0.10
Δn_z (g) ILAF	SAS SAS + ILAF	0.10 0.05	0.25 0.08	0.2 0.1			0.15 0.12	0.09 0.09	0.18 0.10	0.36 0.20	0.11 0.08
Servo (deg)	SAS SAS + ILAF	0.2 0.3	0.3 0.6	0.24 0.33			0.6 1.3	0.05 0.43	0.10 0.55	0.6 1.9	0.08 0.17
Servo Rate (deg/sec)	SAS SAS + ILAF	2.4 3.6	3.3 6.6	2.9 4.0			13.0 28.0	1.2 10.0	2.2 12.4	15.0 47.0	2.5 5.5
Elevon (deg)	SAS SAS + ILAF	0.12 0.20	0.26 0.45	0.22 0.30			0.5 1.2	0 0.17	0 0.3	0.4 1.7	0 0.06
Elevon Rate (deg/sec)	SAS SAS + ILAF	1.4 2.4	2.8 4.8	2.7 3.6			11.0 25.0	0 4.0	0 6.7	10.0 45.0	0 1.9

TABLE VI

EVALUATION OF ILAF FOR SHAKER VANE INPUTS DURING RMS GUST OF 5 FEET PER SECOND

SIMULATOR DATA

Numbers in table represent maximum half amplitudes (plus, minus) for shaker vane inputs

		RMS Atmospheric Turbulence of 5 Feet Per Second									
		Shaker Vane Inputs of ±12.5 Degrees						Shaker Vane Inputs of ±4.0 Degrees			
		First Structural Mode			Second Structural Mode			Third Structural Mode			Fourth Mode
Flight condition K_{ILAF} (rad/g)		0.4, SL -0.075	0.9, 25,000 -0.09	3.0, 70,000 -0.16	0.4, SL -0.075	0.9, 25,000 -0.09	3.0, 70,000 -0.16	0.4, SL -0.075	0.9, 25,000 -0.09	3.0, 70,000 -0.16	0.4, SL -0.075
n_z (g) Pilot	SAS SAS + ILAF	0.25 0.18	0.54 0.31		See mode 3	See mode 3	* *	0.24* 0.3 *	0.65* 0.52*	* *	0.45* 0.35*
n_z (g) SAS	SAS SAS + ILAF	0.25 0.13	0.20 0.12					0.08 0.10	0.2 0.2		0.16 0.12
Δn_z (g) ILAF	SAS SAS + ILAF	0.14 0.09	0.45 0.20					0.13 0.13	0.4 0.24		0.14 0.12
Servo (deg)	SAS SAS + ILAF	0.2 0.4	1.4 1.8					0.05 0.60	1.3 1.7		0.28 0.47
Servo Rate (deg/sec)	SAS SAS + ILAF	2.4 8.8	6.0 18.0					1.0 12.0	8.0 34.0		5.5 21.0
Elevon (deg)	SAS SAS + ILAF	0.12 0.22	1.4 1.8					0 0.87	1.3 1.6		0.10 0.26
Elevon Rate	SAS SAS + ILAF	1.4 3.6	6.0 18.0					0 6.0	4.0 32.0		0.10 10.0

*Indicates statistical evaluation necessary, not practical for pilot evaluation.

NUMBERS IN PARENTHESES INDICATE PEAK PILOT ACCELERATIONS FOR (SAS/SAS + ILAF) FOR SHAKER VANE INPUTS OF ±4.0, ±8.0, ±12.5 DEGREES AND RMS GUSTS OF 0,3,5 FT/SEC

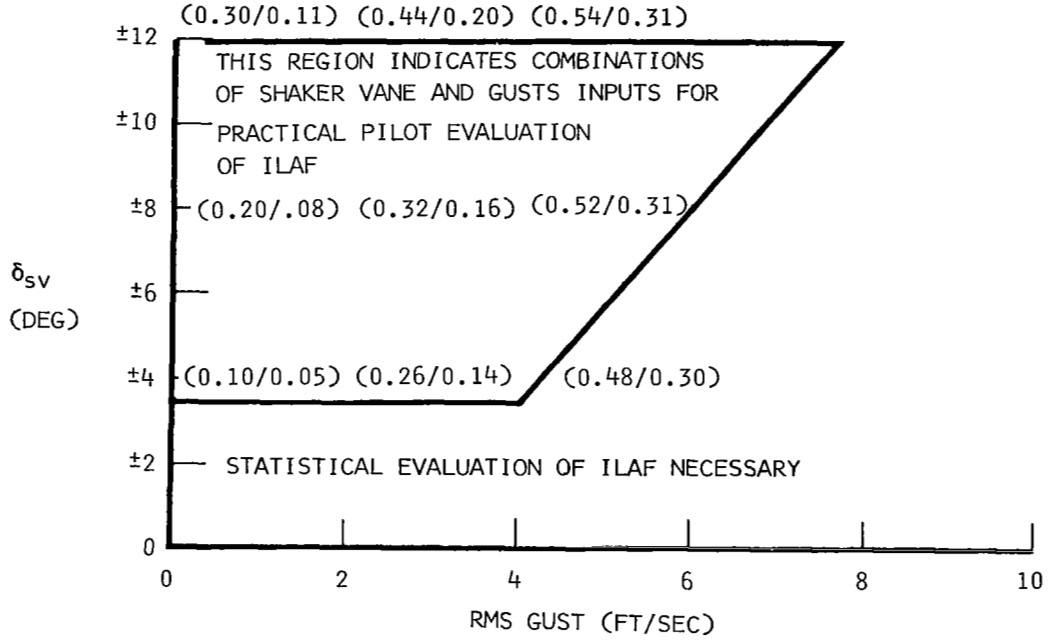

(a) FIRST STRUCTURAL MODE

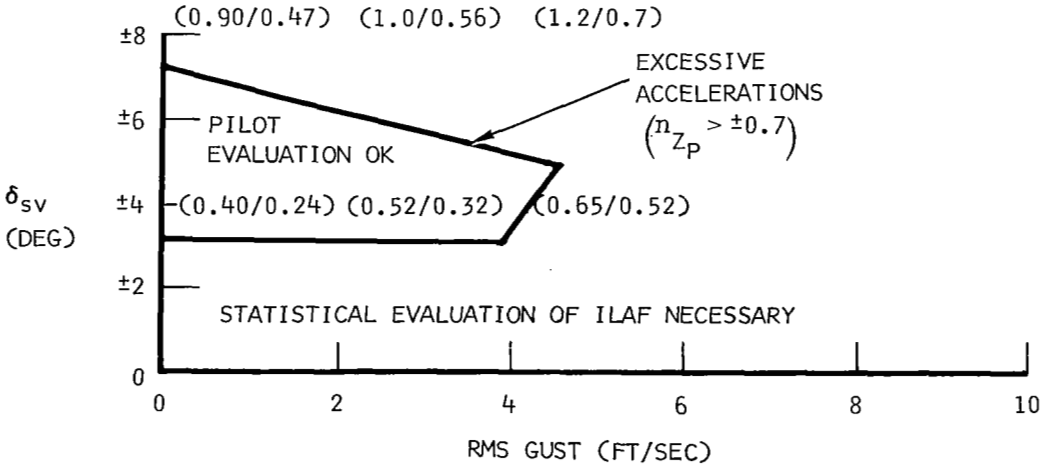

(b) SECOND AND THIRD STRUCTURAL MODES

Figure 43.- Indication of shaker vane limits during evaluation of ILAF in turbulence - simulator data. M = 0.9, 25,000 FT.

additional threshold characteristics. Gusts also excite the rigid-body mode which the ILAF system does not control; therefore, it may be difficult to determine structural mode gust response improvements in flight. It is suggested that shaker vane inputs rather than gust inputs be used for primary evaluation of ILAF during flight tests. Using shaker vane inputs will provide controllable amplitudes and frequencies in contrast with the random nature of gust inputs.

Typical aircraft responses to abrupt pilot column inputs are shown in the time history data of figure 44. The normal acceleration at the pilot station with the normal augmented configuration (SAS) and with ILAF operating (SAS plus ILAF) is shown at the three flight conditions investigated. The column inputs will excite the first mode at all conditions, but the other structural modes are difficult to excite with manual inputs. The data show that the first mode oscillatory response is reduced without a significant change in the short-period response as a result of the improved first mode damping with the ILAF system. Small motions at the third and fourth mode frequencies can be seen with or without ILAF due to the poorly damped modes previously illustrated on the root loci of figures 22a and 22c. These modes are not controlled by the ILAF system and hence, if excited, the oscillation damping is not improved nor is it deteriorated. The column motions during flight will not be as abrupt as in these typical illustration examples.

During the flight simulator test program at the mach 0.9 condition, the analog model of the vehicle was modified to examine the effects of higher uncoupled structural mode frequencies more representative of the ground vibration test results. Aerodynamic and mode shape data were maintained constant. Although the frequencies were different, the data indicated that the mode damping ratio was approximately the same as that prior to increase of the structural mode frequencies in the model.

Other simulator investigations included compensation amplitude-phase variations, outboard actuator lag variations, sensor location variations, ground (zero speed) operation and stability, and combinations of inputs which resulted in system saturation. These data indicate that better ILAF system performance at the third mode can be obtained with additional lead compensation in the ILAF system. This lead was not incorporated in the design, because the present performance levels were satisfactory to meet the program objectives, and stability margins at higher frequency may be reduced with the additional lead. The system operation in saturated conditions always indicated loss of performance rather than a system stability problem.

Effects of Additional Structural Modes in Vehicle Analytical Model

Inspection of power spectral density curves of normal load factors due to gusts obtained from XB-70 flight-test experience (reference 13) indicated that

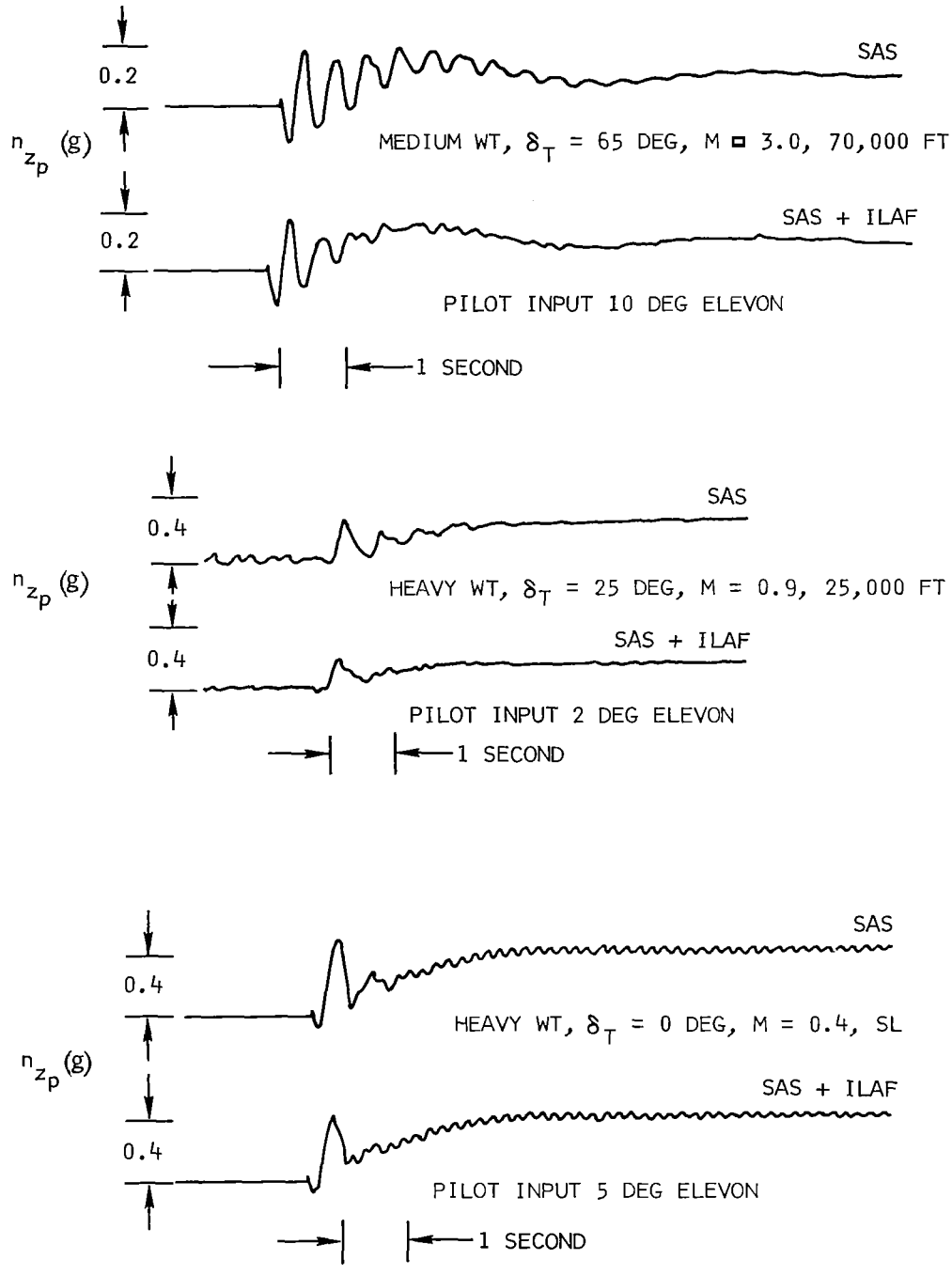

Figure 44.- Pilot acceleration transients for pilot column inputs - simulator data.

there was structural mode activity at mode frequencies higher than the four structural modes utilized in the major study effort. As a simplified approach to obtaining some indication of higher mode activity, it was assumed that five additional modes could be represented by equations in which aerodynamic coupling and the effect of aerodynamics on mode frequencies could be ignored. The damping for the lower of the five additional modes was estimated from flutter analyses results; the higher modes were assumed to have $g_{s_i} = 0.02$.

A light weight, $\delta_T = 65$ degrees, mach 1.40 at 40,000 feet case was selected as the check case. The flight speed being supersonic made it easy to compute the aerodynamic generalized force for the elevon surfaces; all of the forces generated by elevon deflection could be assumed to act on the elevon surface. Thus, for an elevon producing a ΔC_{N_δ} and located at a point having a mode i deflection of ϕ_i, the generalized force coefficient $C\eta_{i_\delta} = \Delta C_{N_\delta}\phi_i$.

Figure 45 is the frequency response plot of normal load factor at the pilot station for a unit shaker vane input where nine structural modes were utilized in the analytical model of the airplane. This plot reflects the previously known influences of the ILAF system operation; namely, the reduced load factor at the lower modes with the ILAF performance dropping off at the higher modes. In addition, the plot shows that ILAF causes an increase in the fifth mode response; the other higher modes remain little affected by the ILAF operation.

Figure 46 shows that the vehicle-control system combination is stable, but that the fifth mode damping has been decreased by ILAF operation. The compensation phase and gain characteristics together with the fifth mode characteristics have caused this situation to exist. The open-loop calculation of $\Delta n_{z_{ILAF}}/\bar{\delta}_1$ was not available for use in the describing function analysis previously discussed.

Figure 47 shows the component elevon response that goes along with figure 46. This plot shows that the ILAF elevon activity is confined to the lower modes as intended except for mode 5. The reader is reminded that the separation of the SAS and ILAF elevon motion components can only be done analytically and such component separation cannot be obtained on the actual vehicle.

Because of the fifth mode response at mach 1.4 with ILAF operating, a check of fifth mode effects was made at mach 0.90. Figure 48 shows the comparative stability plots with SAS plus ILAF operating with the analytical model containing four and five modes. The fifth mode model includes aerodynamic coupling from and into all of the other modes and includes the proper aerodynamic distribution for the elevon loads. These data show that there is some loss of fifth mode damping, but that it is not as critical as at mach

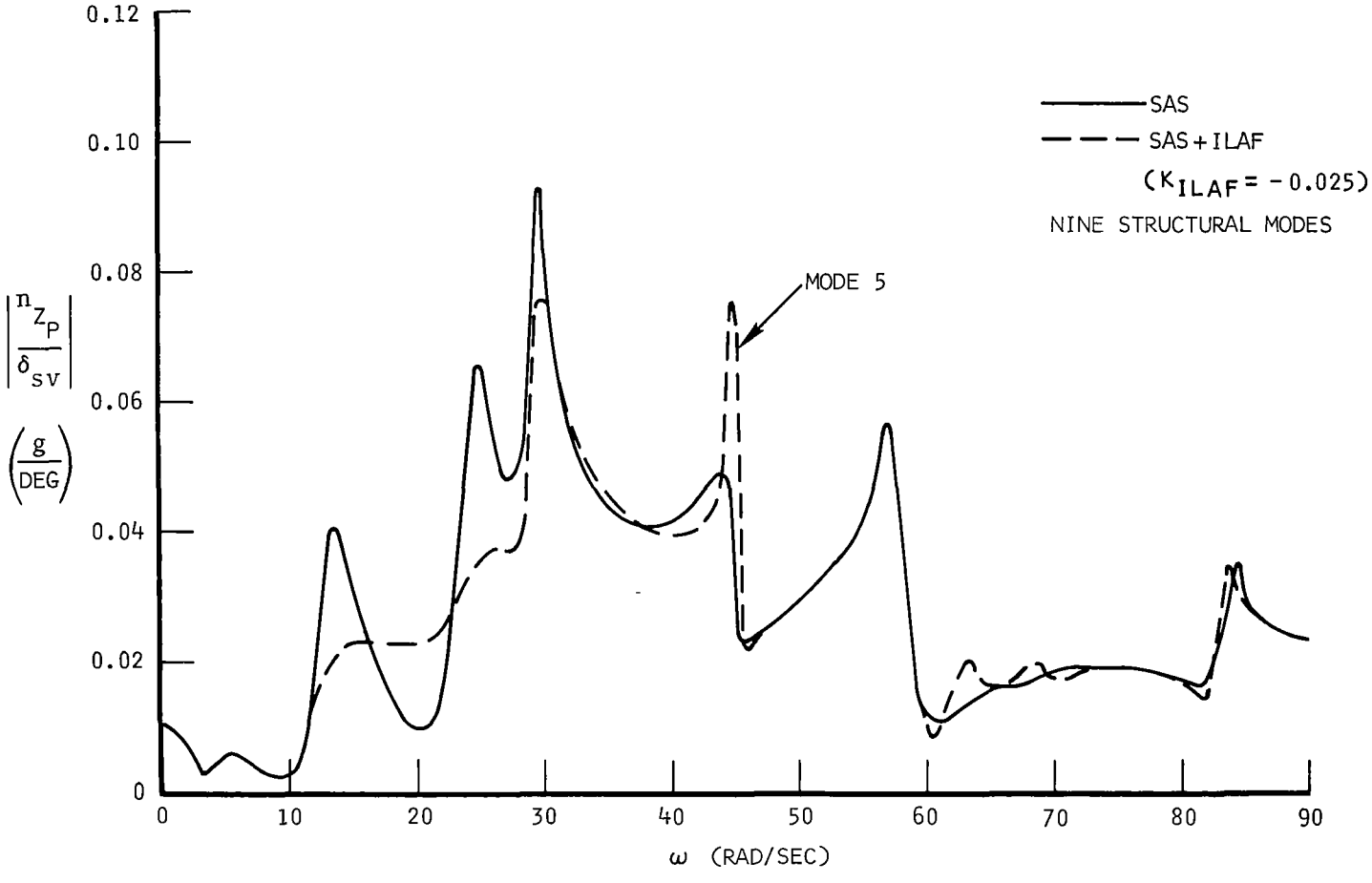

LIGHT WEIGHT, δ_T = 65 DEGREES, M = 1.4, 40,000 FEET

Figure 45.- XB-70 pilot station normal load factor response due to 1 degree of shaker vane excitation, nine structural modes - analytical data.

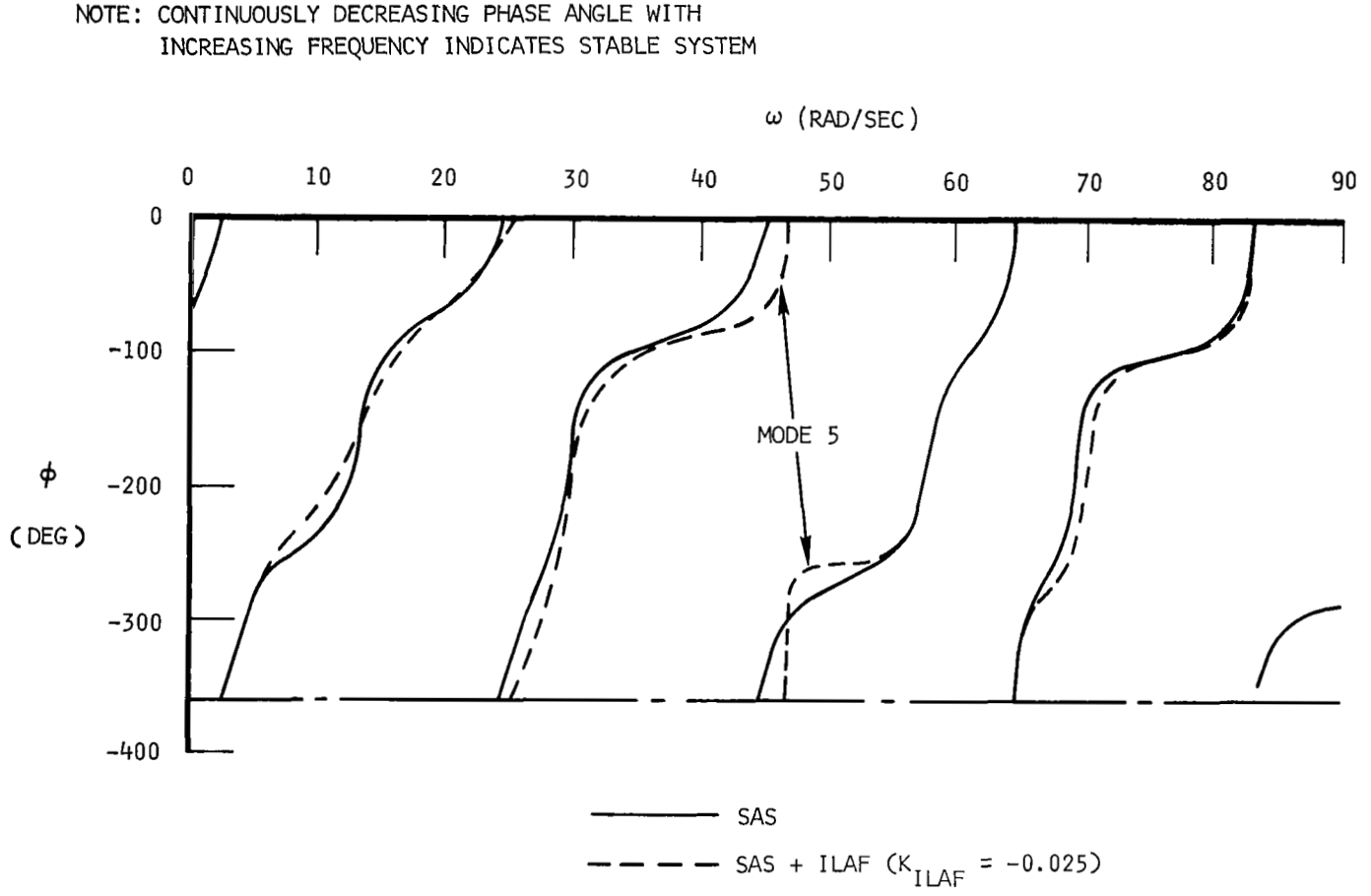

LIGHT WEIGHT, δ_T = 65 DEGREES, M = 1.4, 40,000 FEET

Figure 46.- XB-70 control system stability analysis, characteristic determinant phase angle, nine structural modes - analytical data.

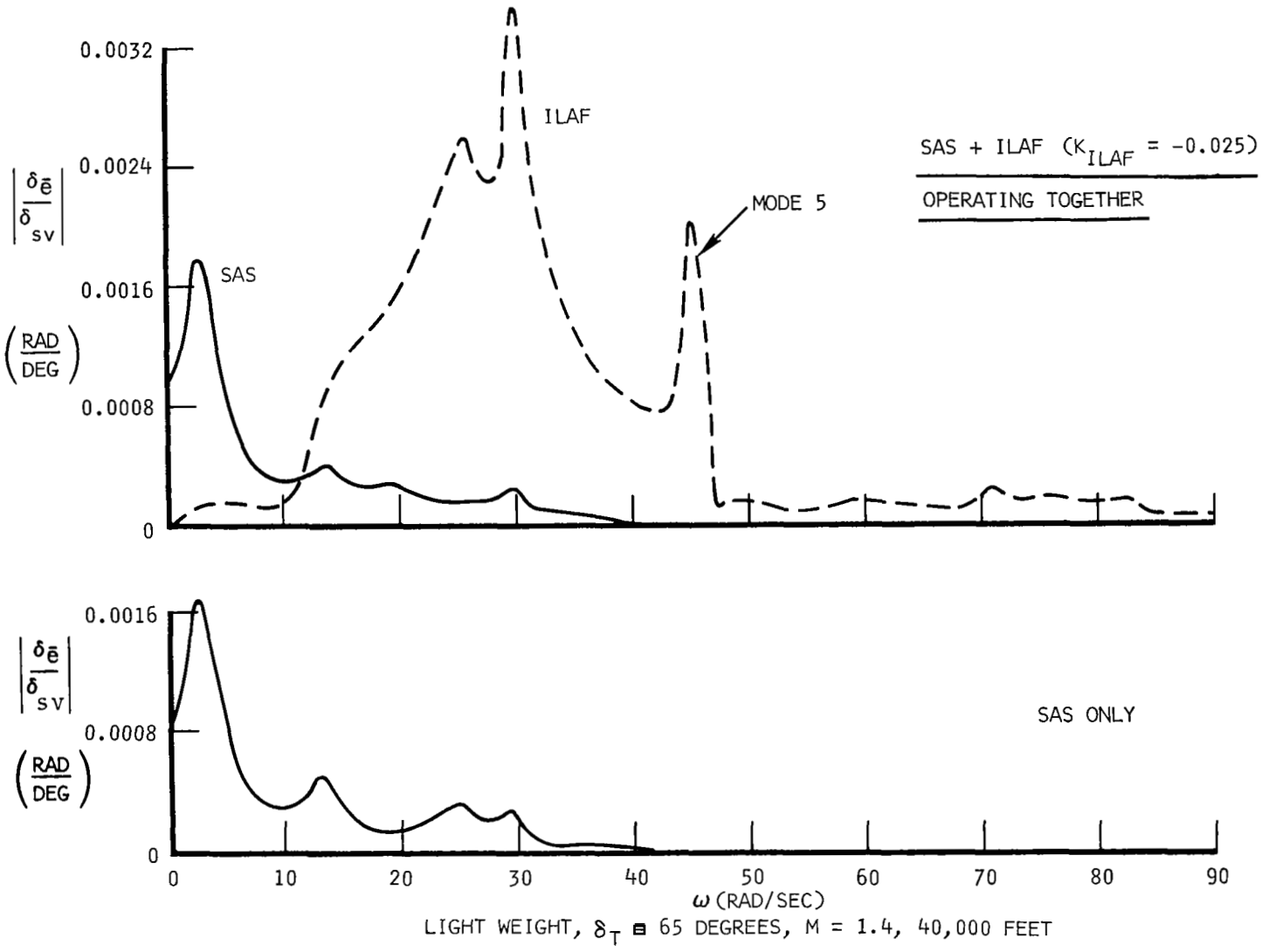

Figure 47.- Elevon deflections due to SAS and ILAF operation, frequency response amplitude for 1 degree of shaker vane excitation, five structural modes - analytical data.

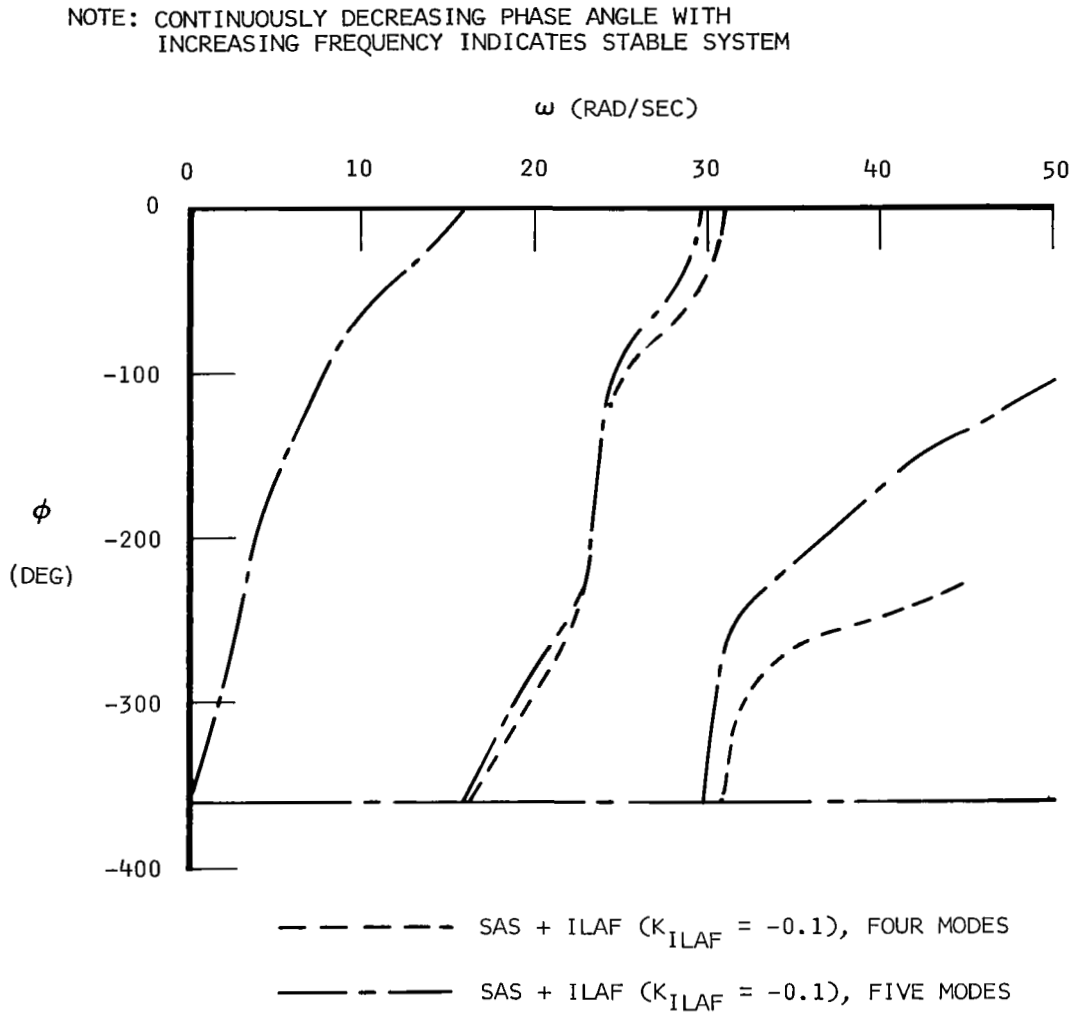

HEAVY WEIGHT, δ_T = 25 DEGREES, M = 0.90, 25,000 FEET

Figure 48.- XB-70 control system stability analysis, characteristic determinant phase angle, effect of fifth mode - analytical data.

1.4; the system remains solidly stable. The describing-function analysis of figure 37b shows an allowable gain of 0.21 rad/g.

The results of this limited study indicate that during flight test of the ILAF system particular attention must be directed at monitoring mode 5 response.

Allowable ILAF System Gains

As has been described, linear digital computer stability analyses were conducted first to obtain a conservative estimate of the system stability margins. This was conservative in the sense that a very destabilizing control surface actuation frequency response was utilized. After data from the simulator and air vehicle were obtained which described the response capability available, nonlinear analyses were initiated. The stability indications from the flight simulator tests include a very good representation of the nonlinearities at low frequencies, but the characteristics above 10 cps are different than those of the air vehicle. Table VII has been assembled from the results of all these studies to permit the estimation of possible maximum ILAF system gains. The conversion indicated on figure 28 permits control panel gain adjustment knob settings to be obtained.

TABLE VII

COMPARISON OF DIGITAL COMPUTER, DESCRIBING FUNCTION ANALYSIS, AND SIMULATOR MAXIMUM ALLOWABLE GAINS

				Maximum Allowable ILAF Gains, K_{ILAF} (rad/g)				
Mach No.	Altitude	Weight	Tips (deg)	Digital Computer **		Describing Functions*		Simulator
				Four Modes	Five Modes	Four Modes	Five Modes	Four Modes
0	SL	Heavy	0	-0.075				
0.18	SL	Heavy	0	-0.050				
0.18	SL	Heavy	0	-0.025				
0.4	SL	Heavy	0	-0.050		-0.50 (ω = 95)		-0.25 (ω = 60)
0.4	SL	Light	0	-0.025				
0.9	25,000 ft	Heavy	25	-0.10	-0.10 +	-0.47 (ω = 72)	-0.39 (ω = 75) -0.21 (ω = 31)	-0.18 (ω = 60)
0.9	25,000 ft	Light	65	-0.10				
1.4	40,000 ft	Light	65		-0.025 + (nine modes)			
3.0	70,000 ft	Medium	65	-0.15		-0.5 (ω = 100)		-0.28 (ω = 60)

*Based upon latest airplane and simulator response characteristics at no-air-load conditions on elevons. Coupling effects of FACS loops at high ILAF gains not included.

**ILAF + FACS included

STRUCTURAL LOADS

As both the simulator and the digital analyses proceeded for the XB-70 with the ILAF system operating, the resulting data were searched for possible critical load conditions. Because the objectives of the ILAF flight test are limited to demonstrating system principles and are not intended to validate an operational system, the loading conditions checked had limiting qualifications as discussed in the following.

The ILAF structural dynamic stability augmentation performance evaluations have focused mainly on the pilot ride qualities. In addition, however, a simplified bending moment reduction performance spot check was conducted. A mode displacement technique was used to calculate the bending moments due to a unit rms gust at three locations: (1) in the fuselage at the wing apex (FS 915), (2) at the wingtip fold, and (3) at the wing chord where the wing joins the fuselage. These data plus the gust power spectral density curve allowed the calculation of rms bending moments due to vertical gusts. These data are shown in figure 49 for the basic vehicle, with SAS only operating, and with SAS plus ILAF operating. The SAS operation reduces the bending moment at all stations. When ILAF is operated in conjunction with SAS, however, there is a nonuniform effect generated. In the fuselage, the bending moment is reduced an additional increment; while at the inboard wing station, the bending moment is larger than with just SAS operating, but less than the basic vehicle value. Little difference is noted at the wingtip fold. One explanation of this trend is found in the fact that the elevon control surfaces are located inboard where they are more effective in controlling fuselage bending than wing bending.

The maximum elevon hinge moment increment during simulation studies was found to occur at mach 0.9 when it was assumed that it would be possible to experience combined vane excitation and gust excitation: it was assumed that vane excitation would be the maximum tolerable (Δn_z = 0.5 at pilot station) and a moderate 5 feet per second rms gust intensity. This combination produced a maximum 40,000 inch-pound increment from trim levels for each elevon panel. However, the airplane is expected to fly in a more critical flight area than that simulated. The mach 1.2 to 1.4 speed range is a more critical hinge moment flight region. It is estimated that the 100,000 inch-pound increment (beyond a maximum trim value of 700,000 inch-pounds) will cover any maximum hinge moment.

In addition to the incremental hinge moment due to ILAF operation, it is expected that the numbers of cycles an actuator experiences will be important. The test technique utilizing the shaker vane will necessitate exciting the vehicle at a fixed frequency until stabilized. Thus, the comparison of data recorded with ILAF system on and ILAF system off will reveal system performance. One of the concerns relative to elevon cycling involves

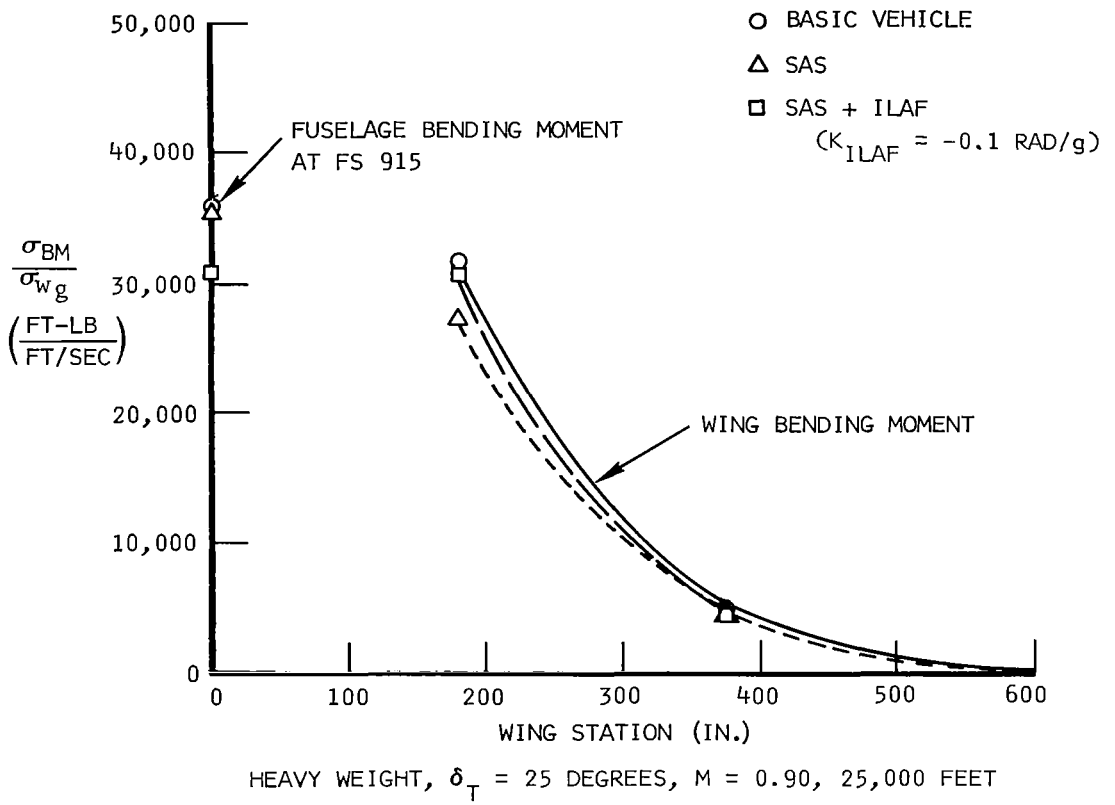

Figure 49.- Typical control system performance in turbulence, rms incremental bending moment at a number of locations on the XB-70 - analytical data.

fretting of the actuator piston rod. Fretting is caused when an actuator is forced at a fixed frequency and amplitude for an extended period of time. These conditions existed on the simulator during the testing performed and actually exceeded in duration any expected flight time. Inspection of the simulator actuator rods and seals did not reveal any fretting. It should be added that these same actuators have seen much service beyond that associated with the ILAF simulation testing. Considering both fretting and general structural fatiguing, it will be prudent to design the flight testing of ILAF to minimize cycle buildup.

In the flight-test program involving ILAF, the following restrictions will be required to avoid overloading the airplane:

(1) The maximum allowable XB-70 flight speeds with the ILAF in operation will be the same as for the basic XB-70 with the exception of the high q_o cutoff interpreted as a mach number limit in figure 50. This limit reflects the aforementioned 100,000-inch-pound hinge moment increment allowable.

(2) The ILAF system will not be operated during deliberate windup turns, pullups, yawing, or rolling maneuvers during early test phases. All initial ILAF system testing will be initiated from a wings level, 1 g trimmed flight condition. This does not preclude eventual testing in moderate ($\sigma_{w_g} = 6$) turbulence, nor limited maneuvering to check handling qualities.

(3) All ILAF system testing will be accomplished using buildup techniques starting with low system gains and near flight conditions analyzed during the design study.

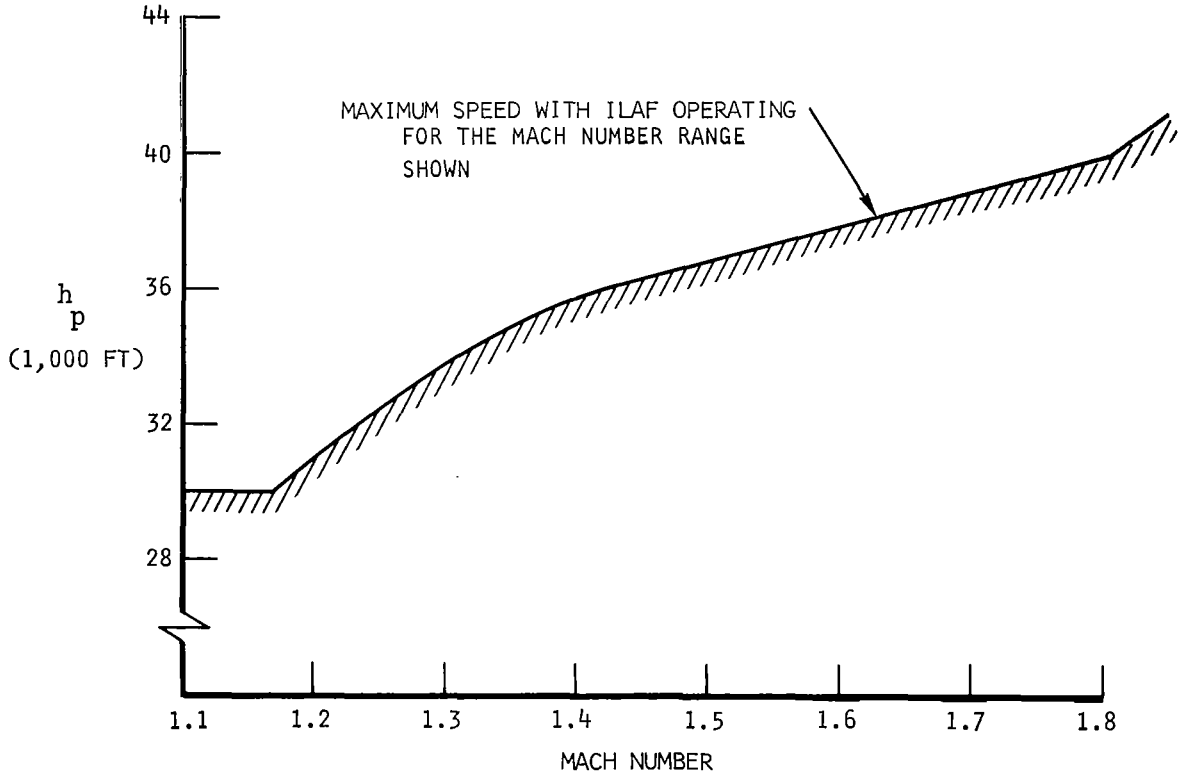

Figure 50.- Structural operating limitations with ILAF system operating.

CONCLUDING REMARKS

The design analysis and predicted performance of the XB-70 longitudinal-symmetric ILAF system indicate that a flight-test program can be safely conducted and sufficient in-flight data obtained to demonstrate the objectives of the program. These objectives are to demonstrate the ILAF technique of improving the aircraft structural mode damping without adverse effect on the short-period handling qualities.

An ILAF system has been synthesized and integrated with the existing XB-70 pitch control system through an application of techniques established during previous analytical research programs. This program has included the analysis, design, fabrication, installation, and checkout of the system prior to flight test. The system has been designed, qualified, and installed using components, techniques, and procedures similar to those used in the original pitch FACS design. The power, environment, and structural interface did not require large modifications to the airplane. This report has included only the results of the design analysis and predicted performance of the system.

The ILAF system features and design selections can be summarized as follows:

(1) The ILAF system operates through the existing pitch FACS.

(2) The ILAF sensing is oriented to sense the structural mode response and to minimize sensing of the short-period motions. The primary factor is the identical location of the accelerometer and force. Another factor is cancellation of short-period motions by a second accelerometer location. Analytical design guides based upon structural mode parameters have been used to determine specific sensor locations.

(3) The accelerometer mounting has been designed for high stiffness to minimize additional motions due to local structure.

(4) A manual gain adjust is provided for gain variation or selection at specific flight conditions. The range of gain adjust or maximum gain is a function of altitude.

(5) The ILAF accelerometer signals are filtered to attenuate transmission at high frequency (above 10 cps), to reduce the transmission at the control surface natural frequency, and to provide the desired characteristics in the lower structural mode frequency range (2 to 10 cps).

(6) The ILAF electronics design installation is located adjacent to the existing pitch FACS electronic computer. Electrical power and environmental

provisions are available in this location. The accelerometers located at the elevons are provided with environmental provisions similar to the existing FACS sensors for possible operation at high speed for prolonged periods of time. The other accelerometer is located in the AICS equipment environmental area. No additional hydraulic source is utilized.

(7) The pitch FACS must be engaged for ILAF operation. The FACS can operate without ILAF. The ILAF system will operate only with the landing gear retracted.

Performance and stability margins have been predicted from the results of analyses which included analytical frequency response techniques and an extensive flight simulator and airplane ground test program. The results are based upon an air vehicle dynamic model which includes selected use of unsteady aerodynamics and detailed control system frequency response characteristics defined during the program. The air vehicle dynamic model includes four structural modes in addition to the whole-vehicle pitch and plunge modes at constant velocity and altitude. Data at four mach number and altitude combinations with several weight, CG, and wingtip position combinations were available. The effects of additional structural modes in the analytical model were investigated at several conditions. Frequency response data available prior to this program were supplemented by additional detailed response data obtained during the flight simulator test program and aircraft ground tests to define in detail the nonlinear response characteristics of the control system over a wide range of frequency and amplitudes. The predicted performance and stability margins indicate that the air vehicle structural response due to turbulence, shaker vane excitation, pilot inputs, or other excitation will be reduced primarily due to effects of increased structural mode damping. Short-period dynamics or transient response should not be affected. The shaker vane response will provide the capability for demonstration of this performance in flight as desired, whereas it will be difficult to schedule evaluation of gust response. The pilot inputs may not excite modes other than the first mode. Very large reductions of the first mode response are predicted. Smaller improvements in the response of other modes are anticipated.

The results have established usable gain levels which have large stability margins while providing some performance improvement. Input and excitation levels are available to demonstrate this performance above the system threshold and yet will allow operation below system saturation. Saturation should not result in system stability problems. The system should also be free of low amplitude residual oscillations which can exist in many systems due to hysteresis effects. As is the case for all systems, continued increase of system gain will cause an instability (in this case, a limit cycle). In the existing ILAF system design, it is believed that maximum gain adjust settings are below the points of potential instabilities. The accuracy of the predicted

performance is, of course, based upon the validity of the analytical models used in the analyses. The nature of the results indicates that areas of uncertainty can be approached with a buildup set of conditions in the flight-test plan with appropriate telemetering and data analysis support.

The areas of uncertainty are (1) the effect of additional structural modes which have not been included in the analyses, (2) the effect of variations in the control surface resonance characteristics, (3) the effect of undefined aerodynamic behavior, (4) the effect of undefined system nonlinearities, and (5) control surface load effects. The effect of these uncertainties can cause lower stability margins. This emphasizes the need for a cautious approach to the flight-test program plan.

APPENDIX A

SYMBOLS AND UNITS

Table A1 contains a list of the symbols used in this report. Table A2 is a conversion table to relate the U.S. Customary Units to the International System of Units.

TABLE A1

SYMBOLS

NOTE: All aerodynamic, mass, and structural data are in body axes systems.

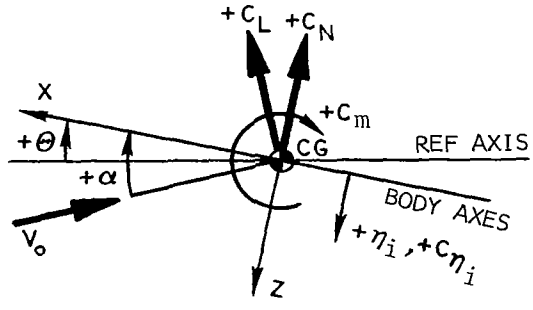

q_o	$(1/2)\ \rho V_o^2$, dynamic pressure
ρ	density of air
$\frac{\Delta P}{q_o}$	pressure coefficient where ΔP is pressure difference between upper and lower surface
V_o	resultant velocity of the center of gravity
w_g	vertical gust velocity
$\Phi_{GUST}\ (\ )$	vertical gust power spectral density; ( ) is either ω, Ω or f

M	mach number
h_p	pressure altitude
$\Lambda_{c/4}$	sweep angle of quarter chord element
λ	taper ratio
AR	aspect ratio
S_w	wing area
$\bar{c}_w$	wing mean aerodynamic chord
ℓ_δ	distance from CG to accelerometer located at control surface
ℓ_{CG}	distance from CG to accelerometer located near CG
ℓ_{c_1}	distance between canard center of pressure and center of gravity; + as defined
ℓ_{c_2}	distance between 3/4 chord point on canard MAC and wing 3/4 $\bar{c}_w$ point; + as defined
ℓ_x, ℓ_y	distance along the X and the Y axis, respectively
$\bar{\ell}_k$	distance from control surface k hinge-line to vehicle CG; + from CG aft
ℓ_k	distance from control surface k hinge-line to surface CG; + from hingeline aft
L	scale of turbulence
I_y	moment of inertia about the Y body axis
Wt	total airplane weight
m	total airplane mass
Δm	incremental mass

m_k	mass of control surface k
$I_{(\ )_{HL}}$	moment of inertia about hingeline; ( ) subscript identifies surface
M_i	the ith mode generalized mass $\iint \phi_i^2 \overline{(x, y)}\ m\ (x, y)\ dxdy$
Θ, θ	Euler pitch angle
q	pitching rate about Y-axis, $d\theta/dt$
α	angle of attack, angle between projection of resultant velocity vector on XZ plane and X body axis
α_C	canard angle of attack
δ	a control surface deflection
δ_S	servo output displacement
δ_{SC}	servo command input
δ_{SV}	shaker vane deflection; positive deflection produces + C_N force
δ_C	canard deflection; positive deflection produces + C_N force
δ_T	wingtip deflection
$\delta_{(\ )}$	elevon deflection; positive deflection produces positive lift (+ C_N) force; ( ) subscript indicates particular elevon surface
$\overline{\delta}_1$	inboard elevon deflection used as a reference when inboard drives outboard elevons
δ_{INBD}	inboard elevon
δ_{OUTBD}	outboard elevons exclusive of inboard elevon (alternate designation to that previously indicated for elevons)

σ_{w_g}	root mean square vertical gust velocity
$\sigma_{\delta_{e_{(\ )}}}$	root mean square elevon deflection; subscript ( ) indicates source of motion
$\sigma_{\dot{\delta}_{e_{(\ )}}}$	root mean square elevon deflection rate; subscript ( ) indicates source of motion
σ_{BM}	root mean square bending moment
ϕ, ϕ_1, ϕ_2	phase angles
$n_{z_{(\ )}}$	normal load factor; ( ) subscript indicates location
Δn_z, $\Delta n_{z_{ILAF}}$	blended vertical accelerometer signal; primary ILAF accelerometer signal minus secondary accelerometer signal
$\Phi_{n_{z_p}}(\ )$	normal load factor at pilot station power spectral density
$\sigma_{n_{z_{(\ )}}}$	RMS normal load factor; ( ) subscript indicates location
g	acceleration of gravity
g_{s_i}	structural damping constant, mode i
ζ_i	$g_{s_i}/2$
η_i	generalized coordinate, mode i
$\phi_i^{(\ )}$	the ith normalized mode shape, i.e., ratio of local deflection to deflection at normalizing point (nondimensional); ( ) superscript denotes location
$\phi_i'(\ )$	slope of ith normalized mode: ( ) superscript denotes location
f	forcing frequency, cps

ω	forcing frequency, radians per second
ω_i	natural frequency of ith mode, radians per second
$\omega_{c.o.}$	cutoff frequency, radians per second
ω_{INS}	frequency at which instability occurs
k	reduced frequency, $\omega b/V_o$ where b is a reference length
Ω	ω/V_o, wave number
F	arbitrary force from control surface, reaction jets and the like
$Z_{(\ )}$	aerodynamic force in Z direction, ( ) subscript denotes source
$N_{(\ )}$	aerodynamic normal force (N = -Z), ( ) subscript denotes source
$L_{(\ )}$	aerodynamic lift force ($L \approx N$), ( ) subscript denotes source
$M_{(\ )}$	aerodynamic pitching moment about Y-axis, ( ) subscript denotes source
$Q_{i(\ )}$	generalized force in ith mode $\iint F_{(x,\ y)}\ \phi_i\ (x,\ y)\ dxdy$ ( ) subscript denotes source
$C_N = \frac{N}{S_w q_o}$	normal-force coefficient
$C_{N_\alpha} = \frac{\partial C_N}{\partial \alpha}$	normal-force curve slope
$(C_{N_\alpha})_{WB}$	wing-body-normal-force-curve slope
$C_{N_{\alpha_c}}$	canard-normal-force-curve slope
$C_{N_{I_{\alpha_c}}}$	canard-interference-normal-force-curve slope (acts on wing)
$C_{N_{\delta(\ )}} = \frac{\partial C_N}{\partial \delta_{(\ )}}$	control-normal-force-effectiveness coefficient, ( ) subscript indicates surface

$C_{N_q} = \frac{\partial C_N}{\partial(q\ \bar{c}_w/2V_o)}$	normal-force-due-to-pitching coefficient
$C_{N_{\dot{\alpha}}} = \frac{\partial C_N}{\partial(\dot{\alpha}\bar{c}_w/2V_o)}$	normal-force-due-to-downwash-lag-and-vertical-acceleration coefficient
$C_{N_{w_g}} = \frac{\partial C_N}{\partial w_g}$	normal-force-due-to-vertical-gust velocity coefficient
$C_{N_{\eta_i}} = \frac{\partial C_N}{\partial \eta_i}$	normal-force-coefficient due to ith mode deflection
$C_{N_{\dot{\eta}_i}} = \frac{\partial C_N}{\partial(\dot{\eta}/V_o)}$	normal-force-coefficient due to rate of change of ith mode
$C_m = \frac{M}{S_w\bar{c}_w q_o}$	pitching-moment coefficient
$C_{m_\alpha} = \frac{\partial C_m}{\partial \alpha}$	pitching-moment-curve slope
$(C_{m_\alpha})_{WB}$	wing-body-pitching-moment-curve slope
$C_{m_{\alpha_c}}$	canard-pitching-moment-curve slope
$C_{mI_{\alpha_c}}$	canard-interference-pitching-moment-due-to-canard-angle-of-attack coefficient
$C_{m_{\delta(\ )}} = \frac{\partial Cm}{\partial \delta(\ )}$	control-pitching-effectiveness coefficient, ( ) subscript indicates surface
$C_{m_{\dot{\alpha}}} = \frac{\partial C_m}{\partial(\dot{\alpha}\bar{c}_w/2V_o)}$	pitching-moment-due-to-downwash-lag-and-vertical-acceleration coefficient
$C_{m_q} = \frac{\partial C_m}{\partial(q\bar{c}_w/2V_o)}$	pitching-moment-due-to-pitching coefficient
$C_{m_{w_g}} = \frac{\partial Cm}{\partial w_g}$	pitching-moment-due-to-vertical-gust velocity coefficient
$C_{m_{\eta_i}} = \frac{\partial C_m}{\partial \eta_i}$	pitching-moment coefficient due to ith mode deflection

$C_{m_{\dot{\eta}_i}} = \frac{\partial Cm}{\partial(\dot{\eta}/V_o)}$ pitching-moment coefficient due to rate of change of ith mode

$C_{\eta_i} = \frac{Q_i}{S_w q_o}$ generalized force coefficient

$C_{\eta_{i_{(\ )}}} = \frac{\partial C_{\eta_i}}{\partial(\ )}$ generalized force coefficient due to variable

$(\ ) = \alpha,\ \frac{\dot{\alpha}\bar{c}_w}{2V_o},\ \frac{q\bar{c}_w}{2V_o}\ \ \delta_{sv},\ \delta_l,\ \delta_e,\ w_g$

$C_{\eta_{i_{I_{\alpha_c}}}} = \frac{\partial C_{\eta_{i_I}}}{\partial \alpha_c}$ generalized force coefficient in mode i due to canard interference

$C_{\eta_{i_{\eta_j}}} = \frac{\partial C_{\eta_i}}{\partial \eta j}$ generalized force coefficient in mode i due to deflection in mode j

$C_{\eta_{i_{\dot{\eta}_j}}} = \frac{\partial C_{\eta_i}}{\partial(\dot{\eta}_i/V_o)}$ generalized force coefficient in mode i due to velocity of mode j

$K_{(\ )}$ control system gain associated with parameter in parentheses (use of self-explanatory)

K_1 real part of canard downwash lag vector

K_2 imaginary part of canard downwash lag vector

K_c flexible-to-rigid ratio, canard

$K_\alpha = \frac{q_o S_w}{mV_o}$

$K_q = \frac{q_o S_w \bar{c}_w}{I_y}$

$K_{\eta_i} = \frac{q_o S_w}{M_i}$

$K_{(\ )_q}$ gain for control system ( ) on input from pitch (q) mode

$K_{(\ )_{\eta_i}}$	gain for control system ( ) on input from symmetric structural (η_i) mode, mode i
$R_{(\ )_{\alpha}}$	real part of frequency dependent control system ( ) input from plunge (α) mode
$R_{(\ )_q}$	real part of frequency dependent control system ( ) input from pitch (q) mode
$R_{(\ )_{\eta_i}}$	real part of frequency dependent control system ( ) input from symmetric structural mode (η_i), mode i
$I_{(\ )_{\alpha}}$	imaginary part of frequency dependent control system ( ) input plunge (α) mode
$I_{(\ )_q}$	imaginary part of frequency dependent control system ( ) input from pitch (q) mode
$I_{(\ )_{\eta_i}}$	imaginary part of frequency dependent control system ( ) input from symmetric structural mode (η_i), mode i
i	$\sqrt{-1}$
j	imaginary axis identification on root locus plots
e	exponential base
S	Laplace operator
A	amplitude ratio
CADS	central air data system
FACS	flight augmentation control system
SAS	stability augmentation system (FACS and SAS notation are used interchangeably herein)
AICS	air induction control system

ILAF	Identically Located Accelerometer and Force
FRL	fuselage reference line
MAC	mean aerodynamic chord
CG	center of gravity
rad/sec	radians per second
rms	root mean square
cps	cycles per second
FS	fuselage station
BP	buttock plane
WP	water plane
LT	left
RT	right
deg	degrees
° F	degrees Fahrenheit
SL	sea level
ft/sec	feet per second
Δ	characteristic determinant; also incremental value
$\lvert\ \rvert$	vector magnitude
$(\dot{})$	dotted parameter in parentheses indicates derivative with respect to time

Subscripts:

k	generalized control surface identification
i, j	generalized structural mode identifications
1	inboard elevon
e	all elevons except inboard
2, 3, 4, 5, 6	identification of individual elevon panels exclusive of inboard panel
sv	shaker vane (or exciter vane)
c	canard
p	pilot station
A	accelerometer location
CG	center of gravity

Superscripts:

F	force application point
A, A_1, A_2	accelerometer locations; generalized and at locations 1 and 2
1	inboard elevon location
e	location of all elevons except inboard
$\bar{e}$	all elevons
x, y, z	coordinate location
c	canard location
p	pilot location
δ	control surface location

All other symbols defined as used.

TABLE A2

CONVERSION TO INTERNATIONAL SYSTEM (SI) UNITS

To convert from	to	multiply by
foot	meter	0.30480
foot/second	meter/second	0.30480
inch	meter	0.02540
pound mass (avoirdupois)	kilogram	0.45359
slug	kilogram	14.59390
pound force (avoirdupois)	newton	4.44822

APPENDIX B

GEOMETRIC CHARACTERISTICS OF THE XB-70-1 AIRPLANE

The physical characteristics of the XB-70-1 airplane are presented in table B1.

TABLE B1

GEOMETRIC CHARACTERISTICS OF THE XB-70-1 AIRPLANE

Total wing -	
Total area (includes 2482.34 sq ft covered by fuselage but not 33.53 sq ft of wing ramp area), sq ft	6,297.8
Span, ft	105
Aspect ratio	1.751
Taper ratio	0.019
Dihedral angle, deg	0
Root chord (wing station 0), ft	117.76
Tip chord (wing station 630 in.) ft	2.19
Mean aerodynamic chord (wing station 213.85 in.), in.	942.38
Fuselage station of 25-percent wing mean aerodynamic chord, in.	1,621.22
Sweepback angle, deg:	
Leading edge	65.57
25-percent element	58.79
Trailing edge	0
Incidence angle, deg:	
Root (fuselage juncture)	0
Tip (fold line and outboard)	-2.60
Airfoil section:	
Root to wing station 186 in. (thickness-chord ratio, 2 percent)	.0.30 to 0.70 HEX (MOD)
Wing station 460 in. to 630 in. (thickness-chord ratio, 2.5 percent)	.0.30 to 0.70 HEX (MOD)
Inboard wing -	
Area (includes 2482.34 sq ft covered by fuselage but not 33.53 sq ft wing ramp area), sq ft	5,256.0
Span, ft	63.44

TABLE B1. - Continued

GEOMETRIC CHARACTERISTICS OF THE XB-70-1 AIRPLANE

Aspect ratio	0.766
Taper ratio	0.407
Dihedral angle, deg	0
Root chord (wing station 0), ft	117.76
Tip chord (wing station 380.62 in.) ft	47.94
Mean aerodynamic chord (wing station 163.58 in.), in.	1053
Fuselage station of 25-percent wing mean aerodynamic chord, in.	1,538.29
Sweepback angle, deg:	
Leading edge	65.57
25-percent element	58.75
Trailing edge	0
Airfoil section:	
Root (thickness-chord ratio, 2 percent)	0.30 to 0.70 HEX (MOD)
Tip (thickness-chord ratio, 2.4 percent)	0.30 to 0.70 HEX (MOD)
Mean camber (leading edge), deg:	
Butt plane 0	0.15
Butt plane 107 in.	4.40
Butt plane 153 in.	3.15
Butt plane 257 in.	2.33
Butt plane 367 in. to tip	0

Outboard wing -

Area (one side only), sq ft	520.90
Span, ft.	20.78
Aspect ratio	0.829
Taper ratio	0.046
Dihedral angle, deg	0
Root chord (wing station 380.62 in.), ft	47.94
Tip chord (wing station 630 in.), ft	2.19
Mean aerodynamic chord (wing station 467.37 in.), in.	384.25
Sweepback angle, deg:	
Leading edge	65.57
25-percent element	58.79
Trailing edge	0

TABLE B1. - Continued

GEOMETRIC CHARACTERISTICS OF THE XB-70-1 AIRPLANE

Airfoil section:		
Root (thickness-chord ratio, 2.4 percent)	0.30 to 0.70 HEX (MOD)	
Tip (Thickness-chord ratio, 2.5 percent)	0.30 to 0.70 HEX (MOD)	
Down deflection from wing reference plane, deg		0, 25, 65
Skewline of tip fold, deg:		
Leading edge in		1.5
Leading edge down		3
Wingtip area in wing reference plane (one side only), sq ft:		
Rotated down 25 deg		472.04
Rotated down 65 deg		220.01
	Wingtips	
	Up	Down
Elevons (data for one side):		
Total area aft of hinge line, sq ft	197.7	135.26
Span, ft	20.44	13.98
Inboard chord (equivalent), in.	116	116
Outboard chord (equivalent), in.	116	116
Sweepback angle of hinge line, deg	0	0
Deflection, deg:		
As elevator		-25 to 15
As aileron with elevators at ±15 deg or less		-15 to 15
As aileron with elevators at -25 deg		-5 to 5
Total		-30 to 30

Canard -	
Area (includes 150.31 sq ft covered by fuselage), sq ft	415.59
Span, ft	28.81
Aspect ratio	1.997
Taper ratio	0.388
Dihedral angle, deg	0
Root chord (canard station 0), ft	20.79
Tip chord (canard station 172.86 in.), ft	8.06
Mean aerodynamic chord (canard station 73.71 in.), in.	184.3
Fuselage station of 25-percent canard mean aerodynamic chord, in.	553.73

TABLE B1. - Continued

GEOMETRIC CHARACTERISTICS OF THE XB-70-1 AIRPLANE

Sweepback angle, deg:	
Leading edge	31.70
25-percent element	21.64
Trailing edge	-14.91
Incidence angle (nose up), deg	0 to 6
Airfoil section:	
Root (thickness-chord ratio 2.5 percent)	0.34 to 0.66 HEX (MOD)
Tip (thickness-chord ratio 2.52 percent)	0.34 to 0.66 HEX (MOD)
Ratio of canard area to wing area	0.066
Canard flap (one of two):	
Area (aft of hinge line), sq ft	54.69
Ratio of flap area to canard semiarea	0.263
Vertical tail (one of two) -	
Area (includes 8.96 sq ft blanketed area), sq ft	233.96
Span, ft	15
Aspect ratio	1
Taper ratio	0.30
Root chord (vertical-tail station 0), ft	23.08
Tip chord (vertical-tail station 180 in.), ft	6.92
Mean aerodynamic chord (vertical-tail station 73.85 in.), in.	197.40
Fuselage station of 25-percent vertical-tail mean aerodynamic chord, in.	2,188.50
Sweepback angle, deg:	
Leading edge	51.77
25-percent element	45
Trailing edge	10.89
Airfoil section:	
Root (thickness-chord ratio 3.75 percent)	0.30 to 0.70 HEX (MOD)
Tip (thickness-chord ratio 2.5 percent)	0.30 to 0.70 HEX (MOD)
Cant angle, deg	0
Ratio vertical tail to wing area	0.037
Rudder travel, deg:	
With gear extended	±12
With gear retracted	±3

TABLE B1. - Concluded

GEOMETRIC CHARACTERISTICS OF THE XB-70-1 AIRPLANE

Fuselage (includes canopy) -	
Length, ft	185.75
Maximum depth (fuselage station 878 in.), in.	106.92
Maximum breadth (fuselage station 855 in.), in.	100
Side area, sq ft	939.72
Planform area, sq ft	1,184.78
Center of gravity:	
Forward limit, percent mean aerodynamic chord	19.0
Aft limit, percent mean aerodynamic chord	25.0
Duct -	
Length, ft	104.84
Maximum depth (fuselage station 1375 in.), in.	90.75
Maximum breadth (fuselage station 2100 in.), in.	360.70
Side area, sq ft	716.66
Planform area, sq ft	2,342.33
Inlet captive area (each), sq in	5,600
Surface areas (net wetted), sq ft:	
Fuselage and canopy	2,871.24
Duct	4,956.66
Wing, wing tips, and wing ramp	7,658.44
Vertical tails (two)	936.64
Canard	530.83
Tail pipes	340.45
Total	17,294.26
Engines	6 YJ93-GE-3
Landing gear -	
Tread, ft	23.17
Wheelbase, in.	554.50
Tire size:	
Main gear (8)	40 x 17.5-18
Nose gear (2)	40 x 17.5-18

APPENDIX C

XB-70 ANALOG-SIMULATOR

The XB-70 analog-simulator was used to study the important effects of hardware nonlinearities, SAS-ILAF interface, and servo-through-elevon natural frequencies on the total integrated system performance and stability. Figure C1 shows a diagram of the simulator and analog computer arrangement. The simulator hardware included (1) SAS and ILAF electronics including notch filter, shaping network, and limiters; (2) SAS servo; (3) mechanical system from servo to inboard actuators; (4) right- and left-hand wing inboard elevon (No. 1) actuators; (5) structure simulating weight of the inboard elevons; and (6) the mechanical control system for pilot column inputs. All ILAF and SAS components were dual as required for the fail-safety design, and allowed testing for potential mismatches and nuisance shutoffs. Neither the outboard elevons (no. 2 to 6) nor the corresponding outboard actuators were available; therefore, these components were analog-simulated on the computer along with the vehicle dynamics and sensor signals. The sensors included the SAS gyro, SAS accelerometer, primary ILAF accelerometer, and secondary ILAF accelerometer. The vehicle response included quasi-static aerodynamics simulation in the pitch, plunge, and four structural modes. Frequency-dependent elevon aerodynamics were simulated for the inboard elevon (No. 1) and the outboard elevons (No. 2 through 6). White noise filtered through a lag network was tape-recorded to simulate random turbulence. An oscillator and a digital frequency indicator were used to provide the shaker vane input for evaluating ILAF.

The outboard elevon actuators were analog simulated by the transfer function $20/(S + 20)$. As can be seen on figure 8 in the main text, this approximated the responses of the outboard actuator for the amplitudes of interest. Frequency responses were obtained on simulator components at various amplitudes and compared with similar data obtained on airplane components. In general, the simulator adequately simulated the airplane; however, the natural frequency of the simulator servo-to-elevon system was found to be 13 cps as compared to 20 cps on the airplane. This required readjusting the notch filter, which resulted in lower phase margins due to increased lag below 13 cps. This lower phase margin, in turn, lowered the maximum allowable gain to avoid instabilities. The increased lag below 13 cps also reduced slightly the ILAF capability of damping mode 3. Simple means of restoring some lead without aggravating the 13 cps limit cycle problem were tried, but without success, and redesign of the lead-lag notch filter just for the simulator could not be justified. Thus, damping of mode 3 and maximum allowable gains determined from simulator data should be interpreted with the servo-to-elevon natural frequency difference between the simulator and airplane in mind.

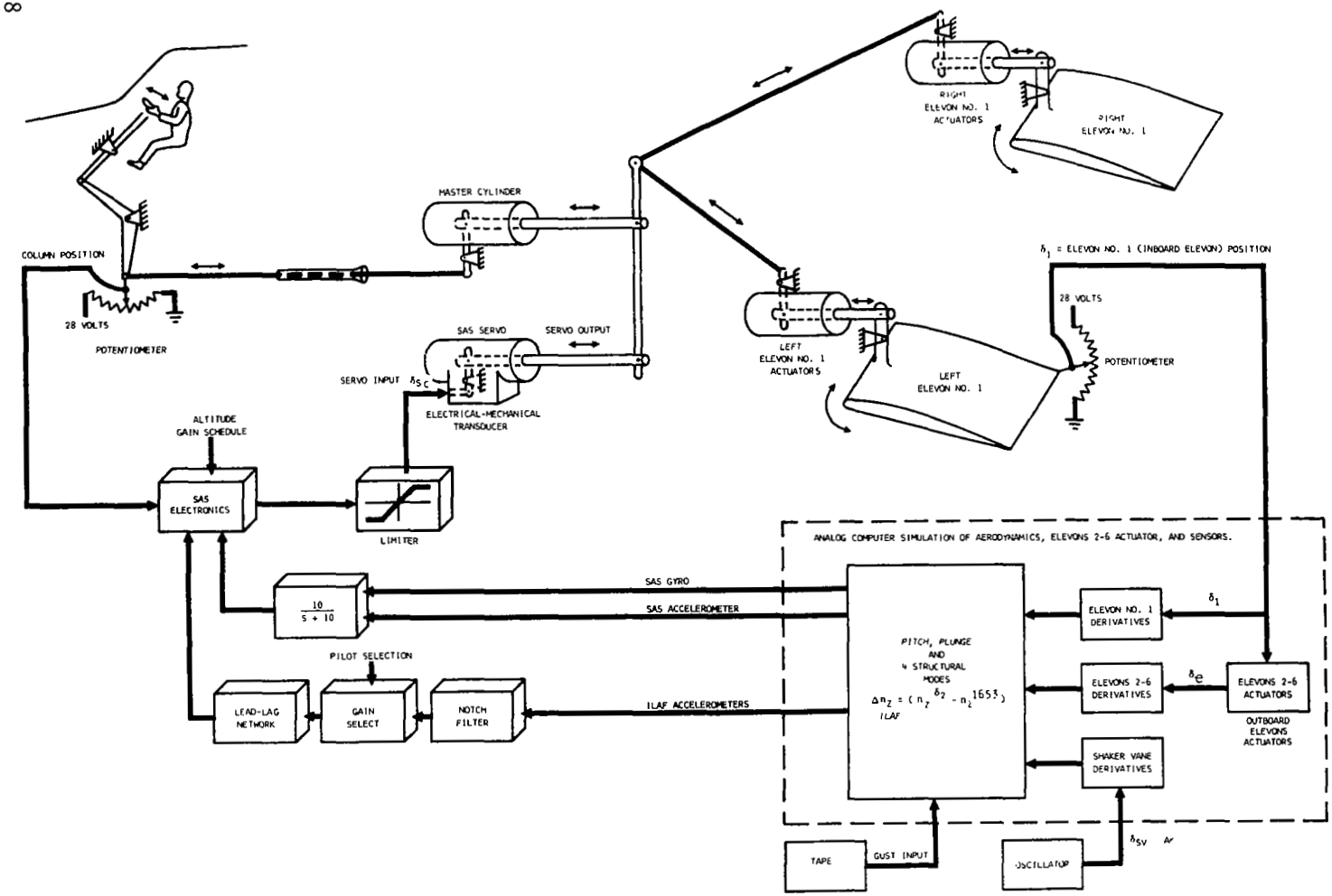

Figure C1.- ILAF system arrangement on the XB-70 simulator.

APPENDIX D

FLEXIBLE AIRPLANE EQUATIONS OF MOTION

The longitudinal-symmetric equations of motion, as used in this study for the flexible XB-70, are presented in this appendix. Two sets of equations are presented. Table D1 contains a linearized set which does not accept frequency-dependent data; this set was used in preliminary stability analyses, analog studies, and to obtain preliminary control system transfer functions for design purposes. Table D2 contains a set of equations expressed in the frequency domain; this set accepts frequency-dependent data. This latter set of equations was used for system evaluations using linear digital programs.

Both sets of equations of motion of the flexible vehicle have the following in common. The equations shown are for the longitudinal-rigid-body pitch and plunge modes and four symmetric structural modes of the complete vehicle. The airplane rigid aerodynamic data and airplane response parameters are in a body reference axes system; the structural mode data and structural response parameters are in the principal body axes system. It has been assumed that:

1. Airspeed (V_o) is constant.

2. Angle of attack (α) is small.

3. Angle of pitch (θ) is small.

4. The rigid-body modes and structural modes are orthogonal.

5. Canard surface aerodynamic data are modified by a flexible-to-rigid ratio (K_c).

6. Canard aerodynamics have been separated from the wing body aerodynamics in the table D2 equations.

7. Motion is determined relative to a trimmed setting.

The units for the equations shown are ft, lb, rad, and sec.

Force, moments, and deflection senses are indicated in the following sketch:

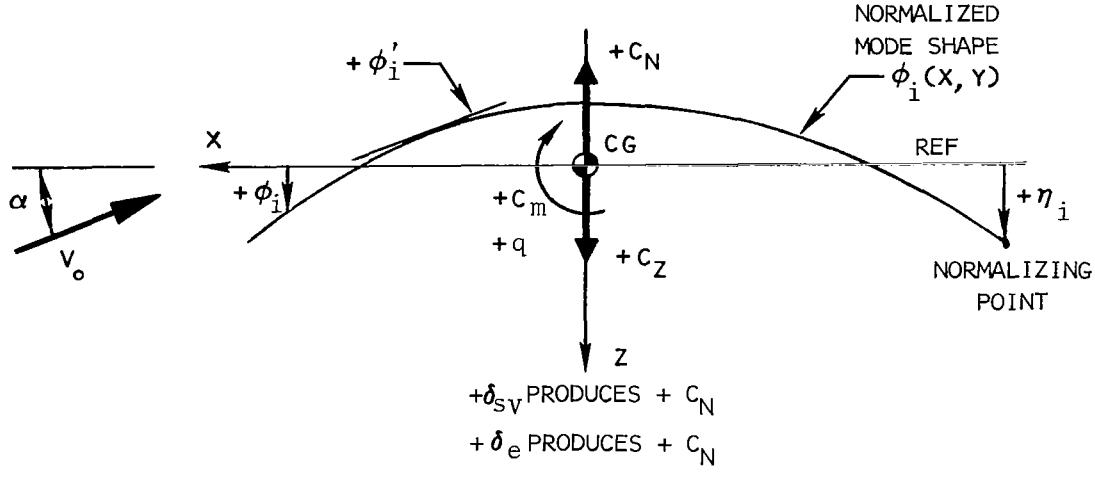

Both sets of equations include a shaker vane and elevon degrees-of-freedom. Each of all six segments of the XB-70 elevons could be represented; however, in practice, the segments were operated as the inboard segment alone and the rest were grouped, necessitating representation of only two sets of elevons. The control surface equations shown in table D2 are of the form: $\delta = K\ (R + iI)\ Y$, where Y is a response variable such as α, K is the gain associated with transfer function indicated, and R and I are the real and imaginary parts, respectively, of the frequency-dependent transfer function δ/Y.

The downwash-lag effects of the canard on the wing are represented in table D2 by the frequency-dependent constants K_1 and K_2. These constants were derived from a trigonometric expansion of expression $e^{-i(\omega l/V_o)}$ which relates the downwash developed at the canard to the downwash impinging on the wing at some later time as the vehicle undergoes sinusoidal oscillation. This downwash effect is approximated in table D1 by the first two terms only of the series expansion of $e^{-i(\omega l/V_o)}$ and combined in the total vehicle derivative; as such, it is only strictly valid for low-frequency oscillations.

The areodynamic data for the basic wing-body are in the form of non-frequency-dependent derivatives, with the exception of gust input. The gust data are entered in the equations of table D2 as real and imaginary numbers at a given frequency. The control surface data also enter the equations in this manner.

No attempt has been made here to derive the equations of motion. The equations as shown should be recognizable by those familiar with the dynamics of flexible vehicles. Those desiring additional enlightenment are referred to an aeroelastic text such as reference 14.

The equations of motion presented in table D2 have been written to emphasize the frequency-dependent aspects of the aerodynamics. This has been done by indicating the real and imaginary parts of the frequency-dependent data. The variables of the problem, the generalized coordinates, are understood to have real and imaginary parts also; they were not explicitly shown in this form in the table because of space limitations. With this bit of background explanation, techniques of solution of the equations of table D2 may be outlined.

The solution technique is that which is developed in reference 15. In brief, it is as follows. The real (R) and imaginary (I) parts of the coefficients must be organized into the following format:

$$\begin{bmatrix} R & -I \\ I & R \end{bmatrix}$$

The generalized coordinates and the forcing loads also must be expressed in the real and imaginary form; that is, as (q_R, q_I) and (F_R, F_I). For n equations of motion, one then has 2n simultaneous equations, of the following form:

$$\begin{bmatrix} R & -I \\ I & R \end{bmatrix} \begin{Bmatrix} q_R \\ q_I \end{Bmatrix} = \begin{Bmatrix} F_R \\ F_I \end{Bmatrix}$$

For a given frequency ω

With this format established, the solution is straightforward using standard simultaneous equation solution techniques.

TABLE D1

EQUATIONS OF MOTION FOR LONGITUDINAL RIGID-BODY AND SYMMETRIC STRUCTURAL MODES, TIME DOMAIN, XB-70, FROM 1-G TRIM CONDITION

RIGID-BODY PLUNGE MODE

$$\dot{\alpha} = q - \left(\frac{\rho_o S_w}{m V_o}\right)\left\{C_{N_\alpha}\alpha + C_{N_{\dot{\alpha}}}\left(\frac{\dot{\alpha}\bar{c}_w}{2V_o}\right) + C_{N_q}\left(\frac{q\bar{c}_w}{2V_o}\right) + \sum_{i=1\text{TO}4} C_{N_{\eta_i}}\eta_i + \sum_{i=1\text{TO}4} C_{N_{\dot{\eta}_i}}\left(\frac{\dot{\eta}_i}{V_o}\right)\right.$$
$$\left. + C_{N_{\delta_{SV}}}\delta_{SV} + C_{N_{\delta_1}}\delta_1 + C_{N_{\delta_e}}\delta_e + C_{N_{W_g}}W_g\right\} - \left(\frac{m_1 l_1}{m V_o}\right)\ddot{\delta}_1 - \left(\frac{m_e l_e}{m V_o}\right)\ddot{\delta}_e$$

RIGID-BODY PITCH MODE

$$\dot{q} = \left(\frac{\rho_o S_w \bar{c}_w}{I_Y}\right)\left\{C_{m_\alpha}\alpha + C_{m_{\dot{\alpha}}}\left(\frac{\dot{\alpha}\bar{c}_w}{2V_o}\right) + C_{m_q}\left(\frac{q\bar{c}_w}{2V_o}\right) + \sum_{i=1\text{TO}4} C_{m_{\eta_i}}\eta_i + \sum_{i=1\text{TO}4} C_{m_{\dot{\eta}_i}}\left(\frac{\dot{\eta}_i}{V_o}\right)\right.$$
$$\left. + C_{m_{\delta_{SV}}}\delta_{SV} + C_{m_{\delta_1}}\delta_1 + C_{m_{\delta_e}}\delta_e + C_{m_{W_g}}W_g\right\} - \left(\frac{\bar{l}_1 m_1 l_1 + I_{1_H}}{I_Y}\right)\ddot{\delta}_1 - \left(\frac{\bar{l}_e m_e l_e + I_{e_H}}{I_Y}\right)\ddot{\delta}_e$$

STRUCTURAL MODES (SYMMETRIC) (Typical Mode i, i = 1 to 4)

$$\ddot{\eta}_i = -g_{s_i}\omega_i\dot{\eta}_i - \omega_i^2\eta_i + \left(\frac{\rho_o S_w}{M_i}\right)\left\{C_{\eta_{i_\alpha}}\alpha + C_{\eta_{i_{\dot{\alpha}}}}\left(\frac{\dot{\alpha}\bar{c}_w}{2V_o}\right) + C_{\eta_{i_q}}\left(\frac{q\bar{c}_w}{2V_o}\right) + \sum_{j=1\text{TO}4} C_{\eta_{i_{\eta_j}}}\eta_j + \sum_{j=1\text{TO}4} C_{\eta_{i_{\dot{\eta}_j}}}\left(\frac{\dot{\eta}_j}{V_o}\right)\right.$$
$$\left. + C_{\eta_{i_{\delta_{SV}}}}\delta_{SV} + C_{\eta_{i_{\delta_1}}}\delta_1 + C_{\eta_{i_{\delta_e}}}\delta_e + C_{\eta_{i_{W_g}}}W_g\right\} - \left(\frac{\phi_i^{1} m_1 l_1 - \phi_i^{1'} I_{1_H}}{M_i}\right)\ddot{\delta}_1 - \left(\frac{\phi_i^{e} m_e l_e - \phi_i^{e'} I_{e_H}}{M_i}\right)\ddot{\delta}_e$$

LOAD FACTOR

$$(n_z)_{\substack{\text{AT ANY}\\\text{STATION}}} = \frac{V_o}{g}(q - \dot{\alpha}) + \frac{l_x}{g}\dot{q} - \sum_{i=1\text{TO}4}^{\text{STA.X}} \phi_i \frac{\ddot{\eta}_i}{g}$$

ROTARY RATES

$$(q)_{\substack{\text{AT ANY}\\\text{STATION}}} = q - \sum_{i=1\text{TO}4}^{\text{STA.X}} \phi_i' \dot{\eta}_i$$

TABLE D2

EQUATIONS OF MOTION FOR LONGITUDINAL RIGID-BODY AND SYMMETRIC STRUCTURAL MODES, FREQUENCY DOMAIN, XB-70, FROM 1-G TRIM CONDITION

PLUNGE MODE (RIGID-BODY)

$$i\frac{\omega\alpha}{K_\alpha} - \frac{g}{K_\alpha} + \left(C_{N_\alpha}\right)_{WB}\alpha + K_c\left(C_{N_{\alpha_c}}\right)\left[\alpha - \left(\frac{l_{c_1}}{V_o}\right)g - \sum_{i=1\text{TO}4}\phi_i^{c'}\eta_i\right] + K_c\left(C_{N_{I_{\alpha_c}}}\right)\left[K_1 + iK_2\right]\left[\alpha - \left(\frac{l_{c_1}}{V_o}\right)g - \sum_{i=1\text{TO}4}\phi_i^{c'}\eta_i\right] + i\,\omega\left(C_{N_{\dot\alpha}}\right)_{WB}\left(\frac{\bar c_w}{2V_o}\right)\alpha + \left(C_{N_{g_I}}\right)_{WB}\left(\frac{\bar c_w}{2V_o}\right)g$$

$$\sum_{i=1\text{TO}4}\left(C_{N_{\eta_i}}\right)_{WB}\eta_i + i\omega\sum_{i=1\text{TO}4}\left[\left(\frac{C_{N_{\dot\eta_i}}}{V_o}\right)_{WB} + K_c\,C_{N_{\alpha_c}}\left(\frac{\phi_i^c}{V_o}\right)\right]\eta_i + i\omega K_c\sum_{i=1\text{TO}4}\left\{\left(C_{N_{I_{\alpha_c}}}\right)\left[K_1 + iK_2\right]\left(\frac{\phi_i^c}{V_o}\right)\right\}\eta_i + \left[\left(C_{N_{\delta_1}}\right)_R + i\left(C_{N_{\delta_1}}\right)_I\right]\delta_1 + \left[\left(C_{N_{\delta_e}}\right)_R + i\left(C_{N_{\delta_e}}\right)_I\right]\delta_e$$

$$-\omega^2\left(\frac{m_1 l_1}{g_o S_w}\right)\delta_1 - \omega^2\left(\frac{m_e l_e}{g_o S_w}\right)\delta_e = -\left[\left(C_{N_{wg}}\right)_R + i\left(C_{N_{wg}}\right)_I\right]w_g \text{ OR } -\left(C_{N_{\delta_{SV}}}\right)_R\delta_{SV}$$

PITCH MODE (RIGID-BODY)

$$-i\left(\frac{\omega}{K_g}\right)g + \left(C_{m_\alpha}\right)_{WB}\alpha + K_c\left(C_{m_{\alpha_c}}\right)\left[\alpha - \left(\frac{l_{c_1}}{V_o}\right)g - \sum_{i=1\text{TO}4}\phi_i^{c'}\eta_i\right] + K_c\left(C_{m_{I_{\alpha_c}}}\right)\left[K_1 + iK_2\right]\left[\alpha - \left(\frac{l_{c_1}}{V_o}\right)g - \sum_{i=1\text{TO}4}\phi_i^{c'}\eta_i\right] + i\omega\left(C_{m_{\dot\alpha}}\right)_{WB}\left(\frac{\bar c_w}{2V_o}\right)\alpha + \left(C_{m_{g_I}}\right)_{WB}\left(\frac{\bar c_w}{2V_o}\right)g$$

$$\sum_{i=1\text{TO}4}\left(C_{m_{\eta_i}}\right)_{WB}\eta_i + i\omega\sum_{i=1\text{TO}4}\left[\left(\frac{C_{m_{\dot\eta_i}}}{V_o}\right)_{WB} + K_c\,C_{m_{\alpha_c}}\left(\frac{\phi_i^c}{V_o}\right)\right]\eta_i + i\omega K_c\sum_{i=1\text{TO}4}\left\{\left(C_{m_{I_{\alpha_c}}}\right)\left[K_1 + iK_2\right]\left(\frac{\phi_i^c}{V_o}\right)\right\}\eta_i + \left[\left(C_{m_{\delta_1}}\right)_R + i\left(C_{m_{\delta_1}}\right)_I\right]\delta_1 + \left[\left(C_{m_{\delta_e}}\right)_R + i\left(C_{m_{\delta_e}}\right)_I\right]\delta_e$$

$$+\omega^2\left[\frac{\bar l_1 m_1 l_1 + I_{1_y}}{(g_o S_w \bar c_w)}\right]\delta_1 + \omega^2\left[\frac{\bar l_e m_e l_e + I_{e_H}}{(g_o S_w \bar c_w)}\right]\delta_e = -\left[\left(C_{m_{wg}}\right)_R + i\left(C_{m_{wg}}\right)_I\right]w_g \text{ OR } -\left(C_{m_{\delta_{SV}}}\right)_R\delta_{SV}$$

STRUCTURAL MODES (SYMMETRIC), MODE 1 SHOWN AS TYPICAL

$$+\omega^2\left(\frac{1}{K_{\eta_1}}\right)\eta_1 - i\omega\left(\frac{g_o\omega_1}{K_{\eta_1}}\right)\eta_1 - \left(\frac{\omega_1^2}{K_{\eta_1}}\right)\eta_1 + \left(C_{\eta_{1_\alpha}}\right)_{WB}\alpha + K_c\left(C_{\eta_{1_{\alpha_c}}}\right)\left[\alpha - \left(\frac{l_{c_1}}{V_o}\right)g - \sum_{i=1\text{TO}4}\phi_i^{c'}\eta_i\right] + K_c\left(C_{\eta_{1_{I_{\alpha_c}}}}\right)\left[K_1 + iK_2\right]\left[\alpha - \left(\frac{l_{c_1}}{V_o}\right)g - \sum_{i=1\text{TO}4}\phi_i^{c'}\eta_i\right] + i\omega\left(C_{\eta_{1_{\dot\alpha}}}\right)_{WB}\left(\frac{\bar c_w}{2V_o}\right)\alpha$$

$$\left(C_{\eta_{1_g}}\right)_{WB}\left(\frac{\bar c_w}{2V_o}\right)g + \sum_{i=1\text{TO}4}\left(C_{\eta_1\eta_i}\right)_{WB}\eta_i + i\omega\sum_{i=1\text{TO}4}\left[\left(\frac{C_{\eta_1\dot\eta_i}}{V_o}\right)_{WB} + K_c\,C_{\eta_{1_{\alpha_c}}}\left(\frac{\phi_i^c}{V_o}\right)\right]\eta_i + i\omega K_c\sum_{i=1\text{TO}4}\left\{\left(C_{\eta_{1_{I_{\alpha_c}}}}\right)\left[K_1 + iK_2\right]\left(\frac{\phi_i^c}{V_o}\right)\right\}\eta_i + \left[\left(C_{\eta_1\delta_1}\right)_R + i\left(C_{\eta_1\delta_1}\right)_I\right]\delta_1$$

$$+\left[\left(C_{\eta_1\delta_e}\right)_R + i\left(C_{\eta_1\delta_e}\right)_I\right]\delta_e + \omega^2\left[\frac{\phi_1'^{e} m_1 l_1 - \phi_1'^{e'} I_{1_H}}{(g_o S_w)}\right]\delta_1 + \omega^2\left[\frac{\phi_1^{e} m_e l_e - \phi_1^{e'} I_{e_H}}{(g_o S_w)}\right]\delta_e = -\left[\left(C_{\eta_{1_{wg}}}\right)_R + i\left(C_{\eta_{1_{wg}}}\right)_I\right]w_g \text{ OR } -\left(C_{\eta_{1_{\delta_{SV}}}}\right)_R\delta_{SV}$$

CONTROL SURFACES (TYPICAL)

$$\delta_{\ell} = K_{\ell_\alpha}\left(R_{\ell_\alpha} + iI_{\ell_\alpha}\right)\alpha + K_{\ell_g}\left(R_{\ell_g} + iI_{\ell_g}\right)g + \sum_{i=1\text{TO}4}K_{\ell_{\eta_i}}\left(R_{\ell_{\eta_i}} + I_{\ell_{\eta_i}}\right)\eta_i$$

NORMAL LOAD FACTOR (INCREMENT FROM TRIM)

$$n_{z_{(\text{AT ANY STATION X})}} = \frac{V_o}{g}\left(g - i\omega\alpha\right) + i\omega\left(\frac{l_x}{g}\right)g + \left(\frac{l_x}{g}\right)g^2 + \frac{\omega^2}{g}\sum_{i=1\text{TO}4}\phi_i^x\eta_i$$

ROTARY RATES

$$g_{(\text{AT ANY STATION X})} = g - i\omega\sum_{i=1\text{TO}4}\phi_i'^{x}\eta_i$$

APPENDIX E

OPERATIONAL CHARACTERISTICS AND PROCEDURES

The ILAF system is controlled from the control panel located between the pilot and copilot at the rear of the center console. The shaker vane controls are also located on the same panel. This panel is shown in figure E1.

ILAF switch.- A two-position switch on the ILAF system control panel is used to engage and disengage the ILAF system. The switch is latched mechanically at OFF so it must be pulled out before it can be moved to ON. To insure that the FACS pitch augmentation is engaged before the ILAF system is turned on, a solenoid must be energized to hold the ILAF switch at ON. This solenoid is energized only if the FACS pitch is engaged and the landing gear is up. When the switch is at ON, ILAF signals are supplied to the FACS pitch augmentation at a gain selected on the ILAF gain adjustment knob. Moving the switch to OFF disengages the ILAF system. If the switch-holding solenoid is deenergized when the switch is at ON, the switch is released to OFF. The solenoid is deenergized (1) if the FACS pitch is shut off, (2) if the automatic disengagement of the FACS pitch or ILAF system occurs, or (3) if the FACS or vane-ILAF emergency disconnect button is actuated.

ILAF gain and adjustment knob.- When the ILAF switch is at ON, rotation of the gain adjustment knob varies the amplitude of the ILAF signal into the FACS pitch augmentation. The knob is on the ILAF control panel and has an index marking range from 0 (zero gain) to 10 (maximum gain). A stop pin on the panel prevents knob movement below 0 and above 10. The knob should be set at 0 before the ILAF switch is moved to ON, and should be returned to 0 before the ILAF switch is turned OFF.

Exciter vane and ILAF system emergency disconnect button.- A hand-held and stowable emergency disconnect button is provided to remove power and disconnect both the ILAF and exciter vane systems without disengagement of the pitch FACS.

Flight augmentation control system disengage button.- Pressing the FACS disengage button on either control wheel shuts off the FACS pitch augmentation, which causes the ILAF system, if engaged, to shut down also.

Flight augmentation control system pitch caution light.- This light, one of four placard-type augmentation system caution lights, comes on to indicate disengagement of the FACS pitch augmentation.

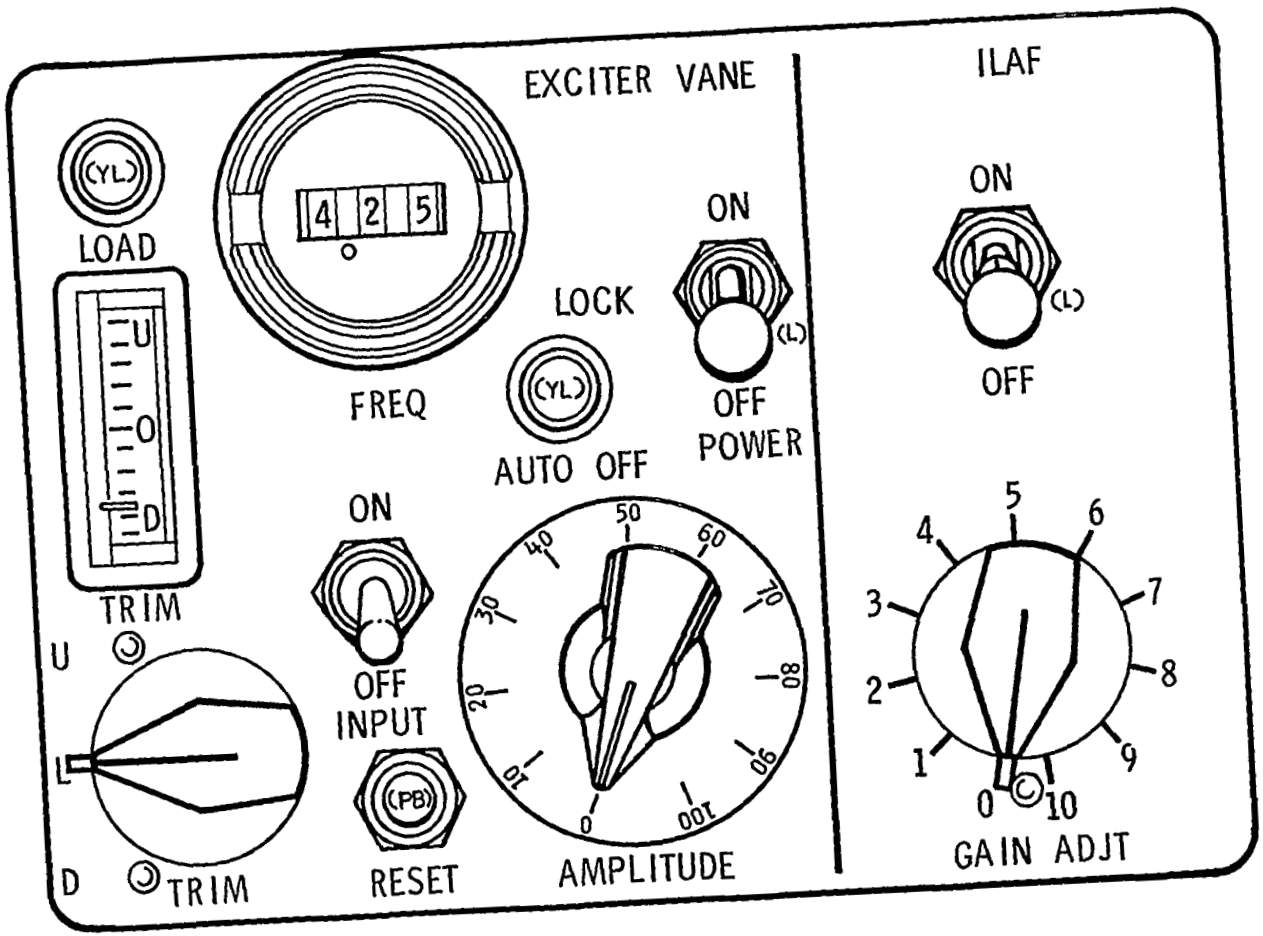

Figure E1.- ILAF and shaker vane control panel.

REFERENCES

1. Andrew, G. M., and Johnson, J. M., Jr, Gust Alleviator, and Rigidity Augmentor for Supersonic Airplanes, IAS Paper No. 62-1, January 1962

2. Andrew, G. M., and Johnson, J. M., Jr, Automatic Control of Aeroelastic Modes, IAS Paper No. 62-86, June 1962

3. Mori, A. S., and Wykes, J. H., "Control System Aspects of an Analytical Investigation into Controlling the Structural Modes of Flexible Aircraft," Proceedings of the SAE-NASA Aerospace Vehicle Flight Control Conference, 13-15 July 1965

4. Wykes, J. H., and Mori, A. S., "Techniques and Results of an Analytical Investigation Into Controlling the Structural Modes of Flexible Aircraft," Proceedings of the AIAA Symposium on Structural Dynamics and Aeroelasticity, 30 August-1 September 1965

5. Wykes, J. H., and Mori, A. S., An Analysis of Flexible Aircraft Structural Mode Control, AFFDL-TR-65-190, June 1966

6. Wykes, J. H., and Knight, R. J., Progress Report on a Gust Alleviation and Structural Dynamic Stability Augmentation System (GASDSAS) Design Study, AIAA Paper No. 66-999, December 1966

7. Smith, R. E., and Lum, E. L., Linear Optimal Theory Applied to Active Structural Bending Control, AIAA Paper No. 66-970, December 1966

8. Smith, R. E., and Lum, E. L., Linear Optimal Control Theory and Angular Acceleration Sensing Applied to Active Structural Bending Control on the XB-70, AFFDL-TR-66-88, February 1967

9. Smith, R. E., Lum, E. L., and Yamamoto, T. G., Application of Linear Optimal Theory to the Control of Flexible Aircraft Ride Qualities, AFFDL-TR-67-136, October 1967

10. Dempster, J. B., and Arnold, J. I., Flight Test Augmentation System for the B-52 Aircraft, AIAA Paper No. 68-1068, October 1968

11. Burris, P.M., and Bender, M.A., Aircraft Load Alleviation and Mode Stabilization (LAMS), AFFDL-TR-68-58, April 1969

12. Landahl, M. T., "Graphical Techniques for Analyzing Marginally Stable Dynamic Systems," AIAA Journal of Aircraft, September-October 1964

13. Kordes, E. E., and Love, B. J., Preliminary Evaluation of XB-70 Airplane Encounters With High-Altitude Turbulence, NASA TN D-4209, October 1967

14. Bisplinghoff, R. L., Ashley, H., and Halfman, R. L., Aeroelasticity, Addison-Wesley Publishing Company, Inc., Reading Mass., November 1957

15. Lanczos, D., Applied Analysis, Prentice Hall, Inc., Englewood Cliffs, N.J., 1956 (page 138)

NASA-Langley, 1970 —— 32